Molecular Interpretation of the Structure, Dynamics and Reactivity of Metal Complexes and Enzymes

Inauguraldissertation

zur

Erlangung der Würde eines Doktors der Philosophie

vorgelegt der

Philosophisch-Naturwissenschaftlichen Fakultät

der Universität Basel

von

Akshaya Kumar Das

von India

Basel, 2018

Genehmigt von der Philosophisch-Naturwissenschaftlichen Fakultät auf Antrag von

Prof. Dr. Markus Meuwly

Prof. Dr. Ursula Roethlisberger

Basel, 27 February 2018

Prof. Dr. Martin Spiess

Dekan

Dedication

This thesis is dedicated to my parents for their encouragment throughout not only my Ph.D, but my entire life.

Acknowledgements

I would like to express my sincere gratitude to Prof. Markus Meuwly for giving me the incredible opportunity to carry out my doctoral research in his group at University of Basel, Switzerland. My immense pleasure to thank my supervisor for his continuous support, able guidance and fruitful scientific discussions. You have set an example of excellence as a researcher, mentor, instructor, and you will always be my role model.

During my scientific career, I am deeply indebted to all my collaborators especially, Prof. Qiang Cui and his group, Prof. Clark R. Landis for their motivational support and scientific discussion. I would also like to thank Prof. Ursula Roethlisberger for willing to be a co-referee of my Ph.D. thesis.

It was a pleasure working with all our present and past group members: Dr. Myung Won Lee, Dr. Tibor Nagy, Dr. Tristan Bereau, Dr. Juan Carlos Castro Palacio, Dr. Pierre-Andre Cazade, Dr. Maurus Schmid, Dr. Florent Hedin, Dr. Juvenal Yosa Reyes, Dr. Prashant Kumar Gupta, Dr. Ana Patricia Gamiz-Hernandez, Dr. Franziska D. Hofmann, Dr. Vijay Solomon Rajadurai, Dr. Maksym Soloviov, Dr. Ganna Berezovska, Dr. Shampa Raghunathan, Dr. Otoniel Denis Alpizar, Zhen-Hao Xu, Oliver Unke, Marco Pezzella, Dr. Leila Mohammadzadeh, Sebastian Brickel, Dr. Krystel El Hage, Dr. Debashis Koner, Dr. Jasmine Lea Desmond, Uxia Rivero Gonzalez, Juan Carlos San Vicente Veliz and Haydar Taylan Turan. Thank you so much for spending wonderful and unforgettable moments. A special Thanks to Dr. Mike Devereux for his computer technical help and support.

I would like to thank official member in the department, Ms. Maya Greuter and Ms. Danni Tischhauser for all their help and support.

I would also like to thank my M.Sc. research advisor, Prof. Nisanth Nair for his constant enthusiasm and encouragement. Finally, I would especially like to thank my amazing family for their love, support and constant encouragement in every aspect of my life. A special thank to my Mom for her unconditional love, patience and immense support, the work in this thesis wouldn't have been possible without your encouragement.

Contents

Abstract

This thesis focuses on the development of molecular mechanical (MM) methods and force fields to model hyper-valent molecules, transition metal complexes and ultimately, the study of enzymatic reactions. Metal specialized VALBOND force fields are developed for transition metals Cu and Fe containing metal complexes and applied to study the structural dynamics of aqueous $[Fe(bpy)_3]$ complexe and the solvation shell around them. In particular, structural rearrangement of solvation shell around the metal complexes during the electronic excitation/redox and spin cross over process were investigated in detail using the VALBOND method. Over the last 30 years, with the advent of ultrafast spectroscopy, particularly time-resolved X-ray absorption spectroscopy (XANES), it is possible to capture the sub-picosecond solvation dynamics around metal ions, providing a basis not only to validate our model but also complementing experimental findings. Specifically, this is done for the Cu ion with bioactive ligands *eg.* imidazole, *i.e* the $[Cu(Imd)_4]^{2+}$ complex, where control of hydration around the metal center was studied thoroughly and it is observed that the intra-molecular degrees of freedom *i.e* planarity in the Cu-Imd plane controls the hydration around the Cu center.

A new Multi-State VALBOND (MS-VALBOND) method was developed for modeling transition metal-containing and hypervalent molecules. This approach is particularly suited for molecules with unusual shapes and systems that need to be described by a superposition of resonance structures, each of which satisfies the octet rule. The implementation is based on the original VALBOND force field and allows smooth switching between resonance structures, each of which can be characterized by its own force field,including varying charge distributions, and coupling terms between the states. Successful implementation of MS-VALBOND in one of the most popular molecular dynamics MD packages CHARMM was tested using a hypervalent molecule ClF_3, the metal complex cisplatin and the S_N2 reaction $BrMe + Cl^- \rightarrow Br^- + MeCl$ in aqueous solution.

Abstract

Finally, an enzymatic reaction the nitric oxide dioxygenation in truncated hemoglobin (trHbN) and its active site mutant Y33A was explored using advanced multi-surface adiabatic reactive molecular dynamics (MS-ARMD). The ligand exchange reaction, $FeNO+O_2 \rightarrow FeO_2+NO$ (starting from a HbNO state), which is the very first step of the NO_3^- formation was studied and found to be the rate determining step. The computed kinetics agrees very well with experiment.

Part I.

Introduction

1. Introduction

1.1. Transition Metals and Coordination Chemistry

Transition metals (TM) are the elements whose d-orbitals are incompletely filled in their neutral and cationic states. They are called TM because their properties lie between the highly reactive s-block elements and the less reactive p-block elements. Also, the properties of transition metals depend on the number of d-electrons and their arrangement in the d-orbitals because the partially filled d-orbitals are affected by the surrounding environment such as ligands or solvents. TM have ionization energies in between the s- and p-block elements. One of the important properties of TM is that they show variable oxidation states due to the low energy difference between them and the valence electrons used in bonding with other elements are present in more than one shell. The elements present in the middle of the d-block, in particular show a wide range of oxidation states (0 to +8). Along with variable oxidation states, TM also possess other physical properties like high melting and boiling points, high density and are very good conductors of heat and electricity. The unpaired $(n-1)d$ electrons of TM are responsible for their paramagnetic properties. The paramagnetic character increases with increase of number of unpaired electrons in the $(n-1)d$ orbitals. TM with paired electrons show diamagnetic character. Iron, titanium and copper are the most abundant transition elements and they have been used as catalysts for several industrial reactions either in their pure form or as compounds, because transition metals can easily inter-convertible from one oxidation state to another and hence helps in various redox reactions. Transition metals play very important roles in the design of both homogeneous and heterogeneous catalysts.

Because TM ions have empty or partially filled d-orbitals that are more exposed to the environment and have high cationic charge and a small size, they have the ability to accept electron pairs from other neutral or charged species (called ligands) to from coordinate bonds ($M + :L \rightarrow ML$) and the resulting compounds are called coordination compounds or coordination complexes. Coordination

chemistry nowadays is based on research from the nineteenth century by Swiss chemist Alfred Werner; he was the first to suggest the correct structure for coordination compounds. His pioneering work focused on the $[Co(NH_3)_6]Cl_3$ molecule, where he suggested that the Co(III) ion is surrounded by six NH_3 ligands, directed towards the corner of an octahedron. The constant number 6 is called the coordination number (secondary valency). For this work he was awarded a Nobel prize in 1913. This concept of secondary valency provided the basis for further development in the field of coordination chemistry.

The coordination number of the metal ion depends both on the type of the metal ion and their oxidation states. For example Mn(II) shows coordination number 6 whereas Mn(VII) prefers a coordination number of four. Also Zn(II) has a preference for a coordination number of four whereas Fe(II) prefers coordination number six. Depending on the coordination numbers, oxidation state, ligands and orientation of the coordinated ligands, the properties of metal complexes change. Unlike alkali or alkaline earth metals where the valence orbital (*s*-orbitals) is spherical, for TM the *d*-orbitals are not spherically symmetric (see Figure 1.1). So, the shape and the number electrons present in the *d*-orbitals becomes crucial in predicting both physical and chemical properties.

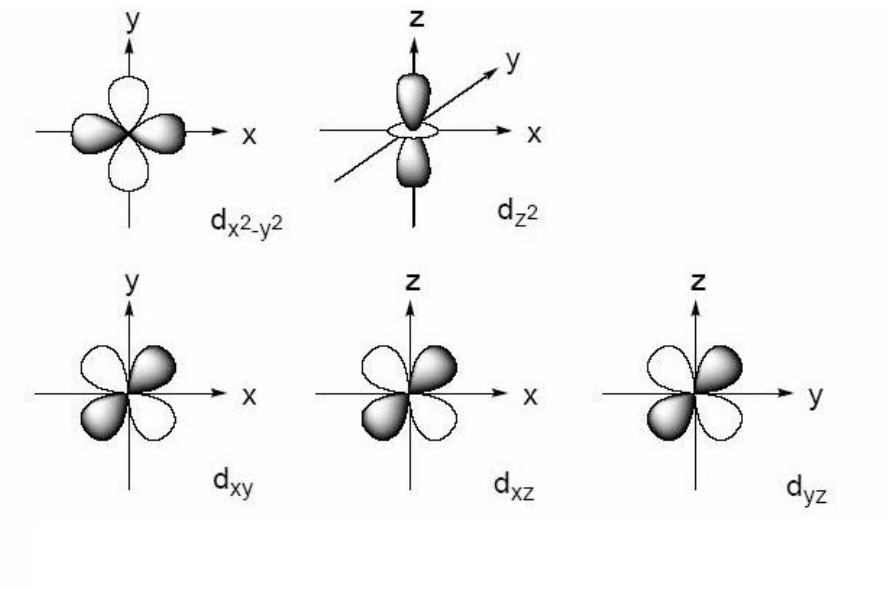

Figure 1.1.: Shape of five *d*-orbitals

In a free TM ion all the *d*-orbitals are degenerate and if six ligands approach uniformly then all of them are equally affected and their energies raised equally due to electrostatic repulsion. However,

when the ligands approach along the vertices of an octahedron then the d-orbitals directed along the axes (d_z^2 and $d_{x^2-y^2}$) are affected more compared to the orbitals directed in between the axes (d_{xy}, d_{xz} and d_{yz}) . So, when the six ligands are placed at each corner of an octahedron, the five d-orbitals lose their degeneracy and the orbitals split into two sets t_{2g} orbitals (d_{xy}, d_{xz} and d_{yz}) and e_g orbitals (d_{z^2} and $d_{x^2-y^2}$) (see Figure 1.2). This breaking of degeneracy of d-orbitals due to the presence of ligands in TM complexes is described by Crystal Field Theory (CFT).

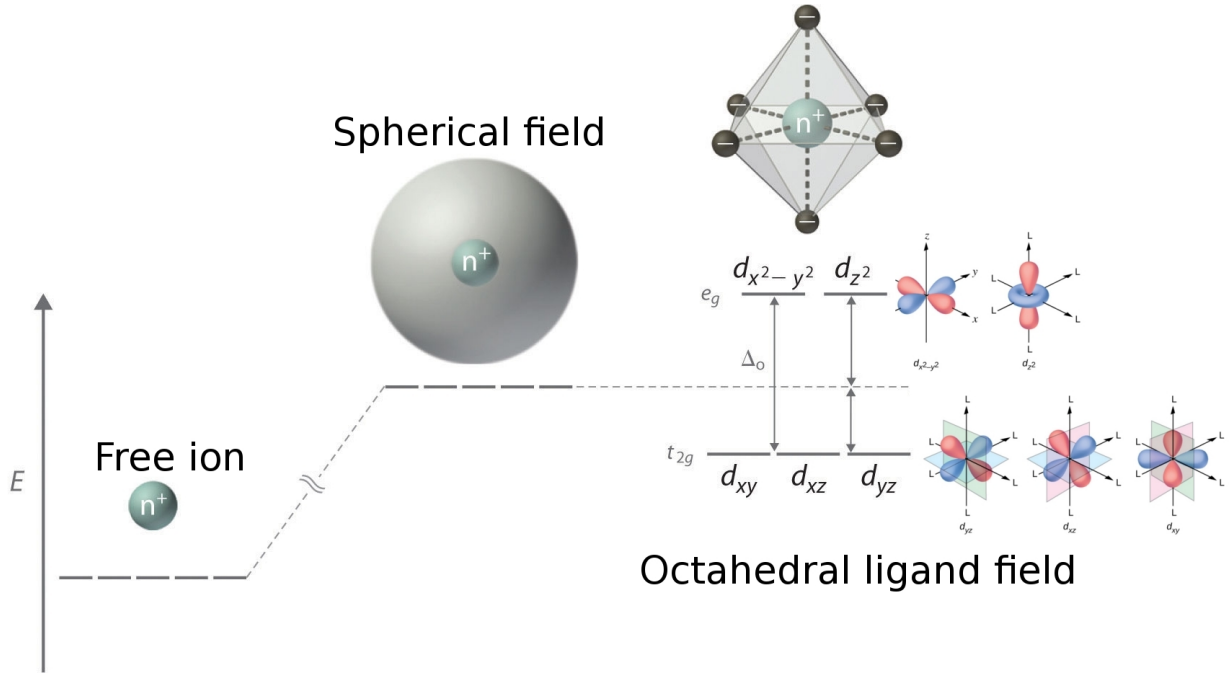

Figure 1.2.: Splitting of d-orbitals in an octahedral ligand field. Δ_0 is the crystal field stabilization energy (CFSE). The energy of e_g orbitals raised by $\frac{3}{5}\Delta_0$ and t_{2g} orbital energies lowered by $-\frac{2}{5}\Delta_0$

The magnitude of the d-orbital splitting depends on the oxidation state of the metal, the nature of the ligand and geometry of the complex. Thus, CFT can be used to predict the energy of d-orbitals and their occupancy. This helps in predicting chemical properties like color and magnetism of TM complexes. Since, the energy gap between the non-degenerate d-orbitals corresponds to the energy of radiation of the visible light, most of the TM complexes are colored due to the d-d transition. From the arrangement of electrons in the non-degenerate d-orbitals, it is possible to predict the magnetic properties from the number of unpaired electrons. TM with d^4 to d^7 electrons can posses both low-spin (LS) and high spin (HS) character depending on the crystal field stabilization energy (CFSE) and the

pairing energy.

Since TM complexes show optical and ferromagnetic properties, they are used in designing solar cell and spintronic materials. Furthermore, many TM complexes incorporate organic molecules as ligands and thus influence their reactivity. The catalytic activity of TM complexes can be tuned by modifying their ligands. Due to the multiple properties of TM complexes such as variable oxidation state and coordination number, their special spectroscopic, magnetic and catalytic properties they are not only used in designing new material but also assists in developing new drugs. For instance TM complexes used in clinical applications like chemotherapeutic agents (cisplatin).

As mentioned earlier, TM can easily change their oxidation state which helps in designing photo-catalytic and photo-redox systems. TM have unpaired *d*-electrons and they can bind easily with molecular oxygen and ends in oxygenation of many natural organic molecules. By means of atmospheric oxygen and solar light both photo-redox and photo-catalytic systems help in oxidation of dissolved organic pollutants. Thus TM complexes play an important role in the environmental processes.

1.2. Structure and Reactivity of Transition Metal Complexes

Structure: Although several experimental techniques have been developed to resolve the TM-complex structures, it has always been a difficult problem. There are several factors which control the geometry of the metal complexes.

1. *Metal atom*: The geometry of the transition metal complexes depend on the nature of the metal atom coordinated to the ligands. Metal complexes with same coordination environment but with different metals of the same oxidation state can have different structures. For example, $[CoCl_4]^{2-}$ and $[PdCl_4]^{2-}$ have the same coordination shell of four Cl^- ions coordinated to the respective metal atoms. However, their geometries are different, $[CoCl_4]^{2-}$ is tetrahedral whereas $[PdCl_4]^{2-}$ is square planar[1].

2. *Nature of the ligands*: The type of ligand coordinated to the metal atom also regulates the geometry of the complex. Both $[Ni(CN)_4]^{2-}$ and $[Ni(Cl)_4]^{2-}$ have the same metal ion and same oxidation state but their coordinated ligands are different. Here, the coordinated ligands are responsible for their different structures, $[Ni(CN)_4]^{2-}$ is square planar and $[Ni(Cl)_4]^{2-}$ is tetrahedral[2,3].

3. *Ligand-Ligand interactions*: Though ligand-ligand interaction is less important for the geometry prediction of the metal complexes, it can not be neglected. The most important ligand-ligand interactions are steric effects, H-bonding and the chelate effect. The steric effect can be followed by considering *cis* and *trans* isomers of a square planar complex $[M(X_2)(PR_3)_2]$ (where, X and R are halogen and alkyl groups respectively). In general the *trans* isomer is more stable than the *cis* isomer due to the reduced steric hindrance of bulky ligands. Also, the effect of H-bonding between the ligands is evident in the $[Cu(H_2Tpy^{NMes})Cl]ClO_4$ complex[4]. Usually, Cu(I) complexes are tetrahedral, however in this case the Cl atom forms a H-bond with the hydrogen atom of the amine group and forms a square planar structure[4].

4. *Chelate effect*: The chelate effect is the extra stability to the complex when a polydentate ligand is bound to the metal atom compared to monodentate ligands[5]. The extra stability comes from the entropic contribution. For example, metal complexes with ethylenediamine (EN) ligand are more stable than their corresponding NH_3 complexes, though both the ligands are very similar (Nitrogen is the donor atom)[5].

Reactivity: The reactivity of transition metal complexes is one of the most important properties and the reason why they have been used in inorganic chemistry, biochemistry, catalysis and geochemistry. In general the reactivity of transition metal complexes is divided into two types: ligand substitution reactions and redox reactions. TM complexes acts as a catalyst due to their labile and redox properties which help them to catalyze a wide range of reactions. The capacity of a metal complex to under go substitution reactions with its ligands is called the lability of the metal complexes. Labile metal complexes undergo faster substitution reactions than rigid complexes[6]. More importantly, TM complexes have been used in asymmetric catalysis to obtain enantiomerically pure compounds[7]. This has lead to a great use of TM complexes as catalysts in the pharma industry for the synthesis of drug molecule.

1.3. Metal Proteins

About 50% of all known proteins require metal ions to carry out their physiological functions[8]. Usually metal ions are coordinated by donor atoms like N, O, and S from the side chain of amino acids or the backbones. Non-amino-acid ligands such as water, anions and small organic molecules can also provide extra donor atoms. When the metal ion is present in the active site of the protein then

its called a metalloenzyme. In metalloenzymes, the metal ion is present in the pocket where the substrate can fit. For most of the metalloenzymes, the active site contains transition metal ions due to the fact that they can easily inter-convert from one oxidation state to another and hence able to bind both soft and hard donors of labile coordination domain in the active site pocket. In general metal ions with small size and high charge prefer to bind strong donors such as N-imidazole(His), corboxylate-(Glu/Asp) whereas weaker ligands S-(Cys/Met) like to bind metal ions with low charge[9]. Thus, oxidation state of the metal ion and the coordination environment in the active site determines their chemical reactivity and properties. Metalloproteins play many important roles in cells, such as oxygen transport, electron transport and redox reactions[10–13]. Two such examples of metalloproteins are *Plastocyanin* and *Hemoglobin* (Hb), the two proteins along with their active site are shown in Figure 1.3. In plastocyanin, the active site contains a cooper ion bound to two His and two Met residues[14]. *Plastocyanin* helps in electron transport processes associated with photosynthesis[15]. It transports electron from Cytochrome complex to Photosystem- I[16]. On the other hand, the active site of Hb contains a Fe ion along with the porphyrin ring and proximal His residue. Hb helps in efficient transport of oxygen from the lungs to the body tissues[17]. Transition metal ions in the active site catalyze organic/inorganic reactions which are hard to achieve *in vitro*.

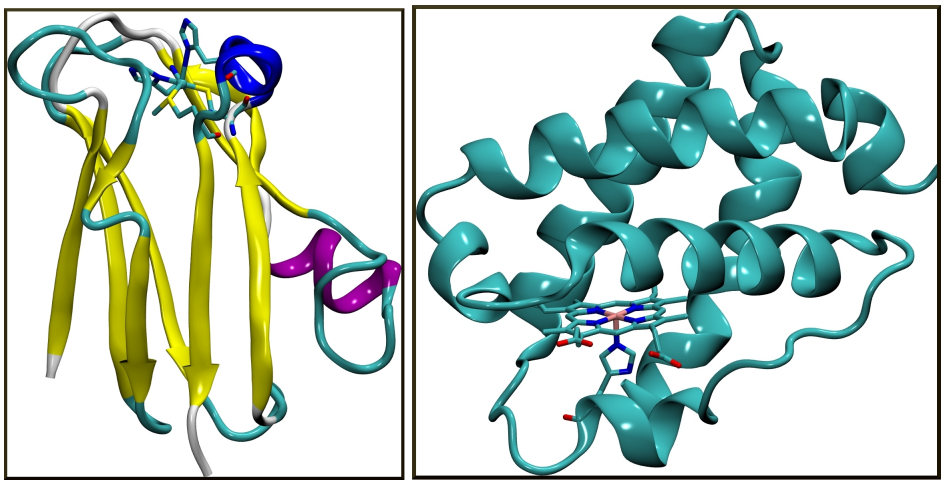

Figure 1.3.: Plastocyanin (left) and Truncated hemoglobin (right) 3D structures. Cu and Fe binding active sites are shown in spheres and bonds. Atom color code used: Cu (cyan), Fe (pink), Nitrogen (blue), Oxygen (red) and Carbon (cyan). Hydrogen atoms were omitted for clarity.

1.4. Ultrafast Solvation Dynamics Around Metal Complexes

In general, chemical and biochemical processes take place in liquids. Thus, the local organization of the solvent molecules around a solute plays crucial role in regulating the chemical properties of the solute in condensed phase. Hence, the reaction rate, mechanism and the selectivity (formation of different isomers) of chemical reactions predominantly depends on the environment. Important properties of solvents that affect the rate and the selectivity are the solubility of the reactant and catalyst, polarity, proticity (hydrogen-bond donating ability) and basicity (hydrogen-bond accepting ability). Since 1940, considering the demand for cheaper and more efficient processes in the synthetic chemical industry, there has been an upsurge of research in the field of catalysis by TM complexes [18,19]. As mentioned earlier TM complexes play very important roles in both homogeneous and heterogeneous catalysis. The dynamical response of the solvent molecules around the catalyst and the reactant plays a crucial role in the rates and selectivity of the products: particularly the solvent molecules react to the changes in volume and electron distribution around the solutes to minimize the free energy of the solution, thus stabilizing (or destabilizing) intermediate states and the activation barrier [20]. Hence, it is of utmost important to understand the organization of solvent molecules around the metal complexes to design not only efficient catalysts but also efficient light-harvesting materials, as this involves charge transfer [21–23]. However, the organization of solvent molecules around the metal complexes occurs very fast on a sub-picosecond scale and makes it difficult to characterize the structural arrangement of solvent molecules around the metal complexes. In recent years, with the development and progress of ultrafast spectroscopic techniques including time-resolved infrared (TRIR) and Raman (TRR) [24,25], time-resolved X-ray liquidography (TRXL) [26], time-resolved X-ray absorption near-edge spectroscopy (XANES) and X-Ray absorption fine-edge spectroscopy (EXAFS) [27–29] has helped to provide the information about the temporal rearrangements of solvent around metal complexes. Over the years, these spectroscopical techniques employed to elucidate excited state intramolecular hydrogen bonding [30], *cis-trans* isomerization in retinal proteins [31,32], dynamics of photocatalysis and reorganization of solvent molecules in response to photo-excitation [20,33,34].

Nonetheless, experimental characterization alone is not sufficient for the molecular level interpretation of the heterogeneous and complex dynamics of the system. On the other hand, atomistic simulations provide much needed and advanced information about structural rearrangements of the system and the reorganization of the solvent molecules around the solute [35–38].

1.5. Challenge for Modeling Transition Metal Complexes

Considering the importance of transition metals and their coordination compounds, characterization of their structures and reactivity is essential for designing efficient catalysts, solar cell materials, and therapeutic agents. Over the years several experimental methods have been applied to characterize their structure, physical properties and reactivity. For structural characterization in the solid state, experimental techniques like X-ray diffraction (XRD), Neutron diffraction, Atomic force microscopy (AFM) *etc.* have been employed[39]. On the other hand, recently developed experimental methods like X-ray absorption near-edge spectroscopy (XANES) and X-Ray absorption fine-edge spectroscopy (EXAFS) were used to characterize the coordination environment of metal complexes in solution[27–29]. However, using the X-ray diffraction method, it is very difficult to assign the position of the H atoms. In particular, metal complexes with agostic interactions (the interaction between metal and a C-H bond, 3c-2e bond) is very difficult to characterize using X-ray experimental techniques. Also, for metal complexes or metal ions in solution, weakly coordinated solvent molecule exchange very quickly with other solvent molecules (on a picoseconds time scale). Thus, it makes difficult to describe the coordination environment of metal ions in solution. On the reactivity prospect, understanding the mechanistic details of TM catalysis is important for designing efficient catalysts in asymmetric synthesis in organic chemistry and hence essential for the pharmaceutical industry. However, understanding the reaction mechanism of transition metal complexes is very difficult because in most of the cases they are involved with an intermediate of very small life time. Therefore, it is hard to capture the structure and properties of intermediate states using experimental techniques such as XANES, EXAFS, EPR, NMR etc[40].

On the other hand, computational methods are very useful in predicting structure, stability and reactivity of transition metal complexes. In the last decades both computational power and advance in theoretical methods made a substantial progress. In particular, quantum mechanical (QM) methods such as density functional theory (DFT) made a significant progress in last two decades. Specifically, DFT with hybrid functionals like B3LYP have been found to predict structure and properties of transition metal complexes to a good accuracy. In recent years huge efforts have been put to construct more accurate functionals, however at some point all the quantum mechanical methods become very computationally demanding. There is a balance between system size and the level of accuracy *i.e.* smaller systems can be computed using higher accuracy methods. Mostly, DFT calculations are limited

to gas-phase or implicit solvent geometry optimization for systems up to 100 atoms. Explicit solvent effect and dynamics of such syectem using DFT is impractical.

As an alternative to DFT, more efficient semi empirical methods such as AM1, PM3 etc. have been employed to model coordination compounds[41–43]. However, these methods requires parametrization which is none trivial. Regardless of the difficulty in parametrization, some of the semi empirical methods such as MNDO/d[44], SAM/1[45], EHMO-ASED[46], ZINDO[47] and PM3-d[48] have been applied to model metal complexes for a wide range of d-electrons. However, these methods are very new and applied to only a few transition metal system like Fe, Ni, Pd. The performance of these methods are very good in predicting structures, they are bad at the energetics this is due to the fact the parametrization was based on the geometries.

In contrast, molecular mechanics (MM) has been employed to model system with large number of atoms (up to 10^6 atoms) like proteins, lipid membrane *etc.* Molecular mechanics approximate the QM potential energy surface with a classical mechanical model called force field and this helps in reducing the total number of degrees of freedom. Hence, MM are more efficient compared to both DFT and semi empirical methods. However, development of general force fields like OPLS[49], CHARMM[50], AMBER[51] *etc.* for TM systems is complicated. Some of the properties of TM complexes which makes them difficult to model using the force field method are listed here-

1. **Variable Coordination Number**: One of the basic properties of transition metal complexes is the preferred coordination number. Coordination number of the transition metal complexes depends on both nature of the metal ion and the ligands[5]. Most of the transition metal ions posses variable coordination number. For example, Cu^{2+} ion shows coordination numbers 4, 5 and 6 depending on the size and type of the ligands[5]. In general, with increasing coordination number around the metal ion, the metal-ligand interaction decrease and hence their distances. When the coordination number changes, both M-L and L-L interactions change. Thus, the states with different coordination numbers require different sets of force field parameters.

2. **Indistinct Topology**: Unlike σ-donor ligands, π-binding ligands can bind to metal ions in different ways. Three different ways of π-binding ligand coordination to transition metal ion are shown in Figure 1.4. Thus for each coordination pattern, different sets of force field parameters are required to describe the bonding in metal complexes with π-binding ligands.

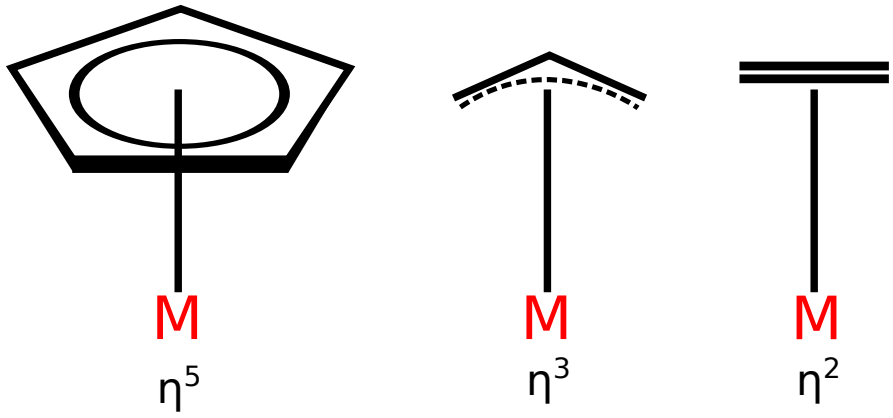

Figure 1.4.: Different modes of binding of π-binding ligands to TM atoms

3. **Variable Oxidation State**: Interplay between oxidation state and geometry in coordination compounds is intricate. In general, with change of oxidation state of the metal center, the geometry of the complex also changes. For example, $[Cu(NH_3)_4]$ complex is tetrahedral in +1 oxidation state whereas for the +2 oxidation state it has a preference for the square planar geometry (see Figure 1.5). Since the geometry of the metal complexes changes with oxidation state, so for each oxidation state it needs a different set of force field parameters to model their geometries accurately.

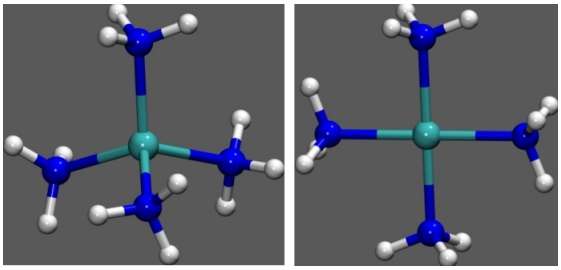

Figure 1.5.: Tetrahedral Cu(I) (left) and square planar Cu(II) geometries (right).

4. **Different Spin States**: Like the oxidation states, the spin states of the metal complexes also controls their geometries. To illustrate the spin state dependent geometry change, consider four-coordinate $[Ni(II)NH_4]$. In it's high spin (HS) state it preferrs a tetrahedral geometry while in the LS it favors a square planar structure[52]. Thus, using conventional MM it requires two sets of parameters to model LS and HS complexes.

5. **Electronic effect or Jahn-Teller Distortion**: Jahn-Teller theorem states that any non-linear

molecular system in a degenerate electronic state will be unstable and will undergo distortion to form a system of lower symmetry and lower energy thereby removing the degeneracy[53]. This means there is no nonlinear molecule that can be stable in a degenerate electronic state. The Jahn-Teller effect is more pronounced for metal ions with high spin d^4, low spin d^7 and d^9 electronic configurations. As mentioned, in an octahedral ligand field the degenerate $d-$orbitals split into two sets t_{2g} and e_g (see Figure 1.2). Consider metal ions with d^9 electronic configurations (Cu^{2+} ion) in an octahedral ligand field, the e_g orbitals can have the configuration $d^2_{z^2}\ d^1_{x^2-y^2}$. Since $d^2_{z^2}$ has more occupancy than $d^1_{x^2-y^2}$, thus the d_{z^2} orbital is screened more by the ligands along the Z-direction and the complex prefers to have an elongated octahedral geometry (see Figure 1.6).

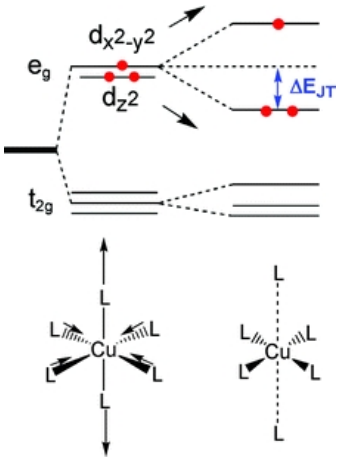

Figure 1.6.: Jahn-Teller distortion in octahedral geometry for d^9 electronic configurations.

So, using conventional force fields to describe the Jahn-Teller distortion requires two different sets of parameters for axial and equatorial ligands.

Therefore, for the correct description of TM complexes using force fields, it needs to incorporate information about the orientation of the ligands and the occupancy of the d-orbitals into the conventional force fields. In recent years several attempts been made to model transition metal complexes using metal specialized force fields. In Chapter 2, some of the metal specialized force field models like LFMM[54], SIBFA and VALBOND[55–58] are described in detail. In this work, the VALBOND-TRANS[59] force field which takes care of the *trans influence* in the transition metal complexes by introducing two distance and energy dependent penalty functions into the VALBOND[55–58] force field is also described in chapter 2 section 2.2.1.4.

Part II.

Theoretical Background

2. Theoretical Background

2.1. Quantum Mechanical Methods

Quantum mechanical methods describe the molecules by wave functions and can be obtained by solving the Schrödinger equation 2.1. These wavefunctions are directly correlated with the structure and energetics of the molecule.

$$\hat{H}\Psi(\mathbf{r},\mathbf{R}) = E\Psi(\mathbf{r},\mathbf{R}) \tag{2.1}$$

$$\left[-\frac{1}{2}\nabla^2 - \frac{Z}{\mathbf{r}}\right]\Psi(\mathbf{r},\mathbf{R}) = E\Psi(\mathbf{r},\mathbf{R}) \tag{2.2}$$

For single electron systems, like the hydrogen atom, the one electron Schrödinger equation (see equation 2.2) can be solved exactly. However, for multi-electron systems the Hamiltonian is rather complicated. Thus, the multi-electron Schrödinger equation 2.3 has not been solved exactly yet. Hence approximations are needed to solve the Schrödinger equation for systems with more than one electron.

$$\left[-\frac{1}{2M_N}\sum_N \nabla_N^2 - \frac{1}{2}\sum_e \nabla_e^2 - \sum_N\sum_i \frac{Z_N}{\mathbf{r}_{iN}} + \sum_i\sum_{j>i}\frac{1}{\mathbf{r}_{ij}} + \sum_{N_A}\sum_{N_B>N_A}\frac{Z_{N_A}Z_{N_B}}{\mathbf{R}_{AB}}\right]\Psi(\mathbf{r},\mathbf{R}) = E\Psi(\mathbf{r},\mathbf{R}) \tag{2.3}$$

Born-Oppenheimer Approximation: The Born-Oppenheimer approximation helps to separate the motion nuclei and electron. This approximation neglects the motion of the nuclei because the atomic mass of the nucleus is much higher than the electron mass. Hence this approximation makes the multi-electron Schrödinger equation simpler and it becomes an *electronic* Schrödinger equation 2.4. Also, the nuclear-nuclear coulombic interaction is just a constant for a fixed set of nuclear positions and

can be included to the electronic energy E_{ele} obtained by solving the electronic Schrödinger equation H_{ele} (see equation 2.4).

$$\left[\underbrace{-\frac{1}{2}\sum_{e}\nabla_{e}^{2}-\sum_{N}\sum_{i}\frac{Z_N}{\mathbf{r}_{iN}}+\sum_{i}\sum_{j>i}\frac{1}{\mathbf{r}_{ij}}}_{H_{\text{ele}}}+\sum_{N_{\text{A}}}\sum_{N_{\text{B}}>N_{\text{A}}}\frac{Z_{N_{\text{A}}}Z_{N_{\text{B}}}}{\mathbf{R}_{\text{AB}}}\right]\Psi(\mathbf{r},\mathbf{R})=E\Psi(\mathbf{r},\mathbf{R}) \tag{2.4}$$

$$\hat{H}_{\text{ele}}\Psi(\mathbf{r},\mathbf{R})=\left[T_{\text{e}}(\mathbf{r})+V_{\text{eN}}(\mathbf{r},\mathbf{R})+V_{\text{ee}}(\mathbf{r})\right]\Psi(\mathbf{r},\mathbf{R})=E_{\text{ele}}\Psi(\mathbf{r},\mathbf{R}) \tag{2.5}$$

Hartree-Fock Approximation: From the above equation 2.5, it is clear that the electronic Schrödinger equation is still intractable. Therefore, to solve the electronic Schrödinger equation the coordinates of the electrons need to be separable. One of the ways to separate electronic coordinates while retaining the electron-electron coulomb interaction V_{ee} is by introducing the independent particle approximation. That is the electrons move independently of each other. However, this approximation only accounts the interaction of electrons in an average way. The best possible way to represent many-body wavefunctions which gives the lowest energy of the system by combining single particle wavefunction into a Slater determinant. This is called Hartree Fock approximation.

The simplest way to represent the N electron wave function is by taking the product of the orthogonal wave functions of the individual electrons (Hartree product)

$$\Psi_{\text{HP}}(\mathbf{x}_1,\mathbf{x}_2,...,\mathbf{x}_N)=\psi_1(\mathbf{x}_1)\psi_2(\mathbf{x}_2).....\psi_N(\mathbf{x}_N) \tag{2.6}$$

However, this doesn't satisfy the *antisymmetry principle.* The general form of total wave function of N electrons which satisfy the Pauli exclusion principle (*antisymmetry principle.*) is formulated by John Slater and called Slater determinant is given by

$$\Psi(\mathbf{x}_1,\mathbf{x}_2,\ldots,\mathbf{x}_N)=\frac{1}{\sqrt{N!}}\begin{vmatrix}\chi_1(\mathbf{x}_1) & \chi_2(\mathbf{x}_1) & \cdots & \chi_N(\mathbf{x}_1)\\ \chi_1(\mathbf{x}_2) & \chi_2(\mathbf{x}_2) & \cdots & \chi_N(\mathbf{x}_2)\\ \vdots & \vdots & \ddots & \vdots\\ \chi_1(\mathbf{x}_N) & \chi_2(\mathbf{x}_N) & \cdots & \chi_N(\mathbf{x}_N)\end{vmatrix} \tag{2.7}$$

The best way to consider the inter-electronic interactions in a N electron wavefunction (represented

by Slater determinant (see equation 2.7)) by minimizing the E_{ele} and is given by

$$E_{\text{ele}} = \frac{\int \Psi^* \hat{H_{\text{ele}}} \Psi d\mathbf{r}}{\int \Psi^* \Psi d\mathbf{r}} \tag{2.8}$$

Using variational method to minimize the E_{ele} under constraints that the orbitals remain mutually orthogonal leads to the following equation

$$\hat{F}_i \phi_i = \epsilon_i \phi_i \tag{2.9}$$

Where $\hat{F}_i$ is the Fock operator and ϵ_i is the orbital energy of ith orbital. For a closed shell system of $2N$ electrons, the Fock operator has the expression

$$\hat{F}_i = h_i + \sum_{j=1}^{N} (2\hat{J}_j - \hat{K}_j) \tag{2.10}$$

h_i is the hydrogen like single electron Hamiltonian given in equation 2.3. $\hat{J}$ and $\hat{K}$ are the Coulomb and exchange integrals and are given by

$$\hat{J}_j(1) = \int \phi_j^*(2)\phi_j(2)\frac{1}{r_{12}} d\mathbf{r}_2 \tag{2.11}$$

$$\hat{K}_j(1)\phi_i(1) = \left[\int \phi_i^*(2)\phi_j(2)\frac{1}{\mathbf{r}_{12}} d\mathbf{r}_2\right] \phi_i(1) \tag{2.12}$$

For Hartree Fock method (HF), for each electron we have to solve equation 2.9 self-consistently using variational principle. For larger systems HF method is computationally demanding as it scales N^4 (where N is the number of basis functions). Hence more sophisticated and efficient methods are required for the electronic structure calculation of complex systems and density functional theory (DFT) comes to the rescue.

2.1.1. Density Functional Theory

Unlike the Hatree Fock method which considers the many-body wavefunction, DFT deals with the electron density which depends only on three x, y and z variables. The foundation behind DFT is that there is a relationship between total electron density and energy. DFT is based on two theorems stated and proven by Hohenberg and Kohn in 1964[60].

Theorem 1: The external potential $v(\mathbf{r})$ is determined to within a trivial additive constant by the ground-state electron density $\rho(\mathbf{r})$.

Theorem 2: The correct ground state density for a system is the one that minimizes the total energy through the functional E[$\rho(\mathbf{r})$].

Following both theorems, the ground state energy of any multi-electron system can be expressed as

$$E(\rho) = T(\rho) + V_{\mathrm{eN}}(\rho) + J_{\mathrm{ee}}(\rho) + E_{\mathrm{xc}}(\rho) \tag{2.13}$$

where ρ is the electron density expressed as $\rho = \sum_i |\psi_i(\mathbf{r})|^2$. In order to find the expression for the $T(\rho)$, Kohn and Sham proposed to calculate the kinetic energy from a non-interacting reference system

$$T_s(\rho) = -\frac{1}{2}\sum_{i}^{N} \langle \psi_i^{\mathrm{ks}} | \nabla^2 | \psi_i^{\mathrm{ks}} \rangle \tag{2.14}$$

where ψ_i^{ks} is the Kohn-Sham orbital and N is the total number of electrons. The nuclei-electron interaction V_{eN} and the electron-electron coulomb interactions J_{ee} can be expressed as

$$V_{\mathrm{eN}}(\rho) = \int \sum_{A=1}^{M} \frac{Z_A \rho(\mathbf{r})}{\mathbf{r} - \mathbf{R}_A} d\mathbf{r} \tag{2.15}$$

$$J_{\mathrm{ee}}(\rho) = \int\int \frac{\rho(\mathbf{r}_1)\rho(\mathbf{r}_2)}{\mathbf{r}_1 - \mathbf{r}_2} d\mathbf{r}_1 d\mathbf{r}_2 \tag{2.16}$$

The last term in equation 2.13 E_{xc} not only describes the exchange and correlation energy but also the difference between the true kinetic energy of the interacting system $T(\rho)$ and non-interacting kinetic energy $T_{\mathrm{s}}(\rho)$. E_{xc} also takes care of the self interaction error by taking the difference between non-classical electron-electron repulsion energy $V_{\mathrm{ee}}(\rho)$ and the coulomb energy $J_{\mathrm{ee}}(\rho)$. Hence, E_{xc} can be expressed as

$$E_{\mathrm{xc}}(\rho) = [T(\rho) - T_{\mathrm{s}}(\rho)] + [V_{\mathrm{ee}}(\rho) - J_{\mathrm{ee}}(\rho)] \tag{2.17}$$

Combining all the energy expressions, the total energy of the N-electron system is given by

$$E[\rho(\mathbf{r})] = -\frac{1}{2}\sum_{i}^{N} \langle \psi_i | \nabla^2 | \psi_i \rangle - \int \sum_{A=1}^{M} \frac{Z_A \rho(\mathbf{r})}{\mathbf{r} - \mathbf{R}_A} d\mathbf{r} + \frac{1}{2}\int\int \frac{\rho(\mathbf{r}_1)\rho(\mathbf{r}_2)}{\mathbf{r}_1 - \mathbf{r}_2} d\mathbf{r}_1 d\mathbf{r}_2 + E_{\mathrm{xc}}[\rho] \tag{2.18}$$

Now, by using the expression for electron density and applying variational principle in order to minimize

the energy of the system, the one-electron Kohn-Sham equation can be expressed as

$$\left[-\frac{1}{2}\nabla^2 - \left(\sum_{A=1}^{M}\frac{Z_A}{\mathbf{r}_{1A}} + \int\frac{\rho(\mathbf{r}_2)}{\mathbf{r}_{12}}d\mathbf{r}_2 + V_{\mathrm{xc}}[\mathbf{r}_1]\right)\right]\psi_i(\mathbf{r}_1) = \epsilon_i\psi_i(\mathbf{r}_1) \tag{2.19}$$

where V_{xc} is the exchange-correlation functional and expressed as

$$V_{\mathrm{xc}} = \frac{\delta E[\rho(\mathbf{r})]}{\delta\rho(\mathbf{r})} \tag{2.20}$$

Finally, the one-electron Kohn-Sham equations 2.19 are solved self-consistently by providing initial guess densities from which new improved sets of wavefunctions and electron densities can be obtained. This procedure continues until convergence is achieved.

The main problem with DFT is that the exact exchange-correlation functional is unknown. The simplest exact exchange-correlation functional is the local density approximation (LDA) and it depends only on the local electron density[61].

$$E_{\mathrm{xc}}^{LDA}[\rho] = \int\epsilon_{\mathrm{xc}}[\rho(\mathbf{r})]\rho(\mathbf{r})d\mathbf{r} \tag{2.21}$$

where ϵ_{xc} is the single electron exchange-correlation energy as a function of electron density. However, it is noticed that the LDA functionals, overestimates the binding energy and under estimates the lattice parameters. Also, it performs very badly for predicting physical properties like energetics and magnetic properties. On the other hand, the generalized gradient approximation (GGA) depends both on the local electron density and it's gradient (see equation 2.22)[61]. GGA functionals performs better towards predicting ground state energy and geometry.

$$E_{\mathrm{xc}}^{\mathrm{GGA}}[\rho] = \int\epsilon_{\mathrm{xc}}[\rho(\mathbf{r}), \nabla\rho(\mathbf{r})]\rho(\mathbf{r})d\mathbf{r} \tag{2.22}$$

In summery, the accuracy in predicting physical and chemical properties of materials using DFT depends on the type of functional used. Some of the LDA functionals are CP, PZ81 and PW92[61]. List of few GGA functionals are PW91, PBE, RPBE and WC[61]. Besides LDA and GGA functionals, hybrid functionals were also developed which consider part of the exact HF exchange. One of the most common hybrid functional is B3LYP (Becke, 3-parameter, Lee-Yang-Parr) functional and it was found to perform reasonably well for predicting geometries and thermochemistry of molecules[62].

2.1.2. Density Functional Tight Binding

Unlike the traditional tight binding method used for the computation of the electronic band structure, self-consistent charge density functional tight-binding (SCC-DFTB) methods have been used to calculate total energy of the system[63,64]. The Density-functional tight binding method (DFTB) is based on Kohn-Sham density functional theory[63,64]. DFTB can be derived from the Taylor series expansion of the DFT total energy. Consider a system composed of atomic densities $\rho^0(\mathbf{r})$, that is no charge transfer occurs between the atoms. But $\rho^0(\mathbf{r})$ doesn't minimize the energy functional. Thus the true density $\rho(\mathbf{r})$ which minimizes the energy functional $E[\rho(\mathbf{r})]$ is slightly perturbed from its reference density i.e $\rho(\mathbf{r}) = \rho^0(\mathbf{r}) + \delta\rho(\mathbf{r})$. Thus the total energy can be expressed by expanding a Taylor series of $E[\rho(\mathbf{r})]$ at $\rho^0(\mathbf{r})$ up to third order in fluctuations $\delta\rho(\mathbf{r})$[64]

$$
\begin{aligned}
E^{\mathrm{DFTB}}[\rho^0 + \delta\rho] = & \frac{1}{2}\sum_{ij}\frac{Z_i Z_j}{\mathbf{R}_{ij}} - \frac{1}{2}\iint\frac{\rho^0(r)\rho^0(r')}{|\mathbf{r}-\mathbf{r}'|}drdr' \\
& - \int V^{\mathrm{XC}}[\rho^0]\rho^0(\mathbf{r})dr + E^{\mathrm{XC}}[\rho^0] \\
& + \sum_i n_i\langle\psi_i|\hat{H}[\rho^0]|\psi_i\rangle \\
& + \frac{1}{2}\iint\left(\frac{1}{|\mathbf{r}-\mathbf{r}'|} + \frac{\delta^2 E^{\mathrm{XC}}[\rho]}{\delta\rho(\mathbf{r})\delta\rho(\mathbf{r}')}\Big|_{\rho^0}\right)\delta\rho(\mathbf{r})\delta\rho(\mathbf{r}')drdr' \\
& + \frac{1}{6}\iiint\frac{\delta^3 E^{\mathrm{XC}}[\rho}{\delta\rho(\mathbf{r})\delta\rho(\mathbf{r}')\delta\rho(\mathbf{r}'')}\Big|_{\rho^0}\delta\rho(\mathbf{r})\delta\rho(\mathbf{r}')\delta\rho(\mathbf{r}'')drdr'dr'' \\
& = E^0[\rho^0] + E^1[\rho^0,\delta\rho] + E^2[\rho^0,(\delta\rho)^2] + E^3[\rho^0,(\delta\rho)^3]
\end{aligned}
\tag{2.23}
$$

From equation 2.23, it is clear that the quality of DFTB depends on the number of terms included. The first order DFTB (DFTB1) contains only two terms $E^0[\rho^0]$ and $E^1[\rho^0,\delta\rho]$ and this leads to a simple eigenvalue problem. Thus, DFTB1 is a non self-consistent tight-binding method. Using the linear combination of atomic orbitals (LCAO) ansatz, the The Kohn-Sham equation can be expressed as[64]

$$
\sum_\nu c_{\nu i}(H^0_{\mu\nu} - \epsilon_i S_{\mu\nu}) = 0 \tag{2.24}
$$

The Hamiltonian $H^0_{\mu\nu}$ and overlap $S_{\mu\nu}$ matrix elements are computed only once and stored in a table. However, DFTB1 method is only suitable for systems like hydrocarbons where charge transfer between atoms is very small[63,64]. On the other hand for systems where there is considerable charge transfer

between atoms higher order terms are important and need to be included. DFTB2 and DFTB3 consider higher order terms; third and fourth terms in equation 2.23 respectively. To maintain the efficiency of DFTB, for DFTB2 the E^2 term contains the density fluctuation $\delta\rho$ is replaced by atomic contributions $\delta\rho = \sum_a \delta\rho_a$ and the atomic contributions are truncated to charge monopoles $\Delta q_a = q_a - q_a^0$ *i.e* Mulliken charge fluctuations in going from the neutral atom to the atom in the molecule. So, the analytical form for the E^2 term is expressed as[63,64]

$$E^2 \approx \frac{1}{2}\sum_{ab} \Delta q_a \Delta q_b \gamma_{ab} \tag{2.25}$$

Where γ_{ab} describes the atomic chemical hardness i.e Hubbard parameters (U_a) and can be derived by taking the second derivative of the total energy with respect to the atomic charge $U_a = \frac{\partial^2 E_a}{\partial q_a^2}$. Since the E^2 term depends on the atomic Mulliken charge and the calculation of Mulliken charge depends on the molecular orbital coefficients. Therefore, the Hamiltonian needed to solve self-consistently, hence the method called self-consistent charge density functional tight-binding (SCC-DFTB)[63,64]. In order to improve the accuracy of DFTB one can go beyond second order by including the third order term E^3 (DFTB3) and can be expressed as

$$E^3 = \frac{1}{6}\sum_a \frac{\partial U_a}{\partial q_a}\Delta q_a^3 \tag{2.26}$$

From the derivation of DFTB, it is clear that several approximations were made and set of parameters were introduced. Thus, DFTB is computationally very efficient compared to DFT, in fact three order of magnitude faster[64]. However, it should be noted that the accuracy of the DFTB depends on the parameter sets. For example, one parameter set may not be able to reproduce both energetics and vibrational frequency accurately[63]. Hence, it is required to tune the parameters and fit them to the appropriate reference systems. Over the years DFTB has been applied to model molecules, clusters and solids. Also, the accuracy of DFTB has been improved by introducing new parameters to capture the dispersion interactions and hydrogen bonding[64]. However, the DFTB method is still restricted to ∼1000 atoms. Hence, more efficient methods are required to simulate large systems like proteins, membranes *etc.* that contain millions of atoms.

2.2. Molecular Mechanical Methods: Force Fields

Many of the systems we would like to study in molecular modelling contain thousands of atoms and are simply too large for sophisticated methods like quantum mechanical methods. On the other hand molecular mechanics (MM) or force field (FF) methods which calculate the energy of the molecules as a function of nuclear coordinates and neglect the electronic effects are very helpful to tackle systems with millions of atoms. Thanks to the Born Oppenheimer approximation without which it wouldn't be possible to formulate the energy of the molecule as a function of only nuclear coordinates. Since MM expresses the total energy of the system by their nuclear coordinates, so it is very useful to describe the ground state properties like equilibrium geometry, energy differences between the conformations etc. In MM it is assumed that the atoms in a molecule are held together by springs. Most of the force fields (like CHARMM[50], AMBER[51], OPLS[49]) describe the potential energy of the molecule in two terms, bonded and non-bonded terms.

$$V(\mathbf{R}) = \sum E_{bonded} + \sum E_{non-bonded} \tag{2.27}$$

Generally, the bonded terms include the energy functions of bonds, angles, rotation of bonds or dihedral angles and improper dihedrals for the out of plane bending.

$$E_{bonded} = \sum_{bond} k_b(b - b_0) + \sum_{angle} k_\theta(\theta - \theta_0) + \sum_{dihedral} k_\phi[1 + cos(n\phi - \delta)] + \sum_{improper} k_\omega(\omega - \omega_0) \tag{2.28}$$

The very first term in equation 2.28 describes the bond stretching, k_b and b_0 are the corresponding force constant and equilibrium bond length respectively. The second term is used for the angle bending, where k_θ is the bending force constant and θ_0 is the equilibrium angle. The third term accounts the dihedral angle, where ϕ is the dihedral angle, δ is the phase shift, n is the periodicity and k_ϕ is the force constant. The last term describes the out of plane bending or improper torsion, where k_ω and ω_0 are the force constant and out of plane equilibrium angle. The various contributions to the force fields are shown in Figure 2.1.

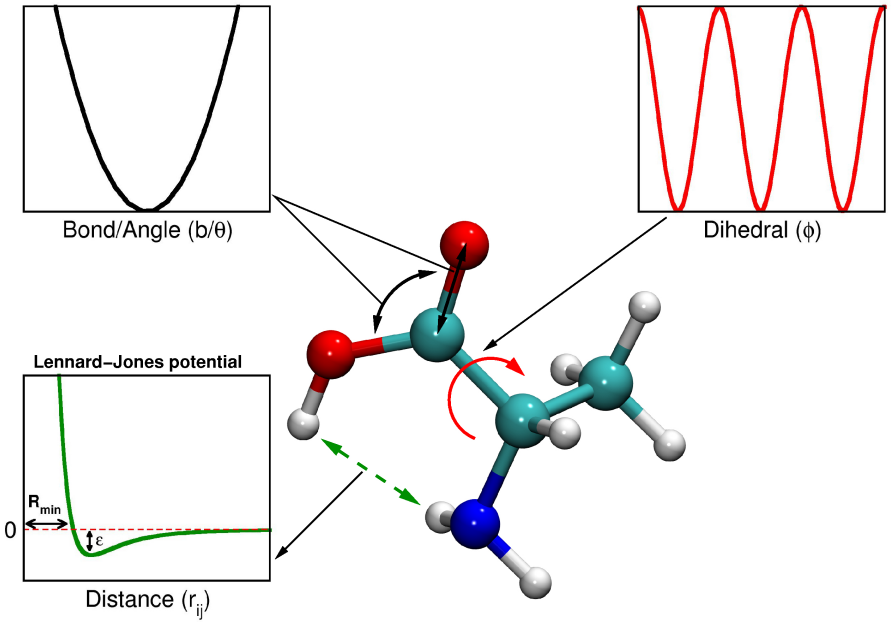

Figure 2.1.: Schematic representation of the force fields along with their potentials: bond stretching, bending, rotation and non-bonded interaction

The $E_{non-bonded}$ term describes the non-bonded interactions between the atom pairs that are not bonded to each other or to a common atom. Further, $E_{non-bonded}$ constitutes electrostatic and van der Waals interaction between the pair of atoms.

$$E_{non-bonded} = \sum_{i<j} \epsilon_{ij} \left[\left(\frac{R_{min_{ij}}}{r_{ij}} \right)^{12} - \left(\frac{R_{min_{ij}}}{r_{ij}} \right)^{6} \right] + \frac{q_i q_j}{4\pi\epsilon_0 r_{ij}} \tag{2.29}$$

The first term in equation 2.29 is the Lennard-Jones potential describe the van der Waals interaction between pairs of non-bonded atoms. Where, $R_{min_{ij}}$ is the distance at which the Lennard-Jones potential is zero, ϵ is the depth of the corresponding Lennard-Jones potential and r_{ij} is the distance between atoms i and j. The second term accounts for the electrostatic interactions between atoms i and j with partial charges q_i and q_j respectively. ϵ_0 is the effective dielectric constant. Lorentz-Berthelot combination rules are used to get the Lennard-Jones parameters for the interaction between pair of different atoms. According the combination rule, the Lennard-Jones potential depth ϵ_{ij} was computed by taking the geometric mean of the ϵ_i and ϵ_j. For $R_{min_{ij}}$, the arithmetic mean between R_{min_i} and R_{min_j} was used. Furthermore, to improve the accuracy of the potential several other terms are incorporated into general force fields such as Urey-Bradley corrections for angle bending and more sophisticated terms to describe the special interactions like hydrogen bonding. However, development

of general force field for coordination compounds are very difficult because of the properties like various coordination number and oxidation state, indistinct topology of $\pi-$bonding ligands, Jahn-Teller distortion etc. Over the years several metal specialized force fields have been developed to model transition metal complexes. In the following section a few of the metal specialized force fields are described in detail.

2.2.1. Force Fields for Metals

Metal specialized force fields introduce additional functionality to the general force fields to model coordination compounds or transition metal complexes. The additional functionality takes care of the metal center and helps to describe the coordination environment around it. While, the general force fields are mainly used for the ligands. Different methods use different supplementary terms to the general force fields to describe the requirements of the metal centers.

2.2.1.1. Ligand Field Molecular Mechanics (LFMM)

Ligand field molecular mechanics (LFMM) is based on the ligand field theory (LFT)[54]. Unlike crystal field theory (CFT) which only consider the electrostatic interactions to describe the interaction of ligands with the metal center, LFT takes care of the overlap of atomic orbitals between the ligand and the metal center. In other words, LFT combines both CFT and molecular orbital theory (MOT). LFMM was developed by Deeth and coworkers by introducing an additional term $LFSE$ (ligand field stabilization energy) to the conventional force field which takes care of the stereo-electronic effects of unfilled $d-$orbitals and helps to describe the the structure and energetics of the metal complexes[54]. Thus, according to the LFMM scheme, the total energy of the system can be expressed as

$$E_{tot} = E_{\text{bond}} + E_{\text{angle}} + E_{\text{dihedral}} + E_{\text{non-bonded}} + LFSE \tag{2.30}$$

The first four terms on the right hand side of equation 2.30 describe the bond, angle, dihedral angle and non-bonded interactions using conventional force fields. The most important term in equation 2.30 is the $LFSE$ which captures the stereo-electronic effect and can be derived by diagonalizing 5×5 ligand field potential matrix V_{LF}

$$< d_i|V_{\text{LF}}|d_j >= \sum_{l}^{N} \sum_{k}^{symmetry} F_{ik}^{l} F_{kj}^{l} e_k^l \tag{2.31}$$

d_i and d_j are the $d-$orbitals. The summation(l) and summation(k) are over all the N ligands and all three symmetry modes of metal-ligand (M-L) bonding (σ, pi_x and π_y) respectively. The F factors contain all the angular dependance of the M-L interactions and described by the angular overlap model (AOM). Basically, all the F factors describe the overlap of $d-$orbitals and suitable ligand orbitals. All the angular functions F for the ligand angular coordinates (θ, ϕ, ψ) are formulated by Schaeffer and put in a table (see Table 1 in[65]). For example, in an octahedral complex with O_h symmetry, the angular coordinates of the six ligands are[54]

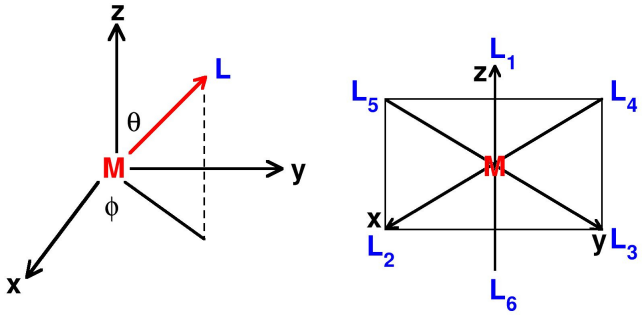

ligands	L_1	L_2	L_3	L_4	L_5	L_6
θ	0	90	90	90	90	180
ϕ	0	0	90	180	270	0

Let's assume L_1 is a monodatent ligand so it's angular coordinate $\psi = 0$. Thus, the F factors for ligand L_1 will have the values

$$F^{L_1}_{z^2,\sigma} = \frac{1}{4}[1 + 3\cos(2\theta)] = 1 \tag{2.32}$$

$$F^{L_1}_{xz,\pi_x} = -\sin(\phi)\cos(\theta)\sin(\psi) + \cos(\phi)\cos(2\theta)\cos(\psi) = 1 \tag{2.33}$$

$$F^{L_1}_{yz,\pi_y} = \cos(\phi)\cos(\theta)\cos(\psi) - \cos(\phi)\cos(2\theta)\sin(\psi) = 1 \tag{2.34}$$

All other F factors for the L_1 ligand are zero. On the other hand, the radial dependent term e_k in equation 2.31 is expressed as a function of M-L distances r and has the form

$$e_k = \sum_{n=0}^{6} a_{n,k,l} r_l^{-n} \tag{2.35}$$

Where a_i are the force field parameters and in general only the first two terms are considered to

minimize the number of parameters. Now, the ligand field stabilization energy can be expressed as

$$LFSE = \sum_{i}^{n} n_i \epsilon(d_i) \tag{2.36}$$

Where n_i is the population of respective $d-$orbitals. Thus, by construction, $LFSE$ is negative and favors low-spin states, while inter-electronic repulsion favors high-spin states[54]. So, the final spin state is a balance between the one-electron stabilization and the two-electron inter-electronic repulsion. This, correction was done by introducing the e_{pair} energy and has the same functional form as in equation 2.35. In addition to the pairing energy, e_{ds} energy is also included to account the $d-s$ mixing in the square planar molecules with $D_{4\text{h}}$ symmetry, because in $D_{4\text{h}}$ symmetry d_{z^2} and valence s orbitals have the same symmetry a_{1g} so they may mix with each other. Like e_{pair}, e_{ds} also has the same functional form as equation 2.35. Since LFMM separates the metal coordination region from the ligand region and helps in describing M-L bond with a Morse potential.

$$E_{\text{M-L}} = D_e\{1 - \exp(\beta(r - r_0))\}^2 - D_e \tag{2.37}$$

where D_e, β and r_0 are the three parameters describing M-L bond dissociation energy, curvature parameter and equilibrium M-L bond length respectively. Over the years, LFMM has been applied successfully to model first row transition metal complexes and considerably to copper containing amine complexes and enzymes. However, the parameterization of LFMM is very cumbersome and thus on the applicability point, methods based on the valence bond theory are more practical.

2.2.1.2. Sum of Interactions Between Fragments Ab Initio - (SIBFA)

The basic idea of SIBFA force fields is based on the energy decomposition of the *ab initio* intermolecular interaction energy. In this approach, a complex molecule is broke down into small rigid fragments and the fragments within a molecule interact through first order Coulomb (E_c) and exchange-repulsion energies and second order charge transfer and polarization energies. Since, parameters are fitted to the optimized geometry of the rigid fragment, in large molecules, the conformational flexibility is incorporated by considering torsional degrees of freedom around the inter-fragment bonds.

SIBFA polarizable force field consists of five different inter-molecular interaction energy terms[66]

$$E_{tot} = E_{\text{ele}} + E_{\text{pol}} + E_{\text{rep}} + E_{\text{ct}} + E_{\text{dis}} \tag{2.38}$$

E_{ele} describes the electrostatic interactions by considering multipole moments derived from the *ab initio* charge density. Multipole moments are very important for describing directional non-covalent interactions[66–69]. In SIBFA, the multipole moments are truncated to up to quadrupole moments. E_{pol} is the polarization energy also derived from *ab initio* calculations. E_{rep} is the short-range electron-electron repulsion energy and is computed between bond-bond, bond-lone pair, and lone pair-lone pair interactions[66]. Charge transfer between fragments is described be E_{ct}. Finally, sum of $1/R^6$, $1/R^8$ and $1/R^{10}$ are used to describe the dispersion energy E_{dis}[66]. In recent years SIBFA force fileds has been applied to model interaction of bioactive ligands with metal atoms to mimic metalloprotein systems.

2.2.1.3. VALBOND

The VALBOND force field is based on Pauling's valence bond theory and was developed by Landis and coworkers[57,58]. VALBOND captures the bending energy not only around the equilibrium angle but also for large distortions by means of 3c/4e bonds in hypervalent molecules (do not fulfil octet rule) and transition metal complexes (duodecte rule). The VALBOND formulation is based on hybrid orbital strength functions[70–72]. Consider two equivalent sp^3 hybrid orbitals $\psi_1 = \frac{1}{2}[|1s\rangle + \sqrt{3}|P_z\rangle]$ and $\psi_2 = \frac{1}{2}[|1s\rangle + \sqrt{3}(\cos\alpha|p_z\rangle + \sin\alpha|p_x\rangle)]$ and they are not necessarily orthogonal . Thus, the two hybrid orbitals ψ_1 and ψ_2 lies along the $Z-$axis and the $XZ-$plane that makes an angle α with the hybrid orbital ψ_1. The strength (S) of the hybrid orbitals obtained from the angular part of the eigenfunction at it's maximum. Therefore, the two sp^3 hybrid orbitals have maximum strength $S^{\max} = 2$. As the two hybrid orbitals are nonorthogonal, so the overlap integral $\Delta = \frac{1}{4}[1 + \sqrt{3}\cos\alpha]$ decreases from the maximum value of 2 and hence S decides the bond forming power of hybrid orbitals. The general functional form of VALBOND[57,58] force field which captures angular distortions for a wide range is expressed as

$$E(\alpha) = k(S^{\max} - S(\alpha)) \tag{2.39}$$

where, k is the scaling factor, S^{max} is the maximum strength function of the hybrid orbitals and $S(\alpha)$ is the strength function of the hybrid orbitals depending on the angle α between two hybrid orbitals. For any sp^md^n hybridization, the maximum strength function of hybrid orbitals is given by

$$S^{\max} = \sqrt{\frac{1}{1+m+n}}(1 + \sqrt{3m} + \sqrt{5n}) \tag{2.40}$$

While the angular dependance strength function $S(\alpha)$ is expressed as

$$S(\alpha) = S^{max}\sqrt{1 - \frac{1 - \sqrt{1 - \Delta^2}}{2}} \tag{2.41}$$

where Δ is the nonorthogonality integral or overlap integral that controls the M-L bond formation strength is expressed as

$$\Delta = \frac{1}{1 + m + n}\left[1 + m\cos\alpha + \frac{n}{2}(3\cos^2\alpha - 1)\right] \tag{2.42}$$

Landis and co-workers applied a general procedure to get the angular dependency of all types of hybrid orbitals (see Figure 2.2). As it considers the angular part of the wave function and thus has the information about the local electron density. Hence, as mentioned earlier the strength function is corresponds to the power of bond formation. However, it should be mentioned that the hybrid orbitals are only based on the angular contribution and neglect the radial part. Therefore, this provides slightly different hybridization compared to the hybridization obtained from the valence bond computations which includes both radial and angular contributions.

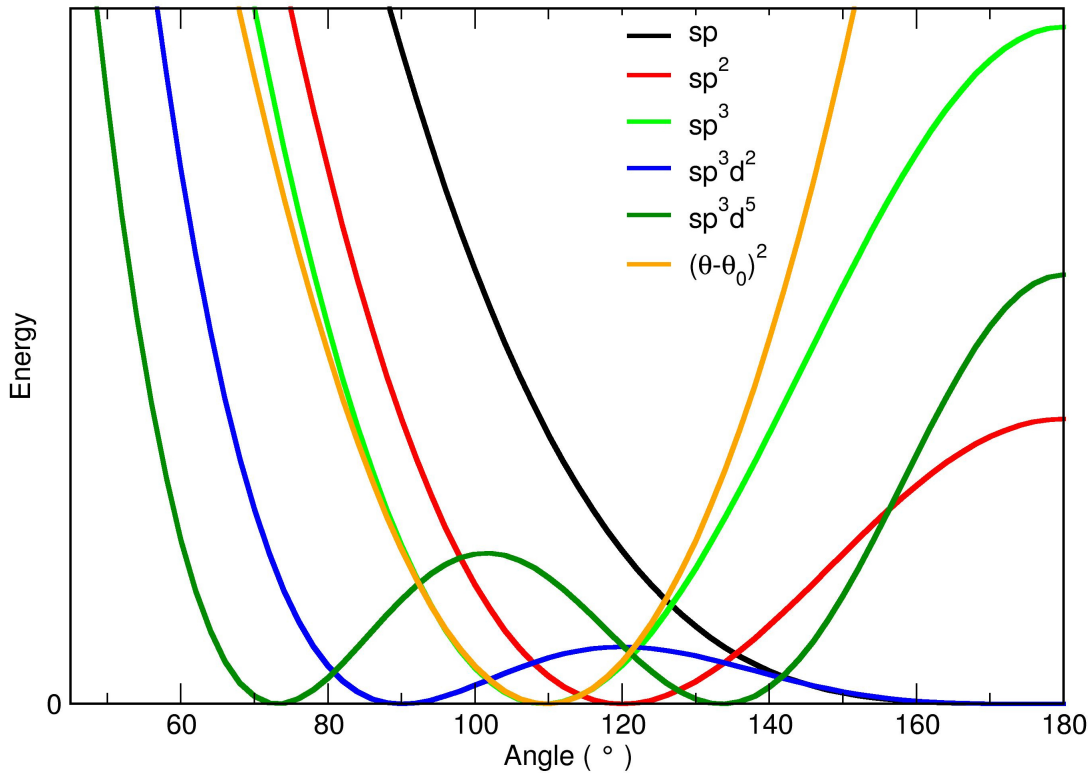

Figure 2.2.: VALBOND potential energy curves for different hybridizations along with harmonic function at 109.7° (orange).

On the other hand, hypervalent molecules involved several resonance structures. Thus the total energy of the molecule is expressed as

$$E_{\text{tot}} = \sum_i c_i E_i \tag{2.43}$$

where c_i is the weight for each of the resonance structures and depends on the geometry of the resonance structures. For example, in the ClF_3 molecule, The central chlorine atom is connected to three fluorine atoms. The chloride radical $Cl^{\bullet}$ and 3 fluorine radicals $F^{\bullet}$ contain 28 (4×7) electrons. where as, the fully electron saturated state (ionic state) formed by F^- and Cl^- has 32 electrons. Hence, 4 electrons are involved in bonding. Two electrons per covalent bond leads to $N = 2$ bonds per resonance structure. Since a maximum of $K = 3$ bonds can be accommodated in the ClF_3 molecule, there are $\binom{N}{K} = \binom{2}{3} = 3$ possible resonance structures. Thus, the total energy of the ClF_3 molecule is expressed as $E = \sum_i^3 c_i E_i$.

The coefficients c_i are computed using equation 2.44.

$$c_i = \frac{\prod_{j=1}^{hype} \cos^2 \alpha_j}{\sum_{i=1}^{resonance} \prod_{j=1}^{hype} \cos^2 \alpha_j} \tag{2.44}$$

Finally, the energy corresponding to each of the resonance structures is expressed as

$$E(\alpha) = BOF \times k[1 - \Delta(\alpha + \pi)^2] \tag{2.45}$$

where k is the scaling factor and Δ is the overlap integral given in equation 2.42. BOF is the bond order factor expressed as the product of the formal bond orders of the two bonds described by the hybrid orbitals and oriented at an angle α. In general, the BOF has values of 0.25 for hypervalent bonds and 1.0 for non-hypervalent bonds.

The VALBOND force field is used in combination with conventional force fields. Actually, VALBOND force field is implemented in CHARMM[50] and the additional VALBOND energy is introduced along with the conventional CHARMM force field. VALBOND[57,58] force fields has been successfully applied to model metal complexes and hypervalent molecules.

2.2.1.4. VALBOND-TRANS

The VALBOND force field doesn't capture the electronic effects in the metal complexes such as *trans influence*. *Trans influence* is the tendency of a ligand to selectively weaken the bond *trans* to itself. For example, in L_1-M-L_2, L_2 is trans to L_1. Thus, the strength and bond length of M-L_2 depends on the type of ligand L_1. To capture the *trans influence* in metal complexes VALBOND force field has to be expanded and this has been done by including two addition penalty functions to the VALBOND force field, one for energy correction and other for bond length correction due to *trans influence*. The modified VALBOND force field is called as VALBOND-TRANS[59].

In the VALBOND force field formalism for the resonance structures linear 3-center/4-electron hypervalent bonds are favored. As the *trans influence* acts along the hypervalent bonds so the *trans influence* is maximum at linear configurations. Thus, the penalty function for the energy correction

due to *trans influence* is introduced at $\Delta(\alpha + \pi) = 1$. So, the energy correction term is expressed as

$$E_{trans} = \sum_{trans} p_{\mathrm{L_1L_2}}[\Delta(\alpha + \pi)^2] \tag{2.46}$$

where $p_{\mathrm{L_1L_2}}$ is the parameter for the energy *trans influence* and depends on the type of ligands involved in the L_1-M-L_2 motif.

The second penalty function for the bond length correction due to trans influence (structural *trans influence*) is given by

$$r_{\mathrm{L_1(L_2)}} = r^0_{\mathrm{L_1}}(1 + S_{\mathrm{L_1}} \cdot i_{\mathrm{L_2}}/100) \tag{2.47}$$

where $r^0_{\mathrm{L_1}}$ is the unperturbed equilibrium M-L_1 bond length, $r_{\mathrm{L_1(L_2)}}$ is the perturbed equilibrium M-L_1 bond length when L_2 is trans to L_1. $S_{\mathrm{L_1}}$ and $i_{\mathrm{L_2}}$ are the bond lengthening intensity of ligand type L_1 and bond lengthening sensitivity of atom type L_2 respectively. Therefore, the relative change in bond lengths due to trans influence is expressed as

$$r_{\mathrm{L_1(L_2)}} = r^0_{\mathrm{L_1}}(1 + S_{\mathrm{L_1}} \cdot \Delta(\alpha + \pi)^2 \cdot i_{\mathrm{L_2}}/100) \tag{2.48}$$

2.3. Molecular Dynamics Simulations

Molecular dynamics simulations (MD) computes the motion of the atoms in a molecular assembly using classical equations of motion or Newtonian dynamics. The step-by-step solution of Newton's equation of motion generates successive configurations called trajectories which contains information about how the positions and velocities of the atoms change with respect to time[73]. According to Newton's second law of motion

$$\begin{aligned} \boldsymbol{f}_i &= m_i \mathbf{a_i} \\ &= m_i \frac{d^2 \boldsymbol{r}_i}{dt^2} \\ \Rightarrow \frac{d^2 \boldsymbol{r}_i}{dt^2} &= \frac{\mathbf{f_i}}{m_i} \end{aligned} \tag{2.49}$$

where m_i, r_i and a_i are the mass, positions (coordinates) and acceleration of atom i at time t and f_i is the force on acting on it. The force on atom i is calculated from the gradient of the potential energy

$V(\boldsymbol{r}^N)$, where $\boldsymbol{r}^N = (\boldsymbol{r}_1, \boldsymbol{r}_2, \boldsymbol{r}_3, \cdots, \boldsymbol{r}_N)$ are the $3N$ atomic coordinates.

$$\boldsymbol{f}_i = -\frac{\partial V}{\partial \boldsymbol{r}_i} \tag{2.50}$$

The potential energy of the system $V(\boldsymbol{r}^N)$ is computed using either quantum mechanical methods or molecular mechanics (force fields). To obtain the trajectory, it is required to solve the differential equation 2.49[73]. There are several algorithms for integrating the equations of motion and used in MD such as finite difference method, Velocity Verlet algorithm, Leapfrog algorithm etc[73,74]. Here, we describe only the Velocity Verlet algorithm[75] as it is used for our simulations. In velocity verlet algorithm, the new positions and velocities of atoms after time δt are computed in three stages[73]. Let us consider at time t, the positions, velocities and accelerations of atoms are $\boldsymbol{r}(t)$, $\boldsymbol{v}(t)$ and $\boldsymbol{a}(t)$ respectively.

$$\boldsymbol{r}(t+\delta t) = \boldsymbol{r}(t) + \delta t \boldsymbol{v}(t) + \frac{1}{2}\delta t^2 \boldsymbol{a}(t) \tag{2.51}$$

$$\boldsymbol{v}(t+\delta t) = \boldsymbol{v}(t) + \frac{1}{2}\delta t[\boldsymbol{a}(t) + \boldsymbol{a}(t+\delta t)] \tag{2.52}$$

For the calculation $\boldsymbol{v}(t+\delta t)$ requires the acceleration at both time t and $t+\delta t$. Thus, first the position of atoms at time $t+\delta t$ were computed using equation 2.51. Then, the velocities at time $t+\frac{1}{2}\delta t$ were determined by

$$\boldsymbol{v}(t+\frac{1}{2}\delta t) = \boldsymbol{v}(t) + \frac{1}{2}\delta t \boldsymbol{a}(t) \tag{2.53}$$

Then the forces were computed for the new positions which gives new accelerations $\boldsymbol{a}(t+\delta t)$ and finally the velocities $\boldsymbol{v}(t+\delta t)$ were computed using

$$\boldsymbol{v}(t+\delta t) = \boldsymbol{v}(t+\frac{1}{2}\delta t) + \frac{1}{2}\delta t \boldsymbol{a}(t+\delta t) \tag{2.54}$$

2.4. Adiabatic Reactive Molecular Dynamics and It's Multi-surface Variant (MS-ARMD)

Ab initio MD where the energy and forces are computed from electronic structure methods allows to simulate chemical reactions. However, *ab initio* energy and force evaluations are computationally very

demanding and does not allow sampling of the configurational space extensively which is essential for determining thermodynamical properties (*eg.* free energy). On the other hand conventional force fields are unable to model chemical reactions because in chemical reactions bond breaking and forming takes place and force fields are meant for a particular diabatic state where the connectivity of the atoms does not change. There are several MM methods that have been developed over the years such as reactive force field (ReaxFF)[76,77], empirical valence bond (EVB)[78], adiabatic reactive molecular dynamics (ARMD)[79] and multi-state adiabatic reactive molecular dynamics (MS-ARMD)[80] which allows to simulate chemical reactions . The important and common feature of these methods is the use of switching function which allow smooth switching between two diabatic states such as reactant and product states.

The new method developed in our group called adiabatic reactive molecular dynamics (ARMD)[81] is a surface crossing method that allows bond breaking and forming in classical molecular dynamics simulations. In this method at least two diabatic potential energy surfaces V_i and V_2 correspond to reactant and product states are considered. The dynamics of the nuclei always takes place on the lowest energy $V_0(\mathbf{r}) = \min[V_1(\mathbf{r}), V_2(\mathbf{r})]$ adiabatic potential energy surface, but at each configuration the energy of higher states are also calculated. During the dynamics, when the energy of the current state equals the one of the higher energy state, the system is resimulated from a few time steps $\frac{t_s}{2}$ (t_s represents switching time) prior to the crossing. During this time window, the two potential energy surfaces are allowed to mix at different proportions by multiplying a suitable time-dependent smooth switching function $f(t)$ with them. Thus, in ARMD formalism the adiabatic potential surface is given by[81]

$$V_{\mathrm{ARMD}}(\mathbf{r}, t) = [1 - f(t)]V_1(\mathbf{r}) + f(t)V_2(\mathbf{r}) \tag{2.55}$$

From equation 2.55, it is clear that the $V_{\mathrm{ARMD}}(\mathbf{r}, t)$ is time dependant. So, in a strict sense it does not obey total energy conservation of the system during crossing. However, for larger systems like proteins it is observed that the total energy is conversed within $\sim$ 1 kcal/mol. On the other hand for gas phase simulations of small molecules, ARMD does not permit energy conservation. To overcome the energy conservation problem in ARMD, a multi-surface (MS) variant of ARMD was developed recently called multi-surface adiabatic reactive molecular dynamics (MS-ARMD)[80] and it conserves energy during the crossing.

In MS-ARMD the effective potential energy is expressed as a linear combination of all the diabatic

potential energy surfaces with coordinate-dependent weights[80]

$$V_{\mathrm{MS-ARMD}}(\mathbf{r}) = \sum_{i=1}^{n} w_i(\mathbf{r}) V_i(\mathbf{r}) \tag{2.56}$$

Where $w_i(\mathbf{x})$ are computed renormalizing the raw weights $w_{i,0}(\mathbf{x})$ obtained from the exponential decay function of the energy difference between minimum energy surface and surface V_i with characteristic energy ΔV

$$w_i(\mathbf{r}) = \frac{w_{i,0}(\mathbf{r})}{\sum_{i=1}^{n} w_{i,0}(\mathbf{r})} \qquad \text{where } \; w_{i,0}(\mathbf{r}) = \exp\left(-\frac{V_i(\mathbf{r})}{\Delta V}\right) \tag{2.57}$$

Since force field parametrization of the reactant and product states is carried out separately. Therefore sometimes it gives unrealistic high-energy around the crossing region. To avoid this problem around the crossing point, the barrier region was adjusted to match energies obtained from electronic structure calculations by using products of Gaussian and polynomial functions (GAPOs)[80]

$$\Delta V^{ij}_{\mathrm{GAPO},k}(\mathbf{x}) = \exp\left(-\frac{\left(\Delta V_{ij}(\mathbf{x}) - V^0_{ij,k}\right)^2}{2\sigma^2_{ij,k}}\right) \cdot \sum_{l=0}^{m_{ij,k}} a_{ij,kl}\left(\Delta V_{ij}(\mathbf{x}) - V^0_{ij,k}\right)^l \tag{2.58}$$

where $V^0_{ij,k}$ and $\sigma_{ij,k}$ are the center of the Gaussian function and the standard deviation of the Gaussian function respectively. Finally, the global MS-ARMD potential energy surface can be expressed as

$$V_{\text{MS-ARMD}}(\mathbf{x}) = \sum_{i=1}^{n} w_i(\mathbf{x}) V_i(\mathbf{x}) + \sum_{i=1}^{n-1} \sum_{j=i+1}^{n} \left[w_i(\mathbf{x}) + w_j(\mathbf{x})\right] \sum_{k=1}^{n_{ij}} \Delta V^{ij}_{\mathrm{GAPO},k}(\mathbf{x}) \tag{2.59}$$

MS-ARMD as implemented in CHARMM is a general tool for constructing global PESs from empirical force fields for modelling chemical reactions in gas, surface and condensed phases, relevant to homogeneous, heterogeneous and enzymatic catalysis[80].

2.5. X-ray absorption near-edge spectra (XANES)

Over the last 30 years, X-ray absorption spectroscopy (XAS) has made a substantial contributions to chemical and biochemical research, particularly for metalloproteins. XAS is the measurement of transitions from core electronic states of the metal to the excited electronic states (LUMO) called X-ray absorption near-edge structure (XANES) and to the continuum referred to as extended X-ray

absorption fine structure (EXAFS)[29]. Unlike X-ray diffraction, XAS is very sensitive to the local structure and thus has been applied to characterize metalloproteins, ions in solutions, catalysis, liquid water and aqueous solutions *etc.*[29,82,83]. As in several of our works, we employed a computational tool to model XANES spectra called Finite Difference Method Near-Edge Spectroscopy (FDMNES)[84]. We intend to provide a detail theoretical description of the model. Since, XAS involved the interaction of matter with light, the total Hamiltonian to describe the system is

$$H = H_M + H_L + H_{M-L} \tag{2.60}$$

where H_M, H_L and H_{M-L} are the Hamiltonians for the matter, electromagnetic field of light and the interaction between matter and light, respectively. Assuming, H_M is time independent, total H can be expressed as

$$H = H_0 + V(t) \tag{2.61}$$

where $H_0 = \frac{\vec{(}p)^2}{2m} + V$ is the time independent Hamiltonian for matter and $V(t)$ is the radiative field inducing small perturbation to matter due to the electromagnetic field of light $V(t) \approx \frac{e}{m}\vec{p} \cdot \vec{A}$, $\vec{p}$, e and m are the transition dipole, charge and mass of the excited electron and $\vec{A}$ is the electromagnetic vector potential. For a plane wave light in the coulomb gauge ansatz

$$\begin{aligned} \vec{A} &= \vec{A_0}\cos(\vec{k}\cdot\vec{r} - \omega t) \\ E &= -\frac{dA}{dt} = \vec{E_0}\sin(\vec{k}\cdot\vec{r} - \omega t) \\ B &= \vec{\nabla}\times\vec{A} = \vec{B_0}\sin(\vec{k}\cdot\vec{r} - \omega t) \end{aligned} \tag{2.62}$$

Where E and B are the electric and magnetic fields respectively. Here, $\vec{E_0} = \omega\vec{A_0}$ ($\vec{A_0} = \hat{\epsilon}\cdot\sqrt{\frac{\hbar}{2\epsilon_0 V\omega_k}}$, $\hat{\epsilon}$ is the polarization unit vector), $\vec{B_0} = \frac{1}{c}E_0$ ($c = \frac{\omega}{|k|}$, k is the wave vector).

Using Fermi's Golden Rule of time dependent perturbation theory, the transition probability W_{fi} from one state to another i.e the probability that a photon with energy $\hbar\omega$ induce a transition of an electron in k-space depends on the V(t) and can be expressed as

$$W_{fi} = \frac{2\pi}{\hbar}|\langle f|V(t)|i\rangle|^2 \cdot \rho_f \tag{2.63}$$

In XAS, the transition probability is related linearly to the linear absorption coefficient μ_{abs} and is given by

$$\mu_{abs}(\omega) = \frac{\text{No. of transitions/unit volume/unit time}}{\text{photon flux}} \tag{2.64}$$

$$\mu_{abs}(\omega) = \frac{\rho_a \cdot \frac{2\pi}{\hbar} \cdot |\langle f|V(t)|i\rangle|^2 \cdot \rho_f}{\frac{\langle S\rangle}{\hbar\omega}} \tag{2.65}$$

Where, ρ_a is the atomic density and the incident photon flux is described as the time averaged magnitude of the Poynting vector $\langle S\rangle = \frac{\epsilon_0 c}{2}{E_0}^2$ divided by photon energy $\hbar\omega$.

In a classical analogue the absorption coefficient has a direct relation to the absorption cross-section

$$\begin{aligned}\sigma(\omega) &= \frac{\mu_{abs}}{\rho_a} \\ &= \sum_f \frac{\hbar\omega \cdot \frac{2\pi}{\hbar} \cdot |\langle f|\frac{e}{m}\vec{p}\cdot\vec{A}|i\rangle|^2 \cdot \rho_f}{\frac{\epsilon_0 c}{2}{E_0}^2}\end{aligned} \tag{2.66}$$

Since, $\vec{A} = \vec{A_0}\cos(\vec{k}\cdot\vec{r} - \omega t) = \frac{A_0}{2}(\mathrm{e}^{i(\vec{k}\cdot\vec{r}-\omega t)} - \mathrm{e}^{-i(\vec{k}\cdot\vec{r}-\omega t)})$ and the only component which has time dependence of $\exp^{i\omega t}$ will induce a transition[85], thus equation 2.66 can be simplified as

$$\begin{aligned}\sigma(\omega) &= \frac{4\pi\omega}{\epsilon_0 c}\cdot\frac{e^2}{m^2}\cdot\frac{A_0^2}{4E_0^2}\sum_f |\langle f|\epsilon\cdot\vec{p}\mathrm{e}^{i\vec{k}\cdot\vec{r}}|i\rangle|^2\cdot\rho_f \\ &= 4\pi^2\frac{\hbar}{m^2\omega}\cdot\alpha\sum_f |\langle f|\vec{\epsilon}\cdot\vec{p}\mathrm{e}^{i\vec{k}\cdot\vec{r}}|i\rangle|^2\cdot\rho_f\end{aligned} \tag{2.67}$$

where $\alpha = \frac{e^2}{4\pi\epsilon_0\hbar c}$ is the structure factor and $\vec{\epsilon}$ describes the polarization vector. There are couple of ways to integrate the equation 2.67, by using the finite difference method or by using multiple scattering theory within the limit of muffin-tin approximation and both methods exist in the FDMNES package[84]. However, the finite difference method is very accurate as it uses the exact potentials but computationally very demanding.

Finally, the spectra is convoluted using a Lorentzian[86,87] with an energy dependant width $\Gamma_f(\omega)$ to account for the spectral broadening because of core-hole width Γ_{hole}

$$\Gamma_{\mathrm{f}}(E - E_{\mathrm{F}}) = \Gamma_{\mathrm{hole}} + \Gamma_{\mathrm{max}} \left(\frac{1}{2} + \frac{1}{\pi} arctan \left(\frac{\pi}{3} \frac{\Gamma_{\mathrm{max}}}{E_l} \left(\epsilon - \frac{1}{\epsilon^2} \right) \right) \right) \tag{2.68}$$

Hence, the convoluted signal is expressed as

$$\sigma_{\mathrm{conv}}(\omega) = \int_{E_{\mathrm{F}}}^{\infty} \sigma(\omega) \frac{1}{\pi} \frac{\Gamma_{\mathrm{f}}(\omega)}{\Gamma_{\mathrm{f}}(\omega)^2 + (\hbar\omega - E)^2} dE \tag{2.69}$$

Here, $\epsilon = \frac{E - E_{\mathrm{F}}}{E_{\mathrm{cent}}}$ and E_{F} is the fermi energy. Γ_{max} is the maximum width and $E_{\mathrm{cent}} - E_{\mathrm{f}}$ is the inflection point, appropriate values are required for these constant in order to obtain reasonable XAS spectra.

Part III.

Applications

3. Inner-Shell Water Rearrangement Following Photo-Excitation of Tris(2,2′-bipyridine)iron(II)

3.1. Abstract

The solvent dynamics in Fe-tris-bipyridine $[Fe(bpy)_3]^{2+}$ upon electronic excitation (oxidation) and subsequent relaxation is followed on the picosecond time scale by using atomistic simulations. Starting from the low spin (LS) $Fe(II)_{LS}$ state the transition to the excited Fe(III) ^{1,3}MLCT (metal-to-ligand charge transfer) state decreases the water coordination in immediate proximity of the central iron atom. This readjustment of the solvent shell occurs on the sub-picosecond time scale. Full relaxation of the water environment would occur on the 10 ps time scale which is, however, never reached as the lifetime of the ^{1,3}MLCT state is only 200 fs. Further relaxation towards the long-lived (665 ps) $[Fe(II)_{HS}(bpy)_3]$ high spin (HS) state does not change the degree of solvation. The results support a model in which the change in the degree of solvation is driven by electronic effects (charge redistribution) and not by structural changes (change in bond lengths). Furthermore, the results are consistent with recent combined X-ray emission (XES) and X-ray diffusion (XDS) scattering experiments which provided evidence for a reduced solvent density upon excitation of the $[Fe(II)_{LS}(bpy)_3]$ initial state. However, the time scale for water exchange dynamics is faster than that found in the experiments.

3.2. Introduction

Iron-containing complexes constitute an important and versatile class of metal complexes. Depending on the strength of the ligands they can exist either in a low (LS) or in a high spin (HS) state. Specifically, the $[Fe(II)(bpy)_3]$ complex exhibits two spin states: a LS singlet ($^1A_1$) and a HS quintet ($^5T_2$).[88,89] Between these two states, excited state charge transfer and spin dynamics takes place (spin crossover - SCO - dynamics) which can be induced by illumination, temperature or pressure changes.[90]

3. Inner-Shell Water Rearrangement Following Photo-Excitation of Tris(2,2′-bipyridine)iron(II)

Switchable transition metal-based systems are potentially interesting for applications in solar cells, data storage or in molecular devices. Often, they are based on ruthenium which is, however, rare and toxic. Iron would be an attractive replacement but due to the very short-lived excited states it has as yet not been widely used for solar energy conversion. However, there has been recent progress with an iron-nitrogen-heterocyclic-carbene compound.[91]

In solution, the SCO process involves a first inter system crossing (ISC) to a metal-to-ligand-charge transfer (^{1,3}MLCT) state followed by relaxation which brings the molecule to the HS state (see Figure 3.1), possibly via one or several triplet ^{3}T intermediates.[88] During the photo excitation energy is dissipated to the environment, potentially including intra-molecular degrees of freedom. However, following the non-equilibrium response of the surrounding solvent molecules towards equilibrium from experiment alone at atomistic scales is difficult. Earlier work based on the analysis of time resolved X-ray spectroscopy experiments suggests that during SCO one to two water molecules are pushed out of the first solvent shell between the [Fe(II)$_{\mathrm{LS}}$(bpy)$_3$] and [Fe(II)$_{\mathrm{HS}}$(bpy)$_3$] states on the 100 ps time scale.[90] Also, an *ab initio* mixed quantum mechanics/molecular mechanics (QM/MM) simulation involving the same two states reveals that the solvent shell around the two states differs by two water molecules.[37]

Solvent molecules around metal complexes are of fundamental and practical relevance both, in catalysis and in solar energy conversion.[21,22,92,93] However, directly observing and characterizing the influence and role of solvent is difficult experimentally mainly because of the transient nature of the process and the finite time resolution of the experiments. Computational approaches applied to metal-containing systems have become more widespread recently due to both, increased computing power and technological advances. Amongst others, tight-binding schemes have been extended to treat copper complexes.[94] Furthermore, force field-based techniques have been successfully applied to the investigation of a range of metal-containing systems.[95–100]

For Fe(bpy)$_3$ the experimental information provided so far is indirect[90] and only one QM/MM trajectory, approximately 25 and 4 ps in length for the LS and HS states, respectively, could be run due to the considerable computational effort of such simulations.[37] Typical experiments provide ensemble-averaged observables, which require statistical averaging over many independent trajectories in the simulations for direct comparison, which is usually not possible with QM/MM simulations of metal-containing

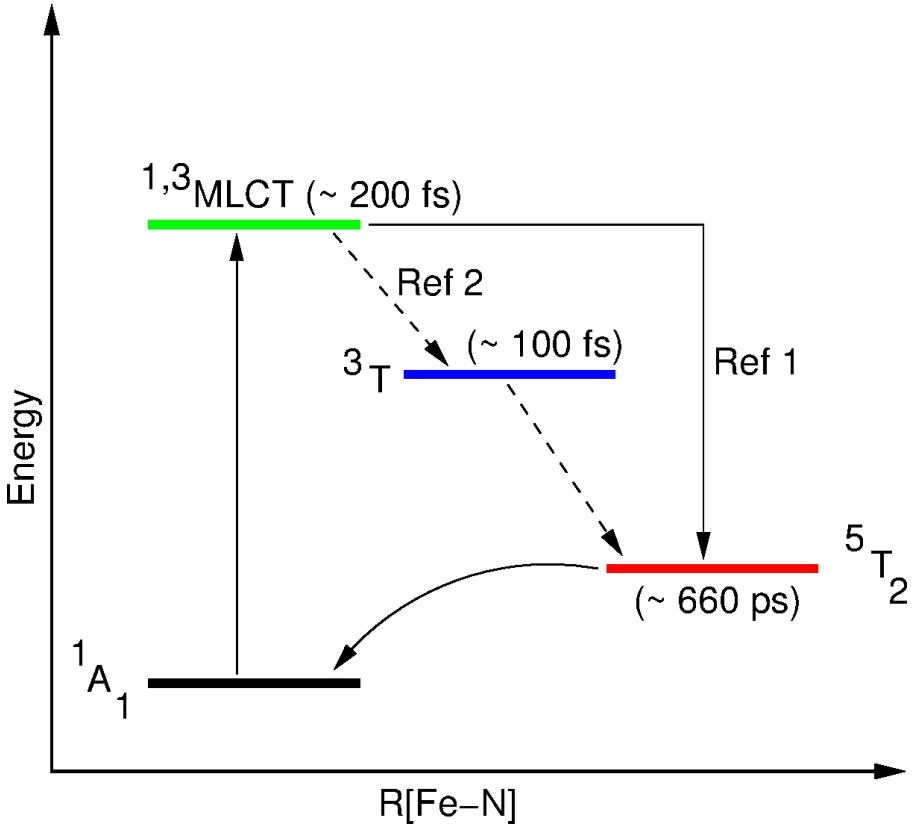

Figure 3.1.: Schematic for SCO involving the aqueous [Fe(II)(bpy)$_3$] complex. The process studied here occurs along the solid arrow. The dashed lines are additional processes on the sub-picosecond time scale analyzed in previous work.[89] The lifetime of each state is reported in brackets. Intermediate triplet states ($^3T_1$) and ($^3T_2$) are labeled as ^{3}T.

systems. In the present work computational strategies are employed which allow rigorous sampling by using valence-bond-based force fields for the species involved. This allows to follow the atomistic dynamics for hundreds of trajectories over extended time scales. First, the force field is validated vis-a-vis experimental structures and infrared frequencies. In a next step, the solvation dynamics of the ground- and excited-state species is followed from equilibrium and non-equilibrium MD simulations.

3.3. Methods

3.3.1. Computational Details

All MD simulations were carried out with the CHARMM[50] suite program, the CHARMM22[101] force field and provisions for VALBOND.[98] The VALBOND force field is based on valence bond theory and capable to more realistically describe angle bending in metal complexes.[102–104] For this, the

harmonic bending energy term in a conventional force field for an L1-M-L2 motif is replaced by a parameterization which depends on the overlap of the hybrid orbitals on the central metal atom, where L1 and L2 are ligands and M is the metal atom. Unlike the simple harmonic approximation, VALBOND bending functions capture the energetics at very large angular distortions and support hypervalent compounds by means of 3-center-4-electron bonds.[103] The remaining parameters for the bipyridine rings were those from the CHARMM22[101] and CHARMM General Force Field (CGenFF[105]).

For the present study, three metal complexes $[Fe(II)_{LS}(bpy)_3]$, $[Fe(II)_{HS}(bpy)_3]$ and $[Fe(III)(bpy)_3]$ were considered. Their structures were optimized and natural bond orbital (NBO)[106] charges were determined using Gaussian09[107] with the 6-31G(d,p)[108] basis set at the B3LYP[62] level of theory. Partial charges on each atom of the ligand and metal atom, for all three systems are summarized in Table 3.1. The van der Waals parameters for Fe are those from 6-coordinate heme[109] ($R_{\min}/2 = 0.65$ Å and $\epsilon = -0.01$ kcal/mol) although additional simulations were carried out with $\epsilon = -0.5$ kcal/mol but no differences were found. This is not too surprising as the Fe-atom is deeply buried within the complex and only electrostatic interactions are expected to be of importance for the interaction with the solvent.

Table 3.1.: NBO charges (in units of e) for the three states of the metal complex obtained from the *ab initio* calculations. For labelling of the atom types see Figure 3.3.

Atoms	$Fe(II)_{LS}$	$Fe(II)_{HS}$	Fe(III)
FEX	0.98	1.33	1.21
NX	–0.49	–0.55	–0.50
CE2	0.18	0.19	0.19
CA1	0.04	0.05	0.06
CA2	–0.25	–0.26	–0.23
CA3	–0.17	–0.17	–0.13
CA4	–0.22	–0.23	–0.21
HP	0.27	0.27	0.28

As a first validation, the global structures of the optimized structures from electronic structure and

force field calculations were compared with experiment. For this, all mutual atom-atom distances were computed for the $Fe(II)_{LS}$ and Fe(III) complexes and compared with the experimental crystal data (see Figure 3.2).[110–113] It is found that the VALBOND optimized geometries favorably agree with experimental crystal structures[113]. Since the crystal structure of $[Fe(II)_{HS}(bpy)_3]$ is not available, its VALBOND force field optimized geometry is compared with the optimized structure from the *ab initio* calculations. Table 3.2 provides a comparison of the most relevant average bond lengths for the three complexes obtained from force field and *ab initio* calculations with the reference structures. It is confirmed that the present force fields faithfully reproduce the structures of the $[Fe(II)_{LS}(bpy)_3]$, $[Fe(II)_{HS}(bpy)_3]$ and $[Fe(III)(bpy)_3]$ complexes.

Table 3.2.: Bond length comparison for $[Fe(II)_{LS}(bpy)_3]$, $[Fe(III)(bpy)_3]$ and $[Fe(II)_{HS}(bpy)_3]$ obtained from FF, *ab initio* (B3LYP/6-31G(d,p)) and experiment.[110–113]

	$Fe(II)_{LS}$			Fe(III)			$Fe(II)_{HS}$	
Bond Type	CHARMM (Å)	*ab initio* (Å)	Expt. X-ray (Å)	CHARMM (Å)	*ab initio* (Å)	Expt. X-ray (Å)	CHARMM (Å)	*ab initio* (Å)
CA - CA	1.375	1.391	1.37-1.39	1.375	1.393	1.37	1.410	1.390
CA - HP	1.080	1.083		1.080	1.083	0.94	1.080	1.083
CA - CE2	1.397	1.397		1.395	1.395	1.38	1.427	1.400
CE2 - CE2	1.476	1.476	1.47	1.471	1.471	1.47	1.493	1.485
CA - NX	1.347	1.343	1.34-1.36	1.346	1.346	1.35	1.357	1.345
CE2 - NX	1.364	1.357	1.34-1.36	1.360	1.361	1.36	1.376	1.357
FEX - NX	2.022	2.022	1.95,1.97	2.005	2.005	1.96	2.200	2.188

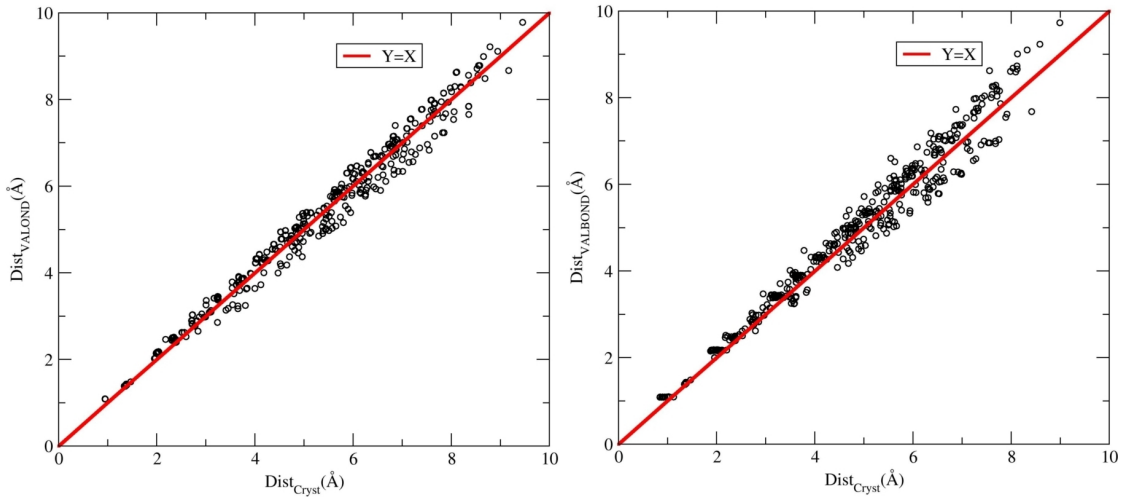

Figure 3.2.: Comparison of atom-to-atom distance between the VALBOND force filed optimized geometry and experimental crystal structure for $[Fe(II)_{LS}(bpy)_3]$ (left) and $[Fe(III)(bpy)_3]$ (right).

Furthermore, to validate the non-bonded parameters, interaction energies between one water molecule and the metal complex were computed for 50 different configurations extracted from a low-temperature (50 K) MD simulation of 50 ps length. Interaction energies were compared with those obtained from *ab initio* calculations at the B3LYP/6-31G(d,p) level of theory and the correlation coefficient was $R^2 = 0.98$ with a slope of 0.97 for the linear fit. This provides further validation for the force field used.

The computational setup for the present study consists of the solvated iron complexes in a pre-equilibrated cubic box of size 37.25 Å containing 1694 water molecules, with 5143 atoms in total (see Figure 3.3). Periodic boundary conditions (PBC) were applied. The non-bonded interactions (electrostatic and Lennard-Jones) were truncated at a distance of 14 Å and switched between 10 and 12 Å. First, the species of interest - solvated $[Fe(II)_{LS}(bpy)_3]$, $[Fe(II)_{HS}(bpy)_3]$ and $[Fe(III)(bpy)_3]$ - were heated and equilibrated for 20 ns at 300 K. Newton's equations of motion were propagated in the NVT ensemble with a Verlet integrator. The water model used in the present work is the standard TIP3P model[114] and all bonds involving hydrogen atoms were constrained by applying SHAKE[115]. The time step used in the simulations was $\Delta t = 1$ fs.

After preparation, equilibrium simulations for the $Fe(II)_{LS}$, $Fe(II)_{HS}$ and Fe(III) compounds were carried out in order to determine reference equilibrium properties including the energetics, the radial

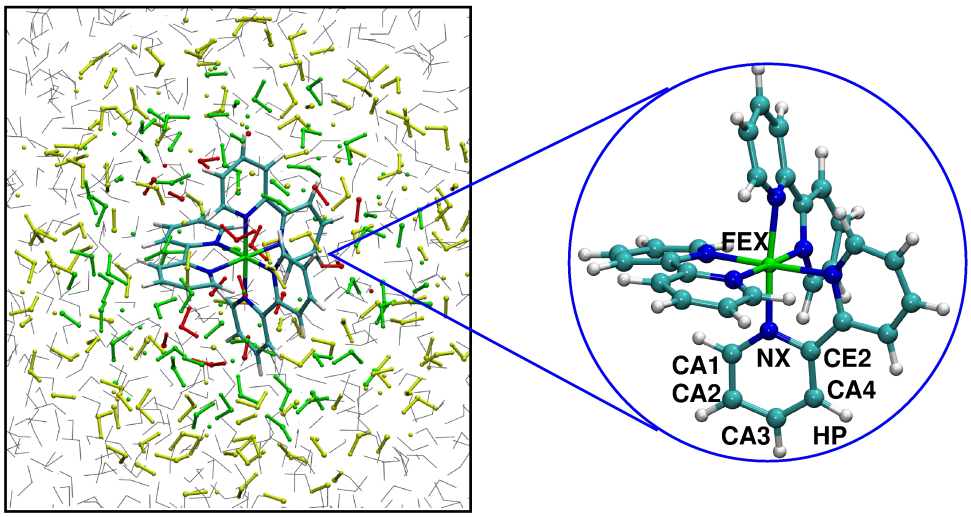

Figure 3.3.: The simulation system, consisting of the $[Fe(II)_{LS}(bpy)_3]$ complex and the solvation environment. Water molecules in the first solvation layer at 6.3 Å are shown in red color, second shell at 9.0 Å in green color, third shell at 11.6 Å in yellow color and bulk water in gray lines. Metal complex with atom types shown in the circle. Atom color code: Carbon (cyan), Nitrogen (blue), Iron (green) and Hydrogen (white).

distribution function (RDF) $g(r)$, and $N(r)$ which is the number of water molecules as a function of the distance r of water-oxygen atoms from the Fe-atom. The structures and velocities along the $Fe(II)_{LS}$ and Fe(III) equilibrium trajectory also served as initial conditions for the non-equilibrium simulations. Overall, 100 initial structures were generated, each separated by 10 ps from each other. Electronic excitation from $Fe(II)_{LS}$ to Fe(III) was induced by instantaneously changing the force field parameters between the two oxidation states (denoted as $Fe(III)^{neq}$). Similarly, the relaxation process of Fe(III) to $Fe(II)_{HS}$ was carried out by changing the force field parameters from Fe(III) to $Fe(II)_{HS}$ (labeled $Fe(II)^{neq}_{HS}$). Such perturbations lead to a non-equilibrium situation from which the system relaxes towards an equilibrium state. Each non-equilibrium simulation was run for 25 ps.

3.3.2. Trajectory Analysis

From the temporal evolution of the coordinates and velocities following observables are calculated.

Radial distribution functions: Radial distribution functions $g(r)$ were computed from the distance-time series of the respective coordinate r for each trajectory obtained from the MD simulation and then averaged over all. $g_O(r)$ and $g_H(r)$ were computed by considering Fe-O_W and Fe-H_W respectively. O_W

and H_W corresponds to the water oxygen and water hydrogen. From the $g(r)$, corresponding $N(r_s)$ for a given solvent shell (up to distance r_s) was computed using equation 3.1

$$N(r_s) = 4\pi\rho \int_0^{r_s} r^2 g(r) dr \tag{3.1}$$

where ρ is the bulk water density. $N_{\mathrm{H}}(r)/N_{\mathrm{O}}(r)$ was also computed to account the organization of water molecules around the metal center. In particular, it provides orientational preference of water molecules around the complex. $N_{\mathrm{H}}(r)/N_{\mathrm{O}}(r) = 2$ corresponds to the bulk water. If the value different from 2 suggests structuring of water molecules around metal complex.

Rotational reorientation times of water: The rotational reorientation time τ_r of a water molecule is computed by fitting an exponential function $R_r(t) = A\exp(-t/\tau_r)$ to the rotational time correlation function computed using $R_r(t) =< \vec{u}(0)\vec{u}(t) >$. All the rotational reorientation time calculations were carried out within the CHARMM program.[50]

Water residence times: Exchange dynamics of water molecules around the metal complex was analyzed by computing their residence time in the different shells as characterized by the radial distribution functions. For a given solvent shell, the residence time is determined from the time correlation function $R(\tau)$[116,117]

$$R(\tau) = \frac{1}{N n_W} \sum_{i=1}^{N} \sum_{j=1}^{n_W} \Theta_j(t)\Theta_j(t+\tau) \tag{3.2}$$

which was fitted to a bi-exponential function (see equation 3.3). In Equation 3.2 N is the number of trajectories, $\Theta_j(t)$ is the step function which describes the presence of a water molecules j in a given shell and n_W is the number of water molecules in the respective shell. If the water molecule j is present in the shell, then $\Theta_j(t) = 1$, otherwise $\Theta_j(t) = 0$. The spatial extent of the water shells r_s are defined by the minima of $g_{\mathrm{O}}(r)$ and a water molecule is considered to belong to a particular shell for $r \leq r_s$.

$$R_2(\tau) = A_1 \exp\left(-\frac{t}{T_1}\right) + A_2 \exp\left(-\frac{t}{T_2}\right) \tag{3.3}$$

The two time constants T_1 and T_2 provide information about the dynamics of water molecules close to the border of the shell and the typical lifetime within a shell and A_1 and A_2 describe the relative importance of each processes.

IR spectra: Vibrational spectra $C(\omega)$ are obtained from the Fourier transform of the dipole-dipole auto-correlation function $C(t)$[118] which was averaged over 2^{15} time steps. The Fourier transform was computed using a Blackman filter.[119] Finally, the IR spectrum is computed using equation 3.4

$$A(\omega) \propto \omega(1 - \exp(-\hbar\omega/(k_B T)))C(\omega) \tag{3.4}$$

where $\hbar$ and k_B are the Planck and Boltzmann constant, respectively, and T is the simulation temperature.

3.4. Results and Discussion

3.4.1. Validation of the Force Field

Before investigating the equilibrium and non-equilibrium dynamics in more detail, the current force fields are further validated by comparing with experimental data. The structural comparison and validation of interaction energies between the complex and a water molecule has already been described above. Furthermore, the infrared spectrum of the $[Fe(II)_{LS}(bpy)_3]$ complex has been investigated experimentally and provides additional reference data for comparison. Table 3.3 summarizes the experimentally measured and computed line positions. There is a shift of ≈ 10 cm^{-1} for the Fe-N and ≈ 100 cm^{-1} for the C-N stretching frequency compared to the experiment, whereas for the C-C stretch this shift is ≈ 50 cm^{-1}.[111,120] These differences could be reduced by slightly modifying the force constants which was, however, not deemed necessary for the current work which is primarily concerned with the solvation dynamics *around* the complex. In the experiments, peaks for the stretching modes are reported to be at 423 cm^{-1} for Fe-N, 1605 cm^{-1} for C-C, 1470 cm^{-1} for C-N and 3080 cm^{-1} for C-H. To further validate the parametrization, the IR spectrum of the ^{15}N isomer is determined and overlapped with the spectrum for the normal isomer. It is found that there is ≈ 5 cm^{-1} of isotopic shift for the Fe-N stretch is in good agreement with a previously reported value of 6 cm^{-1}.[121]

Table 3.3.: Experimental[111,120] and computed IR spectrum of $[Fe(II)_{LS}(bpy)_3]$.

Assignment	Computed frequency cm^{-1}	Experimental frequency cm^{-1}
Fe-N	415	423
C-N	1370	1470
C-C	1555	1605

3.4.2. Equilibrium simulations

In a next step, the equilibrium dynamics of the solvated complexes is considered. The water structuring can be characterized by the Fe-O_W and Fe-H_W RDFs $g_O(r)$ and $g_H(r)$. Their integration provides the running coordination numbers $N_O(r)$ and $N_H(r)$, as described in the Methods section.

The radial distribution function $g_O(r)$ and corresponding coordination number $N_O(r)$ of water oxygen with respect to the Fe atom for all three equilibrium simulations $Fe(II)^{eq}_{LS}$, $Fe(II)^{eq}_{HS}$ and $Fe(III)^{eq}$ are shown in Figure 3.4. For $Fe(II)^{eq}_{LS}$ the first peak in $g_O(r)$ appears at 4.5 Å and a minimum at 5 Å describes the inner solvent shell close to the complex and the peak in the $g_O(r)$ is due to the interaction of the water hydrogen (H_w) with the negatively charged bipyridyl ring and water oxygen with the metal atom. This peak is less pronounced for $Fe(II)^{eq}_{HS}$ and disappears completely for $Fe(III)^{eq}$ (see Figure 3.4) because the amount of negative charge on each ring of the bipyridyl ligand decreases from -0.90 to $-0.83e$ in going from $Fe(II)^{eq}_{LS}$ to $Fe(III)^{eq}$ (see Table 3.1). This also lowers the interaction energy between H_w and the ring. Although the negative charge on the ring for $Fe(II)^{eq}_{HS}$ ($-0.94e$) is larger compared to $Fe(II)^{eq}_{LS}$, the peak is less pronounced due to the increased Fe-N bond length by 0.2 Å. A second maximum in $g_O(r)$ appears at 5.7 Å and a minimum at 6.3 Å, defines the first solvent shell (shell-I) around the Fe atom and this peak appears in all three cases. The running coordination number $N_O(r)$ in the same figure shows that there are 3 and 15 water molecules present in the inner and first solvent shell for $Fe(II)^{eq}_{LS}$. This is in good agreement with previous simulations on $[Ru(II)(bpy)_3]$ and $[Fe(II)(bpy)_3]$[37,100]. However, for $Fe(III)^{eq}$ there are 2 and 15 water molecules present in the inner and first solvent shell, respectively (see Figure 3.4).

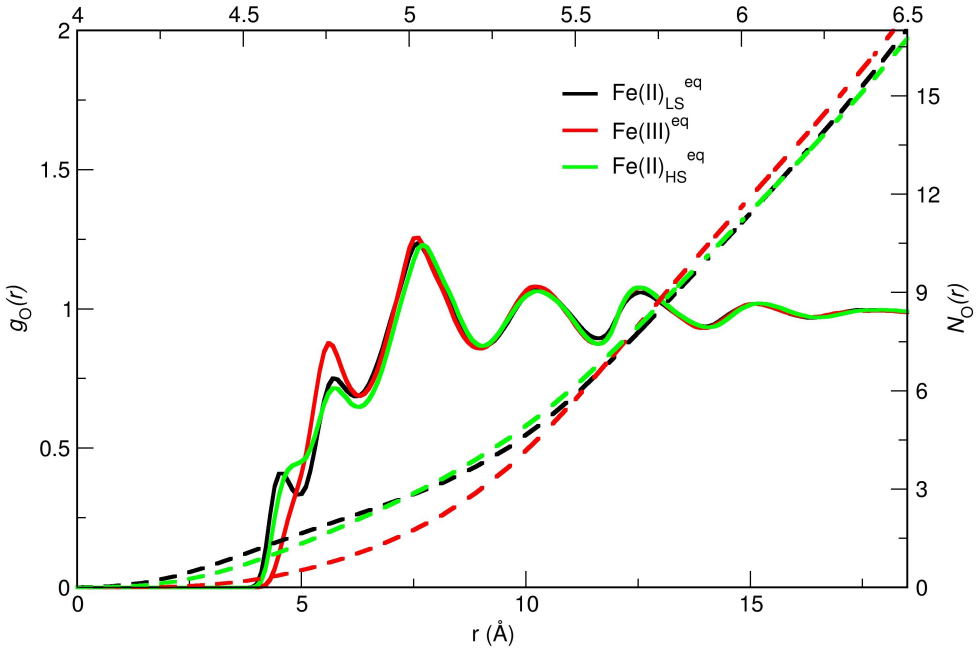

Figure 3.4.: Radial distribution function $g_O(r)$ (solid black, red and green lines, lower $x-$axis with left $y-$axis) and running coordination number $N_O(r)$ (dashed black, red and green lines, upper $x-$axis with right $y-$axis) of water oxygen with respect to the Fe atom obtained from the all three equilibrium simulations Fe(II)$^{eq}_{LS}$, Fe(II)$^{eq}_{HS}$ and Fe(III)^{eq} are shown.

The total charge on each bipyridyl ring is $-0.90e$, $-0.95e$, $-0.83e$ for Fe(II)$_{LS}$, Fe(II)$_{HS}$ and Fe(III), respectively, which yields an electrostatic component of the interaction energy between the closest water molecule and the complex of –6.87, –6.52 and –2.93 kcal/mol for LS, HS and Fe(III) in their energy minimized structures. For all three systems the water-hydrogen H_w always points towards the bipyridyl ring. For a direct comparison, the energetics of the optimized structure of the Fe(II)$_{LS}$ was also analyzed. The interaction energy between a single water molecule and the complex for the three states is –6.87, –6.35 and –2.78 kcal/mol for LS, HS and Fe(III) respectively. The electrostatic interaction between the water molecule and the metal atom are 8.02, 10.92 and 9.99 kcal/mol for LS, HS and Fe(III), respectively, whereas for the ligands in the absence of the metal atom they are –14.88, –17.27 and –12.77 kcal/mol.

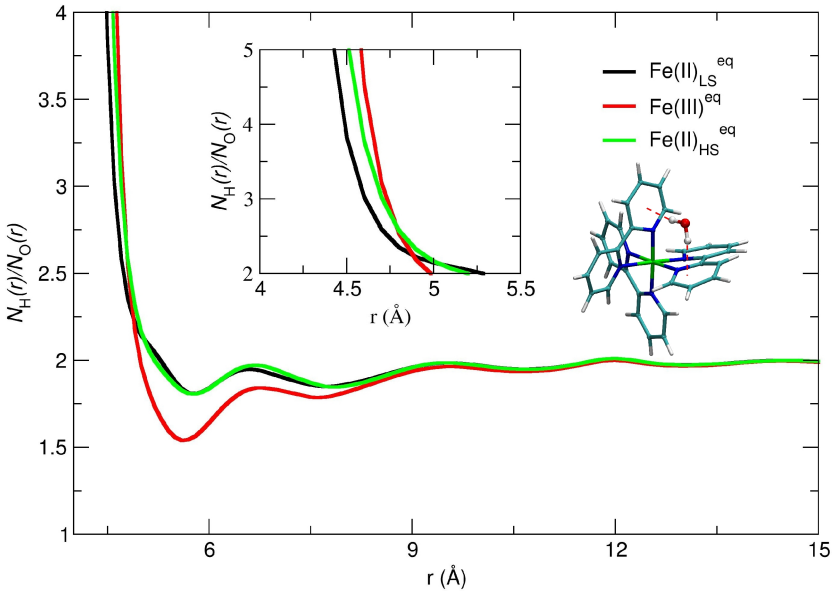

Figure 3.5.: Ratio of running coordination number of water oxygen and water hydrogen with respect to Fe atom obtained from three equilibrium simulations. Inset shows the $N_{\mathrm{H}}(r)/N_{\mathrm{O}}(r)$ ratio in the inner shell and the complex with water molecule shows the preferred orientation of water inside the groove of the complex in $\mathrm{Fe(II)}_{\mathrm{LS}}^{\mathrm{eq}}$.

Additional information regarding the organization of the water molecules can be obtained from analyzing the ratio $N_{\mathrm{H}}(r)/N_{\mathrm{O}}(r)$ (see Figure 3.5). In bulk water, this ratio is $N_{\mathrm{H}}(r)/N_{\mathrm{O}}(r) = 2$. However, due to orientational preference around a solute molecule, it can deviate considerably from this idealized value. At short distances from the metal center there is an over-proportion of hydrogen atoms which can be rationalized from the structure reported in Figure 3.5. With increasing distance there are slightly more oxygen atoms until the bulk value of $N_{\mathrm{H}}(r)/N_{\mathrm{O}}(r) = 2$ is reached for separations larger than about 12 Å.

Within 5 Å from the metal atom $N_{\mathrm{H}}(r)/N_{\mathrm{O}}(r) > 2$ for all three systems (see Figure 3.5) due to the orientation of $\mathrm{H_w}$ towards the center of the complex, the interaction of $\mathrm{H_w}$ with the negatively charged bipyridyl ring and the smaller van der Waals radius $R_{min}/2 = 0.2245$ Å). Around the second maximum of $g_{\mathrm{O}}(r)$ at 6.3 Å, $N_{\mathrm{H}}(r)/N_{\mathrm{O}}(r) < 2$ (1.79 for $\mathrm{Fe(II)}_{\mathrm{LS}}^{\mathrm{eq}}$, 1.81 for $\mathrm{Fe(II)}_{\mathrm{HS}}^{\mathrm{eq}}$ and 1.5 for $\mathrm{Fe(III)}^{\mathrm{eq}}$), reflecting the fact that an over-proportion of water-oxygens are oriented towards the center of the iron complex (i.e. depletion of H-atoms), and then approaches the bulk-value of $N_{\mathrm{H}}(r)/N_{\mathrm{O}}(r) = 2$ asymptotically. The difference between $N_{\mathrm{H}}(r)/N_{\mathrm{O}}(r)$ for $\mathrm{Fe(II)}_{\mathrm{LS}}^{\mathrm{eq}}$ and $\mathrm{Fe(III)}^{\mathrm{eq}}$ remains always above 0.2 for distances up to $r \approx 6$ Å which suggests that the proportion of hydrogen atoms for $\mathrm{Fe(II)}^{\mathrm{eq}}$ is larger compared

to $Fe(III)^{eq}$. This reflects the stronger electrostatic interaction between the water molecule and the ligand for Fe(II) compared to Fe(III). In going from $Fe(II)^{eq}_{LS}$ to $Fe(II)^{eq}_{HS}$, the value of $N_H(r)/N_O(r)$ (1.79 for $Fe(II)^{eq}_{LS}$ and 1.81 for $Fe(II)^{eq}_{HS}$) remains almost unchanged (see Figure 3.5) due to the very similar interaction energies with the solvent. For a distance of $r = 9$ Å from the metal atom, the difference drops to approximately 0.05 and for $r = 12.5$ Å $N_H(r)/N_O(r) \approx 2$ which corresponds to bulk water.

Water reorientation times: The dynamics of the water molecules can be characterized by considering their rotational reorientation. Rotational reorientation times τ_r decrease gradually in going from the first solvent shell to bulk water, as the rotational dynamics of the solvent molecules close to the complex slows down. For bulk water, τ_r is 0.785 ps which is in good agreement with the previously reported value of 0.7 ps from simulations (TIP3P water model)[122]. However it is slower compared to the experimental value of 1.95 ps[123]. For solvent molecules close to the metal complex τ_r increases by 30 % due to the interactions with the metal complexes.

Water residence times: The water residence times were computed using the procedure described in the method section and are given in Table 3.4. Two time constants T_1 and T_2 describe the dynamics, see Figure 3.6. T_1 in all three equilibrium simulations are similar (≈ 0.2 ps). This time scale characterizes the rapid recrossing dynamics at the border of the shell while T_2 is on the several ps time scale and represents the typical lifetime in a given water shell (shells I to III). For simulations of pure water with the MCY model this time has been reported to be 4.5 ps.[116] In previous work the short recrossings were eliminated by introducing a lag time t^* which was set to 2 ps.[116] For the first solvent shell, $T_2 = 3.78$ ps for $Fe(II)^{eq}_{LS}$ which is larger compared to the other two equilibrium simulations and can be qualitatively explained by the increased electrostatic interaction between the water molecules and the complex (see above). Since T_2 describes the lifetime within a given shell and the shells grow in size, T_2 gradually increases with the shell radius due to an increase in the number of solvent molecules. In all three equilibrium simulations the residence time for shell-III is ≈ 11 ps (see Table 3.4) which is consistent with 12.2 ps and 12.4 ps found previously based on force field or mixed QM/MM simulation on aqueous $[Ru(II)(bpy)_3]$.[100,124]

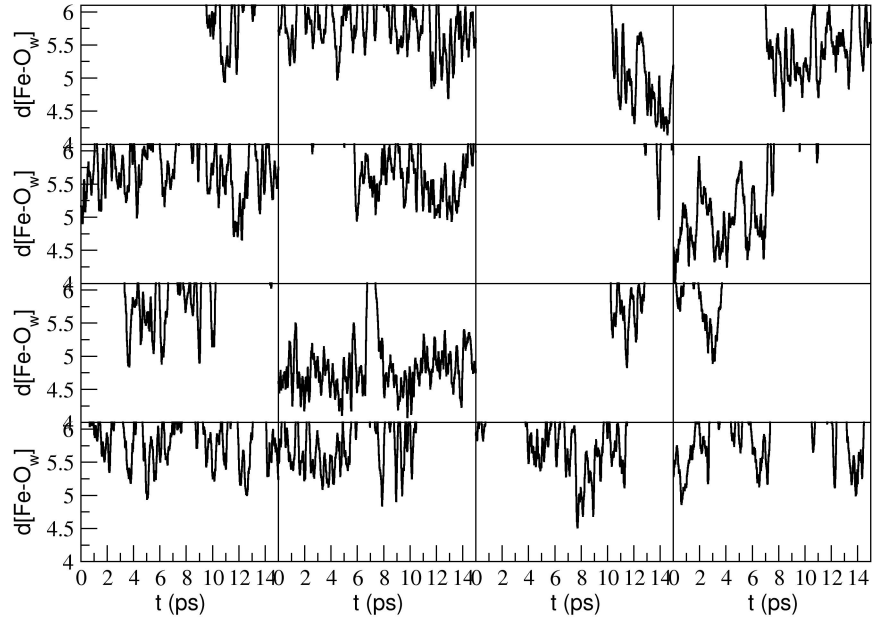

Figure 3.6.: Distances of 16 water oxygen (involved in the exchange process) within 5 Å of the Fe atom during equilibrium simulations of $\mathrm{Fe(II)}^{\mathrm{eq}}_{\mathrm{LS}}$.

The correlation function $C_{\mathrm{O}}(t) =< \delta O(0)\delta O(t) > / < [\delta O(0)]^2 >$ determines the persistence time of a particular water shell (see Figure 3.7). Here $O(t) = 1$ for all water oxygen atoms if they are within a distance R of the Fe-atom, otherwise $O(t) = 0$. $C_{\mathrm{O}}(t)$ was computed by considering all water oxygen atoms for which $O(t) = 1$ at least once during the whole simulation. In other words, $C_{\mathrm{O}}(t)$ describes the persistence time of a particular solvent shell. For shell-I (at 6.3 Å) and one particular simulation of $\mathrm{Fe(II)}^{\mathrm{eq}}_{\mathrm{LS}}$, a bi-exponential function fitted to $C_{\mathrm{O}}(t)$ yields two time constants 5.3 and 39.8 ps (see Figure 3.7). The first time constant characterizes exchange of one water molecule between neighboring shells for this specific simulation and the second time constant is the time required for the complete exchange of water molecules in this shell. Following the complete dynamics of all shell-I water molecules starting from an arbitrary snapshot yields a time of 20 ps for full replacement by water molecules from solvent molecules further away. Also, the magnitude of the longer time scale is consistent with previous work on CN^- for which complete replacement of the first water shell (10 water molecules) was found to occur on the 10 ps time scale.[125] Hence, for $\mathrm{Fe(II)}^{\mathrm{eq}}_{\mathrm{LS}}$, the diffusion and replacement of solvent molecules between neighboring shells occurs on the picoseconds time scale (see Figure 3.7).

Explicit analysis of 15 ps of simulations for $\mathrm{Fe(II)}^{\mathrm{eq}}_{\mathrm{LS}}$ yields $\approx$ 20 water molecules that are involved in the

exchange process within 5 Å from the Fe atom and their distances from the metal center are reported in Figure 3.6. Water molecules with short life times (< 1 ps) are those close to the boundary. The probability distribution of the life time of water molecules (> 1 ps) within 5 Å from the metal center were computed for $Fe(II)^{eq}_{LS}$ (see Figure 3.8) and yield $< \tau >= \frac{\sum_i p_i \tau_i}{\sum_i p_i} = 2.23$ ps which qualitatively agrees with the residence times (3.78 ps, see Table 3.4).

Table 3.4.: Time constants for residence correlation functions $R(\tau)$ for the equilibrium simulations

		Shell-I	Shell-II	Shell-III
	r_s (Å)	$0 < r_s \leq 6.3$	$0 < r_s \leq 9.0$	$0 < r_s \leq 11.6$
$Fe(II)^{eq}_{LS}$	No. of water	15	83	199
	A_1	0.668	0.679	0.666
	A_2	0.132	0.161	0.134
	T_1/ps	0.30	0.37	0.47
	T_2/ps	3.78	7.28	11.59
$Fe(II)^{eq}_{HS}$	No. of water	14	83	198
	A_1	0.652	0.679	0.664
	A_2	0.189	0.160	0.135
	T_1/ps	0.24	0.36	0.47
	T_2/ps	2.94	7.28	11.48
$Fe(III)^{eq}$	No. of water	15	83	199
	A_1	0.661	0.674	0.667
	A_2	0.198	0.161	0.133
	T_1/ps	0.22	0.36	0.47
	T_2/ps	2.45	7.08	11.59

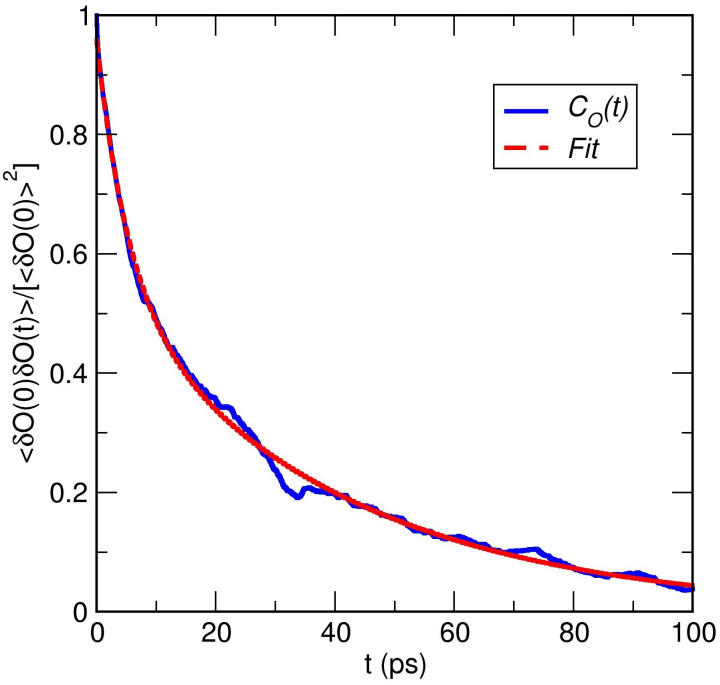

Figure 3.7.: The occupation correlation function $C_{\mathrm{O}}(t)$ of $\delta O(t)$ as a function of time within the distance of 6.3 Å from the metal center for $\mathrm{Fe(II)}_{\mathrm{LS}}^{\mathrm{eq}}$. The red dotted line is a bi-exponential fit.

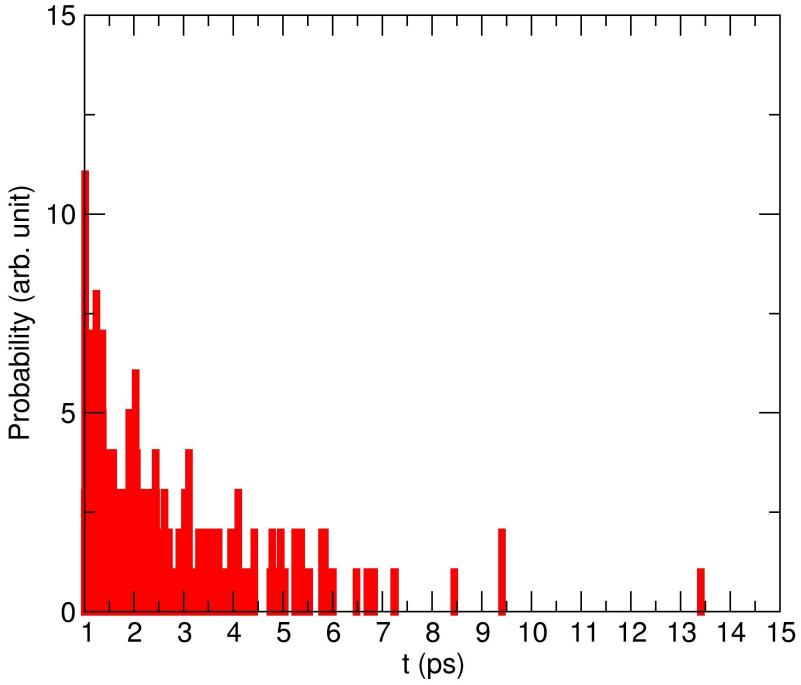

Figure 3.8.: Survival probability distribution $p(\tau)$ for water molecules within 5 Å from the metal center in the equilibrium simulations of $Fe(II)^{eq}_{LS}$.

3.4.3. Non-equilibrium simulations

For the investigation of the solvent reorganization dynamics depending on the oxidation state of the complex, photo-excitation was modeled by instantaneously changing the force field parameters from one state to the other (see Methods). Such a procedure has also been employed for CO- and NO-photodissociation from heme in Myoglobin[126] and for electronic excitation in ClCN[127].

Structural Reorganization of the Solvent after Photoexcitation: To describe solvent structure rearrangement after photoexcitation of $Fe(II)(bpy)_3$, the radial distribution function $g_O(r)$ and the water-coordination number $N_O(r)$ around the Fe-atom was analyzed. As mentioned previously and reported in Figure 3.4 the most pronounced difference in $g_O(r)$ for all three states $Fe(II)^{eq}_{LS}$, $Fe(II)^{eq}_{HS}$ and $Fe(III)^{eq}$ is within 5 Å, see Figure 3.4. Since the differences in $g_O(r)$ beyond 5 Å are rather small we focus only on the inner shell. The photocycle was studied in three steps, first $Fe(II)_{LS}$ was excited to ^{1,3}MLCT and then it relaxed to $Fe(II)_{HS}$, subsequently it returns to the $Fe(II)_{LS}$ state, see Figure 3.1[88]. In the photo excitation of $Fe(II)_{LS}$ to ^{1,3}MLCT the degree of solvation decreases by less

than one water molecules depending on the distance from the iron atom considered. There is no substantial change in the degree of solvation in the other two relaxation processes (see Figures 3.9 and 3.11).

For more insight into the time scale for the geometrical relaxation of solvent structure around the metal center, the coordination number at different times after photo-excitation, relaxation and SCO were determined. Since $N_O(r)$ between the systems differs most at 4.75 Å, this value was used in the analysis. To quantify the time scale for solvent reorganization, a single exponential function was fit to this data in and yields a decay constant of 0.80 and 2.81 ps for $Fe(III)^{neq}$ and $Fe(II)^{neq}_{HS}$, respectively, see Figure 3.10. Such relaxation times agree well with recent experiments which found 1.1 and 3.4 ps from transient absorption spectroscopy.[128]. Hence, in all three cases, the geometrical relaxation of the solvent occurs on the ps time scale (see Figure 3.10). This has also been investigated for systems such as I^-/I^0 in water for which QM/MM simulations and XAS experiments[129,130] have been carried out. The computations yield reorganization times of 3 to 4 ps whereas the picosecond experiments with a time resolution of 70 ps are too slow to be sensitive to the solvent reorganization. Overall, the time scale of the process obtained from the computationally much more demanding QM/MM simulations on solvated halides compare favorably with those reported in the present work.

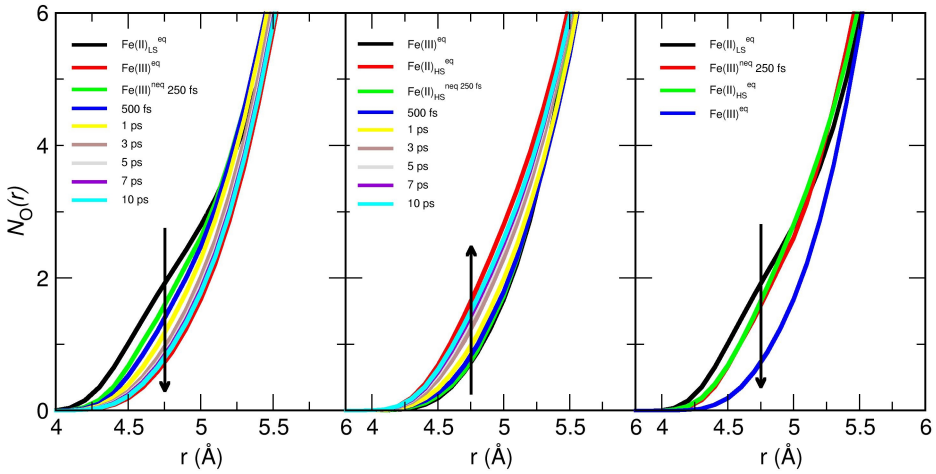

Figure 3.9.: Running coordination number $N_O(r)$ of water oxygen with respect to the Fe atom obtained from non-equilibrium simulations Fe(III)^{neq} (left panel) and Fe(II)$_{HS}^{neq}$ (Fe(III) $\rightarrow$ Fe(II)$_{HS}$) (middle panel) at different time interval (averaged over 100 trajectories). Comparison of water coordination between three equilibrium state with Fe(III)^{neq} at 250 fs (right panel). Black arrows shows the change in water coordination number in the inner shell during the non-equilibrium process. The color codes for the lines are given in the panels.

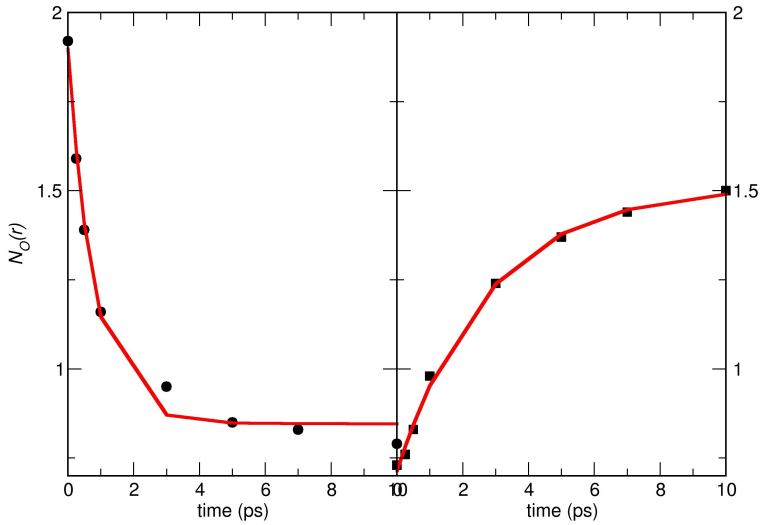

Figure 3.10.: Running coordination number $N_O(r)$ of water oxygen with respect to the Fe atom at 4.75 Å computed at different time intervals during the photo-excitation and fitted to a exponential function: Fe(III)^{neq} (Fe(II)$_{LS}$ $\rightarrow$ Fe(III)) (left) and Fe(II)$_{HS}^{neq}$ (Fe(III) $\rightarrow$ Fe(II)$_{HS}$) (right). $N_O(r)$ data (black points) and fitted function (solid red curve).

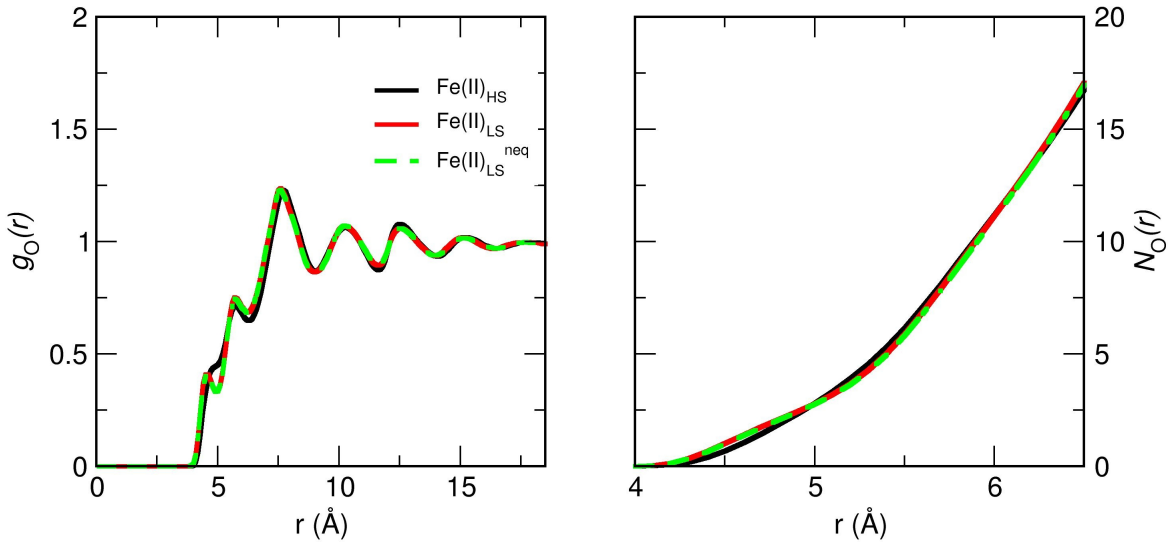

Figure 3.11.: Radial distribution function $g_O(r)$ (left panel) and running coordination number $N_O(r)$ (right panel) of the water oxygen with respect to the metal atom for non-equilibrium $Fe(II)_{LS}^{neq}$ averaged over 25 ps (green dashed line) simulation along with equilibrium $g_O(r)$ and $N_O(r)$ for $Fe(II)_{LS}^{eq}$ (red) and $Fe(III)_{LS}^{eq}$ (black). It is found that full equilibration takes place on the 25 ps time scale.

Residence times: For all three non-equilibrium simulations the water residence time are shorter compared to the corresponding equilibrium simulations. This suggests that during the photo excitation process energy is brought into the system which immediately transfers to the solute and leads the more rapid exchange dynamics of solvent molecules close to the metal center.

3.4.4. Comparison with Experiment and Previous Simulations

The current simulations provide a framework to discuss several previous investigations of the photocycle in $[Fe(bpy)_3]$.[37,88–90] Femtosecond time resolved fluorescence spectroscopy showed that starting from the $[Fe(II)_{LS}(bpy)_3]$ state the system populates the ^{1,3}MLCT (or $[Fe(III)(bpy)_3]$) excited state with a lifetime of ≤ 200 fs.[88] This lifetime was recently confirmed (150 ± 50 fs) from analysis of femtosecond time resolved X-ray fluorescence spectroscopy.[89] Relaxation via intermediate states, such as a ^{3}T state (with an estimated lifetime of 70 ± 30 fs) leads to the $[Fe(II)_{HS}(bpy)_3]$ state which has a lifetime of several hundred picoseconds (665 ps).

A combined X-ray emission (XES) and X-ray diffuse (XDS) scattering experiment with a time resolution of 80 ps provided evidence for a change in the solvent density upon excitation of the $[Fe(II)_{LS}(bpy)_3]$ initial state.[90] The analysis indicated that the density increase occurred on a 100 ps time scale which was linked to ab initio MD simulations run separately for the $[Fe(II)_{LS}(bpy)_3]$ and $[Fe(II)_{HS}(bpy)_3]$ states.[37] These simulations suggested that for the first solvation shell, defined by a radius of 6.3 Å, the water coordination number differs by 2 water molecules, i.e. in the LS and HS state ≈ 17 and ≈ 15 water molecules, respectively, are in the first solvation shell which compares with a conformationally averaged value of 15 and 14 water molecules from the present work. This observation is insofar unexpected as the Fe-N distance increases by 0.2 Å in going from the LS to the HS state and hence *more* space to accommodate water molecules would be available in the HS state. On the other hand it is possible that the charge distribution between $[Fe(II)_{LS}(bpy)_3]$ and $[Fe(II)_{HS}(bpy)_3]$ changes sufficiently to counteract the geometrical changes. Ab initio MD simulations[37] on such systems are very time consuming and therefore in previous work only one trajectory for each state was run for 24 and 4 ps, respectively. Hence, the temporal evolution averaged over a sufficiently large number of snapshots of the system could not be followed.

In the present work the photocycle considered in the fs-TR fluorescence study was followed.[88] Upon excitation to the ^{1,3}MLCT band the degree of solvation decreases on the 250 fs to 500 fs time scale, see Figure 3.9. As this is a vertical transition with negligible change in the Fe-N geometry (see also Fe-N separations in Tables 3.2), the origin of the water expulsion is purely electronic, i.e. the charge redistribution drives the process and not the structural change in the $Fe(bpy)_3$ complex. As the system only populates this state for a few hundred fs and decays to $[Fe(II)_{HS}(bpy)_3]$, the change in solvation between the non-equilibrium ^{1,3}MLCT and the equilibrium $[Fe(II)_{HS}(bpy)_3]$ is relevant. As Figure 3.9 shows, there is negligible difference in the degree of solvation between these two states despite the bond lengthening in $[Fe(II)_{HS}(bpy)_3]$. The number of water molecules expelled from the energized $[Fe(II)_{LS}(bpy)_3]$ state found here is ≈ 1 which differs from the value of 2 from previous simulations which is, however, only based on one quite short QM/MM simulation.[37] It is evident from the present simulations that the degree of solvation decreases on a sub-picosecond time scale and originates from the excitation to the ^{1,3}MLCT band. The experiment reports an estimated increase in the overall solvent density by 0.03 % (no error bar) without accounting for the increased volume and reorientation

of the solvent. This was interpreted as a change of 1 to 2 water molecules upon oxidation. The time scale for the solvent exchange is a few picoseconds, which is more rapid than inferred from the experiments but comparable to previous work on CN^- for which the time scale for solvent exchange was also found to be a few picoseconds from both, simulations and NMR experiments.[125,131] Hence it is possible that while the general conclusion of water expulsion upon oxidation can be verified, the time scales found here and in the experiment correspond to different processes. This is confirmed by the observation that the *equilibrium* fluctuations of the solvent shells occur on the few-picosecond time scale. Consequently, electronic excitation will further speed up the solvent dynamics and it is unlikely that the 100 ps time scale found in the experiments directly reflects water exchange dynamics.

In summary, the present simulations suggest that water expulsion occurs between $[Fe(II)_{LS}(bpy)_3]$ and the ^{1,3}MLCT state, is electronically driven, and occurs on a sub-picosecond time scale. Whether or not an intermediate ^{3}T state is included should not affect the present analysis because the lifetime of this state is very short. The non-equilibrium solvent arrangement of the ^{1,3}MLCT is similar to the $[Fe(II)_{HS}(bpy)_3]$ state and hence no further change in the degree of solvation is expected in this transition.

3.5. Conclusions

Atomistic simulations of solvated $[Fe(bpy)_3]$ using a validated VALBOND force field provide a detailed picture of the degree of solvation and solvation dynamics involving several spectroscopically characterized states. It is found that upon vertical excitation the degree of solvation decreases whereas relaxation from the non-equilibrium excited state to the $[Fe(II)_{HS}(bpy)_3]$ state does not change the solvent shell appreciably. Relaxation of the non-equilibrium ensemble of the ^{1,3}MLCT state to the equilibrium $[Fe(II)_{HS}(bpy)_3]$ state occurs on the picosecond time scale which agrees with recent experiments.[128] The water exchange dynamics in the inner shells close to the metal center take place on the picosecond time scale. Hence, the 100 ps time scale observed experimentally[90] is unlikely to correspond to exchange dynamics of individual water molecules in shells close to the metal center. The use of such force fields allows one to sample the conformational dynamics in a meaningful fashion and to determine averages which can be compared with experimental data and provide atomistic interpretations of the underlying time scales. This is one of the primary advantages of a force field-based approach to characterizing the

dynamics of solutes in solution.

4. Hydration Control Through Intramolecular Degrees of Freedom: Molecular Dynamics of [Cu(II)(Imidazole)$_4$]

4.1. Abstract

Structural characterization of the copper-coordination shell is important in catalysis and biology. Cu-containing domains are prevalent in biological systems and play important roles in oxidation and electron transport process. Here, the solution structure, solvent organization and dynamics around aqueous [Cu(II)(Imidazole)$_4$] was characterized using atomistic simulations. Asymmetric axial water coordination around the metal atom was found which agrees with results from Minuit X-ray absorption near-edge structure (MXAN) experiments. The simulations reveal that exchange of the axial water occurs on the 25 to 50 ps time scale and is facilitated by and coupled to the flexibility of the copper-out of plane motion relative to the nitrogen atoms. Both, concerted and stepwise water exchange of the two axially coordinated water molecules with first-shell water molecules is observed. The results suggest that axial access of a copper center can be fine-tuned by the degree of flexibility of its first coordination sphere.

4.2. Introduction

As the third most abundant transition metal in the human body (75–100 mg)[132–134], copper plays important roles in many biological and chemical processes including oxygen transport (*Haemocyanins*), electron transport (*Plastocynin, Azurin etc.*), nitrogen oxide reduction (*Nitrous-oxide reductase*) or molecular oxygen insertion[11–13,135–137]. Several studies have considered the interaction between transition metals and proteins mainly responsible for neurodegenerative diseases including Alzheimer's

or Parkinson's disease.[138] The multiple roles of Cu are owed to the facile interconversion between reduced Cu(I) and oxidized Cu(II).[139] Cu(I) prefers a tetrahedral coordination of its ligands whereas Cu(II) generally acquires distorted octahedral, square-planar, or square-pyramidal geometries. These differences in geometries lead to appreciable barriers ($\sim$ 55 kcal/mol) in electron transfer reactions and to large differences in reduction potentials ($\sim$ 0.5 V) for the oxidation states[140].

In biological systems, however, these structural differences are considerably reduced due to the constraining effects of the environment and the difference in reduction potentials can be controlled by the choice of coordinating ligands and their hardness or softness.[9] A typical example is the Cu(I)(H_2Tpy^{NMes})Cl complex with a square planar geometry which allows rapid self exchange electron transfer: Cu(I)(H_2Tpy^{NMes})Cl + [Cu(II)(H_2Tpy^{NMes})Cl]PF_6 $\rightarrow$ [Cu(II)(H_2Tpy^{NMes})Cl]PF_6 + Cu(I)(H_2Tpy^{NMes})Cl. NMR line broadening experiments yields an electron transfer rate of $2.4 \times 10^5 M^{-1}s^{-1}$, similar in magnitude to the electron transport rate in biological systems[4]. The tetrahedrality parameter[141] τ_4 of the Cu(I) and Cu(II) complexes are 0.303 and 0.358, respectively, which indicates that the two structures are similar and closer to a square planar arrangement ($\tau_4 = 0$) rather than a tetrahedral geometry ($\tau_4 = 1$). This shifts the reduction potentials of the two species closer to one another and minimizes the energetic requirement for a Cu(I)$\rightarrow$Cu(II) transition.
In protein environments, Cu(I) as the soft acid binds preferably to amino acids involving sulfur (cysteine or methionine) whereas Cu(II) coordinates to amino acids with hard bases including histidine, aspartic and glutamic acid[142]. The imidazole ring, i.e. the side chain of histidine residues, has a high affinity for Cu(II) ions which makes Cu-imidazole complexes directly relevant to understanding Cu(II)-protein interactions. As many protein active sites are water accessible (e.g. Cu/Zn superoxide dismutase or Azurin),[143,144] it is essential to understand the structure of and dynamics around hydrated transition-metal complex ions at the atomic level. This has been done explicitly for a number of metal-ligand complexes, including hydrated iron-tris-bipyridine,[90,145] a di-platinum complex[146], or ruthenium-tris-bipyridine.[35]

Even the coordination of the simplest Cu(II) ion in aqueous solution has been the subject of an intensive debate in recent years[38,147–150]. Although several experimental and theoretical studies were employed to characterize the solution structure of copper complexes, no generally accepted consensus could be reached so far. The primary quest was to clarify whether the Cu(II) ion prefers a penta-

coordinated[150] or a Jahn-Teller distorted hexa-coordinated octahedral configuration[148]. Neutron diffraction experiments suggest that the Cu(II) ion is penta-coordinated and there is rapid exchange between a square pyramidal and trigonal bipyramidal configuration[151]. On the other hand, using the same experimental method, it was observed that the ion is hexa-coordinated in D_2O and ethylene glycol[152–154]. The variability in the result obtained from the diffraction experiment is due to its inability to differentiate between the Cu-O_{axial} and Cu-$O_{equatorial}$ distances. Isotopic substitution in neutron diffraction method is capable of measuring radial distribution functions (RDF) $g_{Cu-O}(r)$ and $g_{Cu-H_w}(r)$ separately[151,155]. However, the RDF was quite broad and the corresponding oxygen occupation $N_{Cu-O}(r)$ is not flat in the first solvent shell. This points towards a penta-coordinated Cu(II) ion in aqueous solution. Also, similarly inconsistent results were reported from X-ray absorption near edge structure (XANES)[156], extended X-ray absorption fine structure (EXAFS)[147,156–159] and low-angle X-ray spectroscopy (LAXS)[147] experiments. This is partly due to the way how structural data is obtained from the spectroscopic measurements. The fitting procedure usually starts from an initial hypothetical structure and iterates until the computed signal agrees to within some residual with that from experiments. Recent EXAFS and Minuit X-ray absorption near edge (MXAN)[157,160] analysis which considers multiple scattering explicitly, suggest that the best fit was obtained with a noncentrosymmetric axially elongated square pyramidal geometry along with a non-bonded axial water at a distance of 2.9 Å. Models with axial imidazole coordination (i.e. with five or six imidazole ligands) had also been tested in the experimental study[160] but had failed and, therefore, were also not considered in the present study.

Computationally, several methods including BOMD[140,161], CPMD[162–165], QM/MM molecular dynamics[166–168], polarizable force field molecular mechanics[169] and gas phase cluster analysis[170–174] have been used to characterize the solution structure of the bare Cu(II) ion in water. Similar to the experiments, computations yield a range of results. Specifically, BOMD and CPMD with the BLYP functional suggest a five coordinated structure whereas polarizable force field simulations find six water molecules in the first solvent shell. However, BOMD/CPMD simulations with the BLYP functional underestimate the binding energy of water molecule to the Cu(II) ion (–16.8 kcal/mol) compared to CCSD(T) (–23.8 kcal/mol)[38] which casts some doubts about their reliability.

Here we employ a valence-bond force field-based and hybrid QM/MM molecular dynamics to study the coordination environment of hydrated [Cu(II)(imidazole)]. X-ray absorption near edge structure

(XANES) spectra are calculated and compared with experiments. This allows comprehensive and quantitative analysis of the solvation structure.

4.3. Computational Methods

The computational system was a [Cu(II)(Imidazole)$_4$] complex in a cubic water box of size 30^3 Å^3 with 857 water molecules (see Figure 4.1). All simulations were performed using CHARMM[50] with provisions for the VALBOND[98] force field to describe the metal complex and the TIP3P[114] for consistency with the CHARMM force field. The VALBOND force field based on the overlap of hybrid orbitals which capture the energetics at very large angular distortions and support hypervalent molecules by means of 3-center-4-electron bonds[103,104]. The remaining parameters for the imidazole ligands were those of the CHARMM force field.[101] SHAKE was applied to constrain all bonds involving hydrogen atoms[115]. The partial charges on the atoms of the complex were obtained from a Natural Bond Orbital (NBO)[106] analysis using the B3LYP[175] functional and the LANL2DZ[176] basis set for Cu and 6-31G(d,p)[108] for all other atoms using the Gaussian09 suite of programs[107].

First the system was energy minimized and then heated to 300 K followed by an NVT equilibration simulation for 1 ns at 300 K using the velocity Verlet integrator[74] with a time step of 1 fs and a Nosé-Hoover thermostat[177] for temperature control. Further 1 ns production run was performed for the hydration analysis around the complex.

For comparison, along with force field simulations, hybrid QM/MM simulations were also performed using the third-order formulation[178] of the density functional tight-binding (DFTB3) method[94,179] as it is implemented in CHARMM[180]. The 3OB parametrization for (ONCH) atoms[181] and copper[182] is used. In an initial attempt, only the metal complex was treated by DFTB3 and all water molecules by molecular mechanics. However, no axial water coordination was found which was counter to the expectation. Therefore, in a next step, the metal complex including the 10 water molecules closest to the complex were included in the QM part (described by DFTB3) (see Figure 4.1) whereas the remaining water molecules are treated with TIP3P. To avoid exchange of QM and MM water molecules, the Flexible Inner Region Ensemble Separator (FIRES) method is applied.[183] The SCF convergence

criterion used for DFTB3 is 10^{-8} E_h. The Van der Waals parameters for the Cu ion were those from Ref.[38]. The system was energy minimized and heated to 300 K. Then the NVT equilibrium simulation was carried out for 1 ns using the Verlet algorithm with a time step of 1 fs. Further 1 ns of production run was performed for the hydration analysis.

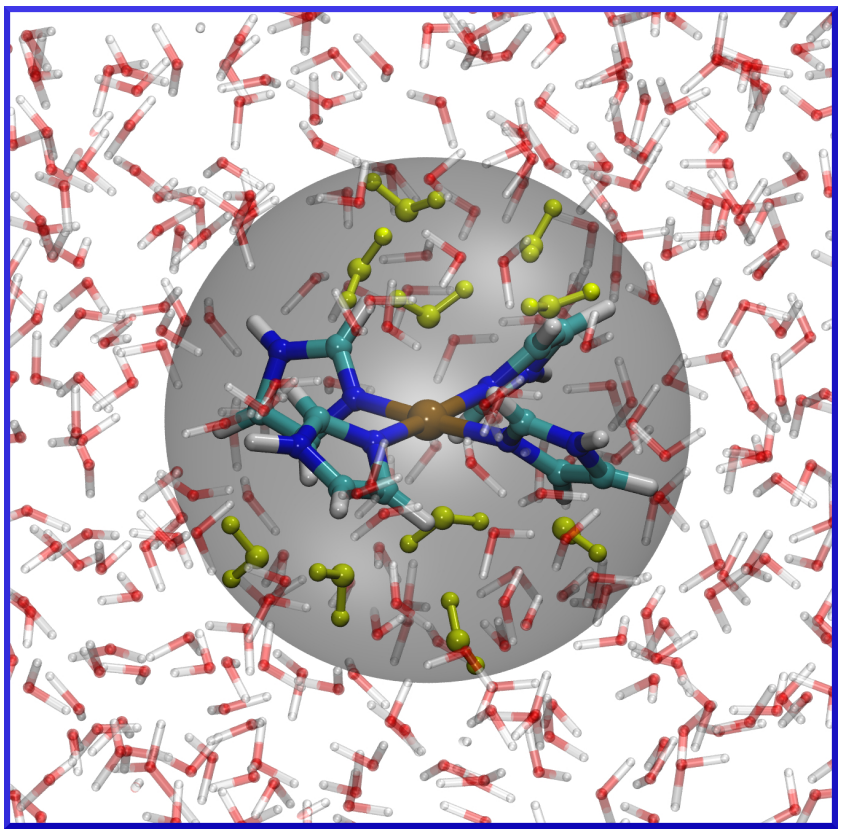

Figure 4.1.: The computational system including one [Cu(II)(Imidazole)$_4$] complex and solvent water molecules. Metal complex along with 10 water molecules in the QM region are shown inside the shaded sphere. QM water molecules shown in yellow color. Atom color code used: Copper (ochre), Carbon (Cyan), Nitrogen (blue), Oxygen (red) and Hydrogen (white)

XANES spectra were calculated from configurations separated by 20 ps along the MD simulations. For this, the FDMNES software[84,87] was used which determines the X-ray absorption cross section σ within the Fermi Golden Rule approximation. The necessary final state wavefunctions were computed using multiple scattering theory (MST) based on a Greens function expansion which yields the nonconvoluted signal $\sigma_{\mathrm{nconv}}(\omega)$. Many body effects and core hole lifetime broadening were included by convoluting

σ_{nconv} with a Lorentzian[86,87]

$$\Gamma_{\mathrm{f}}(E - E_{\mathrm{F}}) = \Gamma_{\mathrm{hole}} + \Gamma_{\mathrm{max}} \left(\frac{1}{2} + \frac{1}{\pi} arctan \left(\frac{\pi}{3} \frac{\Gamma_{\mathrm{max}}}{E_l} \left(\epsilon - \frac{1}{\epsilon^2} \right) \right) \right) \tag{4.1}$$

which yields the convoluted signal

$$\sigma_{\mathrm{conv}}(\omega) = \int_{E_{\mathrm{F}}}^{\infty} \sigma_{\mathrm{nconv}}(E) \frac{1}{\pi} \frac{\Gamma_{\mathrm{f}}(\omega)}{\Gamma_{\mathrm{f}}(\omega)^2 + (\hbar\omega - E)^2} dE \tag{4.2}$$

Here, $\epsilon = \frac{E - E_{\mathrm{F}}}{E_{\mathrm{cent}}}$ and E_{F} is the Fermi energy. The core hole width for copper is $\Gamma_{\mathrm{hole}} = 1.55$ eV, the total height $\Gamma_{\mathrm{max}} = 20$ eV, the inclination $E_{\mathrm{l}} = 30$ eV and the inflection point $E_{\mathrm{cent}} - E_{\mathrm{f}} = 30$ eV. For E_{F} and Γ_{hole} default values are used[84] whereas the remaining parameters are those from the literature.[148,184] The XANES calculation included all atoms (except hydrogen atoms) of the copper complex and several water molecules as specified in the text.

4.4. Results and Discussion

Validation of the VALBOND force field was done by comparing the energetics of 50 gas-phase configurations (from an equilibrium simulation at 50 K) of [Cu(II)(Imidazole)$_4$] with energies calculated at the B3LYP/6-31G(d,p) level of theory for nonmetallic atoms and the LANL2DZ basis set[185] for the Cu atom. Energies from DFTB3 were also computed for the same structures and the root mean square deviation (RMSD$_E$) between DFT and VALBOND is 0.76 kcal/mol compared with 0.91 kcal/mol for DFT and DFTB3 (see Figure 4.2). Hence, the VALBOND force field and DFTB3 agree well with the reference data from electronic structure calculations.

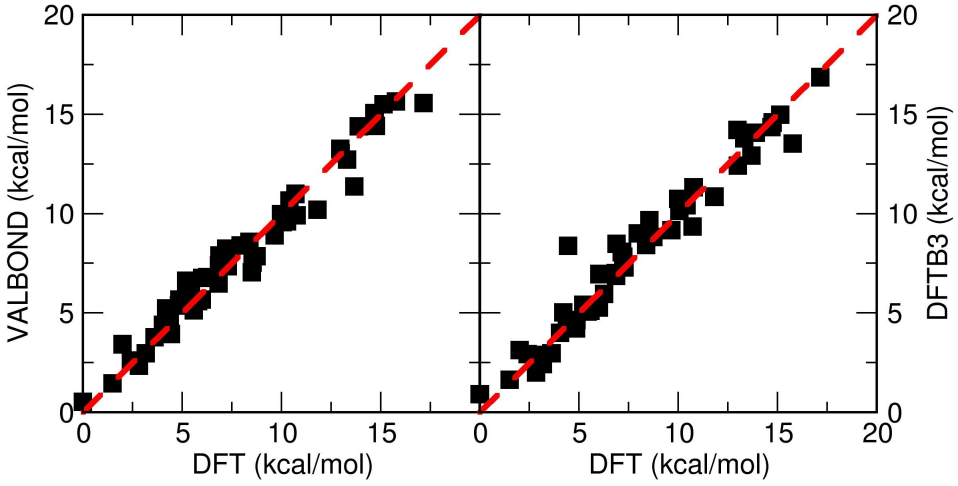

Figure 4.2.: Comparison of energies obtained from DFT, VALBOND force field and DFTB3 methods for 50 structures of [Cu(II)(Imidazole)$_4$]. The red dashed line represents $x = y$.

Additional validation is possible by computing the XANES spectra for the metal complex in solution and comparing with available experiments.[160] For direct comparison with the experiment, the computed spectra were scaled and shifted (to higher energy by ≈ 7 eV) to match the maximum intensity of the experiment[186,187]. In general, the calculated and experimental spectra compare favourably (see Figure 4.3). The pre-edge (Cu 1s $\rightarrow$ 3d transition) peak at ~ 8980 eV was found to be sensitive to the presence of solvent water. Specifically, the experimental pre-edge peak is best reproduced with two axially coordinated water molecules. With one axial water, the pre-edge peak also appears but the signal sharpens when a second axial water molecule is included in computing the XANES signal. Adding the entire first solvation shell does not modify the lineshape any further.

The width of the main peak around 9 keV is well described by the simulations. However, the experiments reveal a double peak structure of the main signal which is not reproduced by the conformationally averaged spectrum (dark green line in Figure 4.3B). The double peak structure appears when considering individual and non-convoluted spectra, see purple, cyan, grey, and orange traces in Figure 4.3B. Depending on the structure for which the XAS spectrum is computed (see bottom inset in Figure 4.3) the peak positions shift slightly with respect to each other but all spectra are double-peaked. When averaged over an ensemble of structures this leads to a smoothing which eventually removes the double-peak structure. The structures in Figure 4.3 confirm the assignment to a square

pyramidal structure from experiments. For higher energies beyond 9050 eV the computed and experimental spectra agree reasonably well although the experimental spectrum is somewhat more structured.

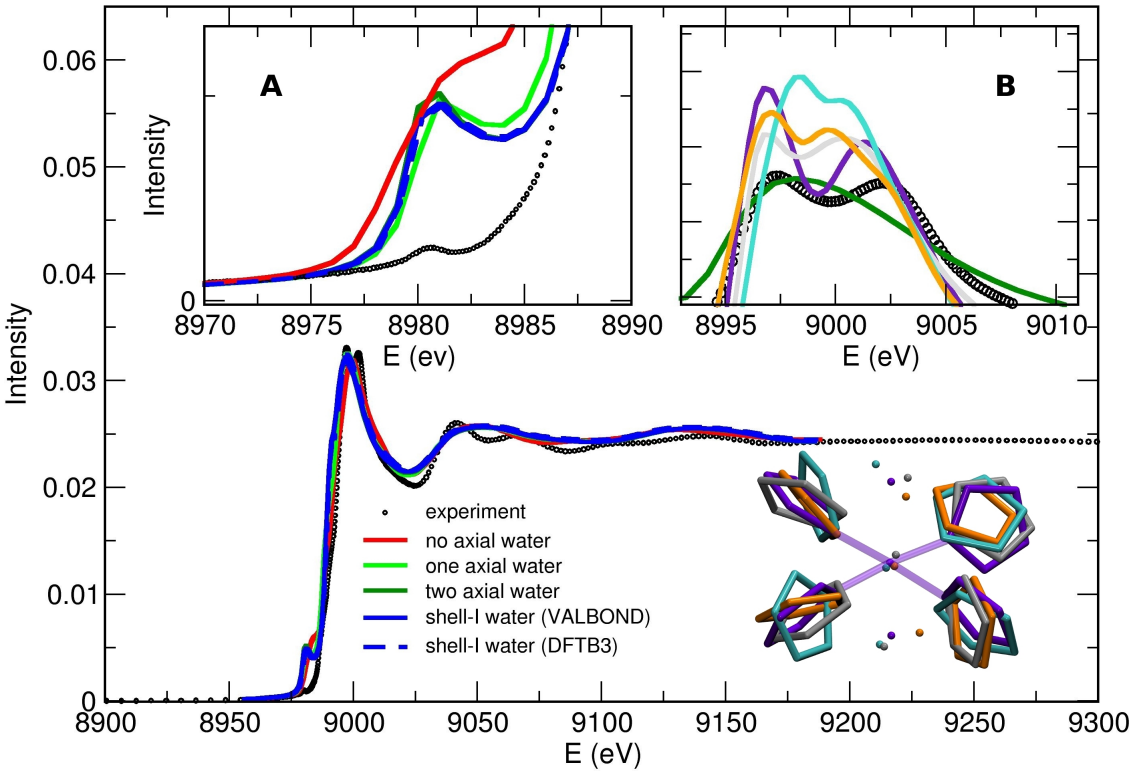

Figure 4.3.: Averaged calculated XANES spectrum for [Cu(II)(Imidazole)$_4$] along with the experimental spectrum[160]. Inset A shows the pre-edge region in the calculated XANES spectra sensitive towards solvent structure (Color code used: same as main Figure). Without water (red), the pre-edge peak is absent, with single water (light green line) the peak appears and further sharpens with a second axial water (dark green line). Including shell-I water molecules does not modify the signal appreciably. Inset B shows the unconvoluted double peak region around 9000 eV for four different configurations (cyan, grey, purple and orange lines and corresponding structures are shown in the inset below) along with their convoluted and averaged spectrum (dark green) and experiment (black circles).

The region between 8970 and 9025 eV is highly sensitive to solvent presence and solvent structure. The influence of structural change of the coordination environment on the convoluted XANES spectra is illustrated in Figure 4.4 which shows that as the two axial water molecules approach the Cu atom,

the peak is shifted towards lower energy and also the intensity of both peaks (8980 eV and 9000 eV) increases. For example, there is an energy shift of 7 eV for the peak at maximum intensity between the two structures where two axial water molecules are closest (black) and farthest (red). For the remaining structures (blue and green) the peak position is between that for the black and red structures as their Cu-O_w distances are intermediate between the black and red structures.

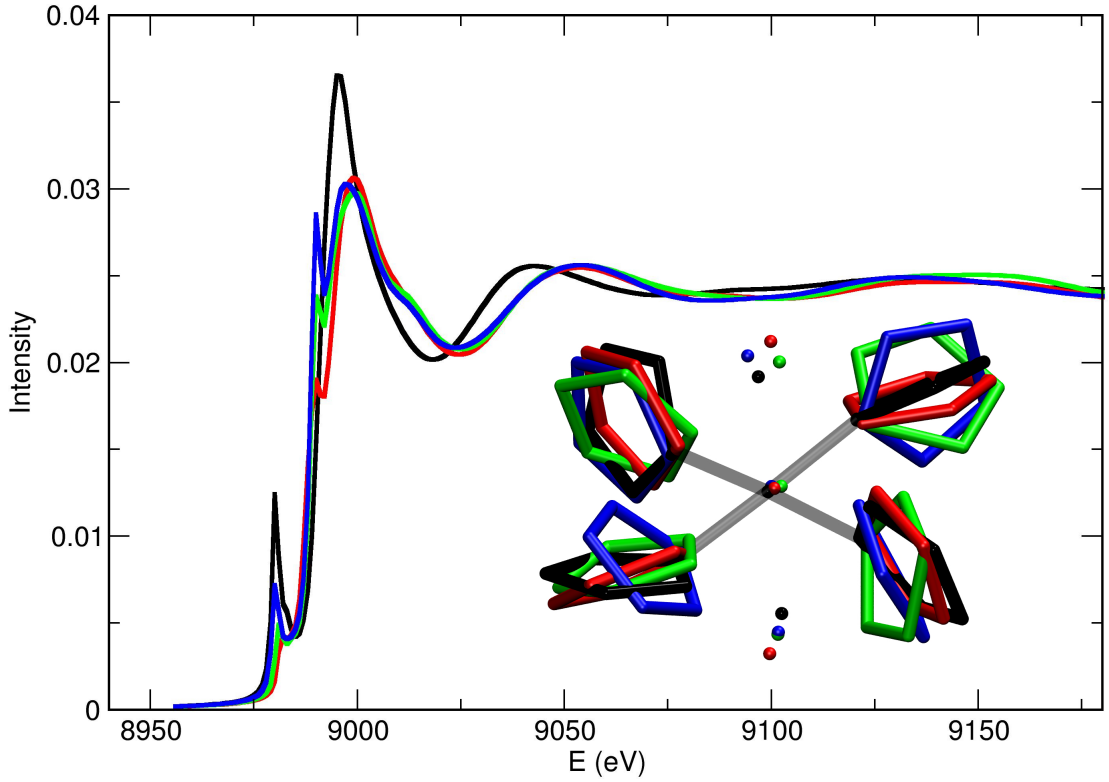

Figure 4.4.: Change in XANES spectrum due to structural change in the coordination environment. Each color represents different orientations of the imidazole ring and different Cu-O_w distances.

The degree of hydration of the metal complex can be determined from radial distribution functions (RDFs) $g_{\mathrm{Cu-O}}(r)$ and the corresponding number of water molecules $N_{\mathrm{Cu-O}}(r_s) = 4\pi\rho \int_0^{r_s} r^2 g_{\mathrm{Cu-O}}(r)dr$ around the Cu atom up to a distance r_s. Here, $\rho = N/V$ is the bulk water density and $N(r_s)$ is considered out to $r_s = 6$ Å which includes the second minimum of the radial distribution function, see Figure 4.5. The equilibrium $g_{\mathrm{Cu-O}}(r)$ and $N_{\mathrm{Cu-O}}(r)$ from simulations using VALBOND and DFTB3 are shown in Figure 4.5. Both methods yield similar $g_{\mathrm{Cu-O}}(r)$ if water molecules are explicitly included

in the quantum region of the DFTB3/MM simulations (red traces in Figure 4.5). The amplitude of the second minimum (at around 5 Å) differs appreciably between VALBOND and DFTB3/MM simulations which is probably related to the constraint imposed by FIRES. The radius of the sphere for the FIRES is 5.4 Å from the metal center, that is the first solvent shell. In addition, water structuring continues out to longer distances for the simulations with VALBOND and shows a continued shell structure. However, only having the copper complex in the quantum region with DFTB3/MM simulations leads to an unrealistic radial distribution function (green trace). The two axially coordinated water molecules are rarely present and the remainder of the solvent shell is clearly understructured.

The most pronounced peak around 2 Å in the $g_{\mathrm{Cu-O}}(r_s)$ from VALBOND and DFTB3/MD simulations with water molecules in the quantum part is due to the axial coordination of the water molecules and integrates to 1.8 and 1.6 water molecules up to a distance of r_s = 3.0 Å for VALBOND and DFTB3, respectively. This asymmetric water coordination agrees with the interpretations of the XANES experiments[160]. The peak around 5Å describes the first solvation shell (Shell-I) which contains 12 and 10 water molecules for VALBOND and DFTB3, respectively. This is also in good agreement with the experiment where 10 water molecules have been reported in the first solvation shell.[160].

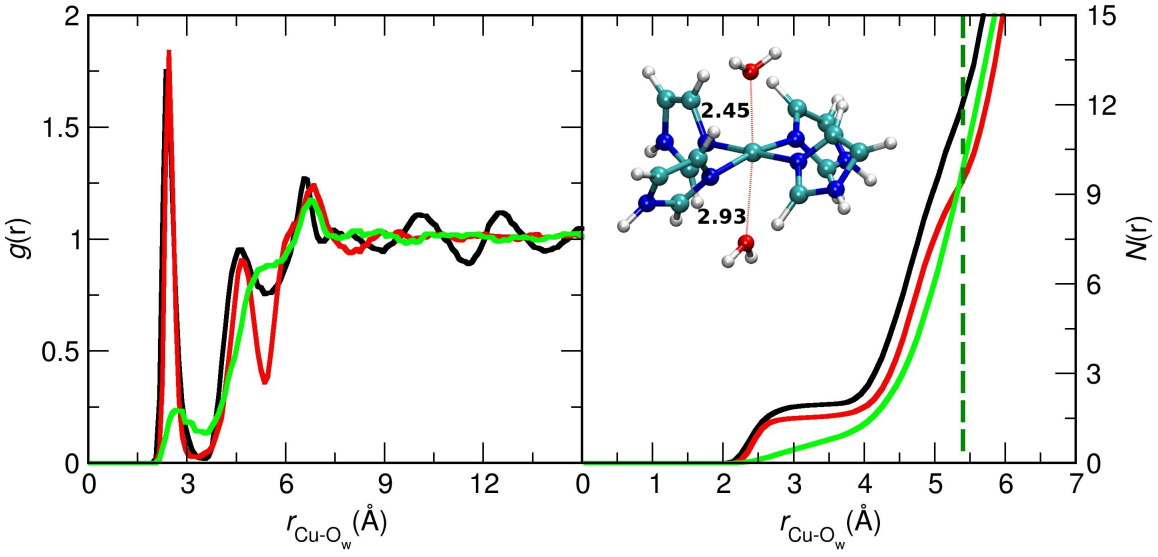

Figure 4.5.: Radial distribution function of water oxygen with respect to the Cu atom $g_{\mathrm{Cu-O}}(r)$ (left) and corresponding coordination number $N_{\mathrm{Cu-O}}(r)$ (right) obtained from the equilibrium simulations using VALBOND (black line) and DFTB3 (green: without water in QM; red: with 10 quantum waters) methods. Dashed green line indicates the first solvent shell. The inset shows the asymmetric water coordination to the metal atom.

In a next step the water dynamics of the two axially coordinated water molecules and their exchange with the first-shell (shell-I) water molecules is considered. A typical occupational trace is shown in Figure 4.6 which highlights that water molecules reside either on the several-ten picosecond time scale (black trace) or only a few picoseconds (red and green traces), i.e. their occupation times differ by about an order of magnitude. It is also demonstrated that the axially bound water molecules (characterized by $d_{\mathrm{Cu-O_W}} \approx 2.5$ Å) exchange with shell-I water molecules (for which $d_{\mathrm{Cu-O_W}} \approx 5.0$ Å).

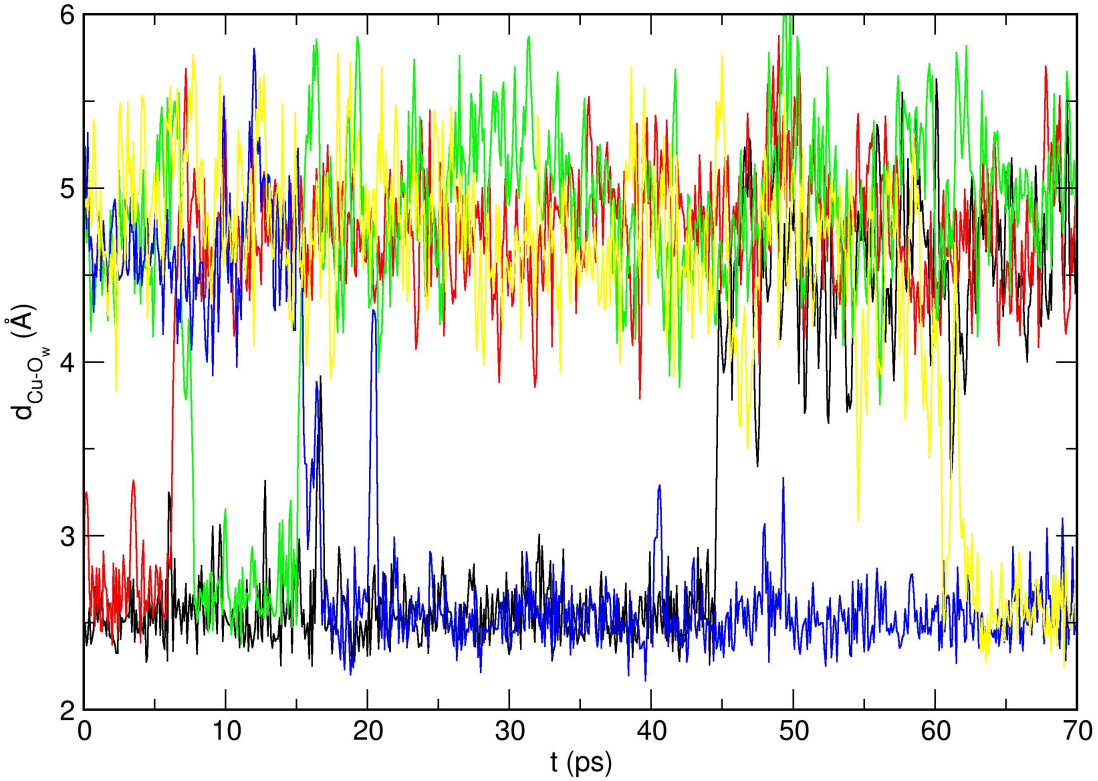

Figure 4.6.: Exchange dynamics of loosely (red and green) and strongly (black, blue) interacting axial water molecules. The separations $d_{\mathrm{Cu-O_W}}$ reflect the maxima of $g(r)$ in Figure 4.5.

It is also of interest to investigate whether water exchange is primarily driven by solvent-solvent interactions or whether coupling between solvent and solute degrees of freedom plays a role. For this, the degree of distortion of the Cu-imidazole plane τ_4 was considered where $\tau_4 = \frac{360-(\psi_1+\psi_2)}{360-2\theta}$ (ψ_1 and ψ_2 are the two greatest (N-Cu-N) valence angles and $\theta = 109.5°$ is the tetrahedral angle) distinguishes between a square planar ($\tau_4 = 0$) and a tetrahedral ($\tau_4 = 1$) coordination.[141] Other internal degrees of freedom (e.g. the rotation of the imidazole rings around the Cu-N bond) were also considered but were found to be uncorrelated with the axial water occupation and exchange dynamics.

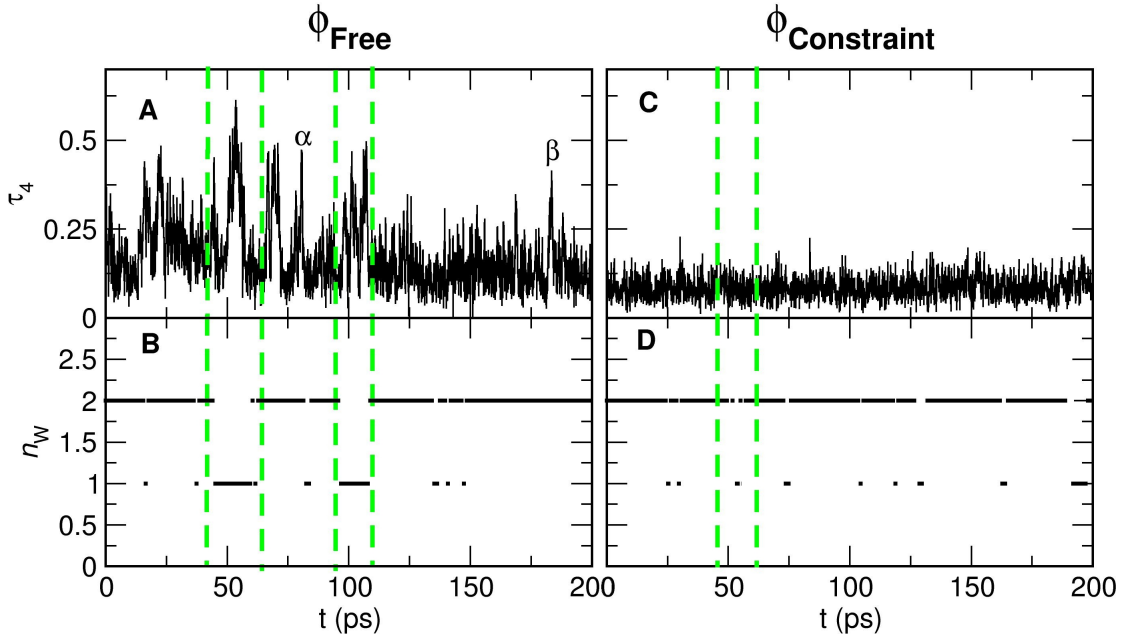

Figure 4.7.: The fluctuations in τ_4 (panels A and C) and their correlation with the axial water occupation n_{W} (panels B and D). Left and right columns are for simulations without and with four Cu-N-N-N dihedral constraints, respectively. The axial position is occupied ($n_{\mathrm{W}} = 1$) if the water-oxygen to Cu distance is less than 3 Å. The dashed vertical lines indicate particular events which are discussed in the text and peaks labelled α and β are further discussed in Figure 4.8. The fractional occupations $p(n_W = 1) = 0.13$ and $p(n_W = 2) = 0.87$ for unconstrained simulations change appreciably (to $p(n_W = 1) = 0.03$ and $p(n_W = 2) = 0.97$) when the dihedral constraint is applied.

Figure 4.7 shows that axial water exchange dynamics is coupled to fluctuations in τ_4. The maximal equilibrium amplitude of $\tau_4 = 0.5$ is midway between a planar an a tetrahedral structure of the complex. During the intervals indicated by green bars in Figures 4.7A and B, τ_4 samples larger values for extended times (10 ps) and the water occupation decreases from $n_W = 2$ to $n_W = 1$. For other large-amplitude excursions (labelled α and β), rapid (coordinated) water exchange takes place. This dynamics is further analyzed by considering time series which show that either a) an axial water molecule leaves the Cu-site followed by a large conformational change along τ_4 (Figure 4.8 left panel) or b) the two processes are synchronized (Figure 4.8 right panel). For both situations there is a correlation between axial water motion and a conformational change of the metal complex.

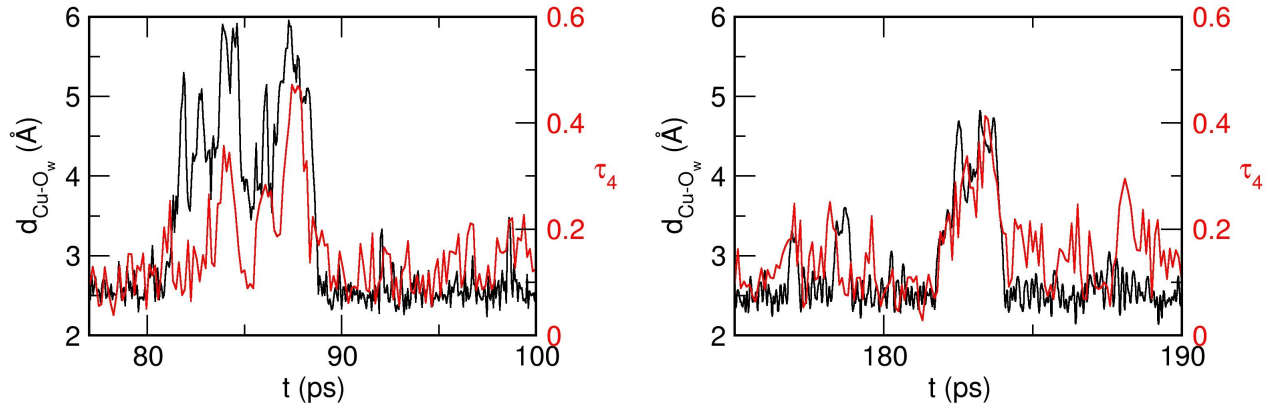

Figure 4.8.: Dynamics of one axial water molecule (black trace) at two different times (indicated by label α and β in Figure 4.7) along with the change in τ_4 (red traces) for simulations without ϕ constraint.

The dynamics considered so far show that exchange between axially coordinated and shell-I water molecules occurs spontaneously and on time scales ranging between a few and several 10 picoseconds. Also, stepwise (indicated by $n_w = 1$ in Figure 4.7) and coordinated (see Figure 4.6 around $t = 5$ ps) exchanges between axial and shell-I water molecules are observed.

For validation that τ_4 controls the coordination and release of axial water molecules, a simulation with constraints along all four Cu-N-N-N dihedral angles (ϕ) to maintain the planarity of the complex was performed. This reduces the fluctuations $\delta\tau_4$ in the Cu-Imidazole planarity (see Figure 4.7C). In these simulations the exchange dynamics of axial water molecules with shell-I water molecules always follows a concerted mechanism (see Figures 4.9 right), the probability for occupation by one axial water molecule $p(n_{\mathrm{W}} = 1)$ decreases substantially from 13 % to 3%, and the exchange dynamics slows down by a factor of two to three. Hence, the fluctuation in the planarity in the Cu-Imidazole plane influences and controls the water exchange dynamics around the [Cu(II)(Imidazole)] complex.

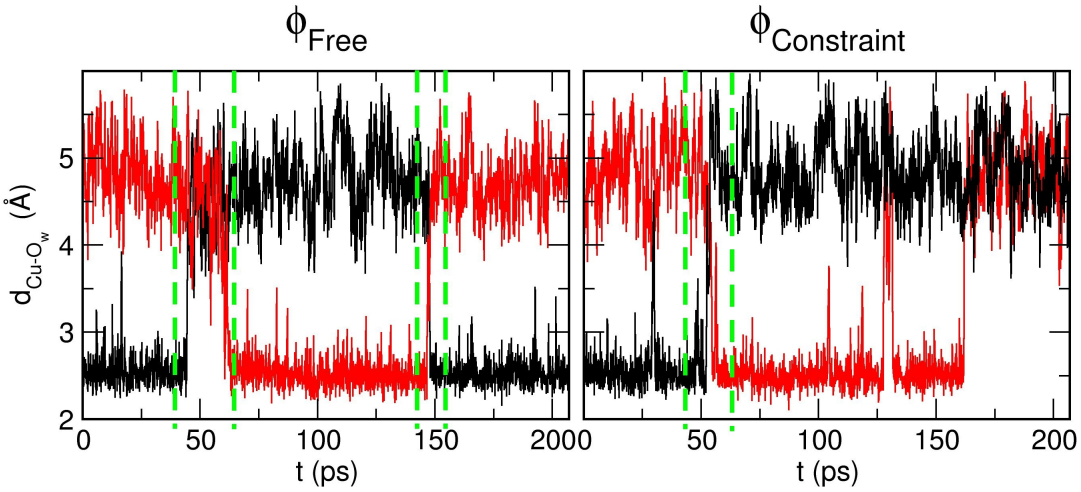

Figure 4.9.: Exchange dynamics of axially coordinated water molecules shown here. Three windows with green dotted lines shows the water exchange dynamics due to the large change in τ_4 (see Figure 4.7).

The water exchange dynamics for the two axially coordinated water molecules was also analyzed by computing their residence times from $C_{\mathrm{O}}(t) = \langle \delta O(0)\delta O(t)\rangle / \langle (\delta O(0))^2 \rangle$. Here, $O(t) = 1$ for all water oxygen atoms if they are within a distance $r_s = 3$ Å, i.e. axially coordinated to the Cu-atom, otherwise $O(t) = 0$, and $\delta O(t) = O(t) - < O(t) >$. $C_{\mathrm{O}}(t)$ was computed by considering all water oxygen atoms for which $O(t) = 1$ at least once during the entire simulation. For the axially coordinated water molecules, $C_{\mathrm{O}}(t)$ follows a bi-exponential decay with two time constants $\tau_1 = 2.5$ ps and $\tau_2 = 25.7$ ps (see Figure 4.10; a single-exponential fit yields an unsatisfactory fit). The short time scale τ_1 characterizes exchange of the weakly bound axial water, see Figure 4.6. The longer time scale τ_2 describes the dynamics of the strongly bound axial water molecule, see black trace in Figure 4.6 and the red trace in Figure 4.9. These two time scales increase by about a factor of two for the $\phi-$constraint simulations, to $\tau_1 = 5.2$ ps and $\tau_2 = 41.5$ ps which underlines the importance of the Cu-N-N-N angle in influencing the hydration dynamics. The amplitudes for the two processes change from 0.79 and 0.21 for the free simulations to 0.38 and 0.62 to those including the $\phi-$constraints, respectively. This indicates that the fraction of strongly bound axial water molecules increases with decreasing out-of-plane flexibility due to the $\phi-$constraint and the two axial positions become more equal.

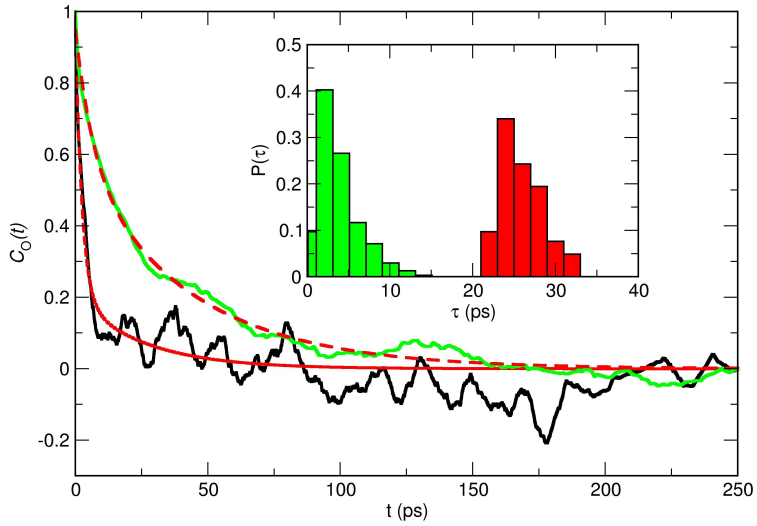

Figure 4.10.: Occupation correlation function as a function of the residence time from simulations without dihedral constraint (black) and with dihedral constraint (green). The two red lines are the corresponding bi-exponential fits. The time constants are 2.5 ps and 25.7 ps for the simulations without dihedral (ϕ) constraint compared with 5.2 ps and 41.5 ps for the $\phi-$constrained simulation. The two time constants correspond to the exchange of loosely and strongly bound water molecules, respectively. The inset shows the time distribution $P(\tau)$ for the exchange of strongly (red) and weakly bound (green) axial water molecules.

Finally, the residence time distribution $P(\tau)$ for all (i.e. weakly and strongly interacting) water molecules within 3 Å from the metal center for both, VALBOND and DFTB3 simulations, yield persistence times of $\sim$ 33 ps for the two water molecules. Only considering the strongly bound water molecule leads to the distribution in the inset of Figure 4.10 which peaks at 25 ps and confirms the assignment of time scale τ_2 from the correlation function to the microscopic process. The residence time distribution for the weakly bound water molecules peaks at 2.7 ps (green distribution in the inset of Figure 4.10). This value also confirms the assignment of time scale τ_1 in the correlation fit to the dynamics of the weakly coordinated axial water molecule, and overall the distributions are consistent with an asymmetric coordination of the two axial water molecules.

4.5. Conclusion

In summary, atomistic and hybrid QM/MM simulations of solvated [Cu(Imidazole)$_4$] using the VALBOND[98] force field and the DFTB3 method[180] confirm a hydrated structure with two asymmetrically coordinated axial water molecules found from analyzing XANES spectra.[160] The exchange dynamics of individual water molecules in the coordinated shell is strongly coupled to the Cu-N-N-N dihedral angle which speeds up the exchange dynamics by a factor of 2. The exchange dynamics of solvent water molecules around the metal atom in the coordinated solvation shell takes place on the 10 ps time scale which was also found for water exchange dynamics for the bare Cu(II) ion in water using NMR experiments and previous theoretical work[188,189]. More generally, such time scales may be generic for hydrated metal complexes as was recently found for Fe(II)tris(2,2′-bipyridine)[90,145] or Ru(II)tris(2,2-bipyridine) in solution.[33–35]

THE JOURNAL OF PHYSICAL CHEMISTRY B

Article

pubs.acs.org/JPCB

Copper Oxidation/Reduction in Water and Protein: Studies with DFTB3/MM and VALBOND Molecular Dynamics Simulations

Haiyun Jin,[†] Puja Goyal,[†] Akshaya Kumar Das,[‡] Michael Gaus,[†] Markus Meuwly,*[,‡] and Qiang Cui*[,†]

[†]Department of Chemistry, University of Wisconsin—Madison, 1101 University Avenue, Madison, Wisconsin 53706, United States

[‡]Department of Chemistry, University of Basel, Klingelbergstrasse 80, 4056 Basel, Switzerland

Supporting Information

ABSTRACT: We apply two recently developed computational methods, DFTB3 and VALBOND, to study copper oxidation/reduction processes in solution and protein. The properties of interest include the coordination structure of copper in different oxidation states in water or in a protein (plastocyanin) active site, the reduction potential of the copper ion in different environments, and the environmental response to copper oxidation. The DFTB3/MM and VALBOND simulation results are compared to DFT/MM simulations and experimental results whenever possible. For a copper ion in aqueous solution, DFTB3/MM results are generally close to B3LYP/MM with a medium basis, including both solvation structure and reduction potential for Cu(II); for Cu(I), however, DFTB3/MM finds a two-water coordination, similar to previous Born−Oppenheimer molecular dynamics simulations using BLYP and HSE, whereas B3LYP/MM leads to a tetrahedron coordination. For a tetraammonia copper complex in aqueous solution, VALBOND and DFTB3/MM are consistent in terms of both structural and dynamical properties of solvent near copper for both oxidation states. For copper reduction in plastocyanin, DFTB3/MM simulations capture the key properties of the active site, and the computed reduction potential and reorganization energy are in fair agreement with experiment, especially when the periodic boundary condition is used. Overall, the study supports the value of VALBOND and DFTB3(/MM) for the analysis of fundamental copper redox chemistry in water and protein, and the results also help highlight areas where further improvements in these methods are desirable.

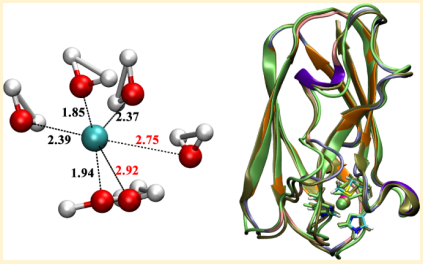

1. INTRODUCTION

Copper is an important metal ion in biology.[1−4] Due to its redox activity, it is involved in many electron transfer proteins and serves as the catalytic cofactor in many enzymes. On the contrary, uncontrolled copper distribution may lead to the generation of undesirable reactive oxygen species or aggregation/misfolding of peptides/proteins,[5−8] resulting in serious diseases. Therefore, it is important to develop effective computational models for copper in different redox states to aid experimental investigation of copper biochemistry.

For condensed phase computations, a full quantum mechanical description remains prohibitively expensive. Therefore, hybrid quantum mechanical/molecular mechanical (QM/MM) methods[9−14] or pure MM models are most applicable. QM/MM models are more general and can be used to probe both chemical reactions and structural properties. To allow adequate sampling, which is essential to most condensed phase applications, an approximate QM method has to be used. In this regard, we have recently reported the parametrization of a density functional tight binding[15,16] (DFTB3[17]) model for copper.[18] By including orbital angular momentum dependence of the Hubbard parameter and its charge derivative, we were able to describe the structural properties of both oxidation states in generally good agreement with "first principle" density functional theory (DFT) methods such as B3LYP[19−21] and B97-1,[22] which were shown to give adequate description for copper complexes of biological relevance (see discussion in ref 18. in relation to previous work[23−25]). We note that the DFTB3 model in the current form has PBE[26] as its "parent functional", which was shown[18] to be less accurate than B3LYP and B97-1 for copper. Thus, although some of the intrinsic limitations of the PBE functional were alleviated during the parametrization process, the energetic properties of copper compounds, such as ligand binding energies and proton affinities, are described only at a semiquantitative level with the first generation of the DFTB3 model. For example, the binding energies for a series of biologically relevant charge-neutral molecules have a mean absolute deviation (MAD) of 3.1 and 4.7 kcal/mol for Cu(I) and Cu(II) compounds, respectively, in comparison to B3LYP/aug-cc-pVTZ; the errors are substantially larger for charged ligands, likely reflecting the use of a minimal basis in DFTB3. Nevertheless, the performance of DFTB3 is substantially better than other semiempirical methods, such as PM6,[27] which is fairly useful for geometries but much less applicable for energetics. Moreover, single-point B3LYP calculations at DFTB3 structures lead to substantially improved energetics for all ligand types, highlighting the good quality of DFTB3 structures.

Special Issue: Bruce C. Garrett Festschrift

Received: October 2, 2015
Revised: December 1, 2015
Published: December 1, 2015

DOI: 10.1021/acs.jpcb.5b09656
J. Phys. Chem. B 2016, 120, 1894−1910

The Journal of Physical Chemistry B Article

In our previous work,[18] the DFTB3 method was tested only against DFT and, in some cases, CCSD(T) methods for gas phase molecules. The computational efficiency of DFTB3 over DFT and *ab initio* methods makes it an attractive QM approach in QM/MM applications. Therefore, in the current study, we further explore the applicability of DFTB3 by studying several condensed phase problems, which involve both solution (Figure 1a,b) and protein (Figure 1c) systems. We focus on

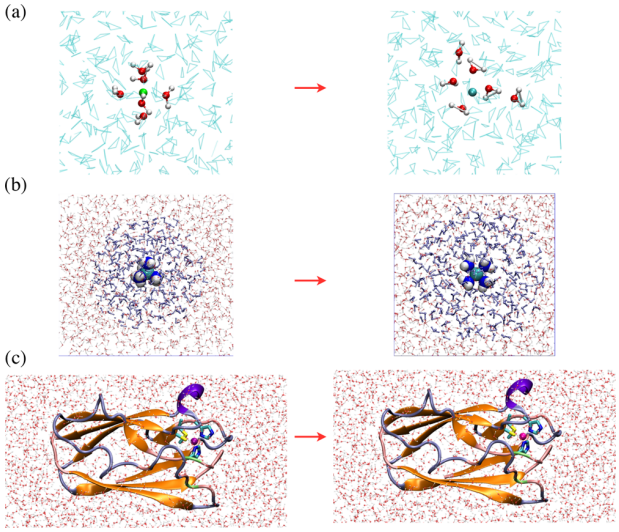

Figure 1. Three systems studied here: (a) copper reduction in water; (b) oxidation of $[Cu^{I}(NH_3)_4]^+$ in water; (c) copper reduction in a blue copper protein, plastocyanin. In (a)−(c), the minimal QM region is highlighted with a different representation compared to the solvent or the rest of the protein. In (c), 3_{10} helices are violet, extended β sheet regions are orange, bridge β sheet regions are lime green, turns are ice-blue, and coils are pink. The figures are generated using VMD.[39]

redox processes in water and protein to investigate whether DFTB3 is able to provide a balanced treatment for the two redox states of copper in condensed phase environments. The properties of interest include structural/coordination environment of the copper ion, especially response(s) to oxidation/reduction, redox potential and reorganization energy.

At the MM level, force field development is not straightforward due to the open-shell nature of Cu(II) and charge transfer effects associated with metal−ligand interactions. Nevertheless, several models have been developed in recent years and met different degrees of success.[28−30] It is difficult to study chemistry or absolute redox potential with MM models, although they can be used to study structural/coordination properties of the copper ion in different redox states. In this study, we focus on the VALBOND model, which was originally proposed by Landis and co-workers to treat large amplitude angular motions of transition metal ligands.[31−33] The model has been recently implemented in CHARMM by Meuwly and co-workers,[34] who showed promising applications in several organometallic systems.[35,36] Here we develop the VALBOND model for copper and compare its performance to DFTB3/MM for $[Cu(NH_3)_4]^{+/2+}$ in water (Figure 1b). We are particularly interested in probing the time dependence of the solvent response to the oxidation of copper ion, a process that can potentially be probed with modern solution X-ray experiments.[37,38] Comparison of VALBOND and DFTB3/MM also helps better refine the VALBOND model, which is computationally even more efficient than DFTB3/MM, for certain protein applications in the future.

In the following, we first describe the computational methodologies (QM/MM and VALBOND) used to study the three condensed phase systems. DFTB3/MM is applied to all three, whereas VALBOND simulations focus on $[Cu(NH_3)_4]^{+/2+}$ in water; in selected cases, as validation, DFT/MM simulations are also carried out. Next, we present results of QM/MM and VALBOND simulations; comparison to experiment is made whenever possible, and the discussion helps highlight the applicability and limitations of the current generation of DFTB3(/MM) and VALBOND models. Finally, we end with a few concluding remarks.

2. METHODS

2.1. Aqueous Copper Ion Simulations with QM/MM Models. The copper ion in water is described with QM/MM simulations in which the copper ion and closest water molecules are treated at the QM level, whereas the remaining water is treated with MM. In most cases, the QM water partition includes only the closest six water molecules, although calculations with a larger QM region (~21 water) are also carried out for comparison; as shown in the Supporting Information, the first solvation shell properties are not very sensitive to the QM region size whereas the second solvation shell properties do exhibit a modest level of dependence, especially for Cu(I). The MM region includes a droplet of 16 Å radius subject to the stochastic boundary condition.[40] In most simulations, the MM water is TIP3P,[41] although a polarizable water model based on Drude oscillator is also tested (see below). To avoid the exchange of QM and MM water molecules, the flexible inner region ensemble separator (FIRES) potential[42] is applied; previous studies[43] and larger QM region studies in the Supporting Information indicate that the FIRES approach gives satisfactory results for structural properties of the copper ion, especially when the QM region does not deviate significantly from spherical symmetry. Equilibrium simulations are carried out for solvated Cu(I) and Cu(II) ions using the mixed Newtonian/Langevin dynamics protocol;[40] in addition, reduction potential is also computed (section 2.1.3). All calculations are carried out using CHARMM;[44,45] DFT/MM calculations are done with the Gaussian09/CHARMM interface.[46]

2.1.1. QM Method. As mentioned in the Introduction, the main goal is to test our recent parametrization of the DFTB3 model for copper. The parametrization was done in the framework of the 3OB set[47] and calculations for Cu(II) containing systems are done with the spin-polarized formulation of DFTB.[48,49] The orbital angular momentum dependence of the Hubbard parameter and its charge derivative is considered only for copper. For comparison, DFT/MM calculations are also carried out in which DFT is either B3LYP, BLYP, or MPWB1K.[50] Based on gas-phase model systems studied previously[18] and here (see below), the B3LYP approach generally gives satisfactory results in comparison to high quality *ab initio* calculations such as CCSD(T) with a large (aug-cc-pVTZ[51]) basis set. BLYP is also tested here because it is the functional used in many previous CPMD/BOMD simulations of solvated copper ions (see below). MPWB1K, a meta-GGA functional, is tested because a recent study[52] found it to work well for several copper complexes. To obtain longer DFT/MM simulations, a small basis that contains the Hay−Wadt effective core potential (Lanl2dz[53]) for copper and 6-31G(d) for other

DOI: 10.1021/acs.jpcb.5b09656
J. Phys. Chem. B 2016, 120, 1894−1910

elements is used; gas phase calculations for copper−water complexes (Tables 1 and 2 and Supporting Information) indicate that this basis set leads to good geometries in comparison to calculations using aug-cc-pVTZ.

2.1.2. MM Method. In most simulations, the TIP3P model is used to describe the MM water. In previous QM/MM studies of metal ion solvation,[42,43] a polarizable water model based on Drude oscillator (SWM4-NDP[54]) was recommended; thus we have also carried out simulations with DFTB3/SWM4-NDP. As shown in the Supporting Information, DFTB3/TIP3P and DFTB3/SWM4-NDP simulations generally give rather similar solvent distribution near the copper ion, except for minor differences in the angular distribution of water, especially those in the second solvation shell.

For interaction among MM molecules, the extended electrostatic model is used for consistency with the QM/MM interactions[55] (see the Supporting Information for a discussion of MM cutoff schemes in reduction potential calculations). van der Waals interactions are switched off beyond 12 Å using the VSWITCH scheme.[56] All water molecules are kept rigid using the SHAKE algorithm[57] during molecular dynamics simulations.

2.1.3. Reduction Potential Calculation. The reduction potential of copper (Cu(II)/Cu(I)) is computed using a dual-topology-single-coordinate (DTSC) approach.[58] In DTSC, the system is propagated with a hybrid potential function that is a combination of potentials of the two end states (Cu(II), Cu(I)) through a coupling parameter λ,

$$\begin{aligned} U(\lambda) &= (1-\lambda)U_{\mathrm{Cu(II)}} + \lambda U_{\mathrm{Cu(I)}} \\ &= U_{\mathrm{Cu(II)}} + \lambda(U_{\mathrm{Cu(I)}} - U_{\mathrm{Cu(II)}}) \end{aligned} \tag{1}$$

The reduction free energy is then given by thermodynamic integration as,

$$\begin{aligned} \Delta F &= \int_0^1 \frac{\partial F(\lambda)}{\partial \lambda}\,\mathrm{d}\lambda \\ &= \int_0^1 \langle \frac{\partial U(\lambda)}{\partial \lambda} \rangle_\lambda \,\mathrm{d}\lambda \\ &= \int_0^1 \langle (U_{\mathrm{Cu(I)}} - U_{\mathrm{Cu(II)}}) \rangle_\lambda \,\mathrm{d}\lambda \end{aligned} \tag{2}$$

where $(U_{\mathrm{Cu(I)}} - U_{\mathrm{Cu(II)}}) = \Delta U$ is referred to as the energy gap below. Eleven λ windows are used for DFTB3/MM, with each window sampled for ∼500 ps. For comparison, B3LYP/MM calculations are also carried out but with only the end states (λ = 0, 1, sampled for 280 ps for Cu^{2+} and 120 ps for Cu^{+}); reduction free energy is then estimated using a linear response model.

In the water droplet set up using the stochastic boundary condition, the system is surrounded by vacuum. Therefore, a Born model[59] is used to estimate the missing bulk solvation free energy contribution. This simply includes the corresponding "ion solvation term",

$$\Delta F_{\mathrm{slv}}^{\mathrm{Born}} = -\frac{Q_{\mathrm{tot}}^{\ 2}}{2R}\left(1 - \frac{1}{\epsilon_{\mathrm{W}}}\right) \tag{3}$$

where Q_{tot} = 2 for Cu(II) and Q_{tot} = 1 for Cu(I), and R = 16 Å (ϵ_{W} = 78). The reduction free energy is given by

$$\begin{aligned} \Delta F_{\mathrm{red}} &= -\Delta F_{\mathrm{slv}}^{\mathrm{Born}}(\mathrm{Cu(II)}) + \Delta F_{\mathrm{droplet}} + \Delta F_{\mathrm{slv}}^{\mathrm{Born}}(\mathrm{Cu(I)}) \\ &= \Delta F_{\mathrm{droplet}} + \Delta\Delta F_{\mathrm{slv}}^{\mathrm{Born}} \end{aligned} \tag{4}$$

Here $\Delta F_{\mathrm{droplet}}$ is the reduction free energy computed (using eq 2) with the water droplet, and $\Delta\Delta F_{\mathrm{slv}}^{\mathrm{Born}}$ is a numerical constant:

$$\begin{aligned} \Delta\Delta F_{\mathrm{slv}}^{\mathrm{Born}} &= -\Delta F_{\mathrm{slv}}^{\mathrm{Born}}(\mathrm{Cu(II)}) + \Delta F_{\mathrm{slv}}^{\mathrm{Born}}(\mathrm{Cu(I)}) \\ &= +30.70\ \mathrm{kcal/mol} \end{aligned} \tag{5}$$

For comparison with the water droplet model using stochastic boundary condition, we have also computed the reduction potential at the DFTB3/MM level with the GSBP (generalized solvent boundary potential)[55,60] and PBC (periodic boundary condition) setups. In GSBP, the entire water droplet is treated as the inner region and the outer region is described as a dielectric continuum (ϵ_{W} = 78); spherical harmonics up to order 20 (i.e., 400 basis functions) are used to expand the reaction field matrix. In the PBC simulations, the metal ion is first solvated by a 32 Å cube of water molecules and then equilibrated with the NPT ensemble; the final box length is 29.8 Å. Ewald summation is applied to QM/MM electrostatics[61] and particle mesh Ewald[62] is used for MM-MM electrostatics with a grid size of ∼1 Å.

2.2. Copper−Ammonia Solution Simulations.

2.2.1. VALBOND in CHARMM. We first briefly review the VALBOND module recently introduced to CHARMM. In the VALBOND force field, based on valence bond theory, hybrid orbital strength functions are used to describe the energetics of distorted bond angles.[31−33,63] The additional force field term describes the energetics not only around the energy minimum but also for very large angle distortions and helps to model hypervalent molecules and transition metal complexes.[34,64]

Nonhypervalent Molecules. For molecules involving $sp^m d^n$ hybridization with an angle θ between the hybrid orbitals, the bending energy is $E(\theta) = k(S^{\max} - S(\theta))$. Here, k, $S^{\max}$ and S are scaling factor (force constant), maximum strength function, and strength function, respectively. For $sp^m d^n$ hybrids the explicit expressions are $S^{\max} = \sqrt{\frac{1}{1+m+n}}(1 + \sqrt{3m} + \sqrt{5n})$, $S(\theta) = S^{\max}\sqrt{1 - \frac{1-\sqrt{1-\Delta^2}}{2}}$, and $\Delta = \frac{1}{1+m+n}\left[1 + m\cos\theta + \frac{n}{2}(3\cos^2\theta - 1)\right]$ is the non-orthogonality integral. For $[Cu^{I}(NH_3)_4]^+$ investigated in the present work, an sp^3 hybridization is used to describe its tetrahedral geometry, similarly to $Ni(CO)_4$. In this case, the maximum strength function evaluates to $S^{\max} = \sqrt{\frac{1}{1+3+0}}(1 + \sqrt{3\times 3} + \sqrt{5\times 0}) = 2.0$.

Hypervalent Molecules. Hypervalent molecules contain atoms having more than eight electrons in their valence shell. Excess electrons in hypervalent molecules are accommodated in $3c-4e^-$ bonds. Thus, for hypervalent molecules one has to take care of the resonance structures and this can be accomplished by weighting factors c_j called mixing coefficients. Hence, the total energy is a weighted sum $E_t = \sum_j c_j E_j$ over all j resonance structures. The mixing coefficients c_j are determined from[31] $c_j = \frac{\prod_{i=1}^{\mathrm{hype}} \cos^2\theta_i}{\sum_{j=1}^{\mathrm{config}} \prod_{i=1}^{\mathrm{hype}} \cos^2\theta_j}$, where *hype* and *config* are the number of hypervalent angles and number of resonance configurations, respectively. The square-planar arrangement for $[Cu^{II}(NH_3)_4]^{2+}$ involves an sd^1 (hypervalent) hybridization with $S^{\max}$ = 2.29 and six resonance configurations are retained in the simulations.

2.2.2. Simulation Setups for Copper−Ammonia in Water. The system consists of a solvated $[Cu^{I}(NH_3)_4]^+$ or $[Cu^{II}(NH_3)_4]^{2+}$ complex, immersed in 1728 TIP3P[41] water molecules in a periodic cubic box of side length 37.25 Å (Figure 1b). All simulations

DOI: 10.1021/acs.jpcb.5b09656
J. Phys. Chem. B 2016, 120, 1894−1910

are carried out using CHARMM[44] with provisions for the VALBOND[34] force field to describe the metal complex.[31−33] All bonds involving hydrogen atoms are constrained by applying SHAKE.[65] The remaining parameters for the ammonia ligand are taken from the CHARMM force field.[66]

The system is prepared for simulations by minimization and subsequent heating to 300 K. This is followed by an *NVT* equilibration simulation at 300 K for 10 ns using a Verlet integrator[67] with a time step of 1 fs using a Nosé−Hoover thermostat[68] for temperature control.

For comparison, hybrid QM/MM simulations are performed using DFTB3[17] and the 3OB parametrization for ONCH[47] and copper[18] is used. The metal complex is described by DFTB3 whereas the water molecules are treated by TIP3P. An *NVT* simulation is carried out at 300 K using the Verlet algorithm with a time step of 0.1 fs for 5 ns. The SCF convergence criterion used for this is 10^{-8} hartree. The van der Waals radii for the Cu(I) and Cu(II) ions are σ_{Cu} = 1.40 and 0.87 Å, respectively.[69,70] Furthermore, simulations with the seven water molecules closest to the Cu atom included in the QM part are carried out. To avoid the exchange of QM and MM water molecules, the FIRES potential is applied.[42]

Along with the DFTB3/MM simulations, a hybrid QM/MM simulation is also performed with B3LYP/MM using the Gaussian09/CHARMM interface.[46] The metal complex is treated with B3LYP and the same basis as for a copper ion in aqueous solution (Lanl2dz for Cu and 6-31G(d) for other QM atoms), and water with TIP3P. Because the calculation is computationally demanding, only ∼100 ps of simulation is performed.

In addition to the equilibrium simulations, we have also carried out nonequilibrium simulations in which the oxidation from Cu(I) to Cu(II) is induced *in silico* by changing the force field parameters between the two oxidation states for VALBOND[34] simulation; in the QM/MM simulations the total charge and number of unpaired electrons is changed and the van der Waals parameters for the metal atoms are also updated. For the VALBOND[34] simulations, after 10 ns of *NVT* simulation, an *NVE* simulation is performed for 1 ns using starting coordinates and velocities obtained from the *NVT* simulation. From this 1 ns of *NVE* trajectory, coordinates and velocities at 100 frames separated by 10 ps are stored and used as initial conditions for the subsequent nonequilibrium simulations. For DFTB3/MM,[17] subsequent to *NVT* simulation, an *NVE* simulation is performed for 100 ps, from which coordinates and velocities at 20 frames separated by 5 ps are selected to initiate the nonequilibrium trajectories.

2.3. Plastocyanin at pH 7. *2.3.1. GSBP Simulations.* Starting from the crystal structure 5PCY,[71] hydrogen atoms are added using HBUILD in CHARMM considering standard protonation states for all titratable residues at pH 7. Then the protein is solvated in a 20 Å sphere of water molecules centered at Cu (consistent with an inner region of radius 22 Å in the GSBP protocol[55,60]). The protein is treated with the CHARMM22 force field[66] whereas the modified TIP3P model is used for the water molecules. Newton's equations-of-motion are solved for the molecular dynamics (MD) region (within 18 Å), and Langevin equations-of-motion are solved for the buffer region (18−22 Å) with a temperature bath of 300 K.[40] All water molecules in the inner region are subjected to a weak GEO (geometrical) type restraining potential to keep them inside the inner sphere with the MMFP module of CHARMM. The GEO restraining potential is in the form of a quartic polynomial on each oxygen atom in water: $k \times \Delta^2(\Delta^2 - V_p)$, where $\Delta = r - r_{off}$, k is the restraining quartic force constant (0.5 kcal/(mol·Å^4)), r is the distance of the oxygen from the center of the simulation sphere, r_{off} is the cutoff distance (22.0 − 1.5 = 20.5 Å) below which the GEO restraint is set to zero, and V_p is an offset value taken to be 2.25 Å^2. These parameters lead to a restraining potential on water that smoothly turns on at 20.5 Å, reaches a well at 21.5 Å with a depth of −0.625 kcal/mol, and then quickly rises to be repulsive beyond 22.0 Å. All protein atoms in the buffer region are harmonically restrained with force constants determined directly from the *B*-factors in the PDB file.[40] Langevin atoms are updated every 20 steps during the simulation to consistently treat protein groups and water molecules that may switch regions during the simulation. Nonbonded interactions within the inner sphere are treated with an extended electrostatics model,[72] in which groups beyond 12 Å interact as multipoles and up to quadrupoles.

In the GSBP[55,60] setup, the static field due to outer region atoms, ϕ^o_s, and the reaction field matrix, **M**, are evaluated using Poisson−Boltzmann (PB) calculations using a focusing scheme that places a 52.8 Å cube of fine grid (0.4 Å) into a larger 158.4 Å cube of coarse grid (1.2 Å). The inner region charge density is expressed using the first 20th-order spherical harmonics with a total of 400 basis functions. The optimized radii of Roux and Nina[73] are adopted to define the solvent−solute dielectric boundary. Dielectric constant of 1.0 and 80.0 are used for protein and solvent, respectively.

For preliminary MM equilibration, Cu, His 37, His 87, Cys 84, Met 92, Pro 36, and Asn 38 are kept fixed in space; a charge of +1 is assigned to Cu and CHARMM charges are used for the rest of the protein. After a 500 ps equilibration (the final structure from which is also used to set up PBC simulations, *vide infra*), the final structure is used to set up DFTB3/MM simulations. The QM region includes Cu and the side chains of His 37, His 87, Cys 84, and Met 92. Link atoms are added between the C_α and C_β atoms for His 37, His 87, and Cys 84; for Met 92, the link atom is added between the C_β and C_γ atoms. The DIV scheme is used for the treatment of MM-host interactions with the QM region.[74]

Post separate minimizations for the Cu(I) and Cu(II) states, two independent 250 ps equilibration runs are carried out for each Cu oxidation state. Thermodynamic integration simulations are carried out to compute the reduction potential in the dual-topology-single-coordinate (DTSC-TI) framework[58] (eq 2). λ = 0.0, 0.2, and 0.4 windows start with equilibrated Cu(II) structures and λ = 0.6, 0.8, and 1.0 windows start with the equilibrated Cu(I) structures. The length of simulation for each λ window is typically about 1 ns; for statistics, see the Supporting Information.

2.3.2. PBC Simulations. Starting from MM/GSBP-equilibrated coordinates for the protein (*vide supra*), to which link atoms have been added corresponding to the same QM region as in GSBP simulations, the protein is solvated in a rhombic dodecahedron of edge length 68 Å. To neutralize the net charge of the protein, K^+ and Cl^- ions are added, keeping the ionic concentration at 0.150 M. Electrostatics interactions between QM and MM atoms are treated using Ewald summation,[61] whereas those among MM atoms are treated using particle mesh Ewald;[67] the grid size is about 1 Å in both cases. van der Waals interactions are truncated at atom−atom distances of 12 Å using the SHIFT scheme.[56]

Respective DFTB3/MM minimized structures for the Cu(I) and Cu(II) states are used to set up 200 ps heating/equilibration runs for each state. Two independent simulations are carried

DOI: 10.1021/acs.jpcb.5b09656
J. Phys. Chem. B 2016, 120, 1894−1910

The Journal of Physical Chemistry B Article

out for each state with a time-step of 1 fs and the Nosé–Hoover thermostat.[68] In the DTSC-TI framework, ~700 ps long simulations are carried out for the λ = 0.0 (i.e., Cu(II)) and the λ = 1.0 (i.e., Cu(I)) windows. The final structures from these simulations are used to initiate runs for the other λ windows: λ = 0.2 and 0.4 windows start from the λ = 0.0 structure whereas λ = 0.6 and 0.8 windows start from the λ = 1.0 structure. For additional simulation statistics, see the Supporting Information.

3. RESULTS AND DISCUSSION

3.1. Copper Ions in Aqueous solution. *3.1.1. Solvation of Copper Ions in Different Oxidation States.* The structural features of a solvated Cu(II) ion have been discussed extensively by previous experimental and computational studies. The debate focused on whether the first solvation shell consists of six water molecules in a Jahn–Teller distorted octahedron configuration or involves only five directly coordinated water molecules. Experimentally, numerous techniques that include neutron diffraction,[75−79] extended X-ray absorption fine structure (EXAFS),[80−85] X-ray absorption near edge structure (XANES),[82] and large angle X-ray diffraction (LAXS)[83] have been applied, and the results are not quite consistent with each other. This is partly because interpretation of EXAFS, XANES, or LAXS data depends on a fitting procedure that requires *a priori* assumptions of the structure; neutron diffraction can measure the four closely bound Cu–O_{eq} distances but can not distinguish the Cu–O_{ax} and Cu–H bonds. With the second-difference isotopic substitution method and neutron diffraction,[79] $g_{CuO}(r)$ and $g_{CuH}(r)$ can be measured separately, but the $g_{CuO}(r)$ plot is rather broad and the $g_{CuO}(r)$ integration plot is not quite flat to indicate the predominant five-coordinated structure in solution.

The latest X-ray scattering study of Hodgson et al.[85] considered three models: square pyramidal, split axial, and distorted Jahn–Teller; the first has a five-coordinated Cu(II) whereas the last two have a six-coordinated Cu(II). With EXAFS analysis, the square pyramidal and split axial fit slightly

Table 1. Calculated Binding Energy for Water to $[Cu(H_2O)_5]^{2+}$ To Form $[Cu(H_2O)_6]^{2+}$ [a]

method	binding energy (kcal/mol)
B3LYP/aug-cc-pVTZ	−19.9
BLYP/aug-cc-pVTZ	−16.8
B3LYP/lanl2dz/6-31G(d)	−25.7
BLYP/lanl2dz/6-31G(d)	−21.2
DFTB3	−21.2
CCSD(T)/aug-cc-pVTZ	−23.8

[a]Optimized at the respective level, except for CCSD(T), for which B3LYP/aug-cc-pVTZ structures are used.

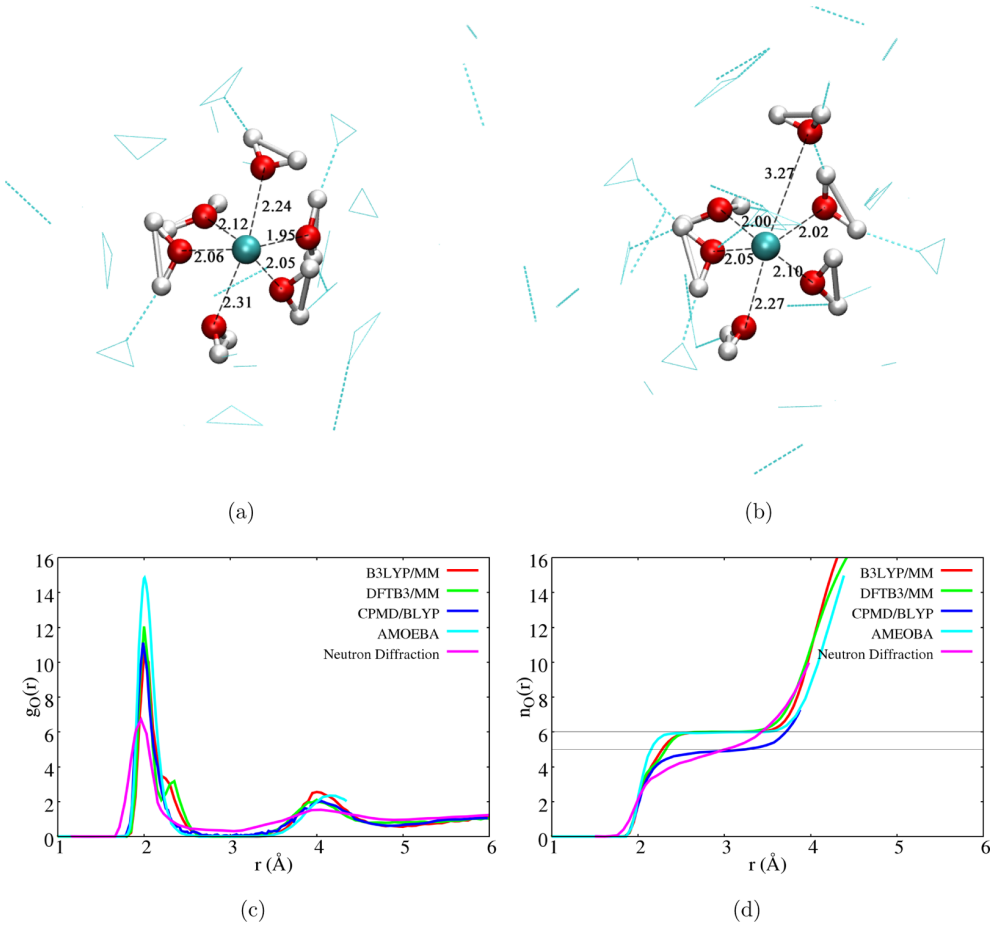

Figure 2. Coordination environment of a Cu(II) ion in water. (a, b) Snapshots from DFTB3/MM simulations that illustrate the six- and five-coordinated species. (c, d) Cu–O radial distribution function and coordination number function from different simulations and neutron diffraction experiment.[79] The CPMD/BLYP results are taken from ref 79 and those from AMEOBA from ref 29.

DOI: 10.1021/acs.jpcb.5b09656
J. Phys. Chem. B 2016, 120, 1894–1910

better than the distorted Jahn−Teller, and the two axial water oxygen atoms differ by about 0.14 Å in terms of distances to Cu(II) in the split axial model. With a MXAN (Minuit X-ray absorption near edge structure) analysis, which considers Cu−H scattering explicitly, a better fit involves two distinct but structurally related noncentrosymmetric axially elongated square pyramidal Cu(II) ions; one involves a nonbonded (sixth) axial water at Cu−O ∼ 3 Å, whereas the other is axially elongated square pyramidal without any trans-axial water ligand.

With computations, different methods have been applied and include QM/MM molecular dynamics,[86−89] Car−Parrinello molecular dynamics (CPMD),[90−93] Born−Oppenheimer molecular dynamics (BOMD),[94,95] gas phase cluster analyses,[96−101] and classical molecular dynamics using a polarizable force field.[29] Again, different conclusions were reached. In the latest BOMD simulations[95] using BLYP,[19,20] and HSE[102] functionals, a five-coordinated Cu(II) was observed; with a ligand-field force field,[29] by contrast, a six-water first solvation shell was observed. We note that the use of BLYP functional in most CPMD/BOMD likely overemphasizes the importance of the five-water first solvation shell. As shown in Table 1, compared to hybrid DFT and CCSD(T) calculations, BLYP underestimates the binding affinity of the sixth water molecule by about 4 kcal/mol.

With the DFTB3/MM simulations, we capture both five- and six-coordinated structures (for snapshots, see Figure 2a,b). The six-coordinated structure properly captures the expected Jahn−Teller distortion in which the axial Cu−O distances are longer than the equatorial values by about 0.2 Å. Indeed, due to Jahn−Teller distortion, the Cu−O radial distribution function has a major peak at Cu−O distance of 2.00 Å and a minor peak at 2.35 Å (Figure 2c); these values are reasonably close to the distances of 1.95 ± 0.02 Å for the equatorial and 2.23 ± 0.11 Å for the closest axial ligand, respectively, from the latest MXAN analysis.[85] In the five-coordinated structure, the two axial ligands may have substantial Cu−O distance difference that approaches 1 Å. Nevertheless, the six-coordinated species is clearly more populated, as indicated by the integrated radial distribution function (Figure 2d). Compared to the recent classical force field simulation,[29] which observed only six-coordinated first solvation shell, the integrated radial distribution function (Figure 2d) rises more slowly as a function of Cu−O distance to the value of six. Interestingly, these features are also observed in B3LYP/MM simulations: the Cu−O radial distribution function has a shoulder at Cu−O distance of 2.25 Å, and the integrated radial distribution function overlaps the DFTB3/MM data well; results from MPWB1K/MM simulations also agree with the B3LYP/MM and DFTB3/MM data (Supporting Information). The agreement between DFTB3/MM and B3LYP/MM results is consistent with the observation that DFTB3 and B3LYP give similar structural and energetic properties for Cu(II)−water clusters in the gas phase (Tables 1 and 2). By contrast, BLYP based CPMD[79] and BOMD simulations,[94,95] as discussed above, led to five-coordinated first solvation shell; this is confirmed here by BLYP/MM simulations (Supporting Information).

For Cu(I), which is nominally a closed-shell ion, the situation is, in fact, also complex. The standard textbook description for Cu(I) has a coordination number of 4,[103] although a concrete experimental characterization is complicated by the instability of Cu(I) toward disproportionation.[104] Indeed, in the gas phase, IR studies of $Cu(H_2O)_n^+$ clusters[105,106] pointed to a linear dihydrate structure similar to that of the Cu^+ diammine complex;[107] mass spectrometry study on water−Cu binding[108] also found that the binding energy of the third water and after dropped by a factor of 2 compared to the first two binding energies. The two-coordination configuration was supported by several theoretical calculations in the gas phase[96,97] and in CPMD/BOMD simulations for a solvated Cu(I).[90,94,95]

Snapshots from B3LYP/MM and DFTB3/MM simulations are shown in Figure 3a,b, respectively. In the DFTB3/MM

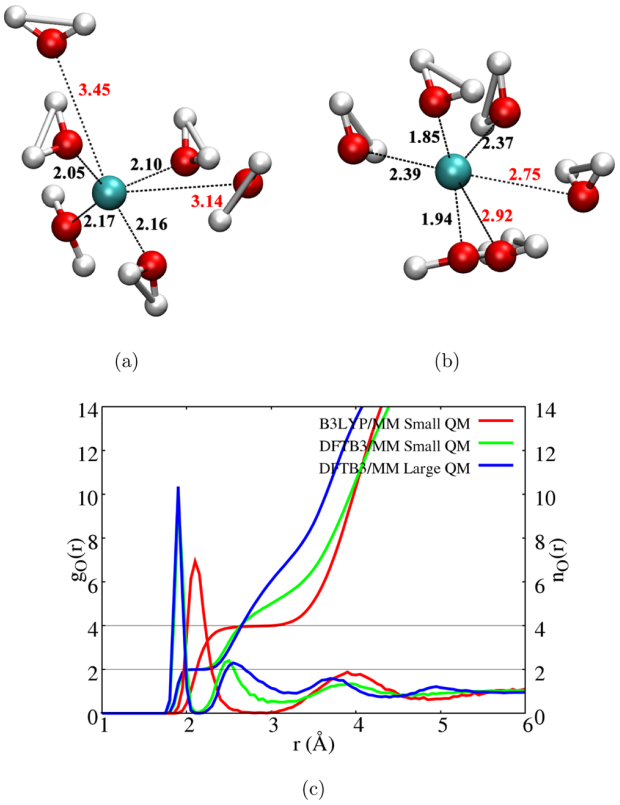

Figure 3. Coordination environment of a Cu(I) ion in water. (a, b) Snapshots from B3LYP/MM and DFTB3/MM simulations; the former features a distorted tetrahedron coordination whereas the latter is dominated with a first solvation shell that contains two closely coordinated water. (c) Radial distribution function of water near Cu(I) and the integrated coordination number. See the Supporting Information for additional discussion on the dependence of second-shell properties on the QM region size and FIRES potential.

simulations, the first solvation shell is dictated by a two-water coordination configuration (Figure 3b); this is most clearly illustrated by the integrated Cu−O radial distribution function (Figure 3c). This feature is not altered by enlarging the QM region, although the second-solvation shell becomes broader in the large-QM region simulations (see additional discussion in the Supporting Information regarding the impact of the DFTB model for water[109] and FIRES potential). The two-water coordination was also observed in previous BOMD simulations using either the BLYP[94,95] or HSE[95] functional. Interestingly, in B3LYP/MM simulations, the solvation structure is rather different and dictated by a distorted tetracoordination configuration (illustrated by a snapshot in Figure 3a, the Cu−O radial distribution function and the integrated coordination number function in Figure 3c).

DOI: 10.1021/acs.jpcb.5b09656
J. Phys. Chem. B 2016, 120, 1894−1910

The Journal of Physical Chemistry B Article

Table 2. Selected Geometrical Properties of $[Cu^{I/II}(H_2O)_n]^{+/2+}$ Optimized by Various Methods in the Gas Phase[a]

method[b]	r_{CuO}	$r_{CuO'}$	$r_{CuO''}$	$r_{CuO'''}$	$\angle_{OCuO'}$
	$[Cu^{II}(H_2O)_5]^{2+}$				
B3LYP/aug-cc-pVTZ	1.98	2.02	2.19		
B97-1/aug-cc-pVTZ	1.98	2.02	2.20		
B3LYP/Lanl2dz/6-31G(d)	1.99	2.04	2.16		
BLYP/Lanl2dz/6-31G(d)	2.04	2.05	2.26		
DFTB3	2.01	2.04	2.22		
	$[Cu^{II}(H_2O)_6]^{2+}$				
B3LYP/aug-cc-pVTZ	2.02	2.31			90.0/180.0
B97-1/aug-cc-pVTZ	2.02	2.31			90.0/180.0
B3LYP/Lanl2dz/6-31G(d)	2.03	2.25			90.0/180.0
BLYP/Lanl2dz/6-31G(d)	2.05	2.28			90.0/180.0
DFTB3	2.03	2.34			90.0/180.0
	$[Cu^{I}(H_2O)_2]^{+}$				
B3LYP/aug-cc-pVTZ	1.91				180.0
B97-1/aug-cc-pVTZ	1.92				180.0
B3LYP/Lanl2dz/6-31G(d)	1.92				180.0
BLYP/Lanl2dz/6-31G(d)	1.92				180.0
DFTB3	1.89				180.0
CCSD(T)	1.90				180.0
	$[Cu^{I}(H_2O)_4]^{+}$ [c]				
B3LYP/aug-cc-pVTZ	2.04	2.11	2.20	2.23	135.2
B97-1/aug-cc-pVTZ	2.04	2.11	2.22	2.26	138.8
B3LYP/Lanl2dz/6-31G(d)	2.03	2.12	2.17	2.23	135.4
BLYP/Lanl2dz/6-31G(d)	2.01	2.05	2.31	2.31	153.1
DFTB3	1.92	1.91	2.43	2.51	173.5

[a]Optimized at the respective levels; distances in Å, angles in degrees. Also see Figure 4 for the labels of relevant distances and angles. [b]For results with additional basis sets, see the Supporting Information. [c]Results included here are for the tetrahedron structure; for discussion of the alternative two-coordinated structure (Figure 4c), see the Supporting Information.

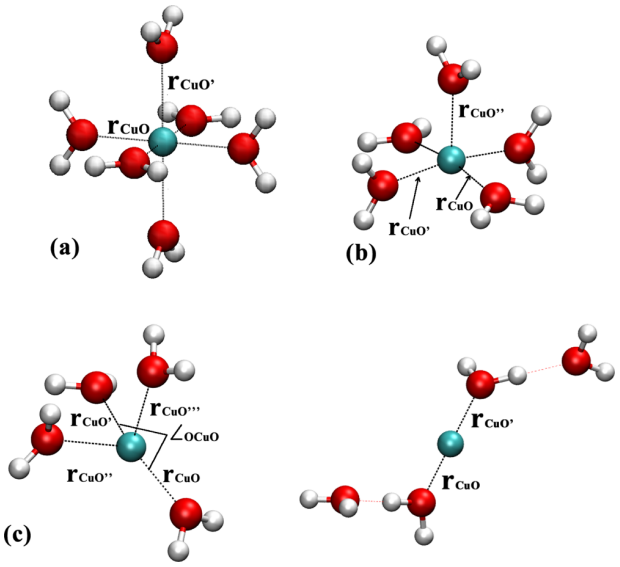

Figure 4. Cu(I)/Cu(II)−water gas phase models studied to compare different computational methods. (a) $[Cu^{II}(H_2O)_6]^{2+}$; (b) $[Cu^{II}(H_2O)_5]^{2+}$; (c) $[Cu^{I}(H_2O)_4]^{+}$. See Table 2 for optimized values of distances and angles; see Supporting Information for additional results, including the relative stability of the two types of $[Cu^{I}(H_2O)_4]^{+}$ configurations in (c).

To understand the difference between DFTB3/MM and B3LYP/MM results, we study small Cu(I)/Cu(II)−water clusters in the gas phase. As shown in Table 2, DFTB3 and B3LYP give very similar results for Cu(II)−water complexes (Figures 4a,b) and for $[Cu^{I}(H_2O)_2^{+}]$; the results are also very similar to those from a few other functionals and CCSD(T). For the $[Cu^{I}(H_2O)_4^{+}]$ cluster, however, the situation becomes complex. With B3LYP and B97-1, a distorted tetrahedron configuration is locally stable in which two Cu−O distances are slightly (~0.1 Å) longer than the other two. With BLYP and PBE, however, the tetrahedron configuration is not locally stable and optimization leads to a linear structure in which Cu(I) is directly coordinated with only two water molecules (Figure 4c). With DFTB3, the tetrahedron-like structure is also locally stable although two Cu−water distances are substantially longer. At all levels, the linear structure stabilized by two hydrogen-bonded waters is locally stable and represents the global minimum of $[Cu^{I}(H_2O)_4^{+}]$; the degree of energy stabilization relative to the tetrahedron-like structure, however, differs (Supporting Information), which apparently leads to different Cu(I) solvation structure in the bulk.

3.1.2. Reduction Potential. Computed reduction potentials and reorganization energies at different levels of theory are summarized in Table 3. At the DFTB3/MM level, the stochastic boundary condition (SBC) simulation with a Born solvation correction gives very similar results as GSBP. Reduction potential directly computed from free energy simulation using the periodic boundary condition (PBC) differs by about 7 kcal/mol from the SBC and GSBP values. As discussed in previous work,[110−113] this magnitude of difference is expected and due to the change of net charge in PBC simulations using Ewald summation. The PBC simulations also give a reorganization energy that is lower by 0.2 eV.

The B3LYP/MM simulation gives a reduction free energy of about −110.0 kcal/mol, which is ~5 kcal/mol (~0.22 eV) higher than the DFTB3/MM simulations and ~4 kcal/mol (~0.17 eV) lower compared to experimental data. Considering the relatively small basis set in the B3LYP/MM simulations and the intrinsic error of B3LYP for copper reduction (see the Supporting Information for a comparison between B3LYP and CCSD(T) for the oxidation/reduction energy of small copper−water clusters), this level of difference from the experimental value is expected; for comparison, the error in the computed reduction potential from BOMD simulations ranged from 0.15 to 1.26 eV when different functionals (BLYP, HSE) and pseudopotentials were used.[95]

To better understand the difference between DFTB3 and B3LYP results, the energy gaps at the two end states (λ = 0, 1) are recomputed by B3LYP/MM (DFTB3/MM) single-point calculations at snapshots collected from DFTB3/MM (B3LYP/MM) trajectories. Interestingly, the results are all similar (within ~1 kcal/mol) to the B3LYP/MM simulation. This is somewhat unexpected because, as discussed above, although DFTB3/MM and B3LYP/MM give a similar solvation environment for Cu(II) (Figure 2), they appear to give fairly different descriptions for a solvated Cu(I) (Figure 3). We then examine the distribution of the energy gap (always calculated at the B3LYP/MM level) for snapshots taken from the DFTB3/MM and B3LYP/MM trajectories for the Cu(I) state, with a specific number (2, 4, 6, or all) of water molecules

DOI: 10.1021/acs.jpcb.5b09656
J. Phys. Chem. B 2016, 120, 1894−1910

The Journal of Physical Chemistry B Article

Table 3. Reduction Potential Calculations for Copper in Solution and in Plastocyanin at pH 7 from QM/MM Simulations[a]

method[b]	$\langle\Delta U\rangle_{\lambda=0}$[c]	$\langle\Delta U\rangle_{\lambda=1}$[c]	Born[d]	ΔF_{red}[e]	$\mathcal{E}_{red}$ (mV)	Λ (eV)[f]
			Cu(II) → Cu(I) in Water			
B3LYP-SBC	−66.3 (0.2)	−215.1 (0.4)	+30.7	−110.0	330	3.22
DFTB3//B3LYP-SBC	−68.1 (0.2)	−215.7 (0.3)	+30.7	−111.2	382	3.20
B3LYP//DFTB3-SBC	−69.3 (0.1)	−212.0 (0.2)	+30.7	−110.0	330	3.09
DFTB3-SBC	−69.1 (0.2)	−222.5 (0.3)	+30.7	−115.1	551	3.33
DFTB3-GSBP	−40.8 (0.1)	−196.0 (0.2)		−114.5	525	3.37
DFTB3-PBC	−52.4 (0.2)	−196.5 (0.3)		−122.4 (−114.7)[g]	867 (525)[g]	3.12
exp[h]				−106.1	159	
			Cu(II) → Cu(I) in Plastocyanin			
DFTB3-GSBP1	−67.0 (0.2)	−121.2 (0.7)		−96.4 (−103.0)[i]	−260 (27)[i]	1.18
DFTB3-GSBP1	−65.9 (0.3)	−123.4 (0.3)		−95.6 (−102.2)[i]	−294 (−8)[i]	1.25
DFTB3-PBC1	−88.8 (0.6)	−145.8 (0.2)		−118.6 (−110.9)[g]	703 (369)[g]	1.24
DFTB3-PBC2	−84.9 (0.4)	−150.5 (0.3)		−117.8 (−110.1)[g]	668 (334)[g]	1.42
exp[h]				−111.0	375	1.296

[a]All energies are in kcal/mol, except for the final reduction potential and reorganization energy, which are given in mV (relative to the standard hydrogen electrode) and eV, respectively. [b]The QM level is indicated (B3LYP uses Lanl2dz for copper and 6-31G(d) for other elements), and MM is the CHARMM22 force field for proteins and a modified TIP3P model for water. DFTB3//B3LYP indicates a single-point energy gap calculated at the DFTB3/MM level using B3LYP/MM trajectories. Three different boundary conditions are used: stochastic boundary condition (SBC), generalized solvent boundary potential (GSBP), and periodic boundary condition (PBC). Extended electrostatics are used for both SBC and GSBP, whereas Ewald is used for PBC (see text for details). [c]Numbers in parentheses are statistical errors. Although multiple λ windows are used, only the end point (λ = 0, 1) values are summarized here. See the Supporting Information for additional data. [d]Born correction is needed for the SBC simulations; a radius of 16 Å is used. [e]Following a linear propagation of statistical errors of free energy derivatives, the statistical error of computed ΔF_{red} is ∼0.1−0.2 kcal/mol for copper reduction in water and ∼0.2−0.5 kcal/mol for plastocyanin. [f]Estimated using a linear model, $\Lambda = \frac{1}{2}(\langle\Delta U\rangle_{\lambda=0} - \langle\Delta U\rangle_{\lambda=1})$. [g]Numbers in parentheses include a correction due to the net charge[110−113] in PBC free energy simulation; a value of 7.7 kcal/mol is taken from ref 113 for Na^+ solvation; for plastocyanin, perturbative analysis indicates that ions in PBC simulations lower ΔF_{red} by about 9 kcal/mol. [h]Measured reduction potential is taken from ref 114 for copper reduction in water; values for plastocyanin are those summarized in refs 115 and 116. [i]Values in parentheses include a smooth boundary correction for GSBP with an inner region charge of −8.75 using Poisson−Boltzmann calculations of 100 snapshots taken from the λ = 0/1 trajectories.[112]

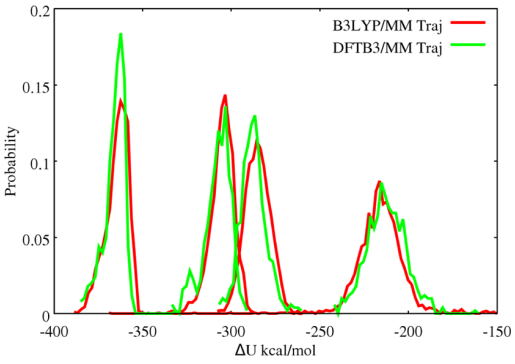

Figure 5. Energy gap distribution (calculated at the B3LYP/MM level) using snapshots taken from B3LYP/MM and DFTB3/MM Cu(I) trajectories. Plotted from left to right are the distributions of energy gap calculated by including two, four, or six closest or all water molecules to the copper center.

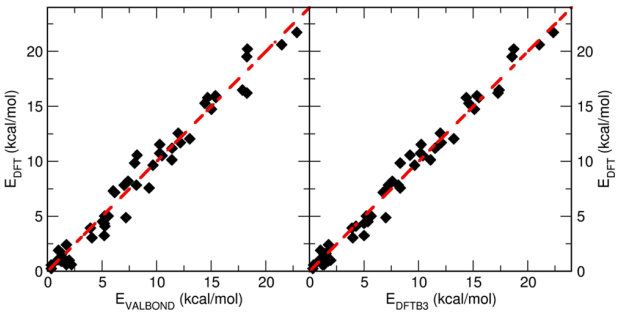

Figure 6. Comparison of energies obtained from the VALBOND force field, DFTB3 and DFT calculations (B3LYP/6-31G(d,p)) for 50 snapshots of $[Cu^{II}(NH_3)_4(H_2O)_2]^{2+}$ taken from the MD simulations.

closest to the copper ion included. As seen in Figure 5, the distributions are remarkably similar when snapshots from B3LYP/MM and DFTB3/MM trajectories are used, regardless of the number of water molecules included. Therefore, we conclude that the energy gap is not highly sensitive to the precise distance and orientation of the nearby water molecules; rather, the mean energy gap appears to be most sensitive to the density of nearby water. This explains why B3LYP/MM and DFTB3/MM trajectories lead to fairly similar reduction potentials despite the notable differences in the solvation structure of Cu(I) as shown in Figure 3.

Compared to the latest work of Sprik and co-workers[95] on BOMD calculations of Cu(II) reduction in water, the errors in the computed reduction potential from the current QM/MM simulations, as noted above, are similar in magnitude. There is striking difference, however, in the magnitude of the reorganization energy. With a linear response model, our estimated reorganization energy is on the order of 3 eV (Table 3), whereas the BOMD values are in the range of 2.0 eV;[95] we note that the deviation of free energy derivatives from a linear model is very modest (Supporting Information). The origin of the difference is not quite clear; we note that our system size is substantially larger and the simulations are also much longer (the box size in ref 95 is 9.86 Å, and most λ windows were simulated for <10 ps), although these differences are unlikely to lead to a difference of 1.0 eV in reorganization energy. The issue is worth investigating in the future by, for example, using Drude oscillator model for the MM water in QM/MM simulations (Supporting Information, we show that this has

DOI: 10.1021/acs.jpcb.5b09656
J. Phys. Chem. B 2016, 120, 1894−1910

The Journal of Physical Chemistry B Article

only small effects on the solvation structure of copper ions in water). Moreover, the limitations in the description of bulk water by the DFT methods as discussed in ref 95 might also contribute.

3.2. Solvent Response to Copper Oxidation in Copper−Ammonia Complex. The VALBOND force field parametrization is first validated by comparing with *ab initio* data calculated at the B3LYP/6-31G(d,p) level of theory. From the MD simulations, the energies for 50 snapshots of the $[Cu^{II}(NH_3)_4(H_2O)_2]^{2+}$ complex, each separated by 5 ps, were computed using VALBOND, DFTB3, and *ab initio* methods.

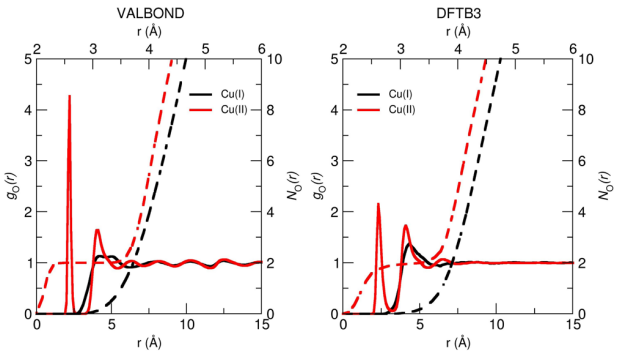

Figure 7. Radial distribution function (RDF) of the water oxygen with respect to the Cu ion obtained from the equilibrium simulation of 10 ns using VALBOND force field (left) and 5 ns using DFTB3/MM (right).

Figure 6 shows a correlation plot for all three methods. Between VALBOND and DFT the $RMSD_E$ (root-mean-square deviation) was 1.1 kcal/mol compared to 0.82 kcal/mol between DFTB3 and DFT. Furthermore, the structures were compared in a similar fashion by correlating all atom to atom distances for the energy optimized geometries from the three methods. The RMSD was found to be 0.29 Å between VALBOND and DFT, and 0.28 Å between DFTB3 and DFT. Hence, for structures and energetics, VALBOND and DFTB3 are in good agreement with DFT.

3.2.1. Equilibrium Simulation. As shown in Figure 7, VALBOND and DFTB3/MM give qualitatively similar $g_{O-Cu}(r)$ although for VALBOND the coordination of water to Cu(II) appears to be stronger as suggested by the higher peak for the first solvation shell. However, the number of water molecules in the first shell, as determined from $N_O(r_s) = 4\pi\rho\int_0^{r_s} r^2 g(r)\,dr$ is identical and a value of 2 is given by both simulations. A similar conclusion can be drawn for Cu(I). Hence, from a structural perspective, the two methods yield comparable results, albeit at different computational speed.

During equilibrium simulations, the number of water molecules within a given solvation shell is not constant as a function of time. For $[Cu^{I}(NH_3)_4]^{+}$ and $[Cu^{II}(NH_3)_4]^{2+}$, these are illustrated in Figure 8. For Cu(I), an insignificant number of water molecules is expected at 3 Å due to the tetrahedral structure of the complex, as found in both VALBOND (Figure 8a,b) and DFTB3/MM (Figure 8c,d) simulations. By contrast, the square-planar structure of the Cu(II) complex allows up to two water molecules to coordinate axially. This is the dominant

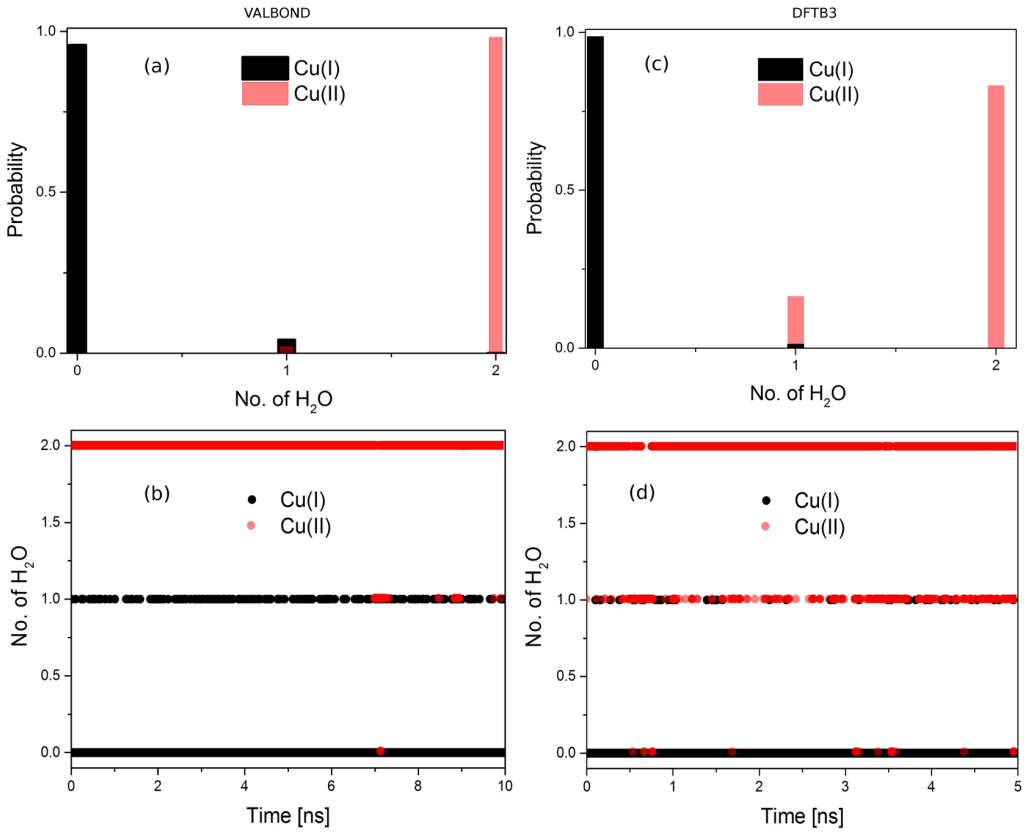

Figure 8. Distribution of water molecules around Cu(I)/Cu(II) ion at a distance of 3 Å obtained from the equilibrium simulation of (a, b) 10 ns using VALBOND and (c, d) 5 ns using DFTB3/MM.

DOI: 10.1021/acs.jpcb.5b09656
J. Phys. Chem. B 2016, 120, 1894−1910

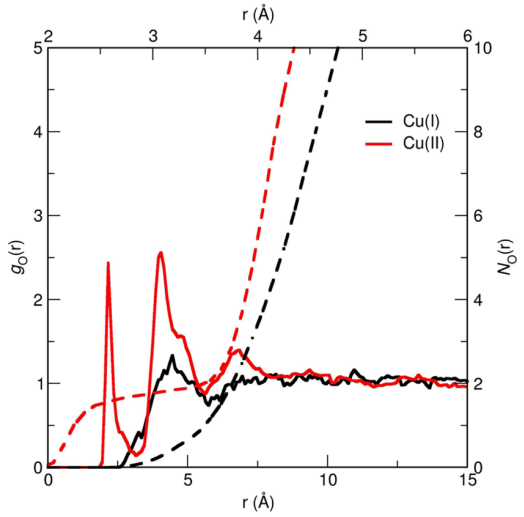

Figure 9. Radial distribution function (RDF) of the water oxygen with respect to the Cu ion obtained from 90 ps of equilibrium B3LYP/MM simulation.

structure using both methods. However, the propensities are slightly different (Figure 8a,c): close to 100% for VALBOND and about 85% for DFTB3/MM (see below). This is consistent with the observation that the $g_{O-Cu}(r)$ pair distribution function is more strongly peaked for the VALBOND simulations and confirms that the copper−water interaction is stronger with VALBOND than with DFTB3/MM; including the first aqueous solvation shell of copper into the QM region in the DFTB3/MM simulations does not change the qualitative trends. Moreover, considering the dynamics of a larger water shell around the Cu(I) ion (Supporting Information) reveals an overall similar occupation pattern for the two methods: the maximum occupation is shifted to slightly smaller numbers of water molecules in the DFTB3/MM simulations, further suggesting reduced interaction between the metal complex and the surrounding solvent.

In the B3LYP/MM simulation of the Cu(II) complex, also 1−2 water molecule(s) are observed to be coordinated to the metal ion, similar to DFTB3/MM simulations; the integrated radial distribution function appears to rise to 2 somewhat slower than DFTB3/MM (compare Figures 7 and 9); thus the situation is similar to the discussion in the last section regarding the coordination number of a Cu(II) ion in water. In DFTB3/MM simulations, regardless of whether the first aqueous solvation shell is QM or MM, the single-water coordination accounts for about 15% of the population (Figure 8b); by comparison, the value is about 22% in the B3LYP/MM simulations.

Regarding comparison to experiments, we note that extended X-ray absorption fine structure (EXAFS) experiments suggested that the most stable average structure of the Cu(II) ammine complex in 4 M pH 10 aqueous NH_3 can be represented as $[Cu^{II}(NH_3)_{4.62}(H_2O)_{0.38}(solv)]^{2+}\cdot 6solv$, where solv = H_2O, NH_3.[117] Here "solv" in the first solvation shell is a localized but chemically unidentified (either H_2O or NH_3) solvent molecule at a distance of ≈3 Å due to to the charge−dipole interaction along the axial direction. Thus, our observation of two axial ligand (water) molecules coordinating Cu(II) qualitatively agrees with EXAFS experimental results. Also, in the second shell (∼4 Å from the metal center) 6 solvent molecules were inferred from the analysis,[117] which is again in good agreement with our coordination number analysis $N_{O-Cu}(r) \approx 5.5$ based on the radial distribution function.

3.2.2. Nonequilibrium Simulation. In state-of-the-art time-resolved X-ray experiments, structural changes and solvent responses upon switching the oxidation state at a metal center can be followed on the picoseconds time scale.[37,38] As a simple attempt to mimic such experiments, oxidation state change is induced by changing the force field parameters instantaneously from Cu(I) to Cu(II) in VALBOND simulations; in DFTB3/MM simulations, the total charge and number of unpaired electrons are changed (see Methods). Structural rearrangement of solvent molecules is monitored by computing time evolved radial distribution functions and coordination numbers of water oxygen with respect to the Cu ion.

Because the most pronounced difference in $g_{O-Cu}(r)$ between Cu(I) and Cu(II) is the peak at ≈2.5 Å (Figure 7), we focus on the time-dependence of this region of the solvent distribution and show the time evolved $N_{O-Cu}(r)$ in Figure 10. The general

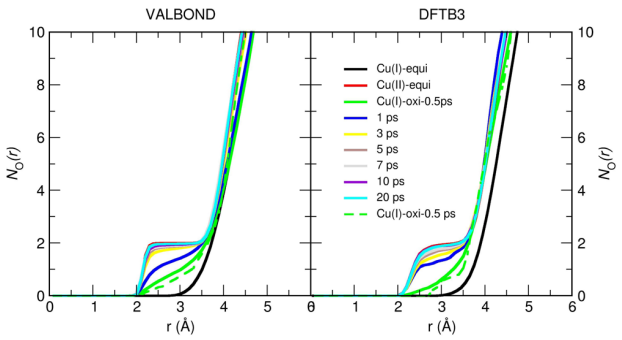

Figure 10. Running coordination number $N_{O-Cu}(r)$ of water oxygen with respect to the Cu ion obtained from the nonequilibrium simulation at different time intervals using VALBOND force field (left panel) (averaged over 100 trajectories except the dotted green line which is only a single trajectory) and using DFTB3/MM (averaged over 20 trajectories except the dotted green line which is only a single trajectory) (right panel) along with the equilibrium $N_{O-Cu}(r)$.

behaviors are again similar in VALBOND and DFTB3/MM simulations. The structural response of the water shell after oxidation takes place within a few picoseconds. Somewhat larger changes occur between 0.5 and 1 ps in the DFTB3/MM simulations than with VALBOND, although in both cases the change of local solvation is essentially complete after 3 ps. The result from a single trajectory (dotted lines in Figure 10) is fairly close to those averaged over many trajectories, indicating that the key features are not sensitive to the initial solvent structure. Taking all data in this section together, we see that VALBOND and DFTB3/MM are consistent in terms of equilibrium and dynamical properties of solvents near the metal complex.

3.3. Reduction Potential of Plastocyanin at pH 7. Blue copper proteins have been widely studied as prototypical electron transfer proteins.[118−121] Several computational studies have also been conducted to analyze factors that dictate the reduction potential under different conditions.[115,122−124] In this work, we focus on the degree to which DFTB3/MM is able to describe the structural and energetic properties of plastocyanin in different copper oxidation states. We leave a more systematic dissection of residual contributions, comparison to related blue copper proteins (e.g., rusticyanin), and the effect of pH[125,126] to future studies.

DOI: 10.1021/acs.jpcb.5b09656
J. Phys. Chem. B 2016, 120, 1894−1910

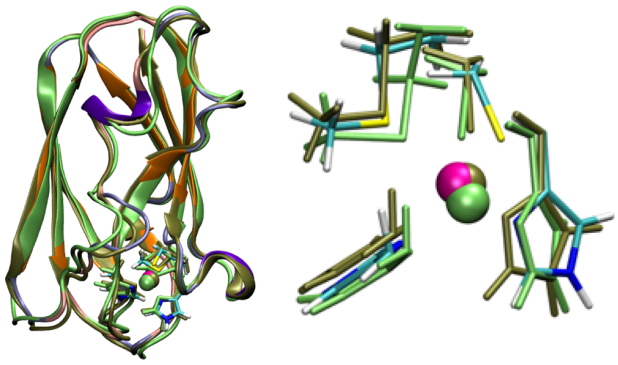

(a) (b)

Figure 11. Overlay of the crystal structure (PDB ID 5PCY) of plastocyanin with representative structures from Cu(I) and Cu(II) PBC simulations. The crystal structure and the representative structures from simulations are aligned on the basis of the backbone heavy atoms. The representative structures from the Cu(I) and Cu(II) PBC simulations are chosen such that they have the smallest backbone heavy atom RMSD relative to the average protein structures in the simulations. The active site in the crystal structure is colored by atom type and the cartoon representation for the protein is colored using the same scheme as in Figure 1c. The representative structure from Cu(I) PBC simulation is lime green, and that from Cu(II) PBC simulation is tan. (a) Overlay of the entire structure. (b) Overlay of the active site region (copper is coordinated with His 37, His 87, Cys 84, and Met 92).

3.3.1. Structural Properties. Overall, the protein remains structurally stable during the course of the simulations at the nanosecond time scale. This is illustrated visually by the overlap of crystal structure and the averaged protein structure from PBC simulations (Figure 11a), and quantitatively by the RMSD values (~1.5 Å for all non-hydrogen atoms) relative to the starting crystal structure during the PBC simulations (Figure 12a,b). In GSBP simulations, because part of the protein is fixed, even smaller changes in the overall protein structure are observed and therefore not shown.

Focusing now on the active site region, the general structural features are again well maintained for both copper oxidation states. This is again illustrated visually by the overlap of crystal structure and the averaged structures from PBC simulations (Figure 11b), and quantitatively by the RMSD values (Figure 12a,b), which are slightly higher for Cu(I) (~0.75 Å) than for Cu(II) (~0.5 Å) simulations. In a recent MM study using the AMOEBA force field,[29] two similar blue copper systems were simulated in their Cu(II) states, and somewhat lower RMSD values (~0.5−0.6 Å) were observed during also two nanoseconds of molecular dynamics.

Looking at the key distances between copper and its ligands (Table 4), the overall agreement is satisfactory for most cases for both GSBP and PBC simulations, especially for the Cu(II) state. In the crystal structures, the most pronounced difference in the active site upon copper oxidation is that the two histidine

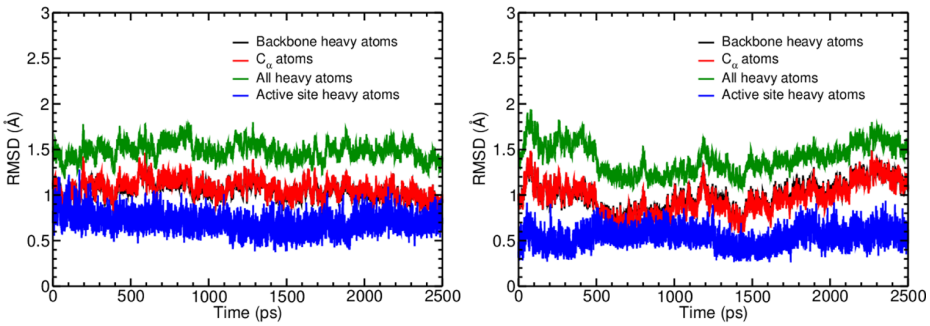

(a) (b)

Figure 12. RMSD for selected atoms during the PBC simulations for (a) Cu(I) and (b) Cu(II) states of plastocyanin.

Table 4. Key Bond Distances (Å) during MD Simulations of Plastocyanin in Comparison to Available Crystal Structures

	Cu−ligand atom				other		
	Nδ(H37)	Nδ(H87)	Sγ(C84)	Sδ(M92)	O(P36)	Sγ(C84)−N(N38)	Sγ(C84)−N(H87)
				Cu(I)			
5PCY[a]	2.1	2.4	2.2	2.9	4.0	3.5	3.9
4PCY[a]	2.1	2.3	2.1	2.9	4.1	3.5	3.9
GSBP1[b]	2.15 ± 0.11	1.95 ± 0.05	2.26 ± 0.06	3.25 ± 0.45	3.98 ± 0.25	3.55 ± 0.17	4.92 ± 0.30
GSBP2[b]	2.14 ± 0.11	1.95 ± 0.05	2.26 ± 0.06	3.21 ± 0.31	3.94 ± 0.25	3.54 ± 0.16	4.96 ± 0.28
PBC1[b]	2.05 ± 0.11	1.95 ± 0.05	2.36 ± 0.16	3.13 ± 0.24	3.95 ± 0.31	3.59 ± 0.18	4.81 ± 0.32
PBC2[b]	2.01 ± 0.11	1.94 ± 0.05	2.46 ± 0.24	3.11 ± 0.21	3.81 ± 0.39	3.52 ± 0.17	4.69 ± 0.40
				Cu(II)			
1PLC[a]	1.9	2.1	2.1	2.8	3.9	3.5	4.2
GSBP1[b]	1.96 ± 0.05	1.95 ± 0.04	2.19 ± 0.05	2.96 ± 0.16	3.43 ± 0.24	3.58 ± 0.15	4.26 ± 0.31
GSBP2[b]	1.96 ± 0.05	1.95 ± 0.04	2.19 ± 0.05	2.96 ± 0.16	3.47 ± 0.24	3.58 ± 0.15	4.35 ± 0.35
PBC1[b]	1.96 ± 0.05	1.95 ± 0.04	2.20 ± 0.05	2.98 ± 0.17	3.46 ± 0.25	3.59 ± 0.16	4.48 ± 0.35
PBC2[b]	1.96 ± 0.05	1.95 ± 0.04	2.20 ± 0.05	2.95 ± 0.16	3.43 ± 0.26	3.57 ± 0.15	4.31 ± 0.34

[a]5PCY [Cu(I)]: pH 7.0, resolution 1.8 Å. 4PCY [Cu(I)]: pH 7.8, resolution 2.15 Å. 1PLC [Cu(II)]: pH 6.0, resolution 1.33 Å. [b]GSBP1/2 indicates the two independent trajectories using GSBP; PBC1/2 indicates the two independent trajectories using PBC.

DOI: 10.1021/acs.jpcb.5b09656
J. Phys. Chem. B 2016, 120, 1894−1910

residues (His 37, His 87) move closer to the copper ion by about 0.2 Å (Cu−Nδ distances). This is partially reproduced by the DFTB3/MM simulations in both GSBP and PBC setups: the Cu−Nδ(His 37) indeed shortens from ∼2.15 Å (∼2.05 Å) to ∼1.96 Å in GSBP (PBC) simulations upon copper oxidation. The Cu−Nδ(His 87) distance, however, remains to be 1.95 Å in all simulations, independent of the redox state, and quite a bit shorter than the values in the crystal structures, especially for Cu(I). On the contrary, Met 92 in Cu(I) is further away from the copper ion in both GSBP and PBC simulations by about 0.2−0.3 Å relative to the crystal structure; the fluctuation of the Cu(I)−S distance, especially in the GSBP simulations (∼0.3−0.4 Å), is also substantially larger than other copper−ligand distances (∼0.05−0.1 Å). In PBC simulations for the Cu(I) state, Cu−S(Cys 84) also has higher fluctuations and, on average, deviates more from the crystal value compared to most other copper−ligand distances. Finally, although Cys 84 and His 87 are fairly close in the crystal structure (∼4 Å), they become further apart in the Cu(I) simulations; the mean distance between S(Cys 84)−Nδ(His 87) falls in the range of 4.7−5.0 Å. By contrast, the hydrogen bond between Cys 84 and Asn 38 remains intact (Table 4).

For the key angles between copper and its ligands (Table 5), the agreement between crystal structures and simulations is overall satisfactory for Cu(II) for both GSBP and PBC calculations. For Cu(I), however, there are several notable deviations, such as S(Met 92)−Cu−S(Cys 84), S(Cys 84)−Cu−Nδ(His 87), and S(Cys 84)−Cu−Nδ(His 37); the deviations are consistent with the larger copper−ligand distance deviations for Cys 84 and Met 92 in Cu(I) simulations. In PBC simulations of Cu(I), the Nδ(His 87)−Cu−Nδ(His 37) angle is also fairly different from the crystal structure value; this is consistent with the observation that His 37 is pulled closer to Cu(I) in those simulations by almost 0.1 Å.

In short, the overall trends concerning the active site structural properties in GSBP and PBC simulations are largely consistent with each other, except for the Cu(I)−His 37 distance, and that the Cu(II) state is generally better behaved (i.e., remains closer to the crystal structure) than the Cu(I) state, in which the copper−sulfur interactions appear to be underestimated by the current DFTB3 model. This is consistent with our previous finding[18] that for the interaction between copper and charged ligands (e.g., deprotonated Cys side chain), the current DFTB3 model still has considerable errors, due most likely to the use of minimal basis. Improvement of polarization using chemical potential equalization[127−129] (or a larger basis for the charged ligands) is likely to reduce the deviations observed here.

3.3.2. Solvation of Active Site. In addition to the copper−ligand geometry, another property of interest is the level of solvation of the active site. In previous PBE/AMBER simulation study,[124] for example, it was observed that the response of nearby water molecules to copper oxidation contributes 80% of the reorganization energy; this notion was also raised in previous experimental studies[130] and is consistent with the small structural changes in the protein structure and active site geometry upon copper oxidation (Tables 4 and 5).

In the current simulations, we also observe notable solvent responses. As shown in Figure 13a,b, the hydration structure of the active site (as measured by the water radial distribution function around copper and Nϵ(His 87)) undergoes considerable change and the general trend is very consistent in independent GSBP and PBC simulations. The copper ion is not

Table 5. Key Bond Angles (deg) during MD Simulations of Plastocyanin in Comparison to Available Crystal Structures

	Nδ(H87)−Cu−Nδ(H37)		Nδ(H37)−Cu−Sδ(M92)		Sδ(M92)−Cu−Sγ(C84)		Sγ(C84)−Cu−Nδ(H87)		Sγ(C84)−Cu−Nδ(H37)		Sδ(M92)−Cu−Nδ(H87)	
						Cu(I)						
5PCY[a]	99		88		113		110		136		106	
4PCY[a]	92		90		114		112		141		102	
GSBP1[b]	101.4 ± 7.8		94.4 ± 7.3		93.8 ± 7.1		148.1 ± 11.5		107.4 ± 7.3		94.3 ± 7.2	
GSBP2[b]	102.5 ± 8.2		94.2 ± 7.3		94.2 ± 7.2		147.9 ± 11.2		106.6 ± 6.7		93.6 ± 7.3	
PBC1[b]	113.9 ± 15.7		91.3 ± 7.9		91.6 ± 7.1		133.1 ± 17.2		109.5 ± 7.5		100.5 ± 8.2	
PBC2[b]	123.3 ± 20.1		92.0 ± 8.4		93.1 ± 8.6		124.6 ± 21.3		109.0 ± 7.5		97.3 ± 9.4	
						Cu(II)						
1PLC[a]	97		89		110		121		132		101	
GSBP1[b]	102.7 ± 5.8		85.5 ± 6.3		98.5 ± 6.3		128.5 ± 11.1		123.9 ± 10.2		104.3 ± 6.6	
GSBP2[b]	102.2 ± 4.9		89.5 ± 6.5		98.7 ± 6.6		131.4 ± 11.4		121.2 ± 10.6		102.5 ± 6.4	
PBC1[b]	102.3 ± 5.5		86.4 ± 6.4		97.2 ± 6.6		131.3 ± 12.4		122.1 ± 11.8		103.1 ± 6.6	
PBC2[b]	102.1 ± 5.0		87.2 ± 6.5		99.6 ± 7.4		129.0 ± 11.7		124.2 ± 10.9		100.8 ± 8.8	

[a]5PCY [Cu(I)]: pH 7.0, resolution 1.8 Å. 4PCY [Cu(I)]: pH 7.8, resolution 2.15 Å. 1PLC [Cu(II)]: pH 6.0, resolution 1.33 Å. [b]GSBP1/2 indicates the two independent trajectories using GSBP; PBC1/2 indicates the two independent trajectories using PBC.

DOI: 10.1021/acs.jpcb.5b09656
J. Phys. Chem. B 2016, 120, 1894−1910

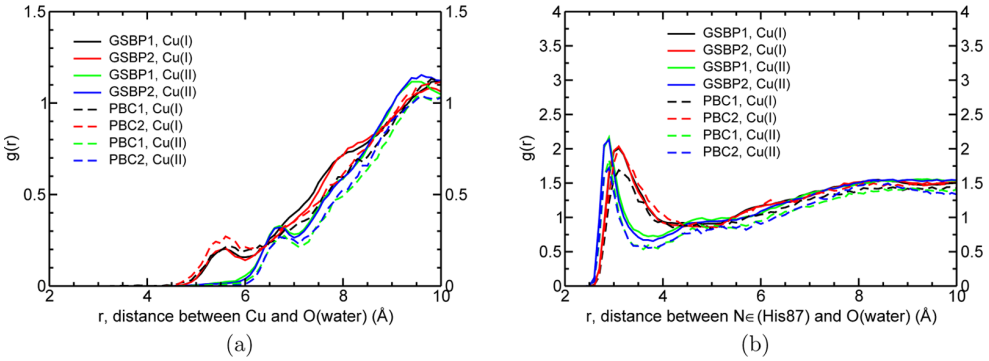

Figure 13. Water oxygen radial distribution function around (a) copper (b) Nϵ of His 87 from independent GSBP and PBC simulations.

directly bound to any solvent; in the Cu(II) state, the more positively charged copper ion induces more structure in the nearby solvent; hence, water molecules are further away from Cu(II) than from Cu(I). The oxidation also leads to a better hydration of His 87, a solvent-exposed ligand of the copper ion. These trends are qualitatively consistent with observations from a previous PBE/AMBER simulation,[124] which was much shorter in length (~8 ps); evidently, the solvent response occurs rapidly, as also witnessed in section 3.2.2.

3.3.3. Reduction Potential and Reorganization Energy. The computed reduction potential and reorganization energy values are summarized in Table 3. As discussed in detail in refs 112 and 113, both GSBP and PBC reduction potential values need to be corrected for boundary condition artifacts; for GSBP, the correction is related to the smooth boundary approximation, and for PBC, the correction is related to Ewald summation for a system with a net charge. With these corrections included, the computed reduction potentials from GSBP and PBC still differ by about 8 kcal/mol. A perturbative analysis[131,132] of charge contributions to the free energy derivatives (i.e., computed energy gaps) indicates that the explicit ions included in the PBC simulations make a notable contribution of about 9 kcal/mol. Although this is likely an upper bound due to the perturbative nature of the analysis,[131,132] the comparison highlights that salt ions may have a considerable contribution to reduction potential, which is not unexpected for an electrostatically driven process. Moreover, as pointed out in ref 112, the more limited degree of structural response allowed in GSBP may also contribute to the difference from PBC simulations; considering the limited change in overall protein structure between the two oxidation states (Figure 11) and similarity in active-site solvation from GSBP and PBC simulations (Figure 13), we expect the magnitude of the effect to be small.

In terms of absolute values, the computed reduction potentials, especially those from PBC simulations, appear to be close to the experimental value. This agreement, however, is likely fortuitous because our previous analysis[133] indicated that higher-level correction for DFTB3 energetics is not negligible; we leave a more quantitative investigation of this issue to future studies. An encouraging observation is that the computed reorganization energy is also in close agreement with experimental measurement and substantially lower than that for copper reduction in solution. As discussed in previous experimental and theoretical analyses,[119,120,122,124] the significant decrease in the reorganization energy, which is essential to the rapid electron transfer rate, is largely due to the shielding of the copper site from solvent and the relatively rigid nature of the protein scaffold.

4. CONCLUSIONS

Development of effective computational methodologies for transition metal ions in solution and biomolecules is an important yet challenging topic of research. In this study, we report our progress in this area by studying copper oxidation/reduction in water and protein using two methods developed in our groups: DFTB3 and VALBOND. Being an approximate density functional method, DFTB3 is more generally applicable and can be used to compute absolute reduction potentials. VALBOND is a molecular mechanical model and therefore needs to be parametrized for specific copper coordination and redox state; its advantage is computational efficiency and can be very effective at studying structural properties and non-equilibrium environmental responses to copper redox chemistry.

By comparing DFTB3/MM and VALBOND results to DFT/MM results and available experimental data, we show that these two methodologies generally provide consistent and satisfactory descriptions of copper coordination in the condensed phase. For example, for a Cu(II) ion, DFTB3/MM and VALBOND capture the presence of both five- and six-coordinated species, as hinted by numerous experimental studies. The absolute reduction potentials and reorganization energies computed from DFTB3/MM simulations fall in the expected range spanned by experimental data. Therefore, we anticipate that the two computational methods are valuable tools for the analysis of copper redox chemistry in the condensed phase. Both methods allow routine sampling at the nanosecond scale, making them complementary to the much more expensive *ab initio* or DFT based QM/MM molecular dynamics simulations.

Our study also highlights a number of subtle issues worth further investigation. For example, although experimental studies favor a five-coordinated Cu(II) ion in water, VALBOND, DFTB3/MM, and hybrid DFT/MM simulations carried out here point to six-coordinated species being more populated; the dominance of five-coordinated species in previous BLYP based simulations appears to be due to the underestimated binding affinity of the sixth water to Cu(II) by BLYP compared to hybrid DFT methods and CCSD(T) calculations. The coordination of Cu(I) in water also remains unclear: DFTB3/MM and previous BLYP simulations point to a two-water first solvation shell, whereas B3LYP/MM seems to favor a tetrahedron-like first solvation shell. Clearly, the

DOI: 10.1021/acs.jpcb.5b09656
J. Phys. Chem. B 2016, 120, 1894−1910

competition between different coordination modes is subtle and deserves more thorough analysis from both computation and experiments. For plastocyanin, quantitative evaluation of the reduction potential using DFTB3/MM trajectories and higher-level energetics is worthwhile; moreover, improving the treatment of charged residues by DFTB3[129] appears essential to a better description of the Cu(I) state in DFTB3/MM simulations.

■ ASSOCIATED CONTENT

Supporting Information

This material is available free of charge via the Internet at http://pubs.acs.org/. The Supporting Information is available free of charge on the ACS Publications website at DOI: 10.1021/acs.jpcb.5b09656.

Additional DFTB3/MM and DFT/MM simulation results for a copper ion in aqueous solution: impact of using a polarizable water model, effect of using a larger QM region, BLYP/MM and MPWB1K/MM simulations, and the effect of cutoff schemes for electrostatic interactions between MM atoms. Also included are additional gas-phase benchmark calculations for copper–water complexes, additional results for copper tetraammonia simulations using VALBOND, and statistical analysis of DFTB3/MM reduction potential calculations for plastocyanin (PDF)

■ AUTHOR INFORMATION

Corresponding Authors

*M. Meuwly. E-mail: m.meuwly@unibas.ch. Tel: +41-61 267 38 21.
*Q. Cui. E-mail: cui@chem.wisc.edu. Tel: +1-608-262-9801.

Notes

The authors declare no competing financial interest.

■ ACKNOWLEDGMENTS

The work at Madison has been supported by NIH grant R01-GM106443. The Basel group gratefully acknowledges financial support from the Swiss National Science Foundation through grant 200021-117810 and to the NCCR-MUST. Computational resources from the Extreme Science and Engineering Discovery Environment (XSEDE), which is supported by NSF grant number OCI-1053575, are greatly appreciated; computations are also partly supported by the National Science Foundation through a major instrument grant (CHE-0840494).

■ REFERENCES

(1) Lippard, S. J.; Berg, J. M. *Principles of Bioinorganic Chemistry*; University Science Books: Mill Valley, CA, 1994.
(2) Gray, H. B.; Stiefel, E. I.; Valentine, J. S.; Bertini, I. *Biological Inorganic Chemistry: Structure and Reactivity*; University Science Books: Mill Valley, CA, 2006.
(3) Andreini, C.; Bertini, I.; Cavallaro, G.; Holliday, G. L.; Thornton, J. M. Metal Ions in Biological Catalysis: from Enzyme Databases to General Principles. *JBIC, J. Biol. Inorg. Chem.* **2008**, *13*, 1205–1218.
(4) Waldron, K. J.; Rutherford, J. C.; Ford, D.; Robinson, N. J. Metalloproteins and Metal Sensing. *Nature* **2009**, *460*, 823–830.
(5) Eskici, G.; Axelsen, P. H. Copper and Oxidative Stress in the Pathogenesis of Alzheimer's Disease. *Biochemistry* **2012**, *51*, 6289–6311.
(6) Kozlowski, H.; Luczkowski, M.; Remelli, M.; Valensin, D. Copper, Zinc and Iron in Neurodegenerative Diseases (Alzheimer's, Parkinson's and Prion Diseases). *Coord. Chem. Rev.* **2012**, *256*, 2129–2141.
(7) Hureau, C. Coordination of Redox Active Metal Ions to the Amyloid Precursor Protein and to Amyloid-β Peptides Involved in Alzheimer Disease. Part 1: An Overview. *Coord. Chem. Rev.* **2012**, *256*, 2164–2174.
(8) Viles, J. H. Metal Ions and Amyloid Fiber Formation in Neurodegenerative Diseases. Copper, Zinc and Iron in Alzheimer's, Parkinson's and Prion diseases. *Coord. Chem. Rev.* **2012**, *256*, 2271–2284.
(9) Warshel, A.; Levitt, M. Theoretical Studies of Enzymic Reactions - Dielectric, Electrostatic and Steric Stabilization of Carbonium-Ion in Reaction of Lysozyme. *J. Mol. Biol.* **1976**, *103*, 227–249.
(10) Field, M. J.; Bash, P. A.; Karplus, M. A Combined Quantum-Mechanical and Molecular Mechanical Potential for Molecular-Dynamics Simulations. *J. Comput. Chem.* **1990**, *11*, 700–733.
(11) Gao, J. In *Reviews in Computational Chemistry VII*; Lipkowitz, K. B., Boyd, D. B., Eds.; VCH: New York, 1995; p 119.
(12) Riccardi, D.; Schaefer, P.; Yang, Y.; Yu, H.; Ghosh, N.; Prat-Resina, X.; Konig, P.; Li, G.; Xu, D.; Guo, H.; et al. *Feature Article:* Development of Effective Quantum Mechanical/Molecular Mechanical (QM/MM) Methods for Complex Biological Processes. *J. Phys. Chem. B* **2006**, *110*, 6458–6469.
(13) Hu, H.; Yang, W. T. Free Energies of Chemical Reactions in Solution and in Enzymes with Ab Initio Quantum Mechanics/Molecular Mechanics Methods. *Annu. Rev. Phys. Chem.* **2008**, *59*, 573–601.
(14) Senn, H. M.; Thiel, W. QM/MM Methods for Biomolecular Systems. *Angew. Chem., Int. Ed.* **2009**, *48*, 1198–1229.
(15) Seifert, G.; Joswig, J. O. Density-Functional Tight Binding - an Approximate Density-Functional Theory Method. *WIREs Comput. Mol. Sci.* **2012**, *2*, 456–465.
(16) Gaus, M.; Cui, Q.; Elstner, M. Density Functional Tight Binding (DFTB): Application to Organic and Biological Molecules. *WIREs Comput. Mol. Sci.* **2014**, *4*, 49–61.
(17) Gaus, M.; Cui, Q.; Elstner, M. DFTB-3rd: Extension of the Self-Consistent-Charge Density-Functional Tight-Binding Method SCC-DFTB. *J. Chem. Theory Comput.* **2011**, *7*, 931–948.
(18) Gaus, M.; Jin, H.; Demapan, D.; Christensen, A. S.; Goyal, P.; Elstner, M.; Cui, Q. DFTB3 Parametrization for Copper: the Importance of Orbital Angular Momentum Dependence of Hubbard Parameters. *J. Chem. Theory Comput.* **2015**, *11*, 4205–4219.
(19) Becke, A. D. Density-Functional Exchange-Energy Approximation with Correct Asymptotic Behavior. *Phys. Rev. A: At., Mol., Opt. Phys.* **1988**, *38*, 3098–3100.
(20) Lee, C.; Yang, W.; Parr, R. G. Development of the Colle-Salvetti Correlation-Energy Formula into a Functional of the Electron Density. *Phys. Rev. B: Condens. Matter Mater. Phys.* **1988**, *37*, 785–789.
(21) Becke, A. D. Density-Functional Thermochemistry. III. The Role of Exact Exchange. *J. Chem. Phys.* **1993**, *98*, 5648–52.
(22) Hamprecht, F. A.; Cohen, A. J.; Tozer, D. J.; Handy, N. C. Development and Assessment of New Exchange-Correlation Functionals. *J. Chem. Phys.* **1998**, *109*, 6264–6271.
(23) Jiang, W.; DeYonker, N. J.; Determan, J. J.; Wilson, A. K. Toward Accurate Theoretical Thermochemistry of First Row Transition Metal Complexes. *J. Phys. Chem. A* **2012**, *116*, 870–885.
(24) Jiang, W.; DeYonker, N. J.; Wilson, A. K. Multireference Character for 3d Transition-Metal-Containing Molecules. *J. Chem. Theory Comput.* **2012**, *8*, 460–468.
(25) Zhang, W.; Truhlar, D. G.; Tang, M. S. Tests of Exchange-Correlation Functional Approximations Against Reliable Experimental Data for Average Bond Energies of 3d Transition Metal Compounds. *J. Chem. Theory Comput.* **2013**, *9*, 3965–3977.
(26) Perdew, J. P.; Burke, K.; Ernzerhof, M. Generalized Gradient Approximation Made Simple. *Phys. Rev. Lett.* **1996**, *77*, 3865–3868.
(27) Stewart, J. J. P. Optimization of Parameters for Semiempirical Methods V: Modification of NDDO Approximations and Application to 70 elements. *J. Mol. Model.* **2007**, *13*, 1173–1213.
(28) Piquemal, J. P.; Williams-Hubbard, B.; Fey, N.; Deeth, R. J.; Gresh, N.; Giessner-Prettre, C. Inclusion of the Ligand Field

Contribution in a Polarizable Molecular Mechanics: SIBFA-LF. *J. Comput. Chem.* **2003**, *24*, 1963−1970.
(29) Xiang, J. Y.; Ponder, J. W. An Angular Overlap Model for Cu(II) Ion in the AMOEBA Polarizable Force Field. *J. Chem. Theory Comput.* **2014**, *10*, 298−311.
(30) Deeth, R. J.; Anastasi, A.; Diedrich, C.; Randell, K. Molecular Modelling for Transition Metal Complexes: Dealing with d-electron Effects. *Coord. Chem. Rev.* **2009**, *253*, 795−816.
(31) Root, D. M.; Landis, C. R.; Cleveland, T. Valence Bond Concepts Applied to the Molecular Mechanics Description of Molecular Shapes 0.1. Application to Nonhypervalent Molecules of the P-Block. *J. Am. Chem. Soc.* **1993**, *115*, 4201−4209.
(32) Cleveland, T.; Landis, C. R. Valence Bond Concepts Applied to the Molecular Mechanics Description of Molecular Shapes 0.2. Applications to Hypervalent Molecules of the P-block. *J. Am. Chem. Soc.* **1996**, *118*, 6020−6030.
(33) Landis, C. R.; Cleveland, T.; Firman, T. Valence Bond Concepts Applied to the Molecular Mechanics Description of Molecular Shapes. 3. Applications to Transition Metal Alkyls and Hydrides. *J. Am. Chem. Soc.* **1998**, *120*, 2641−2649.
(34) Tubert-Brohman, I.; Schmid, M.; Meuwly, M. Molecular Mechanics Force Field for Octahedral Organometallic Compounds with Inclusion of the Trans Influence. *J. Chem. Theory Comput.* **2009**, *5*, 530−539.
(35) Schmid, M. H.; Ward, T. R.; Meuwly, M. Toward a Broadly Applicable Force Field for d(6)-Piano Stool Complexes. *J. Chem. Theory Comput.* **2013**, *9*, 2313−2323.
(36) Hofmann, F. D.; Devereux, M.; Pfaltz, A.; Meuwly, M. Toward Force Fields for Atomistic Simulations of Iridium-Containing Complexes. *J. Comput. Chem.* **2014**, *35*, 18−29.
(37) Penfold, T. J.; Karlsson, S.; Capano, G.; Lima, F. A.; Rittmann, J.; Reinhard, M.; Rittmann-Frank, M. H.; Braem, O.; Baranoff, E.; Abela, R.; et al. Solvent-Induced Luminescence Quenching: Static and Time-Resolved X-Ray Absorption Spectroscopy of a Copper(I) Phenanthroline Complex. *J. Phys. Chem. A* **2013**, *117*, 4591−4601.
(38) Wernet, P.; Kunnus, K.; Josefsson, I.; Rajkovic, I.; Quevedo, W.; Beye, M.; Schreck, S.; Grubel, S.; Scholz, M.; Nordlund, D.; et al. Orbital-specific Mapping of the Ligand Exchange Dynamics of $Fe(CO)_5$ in Solution. *Nature* **2015**, *520*, 78−81.
(39) Humphrey, W.; Dalke, A.; Schulten, K. VMD - Visual Molecular Dynamics. *J. Mol. Graphics* **1996**, *14*, 33−38.
(40) Brooks, C. L., III; Karplus, M. Deformable Stochastic Boundaries in Molecular Dynamics. *J. Chem. Phys.* **1983**, *79*, 6312−6325.
(41) Jorgensen, W. L.; Chandrasekhar, J.; Madura, J. D.; Impey, R. W.; Klein, M. L. Comparison of Simple Potential Functions for Simulating Liquid Water. *J. Chem. Phys.* **1983**, *79*, 926−935.
(42) Rowley, C. N.; Roux, B. The Solvation Structure of Na^+ and K^+ in Liquid Water Determined from High Level Ab Initio Molecular Dynamics Simulations. *J. Chem. Theory Comput.* **2012**, *8*, 3526−3535.
(43) Lev, B.; Roux, B.; Noskov, S. Y. Relative Free Energies for Hydration of Monovalent Ions from QM and QM/MM Simulations. *J. Chem. Theory Comput.* **2013**, *9*, 4165−4175.
(44) Brooks, B. R.; Brooks, C. L.; Mackerell, A. D.; Nilsson, L.; Petrella, R. J.; Roux, B.; Won, Y.; Archontis, G.; Bartels, C.; Boresch, S.; et al. CHARMM: The Biomolecular Simulation Program. *J. Comput. Chem.* **2009**, *30*, 1545−1614.
(45) Cui, Q.; Elstner, M.; Kaxiras, E.; Frauenheim, T.; Karplus, M. A QM/MM Implementation of the Self-Consistent Charge Density Functional Tight Binding (SCC-DFTB) Method. *J. Phys. Chem. B* **2001**, *105*, 569−585.
(46) Zienau, J.; Cui, Q. Implementation of the Solvent Macromolecule Boundary Potential and Application to Model and Realistic Enzyme Systems. *J. Phys. Chem. B* **2012**, *116*, 12522−12534.
(47) Gaus, M.; Goez, A.; Elstner, M. Parametrization and Benchmark of DFTB3 for Organic Molecules. *J. Chem. Theory Comput.* **2013**, *9*, 338−354.
(48) Köhler, C.; Seifert, G.; Gerstmann, U.; Elstner, M.; Overhof, H.; Frauenheim, T. Approximate Density-Functional Calculations of Spin Densities in Large Molecular Systems and Complex Solids. *Phys. Chem. Chem. Phys.* **2001**, *3*, 5109−5114.
(49) Köhler, C.; Frauenheim, T.; Hourahine, B.; Seifert, G.; Sternberg, M. Treatment of Collinear and Noncollinear Electron Spin Within an Approximate Density Functional Based Method. *J. Phys. Chem. A* **2007**, *111*, 5622−5629.
(50) Zhao, Y.; Truhlar, D. G. Hybrid Meta Density Functional Theory Methods for Thermochemistry, Thermochemical Kinetics, and Noncovalent Interactions: The MPW1B95 and MPWB1K Models and Comparative Assessments for Hydrogen Bonding and van der Waals Interactions. *J. Phys. Chem. A* **2004**, *108*, 6908−6918.
(51) Helgaker, T.; Jogensen, P.; Olsen, J. *Molecular Electronic Structure Theory*; Wiley and Sons: New York, 2000.
(52) Ali-Torres, J.; Mirats, A.; Marechal, J.; Rodriguez-Santiago, L.; Sodupe, M. Modeling Cu^{2+}-Aβ Complexes from Computational Approaches. *AIP Adv.* **2015**, *5*, 092402.
(53) Hay, P. J.; Wadt, W. R. Ab initio Effective Core Potentials for Molecular Calculations - Potentials for the Transition-Metal Atoms Sc to Hg. *J. Chem. Phys.* **1985**, *82*, 270−283.
(54) Lamoureux, G.; Harder, E.; Vorobyov, I. V.; Roux, B.; MacKerell, A. D., Jr. A Polarizable Model of Water for Molecular Dynamics Simulations of Biomolecules. *Chem. Phys. Lett.* **2006**, *418*, 245−249.
(55) Schaefer, P.; Riccardi, D.; Cui, Q. Reliable Treatment of Electrostatics in Combined QM/MM Simulation of Macromolecules. *J. Chem. Phys.* **2005**, *123*, 014905.
(56) Steinbach, P. J.; Brooks, B. R. New Spherical-cutoff Methods for Long-range Forces in Macromolecular Simulation. *J. Comput. Chem.* **1994**, *15*, 667−683.
(57) Van Gunsteren, W.; Berendsen, H. Algorithms for Macromolecular Dynamics and Constraint Dynamics. *Mol. Phys.* **1977**, *34*, 1311−1327.
(58) Li, G.; Zhang, X.; Cui, Q. Free Energy Perturbation Calculations with Combined QM/MM Potentials Complications, Simplifications, and Applications to Redox Potential Calculations. *J. Phys. Chem. B* **2003**, *107*, 8643−8653.
(59) Born, M. *Eur. Phys. J. A* **1920**, *1*, 45−48.
(60) Im, W.; Berneche, S.; Roux, B. Generalized Solvent Boundary Potential for Computer Simulations. *J. Chem. Phys.* **2001**, *114*, 2924−2937.
(61) Riccardi, D.; Schaefer, P.; Cui, Q. pK_a Calculations in Solution and Proteins with QM/MM Free Energy Perturbation Simulations. *J. Phys. Chem. B* **2005**, *109*, 17715−17733.
(62) Darden, T.; York, D.; Pedersen, L. Particle Mesh Ewald - An N.Log(N) Method for Ewald Sums in Large Systems. *J. Chem. Phys.* **1993**, *98*, 10089−10092.
(63) Pauling, L. *The Nature of the Chemical Bond*, Third ed.; Cornell University Press: Ithaca, NY, 1960.
(64) Firman, T. K.; Landis, C. R. Valence Bond Concepts Applied to the Molecular Mechanics Description of Molecular Shapes. 4. Transition Metals with -Bonds. *J. Am. Chem. Soc.* **2001**, *123*, 11728−11742.
(65) Ryckaert, J.-P.; Ciccotti, G.; Berendsen, H. J. C. Numerical Integration of the Cartesian Equations of Motion of a System with Constraints: Molecular Dynamics of n-alkanes. *J. Comput. Phys.* **1977**, *23*, 327−341.
(66) MacKerell, A. D., Jr.; Bashford, D.; Bellott, M.; Dunbrack, R. L., Jr.; Evenseck, J. D.; Field, M. J.; Fischer, S.; Gao, J.; Guo, H.; Ha, S.; et al. All-Atom Empirical Potential for Molecular Modeling and Dynamics Studies of Proteins. *J. Phys. Chem. B* **1998**, *102*, 3586−3616.
(67) Frenkel, D.; Smit, B. *Understanding Molecular Simulation: From Algorithms to Applications*; Academic Press: New York, 2001.
(68) Evans, D. J.; Holian, B. L. The Nose-Hoover thermostat. *J. Chem. Phys.* **1985**, *83*, 4069−4074.
(69) Shannon, R. D. Revised Effective Ionic Radii and Systematic Studies of Interatomic Distances in Halides and Chalcogenides. *Acta Crystallogr., Sect. A: Cryst. Phys., Diffr., Theor. Gen. Crystallogr.* **1976**, *32*, 751−767.

DOI: 10.1021/acs.jpcb.5b09656
J. Phys. Chem. B 2016, 120, 1894−1910

(70) Bondi, A. van der Waals Volumes and Radii. *J. Phys. Chem.* **1964**, *68*, 441−451.
(71) Guss, J. M.; Harrowell, P. R.; Murata, M.; Norris, V. A.; Freeman, H. C. Crystal-Structure Analyses of Reduced (CuI) Poplar Plastocyanin at 6 pH Values. *J. Mol. Biol.* **1986**, *192*, 361−387.
(72) Stote, R. H.; States, D. J.; Karplus, M. On the Treatment of Electrostatic Interactions in Biomolecular Simulations. *AIP Conf. Proc.* **1991**, *239*, 117−117.
(73) Nina, M.; Im, W.; Roux, B. Optimized Atomic Radii for Protein Continuum Electrostatics Solvation Forces. *Biophys. Chem.* **1999**, *78*, 89−96.
(74) König, P. H.; Hoffmann, M.; Frauenheim, T.; Cui, Q. A Critical Evaluation of Different QM/MM Frontier Treatments with SCC-DFTB as the QM Method. *J. Phys. Chem. B* **2005**, *109*, 9082−9095.
(75) Neilson, G. W.; Newsome, J. R.; Sandstrom, M. Neutron Diffraction Study of Aqueous Transition Metal Salt Solutions by Isomorphic Substitution. *J. Chem. Soc., Faraday Trans. 2* **1981**, *77*, 1245−1256.
(76) Salmon, P. S.; Neilson, G. W.; Enderby, J. E. The Structure of Cu^{2+} Aqueous Solutions. *J. Phys. C: Solid State Phys.* **1988**, *21*, 1335.
(77) Salmon, P. S.; Neilson, G. W. The Coordination of Cu(II) in a Concentrated Copper Nitrate Solution. *J. Phys.: Condens. Matter* **1989**, *1*, 5291.
(78) Okan, S. E.; Salmon, P. S. The Jahn-Teller Effect in Solutions of Flexible Molecules: a Neutron Diffraction Study on the Structure of a Cu^{2+} Solution in Ethylene Glycol. *Mol. Phys.* **1995**, *85*, 981−998.
(79) Pasquarello, A.; Petri, I.; Salmon, P. S.; Parisel, O.; Car, R.; Tóth, É; Powell, D. H.; Fischer, H. E.; Helm, L.; Merbach, A. E. First Solvation Shell of the Cu(II) Aqua Ion: Evidence for Five-fold Coordination. *Science* **2001**, *291*, 856−859.
(80) Sham, T. K.; Hastings, J. B.; Perlman, M. L. Application of the EXAFS Method to Jahn−Teller Ions: Static and Dynamic Behavior of $Cu(H_2O)_6^{2+}$ and $Cr(H_2O)_6^{2+}$ in Aqueous Solution. *Chem. Phys. Lett.* **1981**, *83*, 391−396.
(81) Beagley, B.; Eriksson, A.; Lindgren, J.; Persson, I.; Pettersson, L. G. M.; Sandstrom, M.; Wahlgren, U.; White, E. W. A Computational and Experimental Study on the Jahn-Teller Effect in the Hydrated Copper (II) ion. Comparisons with Hydrated Nickel (II) Ions in Aqueous Solution and Solid Tutton's Salts. *J. Phys.: Condens. Matter* **1989**, *1*, 2395.
(82) Benfatto, M.; D'Angelo, P.; Della Longa, S.; Pavel, N. V. Evidence of Distorted Five-fold Coordination of the Cu^{2+} Aqua Ion from an X-ray-Absorption Spectroscopy Quantitative Analysis. *Phys. Rev. B: Condens. Matter Mater. Phys.* **2002**, *65*, 174205.
(83) Persson, I.; Persson, P.; Sandstrom, M.; Ullstrom, A.-S. Structure of Jahn-Teller Distorted Solvated Copper(ii) Ions in Solution, and in Solids with Apparently Regular Octahedral Coordination Geometry. *J. Chem. Soc., Dalton Trans.* **2002**, 1256−1265.
(84) Chaboy, J.; Muñoz-Páez, A.; Merkling, P. J.; Sánchez Marcos, E. The Hydration of Cu^{2+}: Can the Jahn-Teller Effect be Detected in Liquid Solution? *J. Chem. Phys.* **2006**, *124*, 064509.
(85) Frank, P.; Benfatto, M.; Qayyam, M.; Hedman, B.; Hodgson, K. O. A High-resolution XAS Study of Aqueous Cu(II) in Liquid and Frozen Solutions: Pyramidal, Polymorphic and Non-centrosymmetric. *J. Chem. Phys.* **2015**, *142*, 084310.
(86) Marini, G. W.; Liedl, K. R.; Rode, B. M. Investigation of Cu^{2+} Hydration and the Jahn-Teller Effect in Solution by QM/MM Monte Carlo Simulations. *J. Phys. Chem. A* **1999**, *103*, 11387−11393.
(87) Schwenk, C. F.; Rode, B. M. New Insights into the Jahn-Teller Effect through Ab Initio Quantum-Mechanical/Molecular-Mechanical Molecular Dynamics Simulations of CuII in Water. *ChemPhysChem* **2003**, *4*, 931−943.
(88) Schwenk, C. F.; Rode, B. M. Extended Ab Initio Quantum Mechanical/Molecular Mechanical Molecular Dynamics Simulations of Hydrated Cu^{2+}. *J. Chem. Phys.* **2003**, *119*, 9523−9531.
(89) Schwenk, C. F.; Rode, B. M. Influence of Electron Correlation Effects on the Solvation of Cu^{2+}. *J. Am. Chem. Soc.* **2004**, *126*, 12786−12787.
(90) Blumberger, J.; Bernasconi, L.; Tavernelli, I.; Vuilleumier, R.; Sprik, M. Electronic Structure and Solvation of Copper and Silver Ions: A Theoretical Picture of a Model Aqueous Redox Reaction. *J. Am. Chem. Soc.* **2004**, *126*, 3928−3938.
(91) Amira, S.; Spangberg, D.; Hermansson, K. Distorted Five-Fold Coordination of Cu^{2+}(aq) from a Car-Parrinello Molecular Dynamics Simulation. *Phys. Chem. Chem. Phys.* **2005**, *7*, 2874−2880.
(92) de Almeida, K. J.; Murugan, N. A.; Rinkevicius, Z.; Hugosson, H. W.; Vahtras, O.; Agren, H.; Cesar, A. Conformations, Structural Transitions and Visible Near-infrared Absorption Spectra of Four-, Five- and Six-coordinated Cu(II) Aqua Complexes. *Phys. Chem. Chem. Phys.* **2009**, *11*, 508−519.
(93) Liu, X.; Lu, X.; Jan Meijer, E.; Wang, R. Hydration Mechanisms of Cu^{2+}: Tetra-, Penta- or Hexa-coordinated? *Phys. Chem. Chem. Phys.* **2010**, *12*, 10801−10804.
(94) Blumberger, J. Cu^{+}_{aq}/Cu^{2+}_{aq} Redox Reaction Exhibits Strong Nonlinear Solvent Response Due to Change in Coordination Number. *J. Am. Chem. Soc.* **2008**, *130*, 16065−16068.
(95) Liu, X.; Cheng, J.; Sprik, M. Aqueous Transition-Metal Cations as Impurities in a Wide Gap Oxide: The Cu^{2+}/Cu^{+} and Ag^{2+}/Ag^{+} Redox Couples Revisited. *J. Phys. Chem. B* **2015**, *119*, 1152−1163.
(96) El-Nahas, A. M.; Tajima, N.; Hirao, K. Binding Energies and Electronic Structures of $Cu^{+}(OH_2)_n$ and $Cu^{+}(NH_3)_n$ (n = 1−4): Anomaly of the Two Ligand Cu^{+} Complexes. *J. Mol. Struct.: THEOCHEM* **1999**, *469*, 201−213.
(97) Burda, J. V.; Pavelka, M.; Šimánek, M. Theoretical Model of Copper Cu(I)/Cu(II) Hydration. DFT and Ab Initio Quantum Chemical Study. *J. Mol. Struct.: THEOCHEM* **2004**, *683*, 183−193.
(98) Frank, P.; Benfatto, M.; Szilagyi, R. K.; D'Angelo, P.; Longa, S. D.; Hodgson, K. O. The Solution Structure of $[Cu(aq)]^{2+}$ and Its Implications for Rack-Induced Bonding in Blue Copper Protein Active Sites. *Inorg. Chem.* **2005**, *44*, 1922−1933.
(99) Bryantsev, V. S.; Diallo, M. S.; van Duin, A. C.; Goddard, W. A., III. Hydration of Copper(II): New Insights from Density Functional Theory and the COSMO Solvation Model. *J. Phys. Chem. A* **2008**, *112*, 9104−9112.
(100) Bryantsev, V. S.; Diallo, M. S.; Goddard, W. A., III Computational Study of Copper(II) Complexation and Hydrolysis in Aqueous Solutions Using Mixed Cluster/Continuum Models. *J. Phys. Chem. A* **2009**, *113*, 9559−67.
(101) Rios-Font, R.; Sodupe, M.; Rodríguez-Santiago, L.; Taylor, P. R. The Role of Exact Exchange in the Description of $Cu(H_2O)_n^{2+}$ (n = 1 - 6) Complexes by Means of DFT Methods. *J. Phys. Chem. A* **2010**, *114*, 10857−10863.
(102) Heyd, J.; Scuseria, G.; Ernzerhof, M. Hybrid Functionals Based on a Screened Coulomb Potential. *J. Chem. Phys.* **2003**, *118*, 8207−8215.
(103) Rorabacher, D. B. Electron Transfer by Copper Centers. *Chem. Rev.* **2004**, *104*, 651−698.
(104) Ciavatta, L.; Ferri, D.; Palombari, R. On the Equilibrium Cu^{2+} + Cu(s) ⇌ 2 Cu^{+}. *J. Inorg. Nucl. Chem.* **1980**, *42*, 593−598.
(105) Iino, T.; Ohashi, K.; Mune, Y.; Inokuchi, Y.; Judai, K.; Nishi, N.; Sekiya, H. Infrared Photodissociation Spectra and Solvation Structures of $Cu(H_2O)_n^{+}$ (n = 0;1−4). *Chem. Phys. Lett.* **2006**, *427*, 24−28.
(106) Iino, T.; Ohashi, K.; Inoue, K.; Judai, K.; Nishi, N.; Sekiya, H. Infrared Spectroscopy of $Cu^{+}(H_2O)_n$ and $Ag^{+}(H_2O)_n$: Coordination and Solvation of Noble-Metal Ions. *J. Chem. Phys.* **2007**, *126*, 194302.
(107) Lamble, G.; Moen, A.; Nicholson, D. G. Structure of the Diammine Copper(I) Ion in Solution. An X-ray Absorption Spectroscopic Study. *J. Chem. Soc., Faraday Trans.* **1994**, *90*, 2211−2213.
(108) Magnera, T. F.; David, D. E.; Stulik, D.; Orth, R. G.; Jonkman, H. T.; Michl, J. Production of Hydrated Metal Ions by Fast Ion or Atom Beam Sputtering. Collision-Induced Dissociation and Successive Hydration Energies of Gaseous Copper+ with 1−4 Water Molecules. *J. Am. Chem. Soc.* **1989**, *111*, 5036−5043.
(109) Goyal, P.; Qian, H. J.; Irle, S.; Lu, X.; Roston, D.; Mori, T.; Elstner, M.; Cui, Q. *Feature Article*: Molecular Simulation of Water and

DOI: 10.1021/acs.jpcb.5b09656
J. Phys. Chem. B 2016, 120, 1894−1910

Hydration Effects in Different Environments: Challenges and Developments for DFTB Based Models. *J. Phys. Chem. B* **2014**, *118*, 11007−11027.
(110) Kastenholz, M. A.; Hünenberger, P. H. Computation of Methodology-Independent Ionic Solvation Free Energies from Molecular Simulations. I. The Electrostatic Potential in Molecular Liquids. *J. Chem. Phys.* **2006**, *124*, 124106.
(111) Kastenholz, M. A.; Hünenberger, P. H. Computation of Methodology-Independent Ionic Solvation Free Energies from Molecular Simulations. II. The Hydration Free Energy of the Sodium Cation. *J. Chem. Phys.* **2006**, *124*, 224501.
(112) Lu, X.; Cui, Q. Charging Free Energy Calculations Using the Generalized Solvent Boundary Potential (GSBP) and Periodic Boundary Condition: A Comparative Analysis Using Ion Solvation and Reduction Potential in Proteins. *J. Phys. Chem. B* **2013**, *117*, 2005−2018.
(113) Lin, Y. L.; Aleksandrov, A.; Simonson, T.; Roux, B. An Overview of Electrostatic Free Energy Computations for Solutions and Proteins. *J. Chem. Theory Comput.* **2014**, *10*, 2690−2709.
(114) Lide, D. R., Ed. *CRC Handbook Chemistry and Physics*, 85th ed.; CRC Press: Boca Raton, FL, 2005.
(115) Li, H.; Webb, S. P.; Ivanic, J.; Jensen, J. H. Determinants of the Relative Reduction Potentials of Type-1 Copper Sites in Proteins. *J. Am. Chem. Soc.* **2004**, *126*, 8010−8019.
(116) Olsson, M. H. M.; Ryde, U.; Roos, B. O. Quantum Chemical Calculations of the Reorganization Energy of Blue-copper Proteins. *Protein Sci.* **1998**, *7*, 2659−2668.
(117) Frank, P.; Benfatto, M.; Hedman, B.; Hodgson, K. O. Solution [Cu(amm)]2+ is a Strongly Solvated Square Pyramid: A Full Account of the Copper K-edge XAS Spectrum Within Single-Electron Theory. *Inorg. Chem.* **2008**, *47*, 4126−4139.
(118) Choi, M.; Davidson, V. L. Cupredoxins - A Study of How Proteins May Evolve to Use Metals for Bioenergetic Processes. *Metallomics* **2011**, *3*, 140−151.
(119) Solomon, E. I.; Hadt, R. G. Recent Advances in Understanding Blue Copper Proteins. *Coord. Chem. Rev.* **2011**, *255*, 774−789.
(120) Hadt, R. G.; Sun, N.; Marshall, N. M.; Hodgson, K. O.; Hedman, B.; Lu, Y.; Solomon, E. Spectroscopic and DFT Studies of Second-Sphere Variants of the Type 1 Copper Site in Azurin: Covalent and Non-local Electrostatic Contributions to Reduction Potentials. *J. Am. Chem. Soc.* **2012**, *134*, 16701−16716.
(121) Warren, J. J.; Lancaster, K. M.; Richards, J. H.; Gray, H. B. Inner- and Outer-Sphere Metal Coordination in Blue Copper Proteins. *J. Inorg. Biochem.* **2012**, *115*, 119−126.
(122) Olsson, M. H. M.; Hong, G.; Warshel, A. Frozen Density Functional Free Energy Simulations of Redox Proteins: Computational Studies of the Reduction Potential of Plastocyanin and Rusticyanin. *J. Am. Chem. Soc.* **2003**, *125*, 5025−5039.
(123) van den Bosch, M.; Swart, M.; Snijdes, J. G.; Berendsen, H. J. C.; Mark, A. E.; Oostenbrink, C.; van Gunsteren, W. F.; Canters, G. W. Calculation of the Redox Potential of the Protein Azurin and Some Mutants. *ChemBioChem* **2005**, *6*, 738−746.
(124) Cascella, M.; Magistrato, A.; Tavernelli, I.; Carloni, P.; Rothlisberger, U. Role of Protein Frame and Solvent for the Redox Properties of Azurin from Pseudomonas aeruginosa. *Proc. Natl. Acad. Sci. U. S. A.* **2006**, *103*, 19641−19646.
(125) Canters, G. W.; Kolczak, U.; Armstrong, F.; Jeuken, L. J. C.; Camba, R.; Sola, M. The Effect of pH and Ligand Exchange on the Redox Properties of Blue Copper Proteins. *Faraday Discuss.* **2000**, *116*, 205−220.
(126) Hulsker, R.; Mery, A.; Thomassen, E. A.; Ranieri, A.; Sola, M.; Verbeet, M. P.; Kohzuma, T.; Ubbink, M. Protonation of a Histidine Copper Ligand in Fern Plastocyanin. *J. Am. Chem. Soc.* **2007**, *129*, 4423−4429.
(127) Kaminski, S.; Giese, T. J.; Gaus, M.; York, D. M.; Elstner, M. Extended Polarization in Third-order SCC-DFTB from Chemical-Potential Equalization. *J. Phys. Chem. A* **2012**, *116*, 9131−9141.
(128) Giese, T. J.; York, D. M. Density-Functional Expansion Methods: Grand Challenges. *Theor. Chem. Acc.* **2012**, *131*, 1−17.
(129) Christensen, A. S.; Elster, M.; Cui, Q. Improving Intermolecular Interactions in DFTB3 Using Extended Polarization from Chemical-Potential Equalization. *J. Chem. Phys.* **2015**, *143*, 084123.
(130) Crane, B. R.; Di Bilio, A. J.; Winkler, J. R.; Gray, H. B. Electron Tunneling in Single Crystals of *Pseudomonas aeruginosa* Azurins. *J. Am. Chem. Soc.* **2001**, *123*, 11623−11631.
(131) Riccardi, D.; Cui, Q. pK_a Analysis for the Zinc-bound Water in Human Carbonic Anhydrase II: Benchmark for "Multi-scale" QM/MM Simulations and Mechanistic Implications. *J. Phys. Chem. A* **2007**, *111*, 5703−5711.
(132) Ghosh, N.; Cui, Q. pK_a of Residue 66 in *Staphylococal nuclease*: Insights from QM/MM Simulations with Conventional Sampling. *J. Phys. Chem. B* **2008**, *112*, 8387−8397.
(133) Gaus, M.; Goyal, P.; Hou, G.; Lu, X.; Pang, X.; Zienau, J.; Xu, X.; Elstner, M.; Cui, Q. In *Molecular Modeling at the Atomic Scale: Methods and Applications in Quantitative Biology*; Zhou, R. H., Ed.; Springer: Berlin, 2014; Chapter Toward Quantitative Analysis of Metalloenzyme Function using MM and Hybrid QM/MM Methods: Challenges, Methods and Recent Applications, p 33.

DOI: 10.1021/acs.jpcb.5b09656
J. Phys. Chem. B 2016, 120, 1894−1910

Supporting Info: Copper Oxidation/Reduction in Water and Protein: Studies with DFTB3/MM and VALBOND Molecular Dynamics Simulations

Haiyun Jin,[†] Puja Goyal,[†] Akshaya Kumar Das,[‡] Michael Gaus,[†] Markus Meuwly,[*,‡] and Qiang Cui[*,†]

[†]*Department of Chemistry, University of Wisconsin-Madison, 1101 University Avenue, Madison, WI 53706, USA*

[‡]*Department of Chemistry, University of Basel, Klingelbergstrasse 80, 4056 Basel, Switzerland*

E-mail: m.meuwly@unibas.ch; cui@chem.wisc.edu

1 Additional results for aqueous copper ion simulations

1.1 Polarizable MM water model

To investigate the effect of including explicit polarization in the MM environment in DFTB3/MM simulations, the SWM4-NDP water model[1] is used. As shown in Fig. S1a, DFTB3/TIP3P and DFTB3/SWM4-NDP simulations give almost identical radial distributions of water oxygen near the Cu(II) ion; small differences are observed for the second solvation shell. Similarly, the angular distributions of water molecules (defined in terms of the angle formed between the dipole vector of water and the Cu-O vector, see Fig. S1b) indicate that the

orientations of water in the first solvation shell are still highly similar in the two simulations; for the second solvation shell, however, notable differences are observed.

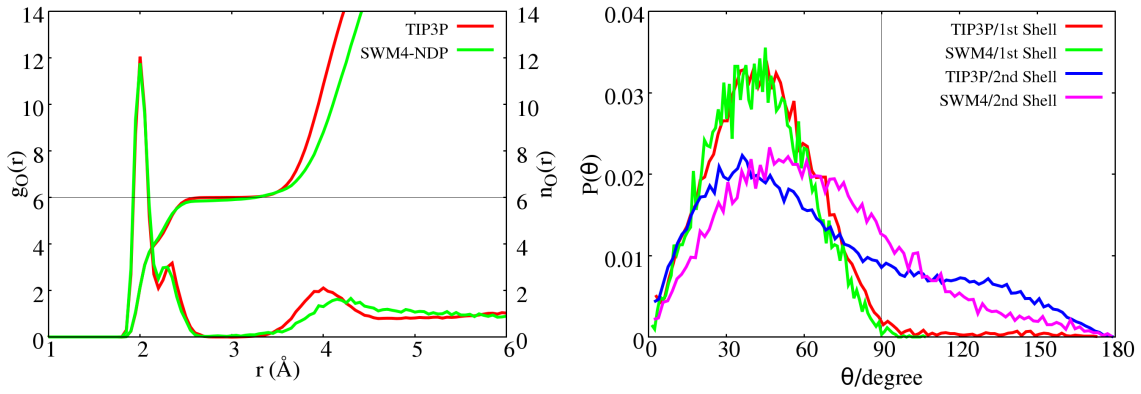

(a) (b)

Figure S1: Comparison of DFTB3/TIP3P and DFTB3/SWM4-NDP simulations of a Cu^{2+} ion in solution. (a) Radial distribution function of water oxygen around the Cu^{2+} ion; (b) Angular distributions for the first and second solvation shells for Cu^{2+}.

1.2 Treating both solvation shells with QM

A larger QM region that includes the second solvation shell is also tested for DFTB3/MM simulations. As shown in Fig. S2a for Cu^{2+}, the main impact of enlarging the QM region on the water radial distribution is that the second solvation shell becomes boarder and includes more water molecules within 4 Å from the copper. The angular distributions of water (Fig. S2b) also indicate that the peak orientations of water in the first solvation shell shifts from 40° to 50°. To test the impact of the QM description of water, we also run DFTB3/MM calculations using the 3OBw model, which has been adjusted to give the proper structure of bulk water at the ambient condition.[2] As shown in Fig. S2c-d, the general trends regarding the dependence on the QM size are similar to those observed with the 3OB model; the second solvation shell from the 6-QM-water and 21-QM-water simulations has smaller difference, which is likely due to the improved distribution of water structure by 3OBw.

For Cu(I), as shown in Fig. 3 in the main text and Fig. S3a, the solvation structure,

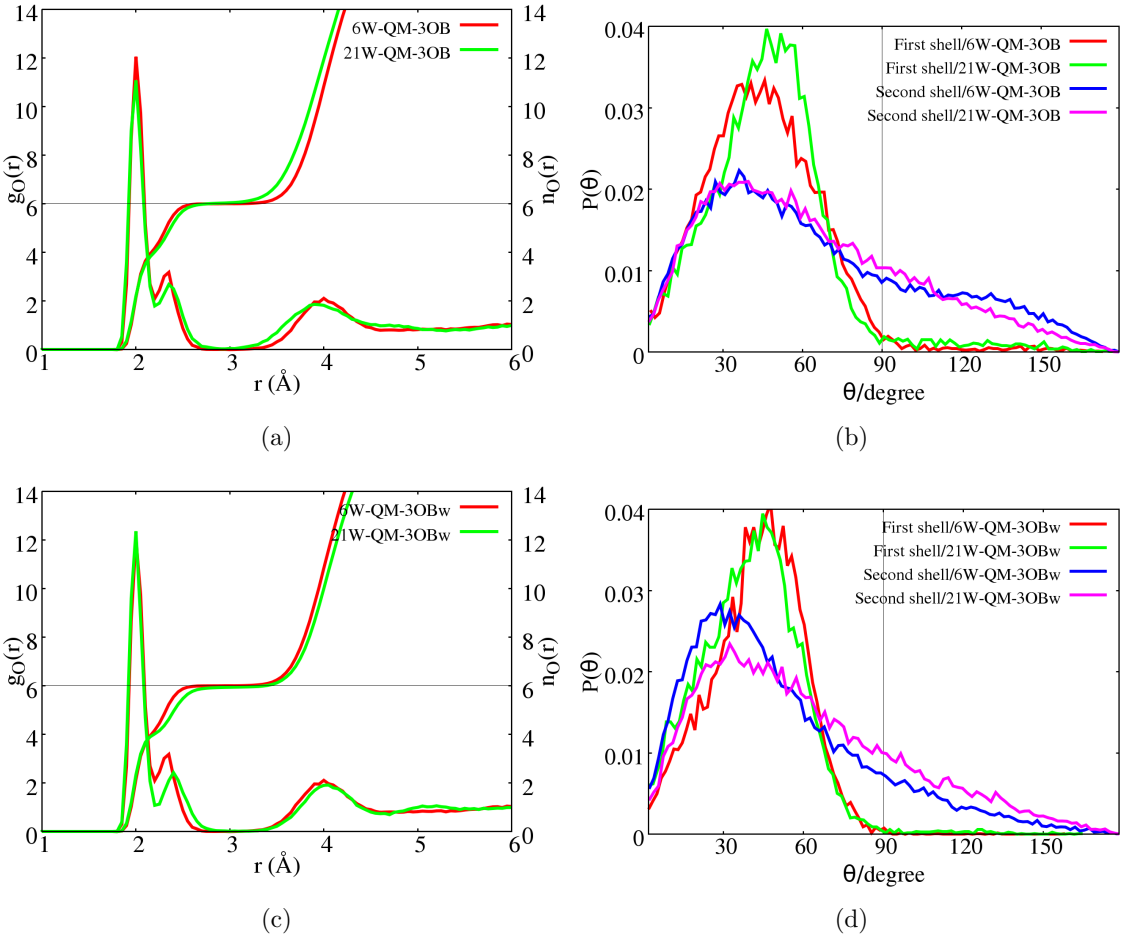

Figure S2: Comparison of DFTB3/TIP3P simulations of a Cu^{2+} ion in solution with different QM regions. (a) Radial distribution function of water oxygen around the Cu^{2+} ion; (b) Angular distribution for the first and second solvation shell for Cu^{2+}. (c-d) Similar properties as (a-b), but using the DFTB3/3OBw[2] model for the QM water.

especially the second solvation shell, is more sensitive to the QM region size. Part of the dependence is likely due to the difference in water structure between DFTB3/3OB and TIP3P; indeed, with the 3OBw model (Fig. S3b), the second solvation shell depends less on the QM size. Another factor is the FIRES approach we have adopted for the QM/MM partitioning; since the FIRES approach is formulated based on radial distances, it works well for a QM region of spherical shape (e.g., the first solvation shell of Cu(II)) but is not ideal for a QM region with a significant degree of asymmetry. With DFTB3/MM, Cu(I) is featured with two strongly bound water and then a few weakly bound water molecules further away. Therefore, for certain number of QM waters, the QM region has a notable degree of asymmetry; in those cases, the FIRES potential prevents MM water molecules from fully participating the second solvation shell, leading to different second-shell radial distribution functions shown in Fig. S3a-b. Therefore, we generally recommend choosing the QM region such that the solvent molecules distribute symmetrically.

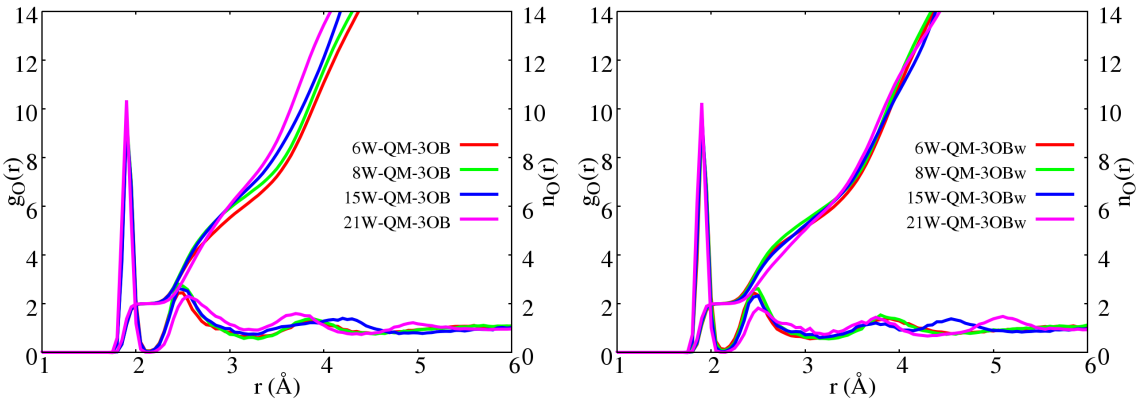

(a) (b)

Figure S3: Comparison of DFTB3/TIP3P simulations of a Cu^+ ion in solution with different numbers of water molecules in the QM region. Radial distribution function of water oxygen around the Cu^+ ion is plotted. The 3OB and 3OBw[2] models are used in (a) and (b), respectively, for the QM water molecules.

1.3 BLYP solvation structure for Cu^{2+}

As discussed in the main text, the five-coordinated Cu^{2+} solvation is observed in neutron diffraction and X-ray scattering experiment and all previous CPMD and BOMD simulations. Most CPMD/BOMD simulations used the BLYP[3,4] functional, though with different basis sets or pseudo potentials. As a comparison, we conduct BLYP/MM simulations on a solvated Cu(II) ion; the basis set used is the same as in B3LYP/MM simulations. As shown in Fig. S4, the BLYP/TIP3P radial distribution overlaps well with the CPMD results and gives a five-coordinated first solvation shell structure with 4 closely bound water at 2.05 Å and one at 2.20 Å. Although we start with a hexacoordinated Cu(II), one of the six water in the first solvation shell diffuses away from the copper ion during the simulation, regardless of the MM model for water (SWM4, TIP3P) (see Fig. S5a-b; compare to the behaviors from B3LYP/MM and DFTB3/MM simulations shown in Fig. S5c-d). As discussed in the main text, this is likely related to the observation that BLYP underestimates the binding affinity of the sixth water to the Cu(II) center in gas phase models.

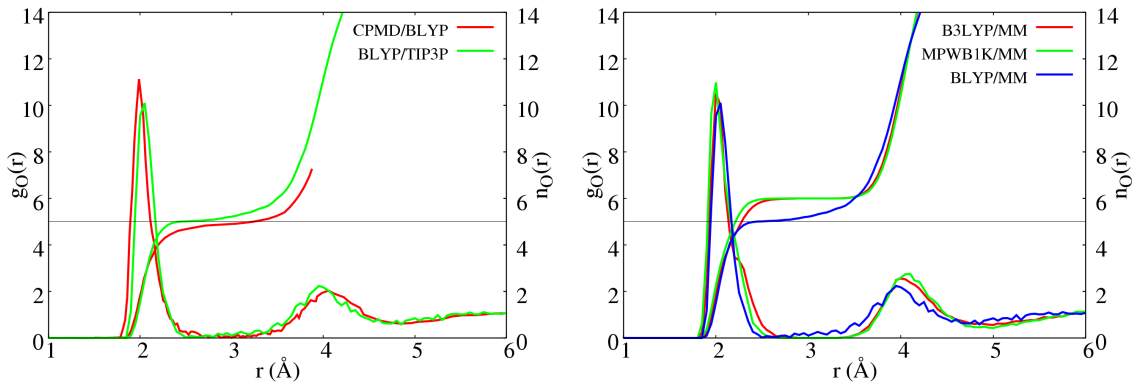

(a) (b)

Figure S4: Radial distribution function of water oxygen around the Cu^{2+} ion obtained from different QM/MM simulations in comparison with previous CPMD/BLYP result.[5]

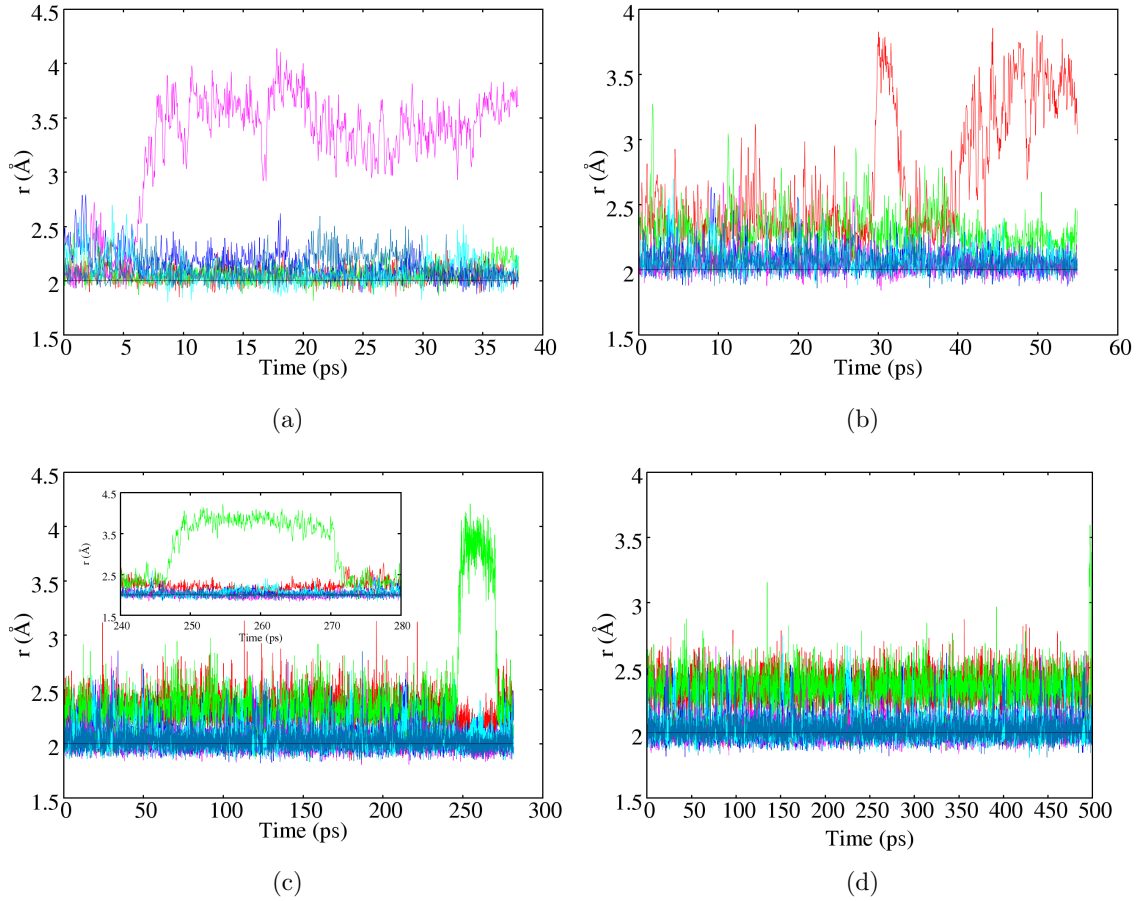

Figure S5: Distance between Cu(II) and QM water oxygen in (a) BLYP/SWM4-NDP, (b) BLYP/TIP3P, (c) B3LYP/TIP3P and (d) DFTB3/TIP3P simulations.

1.4 Effect of cutoff schemes

As discussed in our previous work,[6,7] cutoff schemes in QM/MM simulations have to be carefully chosen to avoid unbalanced QM-MM and MM-MM interactions. In our implementation, QM atoms interact with all MM atoms, thus in principle MM-MM interactions should not be cut off either. In practice, an extended electrostatic model for MM-MM interactions works well; this is what we use in GSBP based simulations; for PBC, PME for MM-MM interactions is also appropriate. Here we again illustrate artifacts that might arise from using other popular cut-off schemes for MM-MM interactions. For example, when not using PME, the default set up in the CHARMM force field is to cut off both electrostatic and van de Waals interaction beyond 12 Å. The cut-off scheme[8] can be energy or force based, and uses either a shift scheme to set the potential energy or force to zero at 12 Å, or a switch scheme that multiplies a smooth switching function with the original potential. We have tested several popular combinations of non-bonded schemes and the results are summarized below. Although the different non-bonded cutoff schemes have very similar water radial distributions (Fig. S6), they lead to rather different angular distributions (see Fig. S7). The force shift scheme in electrostatic interactions behaves most differently compared to the other schemes, and the result has a huge impact on the computed reduction potential (Table S1); the results with force-switch and energy-shift schemes are much closer to those based on extended electrostatics, although there are also notable differences. Therefore, we again recommend the use of extended electrostatics for non-PBC simulations.

1.5 Gas phase structure optimization

To understand the intrinsic limitations of different functionals and effects of basis sets, the structure of $Cu(H_2O)_6{}^{2+}$, $Cu(H_2O)_5{}^{2+}$, $Cu(H_2O)_4{}^{+}$ and $Cu(H_2O)_2{}^{+}$ are calculated with a series of methods and the results are summarized in Tables S3 to S2 (also see Table 2 in

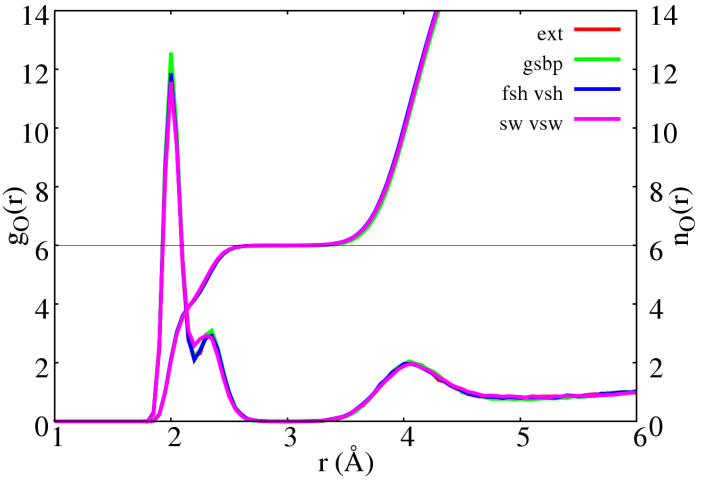

Figure S6: Radial distribution function of water oxygen around Cu^{2+} in DFTB3/MM simulations with different cutoff schemes for MM electrostatics (see footnote of Table S1 for notation).

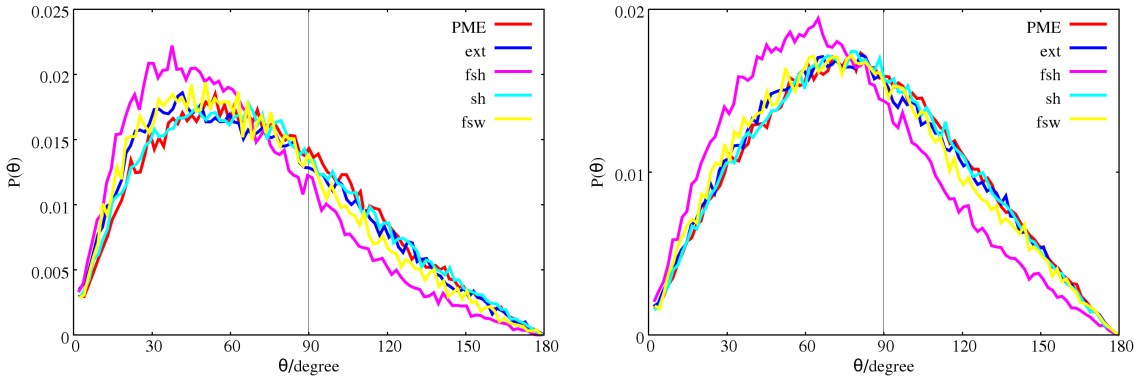

(a) (b)

Figure S7: Angular distribution of water molecules between 4∼6 Å (left) and 6∼8 Å (right) from the Cu^{2+} ion in DFTB3/MM simulations with different cutoff schemes for MM electrostatics (see footnote of Table S1 for notation). In PBC simulations, the Particle-Mesh-Ewald (PME) approach is used; the other cutoff schemes are for Stochastic Boundary Condition (SBC) simulations.

Table S1: Energy gap and reduction free energy (in kcal/mol) from DFTB3/MM simulations with different cutoff schemes for MM electrostatics in Stochastic Boundary Condition simulations [a]

Scheme	$< \Delta U >_{\lambda=0}$	$< \Delta U >_{\lambda=1}$	ΔF_{red} [b]
Atom fsh vsh	+36.1 (0.2)	–162.1 (0.2)	–30.3
Atom fsw vsh	–35.1 (0.6)	–200.4 (1.0)	–87.1
Atom sh vsw	–62.1 (0.1)	–211.8 (0.2)	–106.2
Extended vsw	–69.1 (0.2)	–222.5 (0.3)	–115.1
Extended vsh	–68.7 (0.2)	–222.2 (0.4)	–114.8
Experiment[9]			–106.1

[a] Atom: Atom based cutoff; Extended: Extended electrostatics. fsh: force-shift; fsw: force-switch for electrostatics; sh: energy-shift for electrostatics; sw: energy-switch for electrostatics. vsh: energy-based shift for van der Waals; vsw: energy-based switch for van der Waals. [b] After a Born correction of +30.70 kcal/mol.

the main text). For Cu(II), the structures from all calculations are generally very similar to each other: all methods lead to hexa-coordination with the two axial ligands about 0.3 Å further away than the equatorial ligands, and the main difference between various methods lies in the Cu-O distance of the two axial ligands. The longest distance is found with DFTB3 (2.339 Å) and the shortest with B3LYP and a small basis set (2.247 Å).

For Cu(I), larger differences among different methods are observed, most notably for $Cu(H_2O)_4^+$. B3LYP with all basis sets optimize the system to a tetrahedron type of structure (Fig. S8a) with the shorter set of Cu-O bond distances around 2.0∼2.1 Å and the longer set 2.2∼2.3 Å. In fact, for both Cu(I) and Cu(II), we note that the B3LYP results do not depend much on the basis, supporting the use of lanl2dz/6-31G(d) in QM/MM calculations reported in the main text. By contrast, BLYP results show much more significant dependence on the basis set. BLYP/Lanl2dz/6-31G(d) agrees better with the B3LYP results (Fig. S8b), while BLYP/6-31G(d) or 6-31+G(d,p) has difficulties in maintaining the tetrahedron coordination and favors having only two water directly bound to the copper ion (Fig. S8c). Interestingly, the result of DFTB3 lies in between: it leads to two short (1.9 Å) Cu-O bonds and two longer (2.5 Å) bonds (Fig. S8d). With all methods tested, the symmetric two-coordinated species stabilized by two additional water (Fig. S8e) is the global minimum for $Cu(H_2O)_4^+$.

The relative stability of four-coordinated and symmetric two-coordinated structures (Table S3), however, varies; for example, DFTB3 favors the two-coordinated species by almost 10 kcal/mol, while B3LYP/Lanl2dz/6-31G(d) is fortuitously close to CCSD(T)/aug-cc-pVTZ and gives a value $\sim$ 5 kcal/mol. This explains why the two-coordinated is still favored by DFTB3/MM in the condensed phase while the four-coordinated species takes over in B3LYP/MM simulations.

Table S2: Geometrical properties of $[Cu(I/II)(H_2O)_n]^{+/2+}$ optimized by various methods in the gas phase[a]

Method[b]	r_{CuO}	$r_{CuO'}$	$r_{CuO''}$	$r_{CuO'''}$	$\angle_{OCuO}$
$[Cu(II)(H_2O)_5]^{2+}$					
B3LYP/6-31+G(d,p)	1.98	2.02	2.20		
BLYP/6-31+G(d,p)	2.02	2.05	2.24		
PBE/6-31+G(d,p)	2.00	2.02	2.22		
$[Cu(II)(H_2O)_6]^{2+}$					
B3LYP/6-31+G(d,p)	2.02	2.31	–	–	90.0/180.0
BLYP/6-31+G(d,p)	2.03	2.36	–	–	90.0/180.0
PBE/6-31+G(d,p)	2.01	2.32	–	–	90.0/180.0
$[Cu(I)(H_2O)_2]^{+}$					
B3LYP/6-31+G(d,p)	1.90	–	–	–	180.0
BLYP/6-31+G(d,p)	1.90	–	–	–	180.0
PBE/6-31+G(d,p)	1.88	–	–	–	180.0
$[Cu(I)(H_2O)_4]^{+}$ [c]					
B3LYP/6-31+G(d,p)	2.02	2.11	2.22	2.26	140.6
BLYP/6-31+G(d,p)	1.87	1.92	3.47	3.69	180.0
PBE/6-31+G(d,p)	1.84	1.89	4.76	3.83	180.0

[a] Optimized at the respective levels; distances in Å, angles in degrees. Also see Fig. 4 in main context for the labels of relevant distances and angles. [b] See Table 2 in main context for results with additional basis sets. [c] Geometry optimization starts with a tetrahedron structure, for which some methods (BLYP/6-31+G(d,p) and PBE/6-31+G(d,p)) converge to the asymmetric two-coordinated species shown in Fig. S8c. For the symmetric two-coordinated structure, which is a local minimum for all methods studied here, see Fig. S8e.

1.6 Vertical reduction and oxidation energies in the gas phase

The vertical reduction and oxidation energies for various copper-water complexes are calculated and tabulated in Table S4 to gauge the magnitude of intrinsic errors in the DFTB3 and B3LYP calculations.

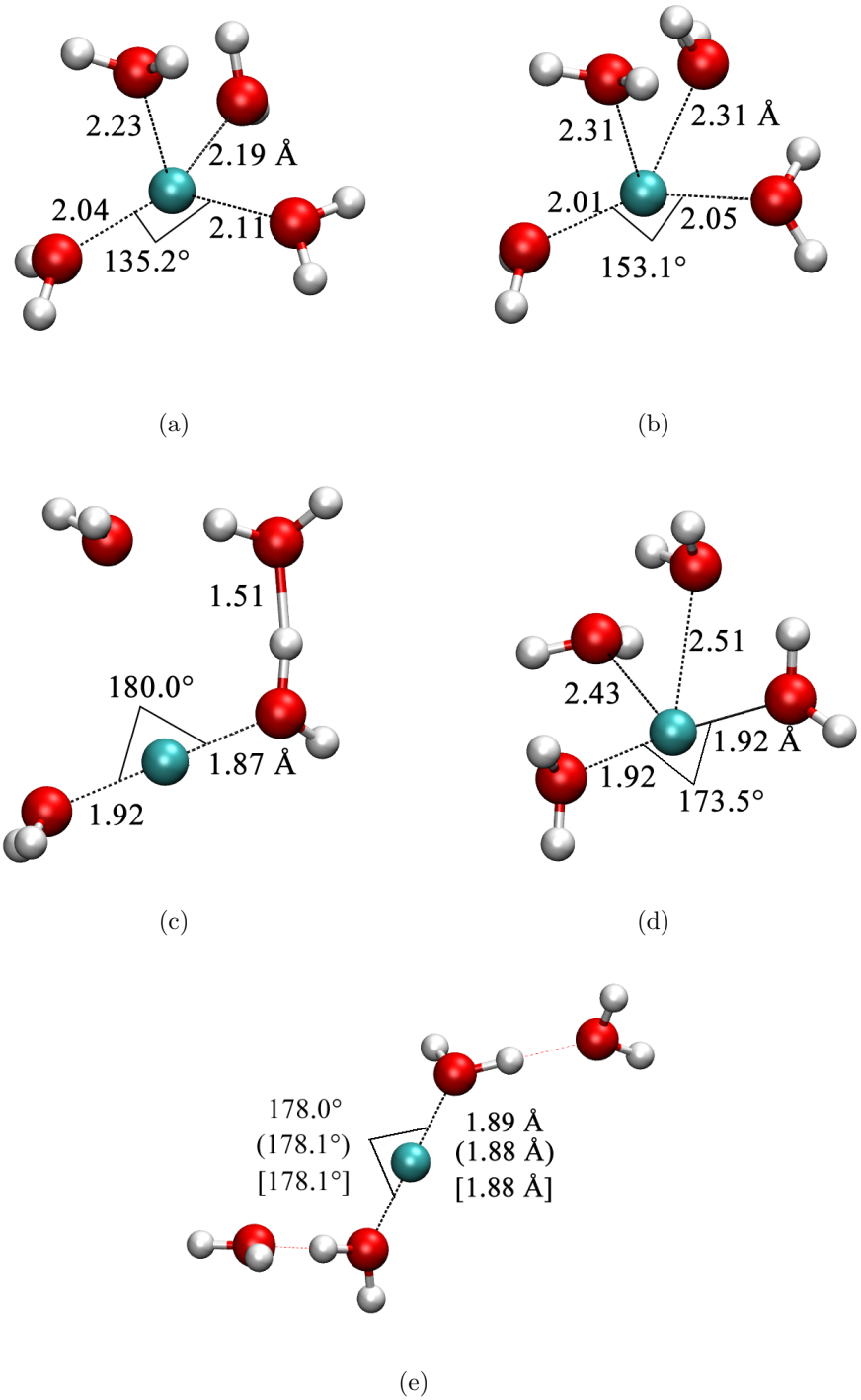

Figure S8: Four- and two-coordinated $[Cu(I)(H_2O)_4]^+$ structures (distances in Å, angles in degrees) optimized at different levels of theory. Optimizations in (a-d) start from the same initial tetrahedron structure. (a) B3LYP/aug-cc-pVTZ; (b) BLYP/Lanl2dz/6-31G(d); (c) BLYP/6-31+G(d,p); (d) DFTB3. (e) The symmetric two-coordinated structure at B3LYP/aug-cc-pVTZ, BLYP/Lanl2dz/6-31G(d) and DFTB3 levels. See Table S3 for energetics.

Table S3: Relative energy (kcal/mol) of four- and symmetric two-coordinated Cu(I)-water complexes at structures optimized by B3LYP/aug-cc-pVTZ in the gas phase[a]

Method	Basis set	Four-coordinated	Two-coordinated
DFTB3	-	0.0	-10.5
B3LYP	Lanl2dz/6-31G(d)	0.0	-4.0
B3LYP	6-31+G(d,p)	0.0	-9.5
B3LYP	aug-cc-pVTZ	0.0	-9.4
BLYP	Lanl2dz/6-31G(d)	0.0	-5.3
BLYP	6-31+G(d,p)	0.0	-11.6
PBE	6-31+G(d,p)	0.0	-10.7
CCSD(T)	aug-cc-pVTZ	0.0	-5.2

[a] See Fig. S8a and S8e for structures.

Table S4: Vertical reduction and oxidation energy (in kcal/mol) of copper-water complexes in the gas phase

System	CCSD(T)[a,c]	B3LYP[a]	B3LYP[b]	DFTB3[c]
Vertical reduction energy				
$[Cu(II)(H_2O)_2]^{2+}$	-349.9	-355.4	-357.0	-345.5
$[Cu(II)(H_2O)_4]^{2+}$	-261.5	-260.8	-261.9	-249.8
$[Cu(II)(H_2O)_6]^{2+}$	-225.8	-226.6	-221.5	-216.2
Vertical oxidation energy				
$[Cu(I)(H_2O)_2]^{+}$	+352.7	+366.2	+369.4	+347.6
$[Cu(I)(H_2O)_4]^{+}$	+299.2	+298.4	+299.3	+289.9
$[Cu(I)(H_2O)_6]^{+}$	+261.0	+260.2	+253.8	+248.1

[a] Basis set: aug-cc-pVTZ; [b] Basis set: lanl2dz/6-31G(d); [c] At B3LYP/aug-cc-pVTZ structures.

2 Free energy derivatives from DFTB3/MM simulations for Cu(II) reduction in water

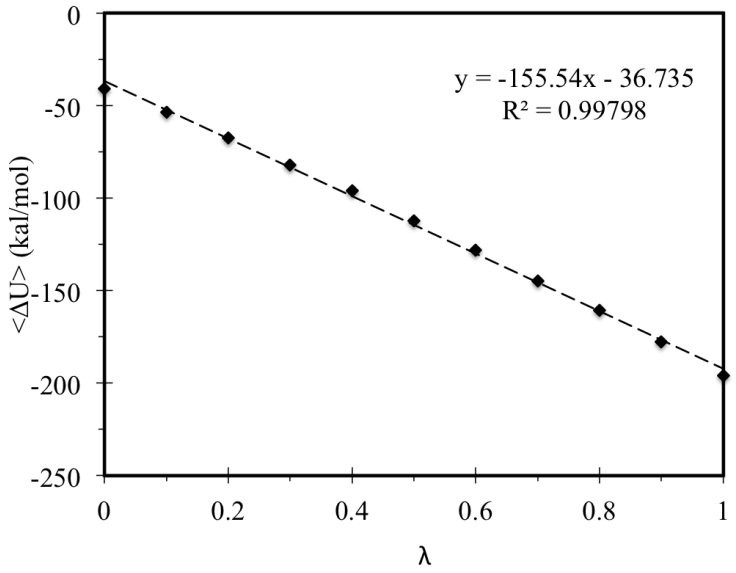

Figure S9: Free energy derivatives calculated with DFTB3/TIP3P for Cu(II) reduction in water. The derivatives depend linearly on the coupling parameter λ. The data are from GSBP simulations and include $\sim$ 500 ps production run per λ window.

3 Additional results for copper tetra-ammonia simulations

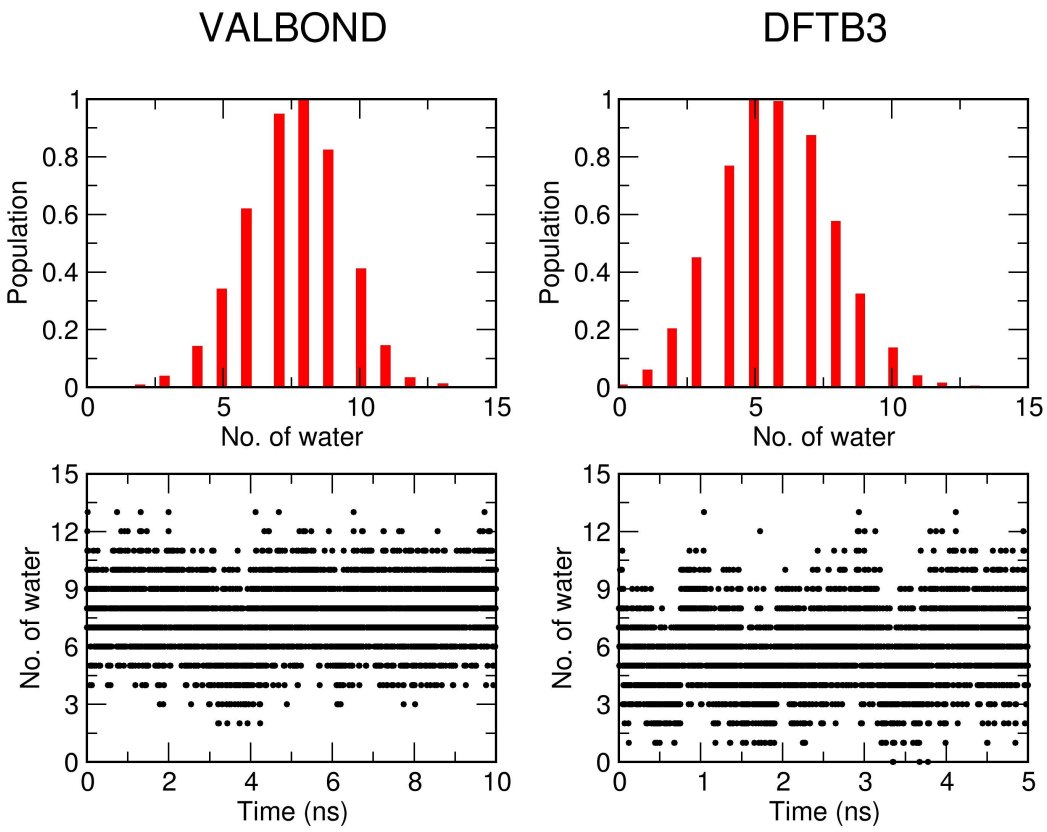

Figure S10: Distribution of water molecules around Cu(I) at a distance of 4.5 Å obtained from the equilibrium simulation of 10 ns using VALBOND (left panel) and 5 ns using DFTB3/MM (right panel) are shown here.

The effect of the partial charge on the copper ion (with concomitant adjustment on the bonded nitrogen atoms to ensure neutrality of the complex) on the $g_{\mathrm{O-Cu}}(r)$ for VALBOND simulation is tested by sampling a range of values for the Cu(II) partial charge. As shown in Fig. S11, a value of $+0.58e$ on the copper leads to the $g_{\mathrm{O-Cu}}(r)$ reasonably close to that from B3LYP/MM and DFTB3/MM (Fig. 7 in the main text) simulations. The value of +0.58 is fairly close to the Mulliken charge on Cu (+0.60) in $[\mathrm{Cu(II)(NH_3)_4(H_2O)_2}]^{2+}$ at the B3LYP level. These observations support the discussion in the main text that the

VALBOND model using an integer charge for the copper ion tends to overestimate the interaction between copper and nearby water molecules.

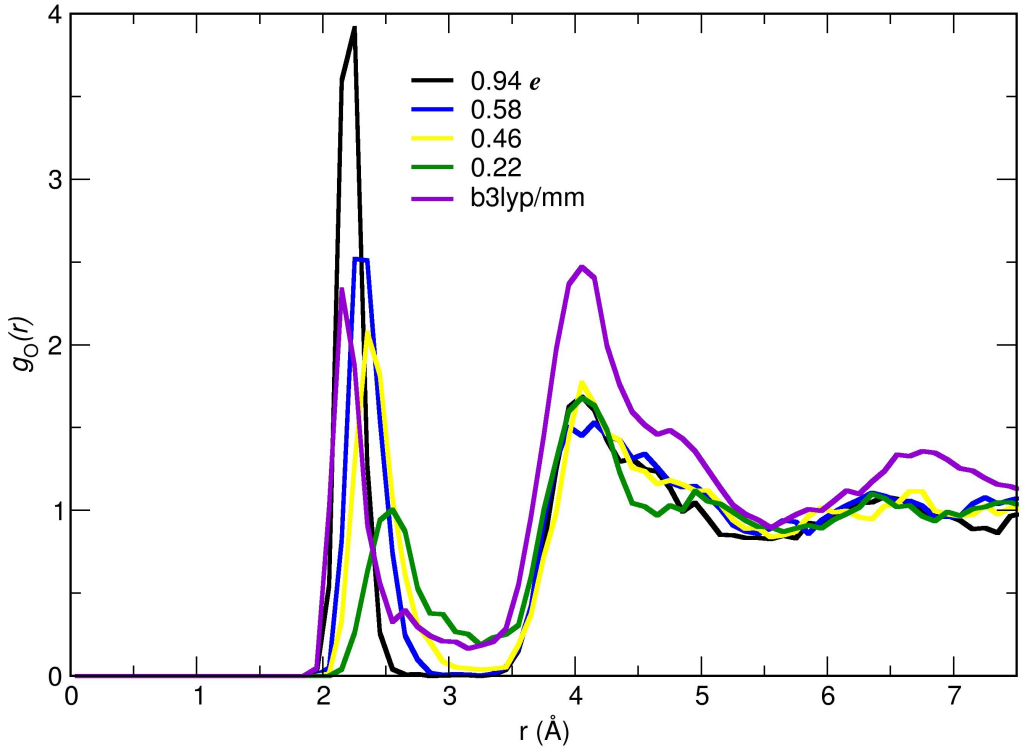

Figure S11: $g_{\mathrm{O-Cu}}(r)$ for Cu(II) with different charges on the Cu obtained from the VALBOND simulation for $[\mathrm{Cu(II)(NH_3)_4}]^{2+}$ in water.

4 Additional results for plastocyanin

Table S5: Free energy derivatives, reduction potential (ΔF_{red}), reorganization energy (Λ) and Statistical analysis of thermodynamic integration simulations for plastocyanin at pH 7[a]

	GSBP		PBC	
λ	Set 1	Set 2	Set 1	Set 2
0.0	-67.0(0.2)	-65.9(0.3)	-88.8(0.6)	-84.9(0.4)
0.2	-79.0(0.7)	-82.0(0.6)	-102.1(0.2)	-99.7(0.4)
0.4	-94.0(0.2)	-88.4(0.2)	-114.4(0.3)	-112.3(0.3)
0.6	-101.8(0.9)	-101.1(0.3)	-125.9(0.2)	-124.3(0.3)
0.8	-115.4(0.6)	-112.5(0.1)	-134.8(0.2)	-134.5(0.2)
1.0	-121.2(0.7)	-123.4(0.3)	-145.8(0.2)	-150.5(0.3)
ΔF_{red} [b]	-96.4(0.99)	-95.6(0.99)	-118.6(1.00)	-117.8(1.00)
Λ [c]	1.18	1.25	1.24	1.42

	GSBP				PBC			
	Set 1		Set 2		Set 1		Set 2	
λ	prod(equ)[d]	τ(n)[d]	prod(equ)	τ(n)	prod(equ)	τ(n)	prod(equ)	τ(n)
0.0	2.800(2.182)	1(552)	2.800(2.346)	2(270)	2.515(0.816)	26(66)	2.514(2.071)	3(145)
0.2	2.800(1.353)	43(34)	2.800(2.330)	16(30)	1.734(0.563)	3(416)	1.735(1.071)	5(127)
0.4	2.800(1.714)	2(528)	2.800(1.892)	1(797)	1.733(1.397)	1(318)	1.733(1.348)	2(251)
0.6	2.800(1.954)	38(23)	2.800(1.741)	3(318)	1.800(0.393)	3(522)	1.800(0.261)	7(233)
0.8	2.800(1.422)	65(22)	2.800(1.067)	2(985)	1.800(0.780)	2(468)	1.800(1.283)	2(285)
1.0	2.800(2.714)	2(36)	2.800(1.963)	5(155)	2.444(1.252)	3(378)	2.512(1.567)	4(269)

[a] The free energy derivatives are given in kcal/mol, and the values in parentheses are statistical errors. No smooth boundary or net-charge correction is applied to the GSBP and PBC free energy derivatives. [b] Computed (in kcal/mol) on the basis of the linear fit of the free energy derivatives vs. λ and subsequent integration over λ; the values in parentheses are the R^2 values for the linear fit. [c] Reorganization energy in eV. [d] Statistical analysis: prod(equ) gives the total amount of simulation time (in nanoseconds) and the segment identified as equilibration (in parentheses). τ gives the size of the block (in picoseconds), and n gives the total number of blocks in the final free energy derivative calculations.

References

(1) Lamoureux, G.; Harder, E.; Vorobyov, I. V.; Roux, B.; MacKerell Jr., A. D. A Polarizable Model of Water for Molecular Dynamics Simulations of Biomolecules. *Chem. Phys. Lett.* **2006**, *418*, 245 – 249.

(2) Goyal, P.; Qian, H. J.; Irle, S.; Lu, X.; Roston, D.; Mori, T.; Elstner, M.; Cui, Q. *Feature Article*: Molecular Simulation of Water and Hydration Effects in Different Environments: Challenges and Developments for DFTB Based Models. *J. Phys. Chem. B* **2014**, *118*, 11007–11027.

(3) Becke, A. D. Density-Functional Exchange-Energy Approximation with Correct Asymptotic Behavior. *J. Chem. Phys.* **1988**, *38*, 3098–3100.

(4) Lee, C.; Yang, W.; Parr, R. G. Development of the Colle-Salvetti Correlation-Energy Formula into a Functional of the Electron Density. *Phys. Rev. B* **1988**, *37*, 785–789.

(5) Pasquarello, A.; Petri, I.; Salmon, P. S.; Parisel, O.; Car, R.; Tóth, É.; Powell, D. H.; Fischer, H. E.; Helm, L.; Merbach, A. E. First Solvation Shell of the Cu(II) Aqua Ion: Evidence for Five-fold Coordination. *Science* **2001**, *291*, 856–859.

(6) Schaefer, P.; Riccardi, D.; Cui, Q. Reliable Treatment of Electrostatics in Combined QM/MM Simulation of Macromolecules. *J. Chem. Phys.* **2005**, *123*, Art. No. 014905.

(7) Riccardi, D.; Schaefer, P.; Cui, Q. pK_a Calculations in Solution and Proteins with QM/MM Free Energy Perturbation Simulations. *J. Phys. Chem. B* **2005**, *109*, 17715–17733.

(8) Steinbach, P. J.; Brooks, B. R. New Spherical-cutoff Methods for Long-range Forces in Macromolecular Simulation. *J. Comput. Chem.* **1994**, *15*, 667–683.

(9) Lide, D. R., Ed. *CRC Handbook Chemistry and Physics*, 85th ed.; CRC Press, 2005.

5. Multi-State VALBOND for Atomistic Simulations of Hypervalent Molecules, Metal Complexes and Reactions

5.1. Abstract

The implementation, validation and application of the Multi-State VALBOND (MS-VALBOND) method for transition metal-containing and hypervalent molecules is presented. This approach is particularly suited for molecules with unusual shapes and systems that need to be described by a superposition of resonance structures, each of which satisfies the octet rule. The implementation is based on the original VALBOND force field and allows to smoothly switch between resonance structures, each of which can be characterized by its own force field, including varying charge distributions, and coupling terms between the states. The implementation conserves total energy for simulations in the gas phase and in solution and is applied to a number of topical systems. For the small hypervalent molecule ClF_3 the barrier for pseudorotation is found to be 4.3 kcal/mol which compares favourable with the experimentally measured value of 4.8 kcal/mol. A transition metal-containing complex is cisplatin, characterized by 6 resonance states, for which the vibrational spectrum is found to be in good agreement with experiment. Finally, umbrella sampling simulations of the S_N2 reaction $BrMe + Cl^- \rightarrow Br^- + MeCl$ in solution yields a barrier height of 24.6 kcal/mol, in good agreement with experiment (24.7 kcal/mol).

5.2. Introduction

Atomistic simulations are a powerful means to investigate the structure and dynamics of complex systems, such as proteins in solution. Over the past 10 to 15 years the quality of such simulations has continuously improved not least due to the availability of increasingly accurate but empirical

energy functions. Initially, their development focused on the chemical structure and dynamics of macromolecules, including peptides and proteins[49–51,190–193]. More recently, considerable progress has been made by incorporating effects due to anisotropic charge distributions (multipolar electrostatics) and polarizability.[194–200] Such approaches have been very successful for applications in thermodynamics, computational spectroscopy or for investigating ligand binding to proteins.

However, when the complexity of the electronic structure of the compounds considered increases, as is the case for halogenated molecules or systems involving transition metals (TMs), even such more refined energy functions have their limitations. The situation is particularly demanding for metal-containing systems. Ideally, it would be possible to investigate the dynamics of such systems using mixed quantum mechanical/molecular mechanics molecular dynamics simulations (QM/MM MD).[201–203] In QM/MM the total system is divided into a (typically small) region for which the energy is calculated quantum mechanically - i.e. from electronic structure methods - and an environment which is treated with a conventional force field. However, due to the N^3 scaling of the secular determinants that need to be diagonalized, where N is the number of basis functions used in the QM part, routine applications can only be envisaged for systems including several tens of heavy atoms in the quantum region (fewer if metals are involved), and by using density functional theory (DFT) to describe the energetics. Typical simulation times that can be afforded under such circumstances are on the order of several 10 picoseconds which is usually too short for reactions with appreciable activation energies.[204] An exception to this are semiempirical quantum methods, such as density functional tight binding (DFTB)[38,178]

Hence, if the energetics and dynamics of reactive processes involving metals needs to be characterized, alternative methods to describe the energetics of the systems are required. Transition metals play important roles for processes including electron transport, oxidation reactions, or oxygen transport.[10–13] Also, metal complexes find broad applications for both homogeneous and heterogeneous catalysis in organic synthesis[7]. However, atomistic simulations using empirical force fields for metals in particular and hypervalent compounds in general pose particular challenges. The difficulty arises due to variable coordination number (as exemplified for $Co(CO)_4$, $Cr(CO)_5$, or $Cr(CO)_6$), indistinct topology (π ligands can bind to metal in different ways), the different oxidation states (eg. Cu(I) and Cu(II) shows tetrahedral and square planar geometries respectively)[38,205–207] and the coupling of electronic and

vibrational degrees of freedom (i.e. Jahn- Teller distortion).

In the past, several methods reminiscent of empirical force fields have been developed to treat transition metal complexes and organometallics. The main idea underlying metal force fields is to extend a conventional force field with one or several additional terms to capture specific properties of TMs. These include large angle distortions including bending potentials with several minima, the effects due to $d-$electrons (such as the Jahn-Teller effect) or binding of TMs to the $\pi-$electron cloud (as in ferrocenes). As an example, the difference in bonding of axial versus equatorial ligands to a TM can be described by two different parameter sets for the two types of ligands. On the other hand, such an effect can be captured within the framework of ligand field stabilization as it has been done in ligand field molecular mechanics (LFMM).[54] Such an approach is also capable of capturing stereo-electronic effects of partially filled *d*-orbitals in coordination compounds.

Alternatively, the VALBOND force field[55–58], which is based on valence bond theory and hybrid orbital strength functions, is able to describe the angular distortions for a wide range around the metal center. According to the VALBOND formalism[55–58], hypervalent molecules are molecules that exceed an octet electron count (e.g. ClF_3 or SF_6). Hypervalent molecules i.e. molecules where certain atoms have more than the formal 8 electrons, are treated by using resonance structures that formally fulfill the octet rule (or duodectet rule). For metal complexes which primarily use the *n*s and (*n*-1)d metal orbitals in forming bonds, electron counts in excess of 12 electrons are considered hypervalent.[208] Therefore, most common transition metal complexes are considered to be hypervalent and approaches such as VALBOND or VALBOND-TRANS are useful to follow the structural dynamics of TM-complexes[57–59]. In the original VALBOND formalism hypervalent molecules were represented by combinations of 2-center-2-electron and 3-center-4-electron bonds; in the localized framework 3-center-4-electrons comprise resonance among two primary Lewis-like configurations. This approach was successful for hypervalent first row molecules (such as ClF_3) as well as TM-complexes.[55–58] Originally, it was only an angle potential. Later it was extended to model the *trans*-influence in metal complexes by introducing two energy and distance dependent penalty functions to the original VALBOND and the method called VALBOND-TRANS[59].

Besides a structural characterization of metal complexes and the dynamics around them, studying chem-

ical reactions (with or without metals) is fundamental in chemistry and biology. Since chemical reactions involve breaking and making of chemical bonds, conventional force fields can not be used to simulate chemical reactions[76]. However, over the years several force field method such as reactive force field (ReaxFF)[76,77], empirical valence bond (EVB)[78], ARMD[79] and multi-state adiabatic reactive molecular dynamics (MS-ARMD)[80] have been developed to simulate chemical reactions. However, to the best of our knowledge no methods been developed to simulate metal complexes and chemical reactions together.

Here, we set out to generalize VALBOND[55–58] by developing a comprehensive framework approach based on resonance among structures that fulfill the octet rule. This new approach treats angular degrees of freedom within a valence bond description and further includes chemical bonds, dihedrals and van der Waals contributions by flexible parametrizations of individual resonance structures ("states"). The new method is referred to as multi-state VALBOND (MS-VALBOND). The MS-VALBOND method can also be used to simulate chemical reactions. This method also explicitly treats differences in charge distributions between the resonance structures/states. The method was implemented in CHARMM[50] and was tested by applying it to three different model cases including the hypervalent molecule ClF_3, a prototypical metal complex (cisplatin) and the chemical reaction of $BrMe + Cl^- \rightarrow Br^- + MeCl$.

5.3. Computational Methods

Two models of bonding in hypervalent molecules previously have been proposed: the original Pauling approach expanded the valency by using extravalent orbitals (*e.g.*, d-orbitals for main group elements) to accommodate electrons that exceed the octet. Alternatively, hypervalency has been described using an ionic resonance model in which linear arrangements of three atoms undergo three-center/four-electron (3c/4e) bonding. The latter model, which is supported by modern analyses of electronic structure[209], was originally presented in the context of MO theory by Pimentel[210] and Rundle[211]. However, Coulson[212] showed that the VB description involving resonance between octet-conforming configurations [Y: X-Y $\leftrightarrow$ Y-X :Y] essentially is equivalent to the MO density distribution. The dominance of such resonance structures is further supported by NBO analyses[208,213] and ab initio VB computations[214]. In the NBO framework, the 3c/4e bond corresponds to a donor-acceptor interaction comprising donation of a lone pair of electrons from Y into the X-Y antibond.

The present approach addresses several limitations of empirical force fields for hypervalent molecules in general and metal-containing complexes in particular. First, the angular terms AXB (where A and B are atoms of ligand and X is a metal or hypervalent center) are treated by VALBOND which enables description of geometries for the bending degrees of freedom around metal centers. Secondly, each relevant resonance structure is treated as a different connectivity ("state"). The total energy of the system is described by the Hamiltonian

$$H = \begin{bmatrix} H_{1\,1} & H_{1\,2} & \cdots & H_{1\,n} \\ H_{2\,1} & H_{2\,2} & \cdots & H_{2\,n} \\ \vdots & \vdots & \ddots & \vdots \\ H_{n\,1} & H_{n\,2} & \cdots & H_{n\,n} \end{bmatrix} \tag{5.1}$$

where the diagonal elements are the force fields of each connectivity/resonance structure H_{ii} and the off-diagonal elements are the couplings H_{ij} between them. This formulation is akin to an the empirical valence bond (EVB) ansatz.[78,215] For a single molecule this offers the opportunity to treat the same chemical bond with different parametrizations so that effects such as alteration between single, double or partial-double bonds of one and the same bond depending on the environment can be captured. This information would be available in the strength (force constant k) and equilibrium bond length r_e. It should also be possible to represent different oxidation states, e.g. Cu(I) and Cu(II)[38]. Furthermore, the trans-influence[59] (known from metal-complexes) which was incorporated in VALBOND-TRANS, can be readily included. This can be achieved through suitable parametrization of the off-diagonal elements which is described further below.

Diagonalization of **H** yields n eigenvalues and eigenvectors and the lowest eigenvalue E_0 with eigenvector $\vec{\nu_0} = (\nu_0^{(\mathrm{I})}, \nu_0^{(\mathrm{II})}, \nu_0^{(\mathrm{III})}, ..., \nu_0^{(\mathrm{N})})$ is used for propagation of the system.

$$E(\Psi_{tot}) = \langle \Psi_{tot} | H | \Psi_{tot} \rangle \tag{5.2}$$

The contribution of state i towards the ground state energy E_0 is $p_i = \nu_0^i \nu_0^i$. As all elements in **H** depend on internal coordinates, transitions between states along a trajectory can be followed by

considering the populations p_i of the states.

5.3.1. Parametrization of the Diagonal Elements

Each diagonal term describes a resonance structure. Thus each diagonal matrix element is treated and parametrized independently (see section 5.4.1). The diagonal element ($H_{i\,i}(\mathbf{X})$) represents the energy of the i^{th} resonance structure for a given configuration $\mathbf{X}$. Bonds which break and form or which change dissociation energy or equilibrium structure between the states are described by Morse bonds (see equation 5.3).

$$V_M(r) = D_e((1 - e^{-\beta(r-r_e)})^2 - 1) \tag{5.3}$$

In equation 5.3, r is the separation between the atoms in the bond, r_{e} is the equilibrium distance, D_{e} is the dissociation energy of the bond, and β describes the steepness of the short range part of the potential. Angles are described by the VALBOND formalism[55] which is rooted in valence bond theory.[70]

Similarly, following previous work[76], intramolecular van der Waals interactions are also described by Morse potentials but with small dissociation energy. This functional form has been shown to provide a better representation of the energy, especially at the short distances on the repulsive side of the energy function. Resonance structures for 3-center-4-electron bonds nearly always involve short separation in which distances (e.g., the $\text{F}_{\text{D}} - \text{Cl}_{\text{A}}$ distance in resonance structure I in Figure 5.1) are on the repulsive side of the non-bond potential. The non-bonded parameters of individual atoms were obtained by fitting Morse potential to the *ab initio* potential energy curve obtained along the Cl–He and F–He bond. Helium was used as a probe because it interacts negligibly with its environment and provides a meaningful starting point for further refinement of the parameters (see Figure 5.2). To describe the non-bonded interactions between non-identical atoms combination rules akin to the Lorentz-Berthelot rules are used: $D_{ij} = \frac{D_i + D_j}{2}$, $\beta_{ij} = \frac{\beta_i + \beta_j}{2}$ and $r^e{}_{ij} = \frac{r_i^e + r_j^e}{2}$. It would also be possible to represent the van der Waals interactions with a conventional 12-6 form or an exponential decay with a long-range dispersion term.

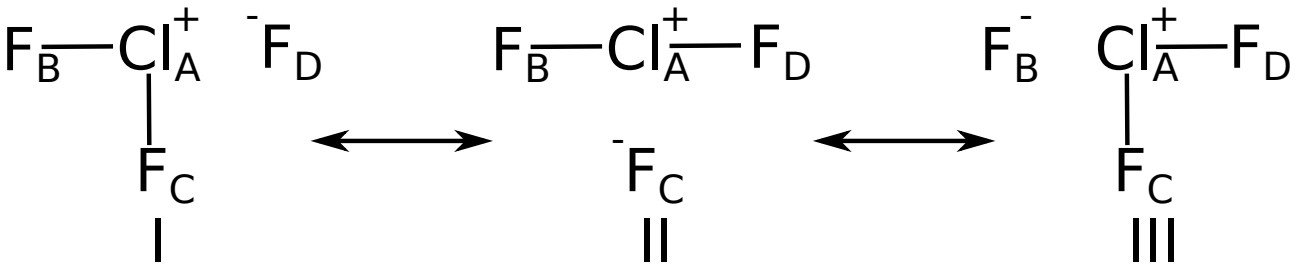

Figure 5.1.: The three resonance structures, I to III, for hypervalent ClF_3 such that each structure fulfills the octet rule. In resonance structure I, two fluorine atoms (F_B and F_C) form a bond to the Chlorine atom Cl_A to give octet-consistent ClF_2^+. The third atom, F_D, is the octet-consistent fluoride anion F^-.

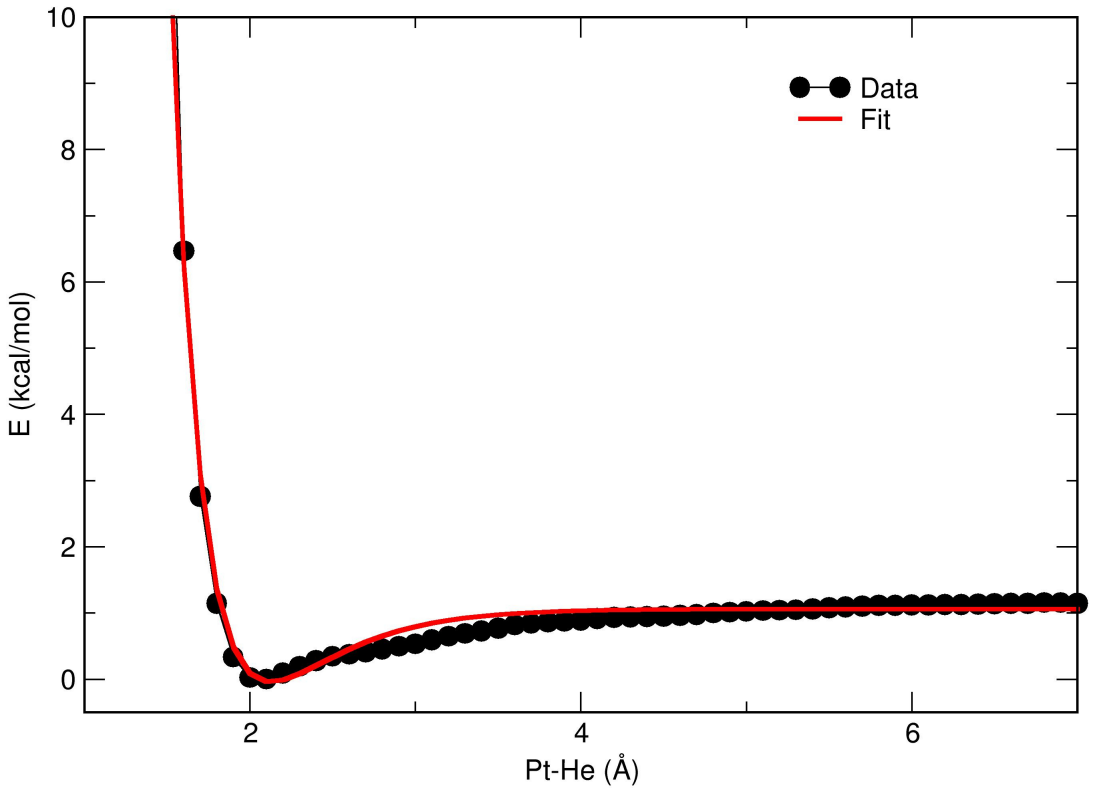

Figure 5.2.: Pt-He Morse potential energy curve for the Van der Waals parameters. This is the potential energy curve along the Pt-He bond obtained from the *ab initio* calculation the level of B3LYP/6-31G(d,p) except Pt (LANL2DZ basis) (black points) with fitted Morse potential (red line).

To illustrate the application of the formalism the example of ClF_3 is considered, see Figure 5.1. The number of bonds and resonance structures required to describe the system depends on the number of

valence electrons. To satisfy the octet rule one must only consider covalent i.e. 2-center-2-electron bonds. In ClF_3, three fluorine atoms are connected to the central chlorine atom. The chloride radical $Cl^{\bullet}$ and 3 fluorine radicals $F^{\bullet}$ contain 28 (4×7) electrons. The fully electron saturated (ionic) state formed by F^- and Cl^- would contain 32 electrons, hence 4 electrons are involved in bonding. Two electrons per covalent bond leads to $N = 2$ bonds per resonance structure. As a total of $K = 3$ bonds can be accommodated in ClF_3, there are $\binom{N}{K} = \binom{2}{3} = 3$ possible states (resonance structures) that need to be described, see Figure 5.1.

The force field description for resonance structure I consists of two bonds, which are represented each as a Morse potential with a set of fitted parameters and a VALBOND angle energy.

$$V(I) = V_M(r_{\mathrm{AB}}) + V_M(r_{\mathrm{AC}}) + V(\alpha_{\mathrm{BAC}}) \tag{5.4}$$

The angle α_{BAC} between these bonds with the atom A at its apex is treated using valence bond theory. Within valence bond theory, for central atom A with $sp^m d^n$ hybridization the energy depends only on the force constant k[70–72].

The angle α_{BAC} between these bonds with the atom A at its apex is treated using valence bond theory. Within valence bond theory, for central atom A with $sp^m d^n$ hybridization the energy depends only on the force constant k[70–72].

$$V(\alpha_{\mathrm{BAC}}, k, m, n) = k(S^{max} - S(\alpha)) \tag{5.5}$$

The general expression for the strength of hybrid orbitals S as derived by Pauling[72] is

$$S(\alpha) = S^{max}\sqrt{1 - \frac{1 - \sqrt{1 - \Delta^2}}{2}} \tag{5.6}$$

where S^{max} is the maximum of the strength function of hybrid orbitals and Δ is the overlap integral and their functional forms are given by

$$S^{max} = \sqrt{\frac{1}{1 + m + n}}(1 + \sqrt{3m} + \sqrt{5n}) \tag{5.7}$$

$$\Delta = \frac{1}{1+m+n}(1 + m\cos\alpha + \frac{n}{2}(3\cos^2\alpha - 1)) \tag{5.8}$$

In VALBOND, the overlap (Δ) between two hybrid (bond-)orbitals (ψ_1, ψ_2) is expressed as a function of the hybridizations m and n which are the formal p and d hybridizations. The force constant k can be chosen to best describe the bending frequency.

The nonbonded interactions in ClF_3 for resonance structure I (see Figure 5.1) are described by

$$V(r) = V_M(r_{\mathrm{AD}}; r_{\mathrm{e,AD}}, D_{\mathrm{e,AD}}, \beta_{\mathrm{AD}}) + \tag{5.9}$$

$$V_M(r_{\mathrm{BD}}; r_{\mathrm{e,BD}}, D_{\mathrm{e,BD}}, \beta_{\mathrm{BD}}) + \tag{5.10}$$

$$V_M(r_{\mathrm{CD}}; r_{\mathrm{e,CD}}, D_{\mathrm{e,CD}}, \beta_{\mathrm{CD}})$$

with cyclical permutations for the other two states II and III. The parameters for these diagonal matrix elements (2c-2e bonds) are fitted for the resonance structure, i.e. they are fitted for ClF_2^+ in the case of ClF_3.

5.3.2. Parametrization of the Off-Diagonal Elements

The off-diagonal terms describe the coupling between states i and j. Within the present context, these are stabilizations between two resonance structures. The resonance between structures i and j are modeled as a scaled Morse potential depending on the angle between the bonds that are modified upon resonance from one to another resonance structure (see Figure 5.3) according to

$$V(i \to j) = (\cos(\omega_{\mathrm{CAD}}) - 1)^2 * V_M(r_{\mathrm{AD}}) \tag{5.11}$$

The reverse resonance ($j \to i$) is modeled along the same line

$$V(j \to i) = (\cos(\omega_{\mathrm{CAD}}) - 1)^2 * V_M(r_{\mathrm{AC}}) \tag{5.12}$$

In order to maintain the symmetry of the Hamiltonian, the final off-diagonal element is

$$V_{ij} = V_{ji} = V(i \to j) + V(j \to i) \tag{5.13}$$

The off-diagonal Morse parameters are then fitted to reproduce reference electronic structure data, vide infra. Effects such as the trans influence[216] or Jahn-Teller distortion[217] (coupling of vibrational and electronic degrees of freedom) can be readily included by suitably parametrizing the off-diagonal elements that reflect these effects.

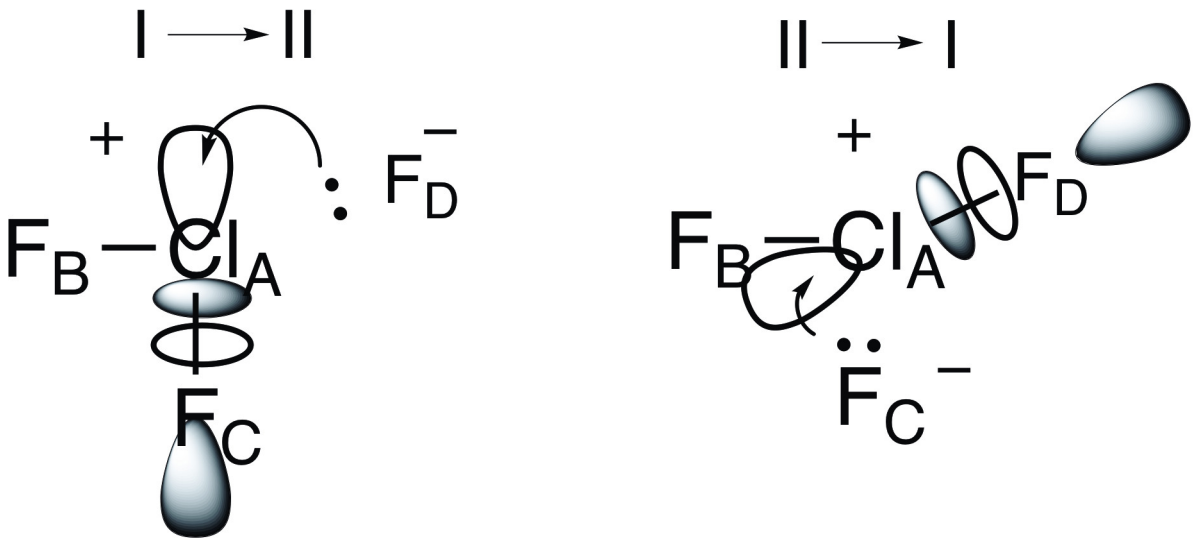

Figure 5.3.: Resonance structures I and II, comprising ionic $[BAC]^+$ D^- and $[BAD]^+$ C^- Lewis configurations, respectively, undergo resonance via donation:acceptor interaction of F^- lone pairs with vacant Cl-F anti bonds. For example, resonance structure I is transformed by donation of a lone pair on the anion F_D into the (Cl_A–F_C) anti-bond; such donor-acceptor interactions are the equivalent of "arrow-pushing" depictions of resonance. Shaded and empty circles indicate the lobes of the anti-bonding orbital and, for clarity, the molecular geometry shown is slightly distorted from the equilibrium T-shape. The strength of the donor-acceptor interaction depends on the overlap of donor and acceptor orbitals, hence, on the molecular geometry. At the geometry depicted above, the I→II overlap is substantially larger than the II→I overlap due to the more co-linear arrangement of the lone pair hybrid and the anti bonding orbital.

For ClF_3 the resonance between states i and j is modelled as the donation of the free electron pair into the anti-bonding orbital of the bond that is broken[208]. For the resonance between states I and II, the AC bond is broken while bond AD is formed. Considering p orbitals, the donation of the free electron pair from F_D into the anti-bond depends on the angle between the three atoms A, C, and D. Scaling of the off-diagonal term (see Figure 5.4) is achieved with the term $(\cos(\alpha_{DAC}) - 1)^2$ which switches between a minimal amplitude ($\omega_{CAD} = 0°$) and a maximum amplitude $\omega_{CAD} = 180°$, thus modeling the expected donor-acceptor overlaps.

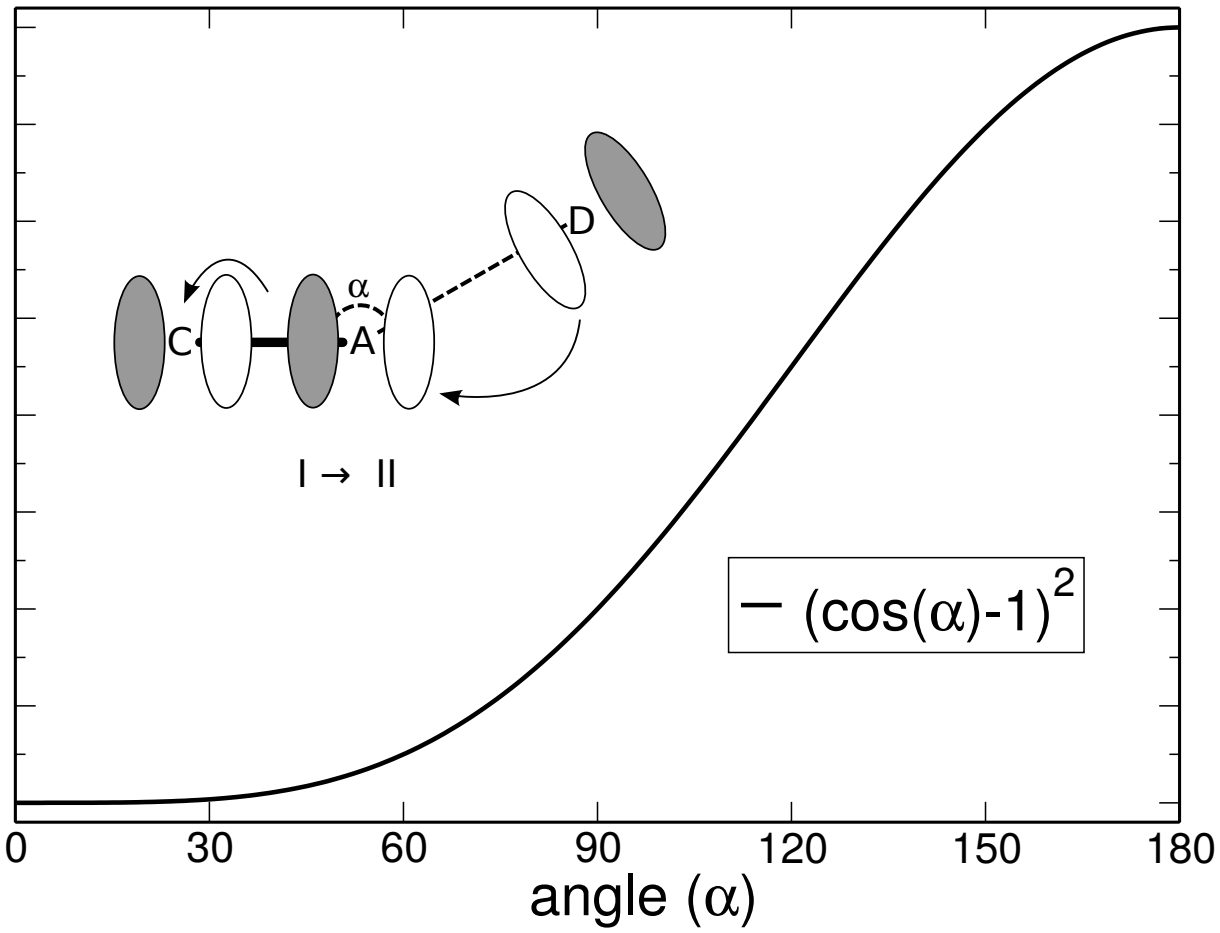

Figure 5.4.: Considering p orbitals, the donation into the anti-bond depends on the angle between the three involved atoms. For this, the off-diagonal term is scaled with $(cos(\alpha_{DAC}) - 1)^2$ which is minimal at an angle of 0° at maximal at 180° where α is the angle between two overlapping orbitals.

5.3.3. Solute-Solvent Electrostatic Interaction in MS-VALBOND

Because including all solvent molecules into the description of the states would be computationally demanding, it is preferable to perform a mixed MS-VALBOND/MM simulation in the spirit of a QM/MM approach. Since for each resonant structure included in the simulation the charge distribution typically differs, electron flow (or charge reorganization) needs to be followed during transitions between states. The different charge distributions characterizing each individual state lead to different solvent-solute interactions for each state and the forces need to be determined such that total energy is conserved. This concerns primarily the electrostatic interactions $E_{\text{elstat}} = \frac{Q_{\text{solv}} q_k}{|R-r|}$ where the Q_{solv} are the static solvent charges, q_k are the solute charges of atom k which fluctuate due to the different resonant structures, and $|R-r|$ is the separation between the MM-charge Q and the MS-VALBOND (state-dependent charge) q.

For most of the structures along an MD trajectory the charge q_k on a particular atom k will be that of one specific state i with weight $w_i \approx 1$ and all other weights $w_j \approx 0$. However, in the neighborhood of a crossing between two (or more) states i and j several weights will differ from 0. Because the weights depend on the geometry of the part which is treated with MS-VALBOND, the charge on atom k will also depend on the geometry which effectively amounts to a fluctuating charge

$$q_k(\boldsymbol{r}) = \sum_{i=1}^{n_{\text{states}}} w_i(\boldsymbol{r}) q_k^i \tag{5.14}$$

where q_k^i is the charge on atom k in state i and the total charge of the solute must be constant $\sum_{k=1}^{N_{atom}} q_k(\mathbf{r}) = q_{\text{solute}}$ for each state (I). The weight $w_i = (\nu_0^{(\text{i})})^2$ is the population of resonance structure I which is determined from eigenvector elements $\nu_0^{(\text{i})}$ by diagonalizing the $N \times N$ matrix as in equation 5.1. Since the weights $w_i(\mathbf{r})$ depend on the internal coordinates through the eigenvectors $\nu_0^{(i)}$, the derivatives of $w(\mathbf{r})$ with respect to all internal degrees of freedom are required. Although this would, in principle, be possible to be done analytically, it is computationally expensive and cumbersome.

Therefore, the derivatives $\frac{\partial w_i(\mathbf{r})}{\partial \mathbf{r}}$ are determined numerically according to

$$\begin{aligned} f_{k,x} = & -\frac{d}{dx}\left(\frac{Q_{\text{solv}} q_k(\boldsymbol{r})}{|X-x|}\right) \\ & = -Q_{\text{solv}}\left[\frac{1}{|X-x|}\frac{dq_k(\boldsymbol{r})}{dx} + q_k(\boldsymbol{r})\frac{d}{dx}\left(\frac{1}{|X-x|}\right)\right] \\ & = -Q_{\text{solv}}\left[\frac{1}{X}\frac{q_k dw_k(\boldsymbol{r})}{dx} + q_k(\boldsymbol{r})\frac{d}{dx}\left(\frac{1}{|X-x|}\right)\right] \\ & \approx -Q_{\text{solv}}\left[\frac{q_k(x+h,y,z) - q_k(x-h,y,z)}{2h|X-x|} + q_k(\boldsymbol{r})\frac{d}{dx}\left(\frac{1}{|X-x|}\right)\right] \end{aligned} \tag{5.15}$$

where, X and x are the coordinates of the solvent and solute atoms, respectively.

5.4. Applications

MS-VALBOND parametrizations and simulations were performed for the ClF_3 molecule, cisplatin and the $BrMe + Cl^- \rightarrow Br^- + MeCl$ reaction. ClF_3 is a paradigm system for a small hypervalent molecule with an unusual shape. Cisplatin is a hypervalent transition metal complex used as an anti-cancer chemotherapeutic agent[218,219] and the S_N2 reaction $BrCH_3{+}Cl^- \rightarrow Br^-{+}CH_3Cl$ has been characterized experimentally[220,221] in the gas- and condensed phase which provides necessary benchmark/validation and it is also one of the standard systems for QM/MM simulations.[222] These three test systems serve as typical examples to illustrate and test the applicability of MS-VALBOND.

5.4.1. Dynamics of ClF_3 in Gas Phase and in Solution

For the parametrization of the diagonal states of ClF_3 the core fragment ClF_2^+ was considered. A Morse potential was fitted to reference *ab initio* data for the Cl-F bond obtained at the CCSD/aug-cc-pVDZ[223,224] level of theory, computed on a grid ranging from 1.3 Å to 4.0 Å with a 0.1 Å increment for all six angles 60°, 90°, 100°, 120°, 150° and 180°. The F-Cl-F angle α is described by VALBOND and the force constant was fitted to reproduce reference calculations at 60°, 90°, 100°, 120°, 150° and 180°. All fitted force field parameters for three resonance structures are provided in Table 5.1.

Table 5.1.: MS-VALBOND parameters for all three resonance structures of ClF3 molecule (see Figure 5.1). Dashed line represents the non-bonded interactions

Term	**State I**			**State II**			**State III**		
Bond (Morse V_M)	D_e (kcal/mol)	β (Å^{-1})	r_e (Å)	D_e (kcal/mol)	β (Å^{-1})	r_e (Å)	D_e (kcal/mol)	β (Å^{-1})	r_e (Å)
$V_M^{\mathrm{Cl_A-F_B}}$	78.812	2.058	1.657	78.812	2.058	1.657			
$V_M^{\mathrm{Cl_A-F_C}}$	78.812	2.058	1.657				78.812	2.058	1.657
$V_M^{\mathrm{Cl_A-F_D}}$				78.812	2.058	1.657	78.812	2.058	1.657
Non-bonded (Morse V_M)	D_e (kcal/mol)	β (Å^{-1})	r_e (Å)	D_e (kcal/mol)	β (Å^{-1})	r_e (Å)	D_e (kcal/mol)	β (Å^{-1})	r_e (Å)
$V_M^{\mathrm{Cl--F_D}}$	1.192	1.320	3.537						
$V_M^{\mathrm{Cl--F_C}}$				1.192	1.320	3.537			
$V_M^{\mathrm{Cl--F_B}}$							1.192	1.320	3.537
$V_M^{\mathrm{F_B--F_C}}$				0.861	1.601	2.919	0.861	1.601	2.919
$V_M^{\mathrm{F_B--F_D}}$	0.861	1.601	2.919				0.861	1.601	2.919
$V_M^{\mathrm{F_C--F_D}}$	0.861	1.601	2.919	0.861	1.601	2.919			
Angle (VALBOND)		Hybridization	k		Hybridization	k		Hybridization	k
$\mathrm{F_B-Cl_A-F_C}$		sp^{10}	236.597						
$\mathrm{F_B-Cl_A-F_D}$					sp^{10}	236.597			
$\mathrm{F_C-Cl_A-F_D}$								sp^{10}	236.597
Non-bond(solute-solvent)	Charges (e)	ϵ (kcal/mol)	$R_{min}/2$(Å)	Charges (e)	ϵ (kcal/mol)	$R_{min}/2$(Å)	Charges (e)	ϵ (kcal/mol)	$R_{min}/2$(Å)
Cl	0.150	-0.320	1.930	0.150	-0.320	1.930	0.150	-0.320	1.930
F	-0.050	-0.135	1.630	-0.050	-0.135	1.630	-0.050	-0.135	1.630
$\mathrm{O_w}$	-0.834	-0.152	1.768	-0.834	-0.152	1.768	-0.834	-0.152	1.768
$\mathrm{H_w}$	0.417	-0.046	0.225	0.417	-0.046	0.225	0.417	-0.046	0.225
				Off-diagonal					
	Bond (Morse)			Angles					
Resonance	D_e (kcal/mol)	β (Å^{-1})	r_e (Å)	Angle	Hybridization	k			
I $\longleftrightarrow$ II	31.163	2.103	1.396	$\mathrm{F_C-Cl_A-F_D}$	sp^{10}	236.597			
I $\longleftrightarrow$ III	31.163	2.103	1.396	$\mathrm{F_B-Cl_A-F_D}$	sp^{10}	236.597			
II $\longleftrightarrow$ III	31.163	2.103	1.396	$\mathrm{F_C-Cl_A-F_b}$	sp^{10}	236.597			

Table 5.2.: Comparison of selected geometrical parameters for ClF_3 with their corresponding NMR data[225]. The bond distances are in Å and angles are in degree.

Geometric parameters	MS-VALBOND	CCSD	NMR structure
Cl-$F_{B,D}$	1.76	1.74	1.70
Cl-F_C	1.68	1.64	1.60
F_B-Cl-F_D	172.2	173.6	174.6
F_B-Cl-F_C	93.9	86.8	87.3
F_B-Cl-F_C(-)F_D	180.0	180.0	180.0

In the second step the parametrization of the off-diagonal terms was carried out by considering six degrees of freedom in ClF_3 system: Cl-F_B, Cl-F_C, Cl-F_D, F_B-Cl-F_C, F_C-Cl-F_D and F_B-Cl-F_C(-)F_D dihedral angle. The off-diagonal force field parameters for ClF_3 are also provided in Table 5.1.

With the FF available, first the system was energy minimized, heated to 300 K and then equilibrated for 500 ps. Further 500 ps of NVE simulations were performed for the analysis. The solvated system was generated by immersing the solute molecule in a cubic TIP3P water box[114] of length 30 Å .

As a validation, the energy minimized geometry was compared with experimental data[225] and with the optimized structure obtained at the CCSD/aug-cc-pVDZ level of theory (see Table 5.2). In general, the geometrical parameters for bond lengths and bond angles obtained from MS-VALBOND agree well with both sets of reference data. The Cl-$F_{B,D}$ bond lengths from MS-VALBOND deviate by –0.02 Å and –0.06 Å from the CCSD calculations and experiment, respectively. Similar observations are made for the Cl-F_C bond which differs by –0.04 Å and –0.08 Å from the CCSD calculations and experiment. For the F_B-Cl-F_D angle the difference between MS-VALBOND calculations and the reference data is $\sim 2^\circ$ (see Table 5.2) which increases to 6° for the F_B-Cl-F_C angle. All three approaches yield a planar geometry of the molecule.

During the entire NVE simulation the total energy is conserved to within fractions of a kcal/mol whether the simulation is carried out in gas phase or in aqueous medium (see Figure 5.5). For ClF_3 in the gas phase, the energy fluctuates within 0.005 kcal/mol (bottom left in Figure 5.5) around its average value which increases to 0.2 kcal/mol in solution (red distribution bottom right in Figure 5.5). The energy fluctuations δE for the same simulation without the solute (i.e. pure water) is comparable, ~ 0.2 kcal/mol (blue distribution bottom right Figure 5.5). It is also of interest to consider the weights

of the different resonance structures I to III, see top panels in Figure 5.5. To describe the correct geometry of the ClF_3 molecule, a sp^{10} hybridization was used as had been done in previous work.[56] Since all the sp^{10} hybrid orbitals have very high $p-$character the equilibrium angle between them is close to 90°. Therefore, resonance structures with an F-Cl-F equilibrium angle close to 90° (equivalent states I and III) are lower in energy and more highly populated (green and black traces in top row of Figure 5.5) compared to state II (red trace). Whether the simulation is carried out in gas-phase or in aqueous solution the weights of each of the resonance structures remain similar (see Figure 5.5) although the fluctuations increase somewhat in water.

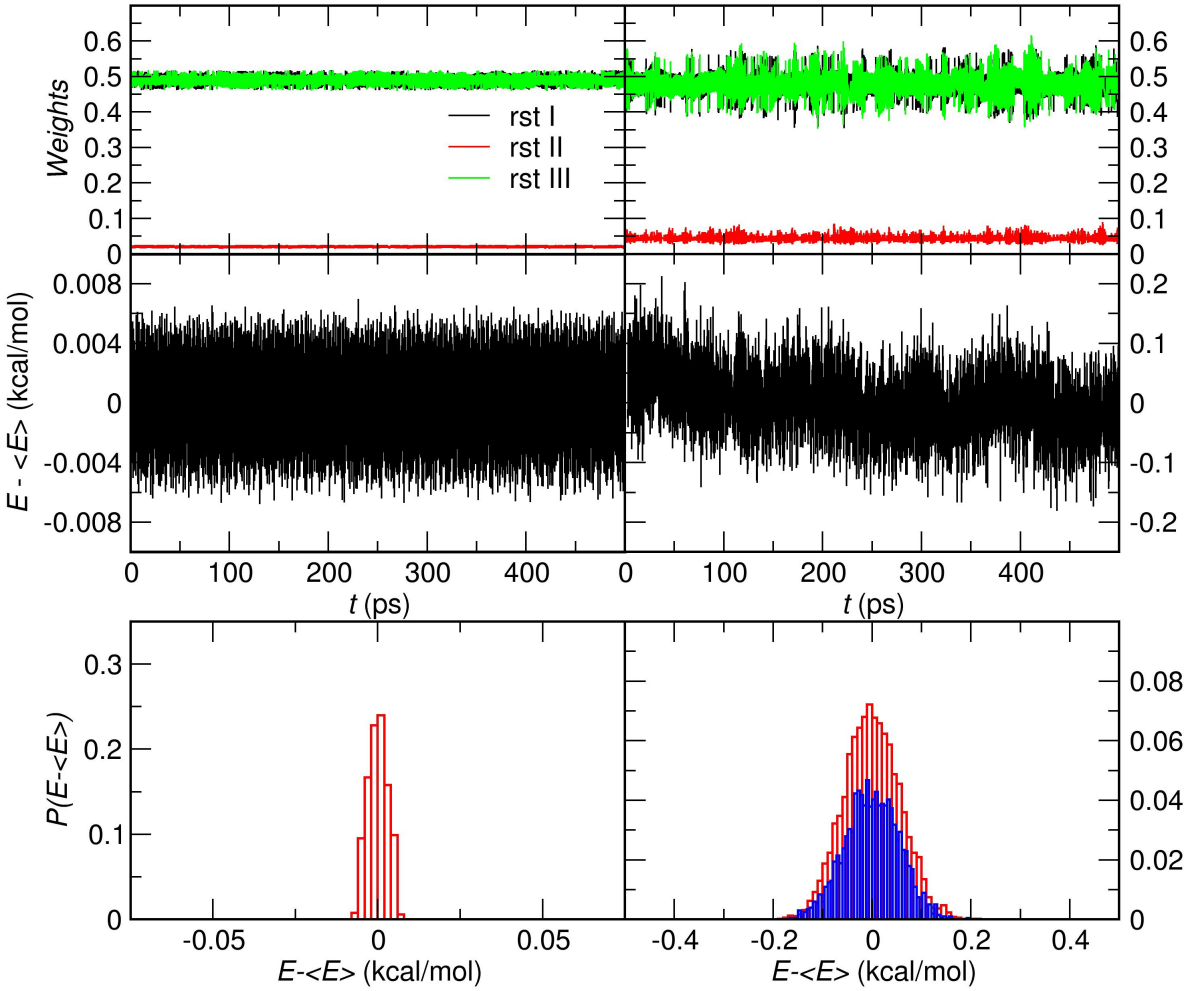

Figure 5.5.: Weights (top), energy fluctuation (middle) and distribution around the mean (bottom) for simulations of ClF_3 in the gas phase (left) and in aqueous solution (right). The top panel shows the contribution of each resonance structure I to III (see Figure 5.1) towards the total structure of the ClF_3 molecule during the MD simulations. The energy fluctuations for simulations with (red) and without (blue) the solute in water are shown in the bottom right panel.

Combining all three resonance structures it is possible to describe pseudorotation in ClF_3 i.e F atoms exchange between apical and equatorial positions. For this, an MD simulation was started at the transition state separating the apical and equatorial positions. Figure 5.6 panel A shows the change of $F_B - Cl_A - F_C$ angle and describes the switching of F_C position from equatorial to apical. Hence, the MS-VALBOND force field allows to estimate the barrier involved for the transitions among different T-shape arrangements. By considering the $F_B - Cl_A - F_C$ angle, free energy for the pseudorotation in

ClF_3 was computed and found to be 4.3 kcal/mol (see Figure 5.6) which agrees very favourably with the experimental energy of 4.8 kcal/mol from NMR experiments[225].

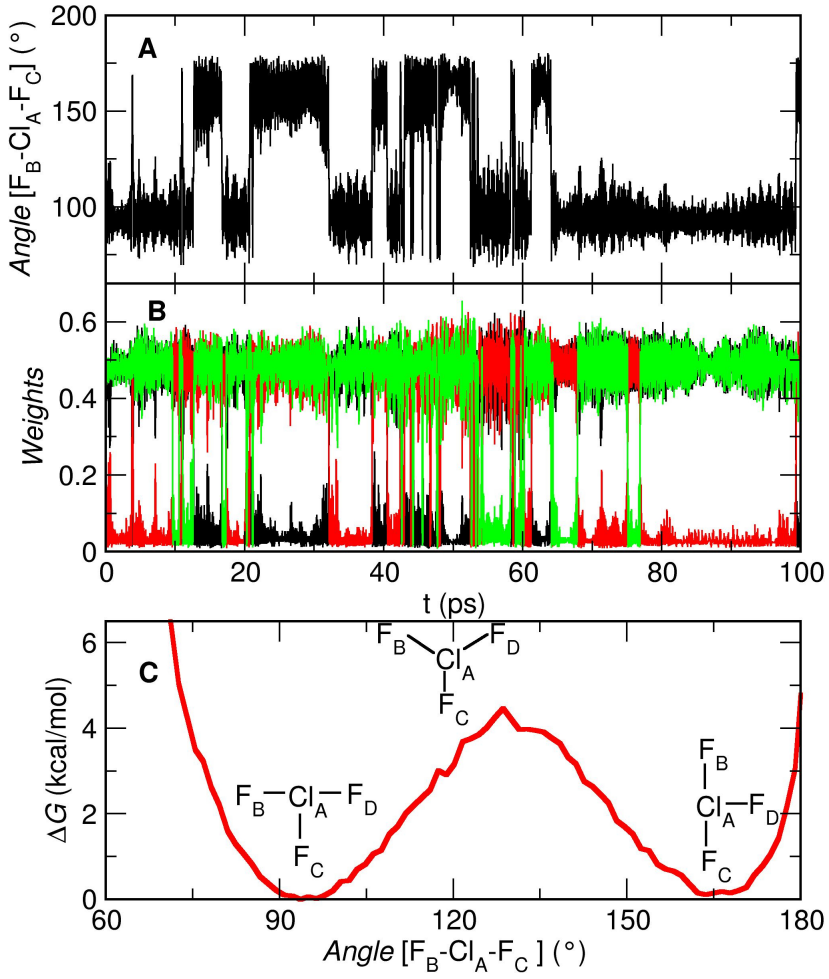

Figure 5.6.: Change of F-Cl-F angle (panel A) and weights (panel B) during the dynamics of ClF_3 in the gas phase. The computed free energy profile for the pseudorotation in ClF_3 is shown in panel C. Insets in panel C are the structures representing the two isoenergetic minima and the TS states separating them and involved in the pseudorotation of ClF_3. Color code in panel B: resonance structure I (black), II (red) and III (green).

5.5. Structure and Dynamics of Cisplatin

Cisplatin (*cis*-diamminedichloridoplatinum(II) (CDDP)) is a Platinum-containing metal complex with two ammonia and two chloride ligands cis to each other. Cisplatin is one of the most important

and effective anti-cancer agents used in the treatment of various types of cancers including testicular, ovarian, cervical, or breast cancer[218,219]. Furthermore, this compound is also used in Auger therapy[226]. Experimentally, cisplatin was also well characterized spectroscopically which provides a useful basis to validate the present calculations in a meaningful fashion.[227]

The six relevant resonance structures (in cisplatin, Pt is sd^1 hybridized) are shown in Figure 5.7. For parametrizing the diagonal states, the Pt-Cl and Pt-N(H_3) bonds were fitted to reference data from electronic structure calculations with the B3LYP functional[62] and the LANL2DZ basis[176] set for Pt and 6-31G(d,p)[108] for all other atoms, respectively. The necessary reference data were collected by scanning along the Pt-Cl bond in $PtCl_2$ and along the Pt-N bond in $[Pt(NH_3)_2]^{2+}$ on a grid from 1.5 Å to 5.5 Å with an increment of 0.1 Å. To these references data two Morse potentials for Pt-N and Pt-Cl bonds were fitted and parameters are given in Table 5.3.

Table 5.3.: MS-VALBOND parameters for all the resonance structures of cisplatin. For the off-diagonal Morse potential, appropriate combination of individual Morse potentials of different bonds involved in the breaking and forming in going from one resonance structure to other needed to be considered. For example, transition between state I to II, one Pt-N bond breaks and one Pt-Cl bond forms (see Figure 5.7), so the combination is [N − Pt − Cl].

Bond (Morse)	D_e (kcal/mol)	β (Å^{-1})	r_e (Å)			
Pt-N	56.909	1.702	2.050			
Pt-Cl	83.655	1.620	2.201			
Angle (VALBOND)		Hybridization	k			
N-Pt-N		sd^1	500			
Cl-Pt-Cl		sd^1	500			
N-Pt-Cl		sd^1	500			
Nonbonded (Morse)	D_e (kcal/mol)	β (Å^{-1})	r_e (Å)			
$V^{\mathrm{Pt---N}}$	1.170	1.337	3.535			
$V^{\mathrm{Pt---Cl}}$	1.175	1.336	3.537			
$V^{\mathrm{Cl---Cl}}$	0.861	1.600	2.918			
$V^{\mathrm{Cl---N}}$	0.860	1.601	2.915			
$V^{\mathrm{N---N}}$	0.857	1.604	2.912			
		Off-Diagonal				
Bond (Morse)	D_e(kcal/mol)	β (Å^{-1})	r_e (Å)	D_e (kcal/mol)	β (Å^{-1})	r_e (Å)
[N − Pt − N]	14.128	2.103	1.500	14.128	2.103	1.500
[N − Pt − Cl]	14.128	2.103	1.500	7.698	0.790	2.385
[Cl − Pt − Cl]	7.698	0.790	2.385	7.698	0.790	2.385
Angle	Hybridization	k				
N-Pt-N	sd^1	500				
Cl-Pt-Cl	sd^1	500				
N-Pt-Cl	sd^1	500				

For the parametrization of the off-diagonal terms, the element V_{12} (transition between states I and II) is considered as an example. In going from resonance structure I to II, one Pt-N bond breaks and one Pt-Cl bond forms. Therefore, the off-diagonal term is described by a sum of two Morse potentials $V_{\mathrm{Pt-N}}$ and $V_{\mathrm{Pt-Cl}}$ which are combined according to $[\cos(\theta) - 1]^2 V_{\mathrm{Pt-N}} + [\cos(\theta) - 1]^2 V_{\mathrm{Pt-Cl}}$, see Methods. Here, θ is the N-Pt-Cl angle and the corresponding bending potential is described by VALBOND. Thus, in total six parameters (three for each Morse) need to be fitted to the reference data. For that, five degrees of freedom were considered; the Pt-Cl and Pt-N(H_3) distances, and the Cl-Pt-Cl, Cl-Pt-N(H_3) and (H_3)N-Pt-N(H_3) angles for the parametrization of the off-diagonal elements. A total of 5821 reference energies and the reference structures were generated by considering five degrees of freedom; the Pt-Cl and Pt-N(H_3) distances (1.5 Å to 3.9 Å with 0.2 increment), and the Cl-Pt-Cl, Cl-Pt-N(H_3) and (H_3)N-Pt-N(H_3) angles (ranging from 60° to 120° with $\Delta\theta = 10°$). The off-diagonal parameters were fitted to reference *ab initio* data by non-linear least square fitting using NL2SOL algorithm [228].

The partial charges on each atom were those from a Natural Bond Orbital (NBO) [106] analysis of the [Pt(NH_3)$_2$$Cl_2$] complex in its energy minimized structure using the B3LYP functional and the LANL2DZ basis set for Pt and 6-31G(d,p) for all other atoms. Van der Waals interactions within the solute were again modeled using Morse potentials and are parametrized with respect to interaction between each atom and He as a probe (see above). If the atoms are bonded to each other or to a common atom then they are considered as bonded. For example, in resonance structure I (see Figure 5.7), two Cl atoms are unbound and all the non-bonded interactions with Pt, N and Cl atoms were computed. The Morse parameters for each atom were obtained by fitting the Morse potential with the potential energy curve obtained along the Pt/Cl/N–He bond, see Methods. The remaining parameters for the NH_3 ligand are those from the CGenFF force field [101] and a summary of all parameters is provided in Table 5.4.

Table 5.4.: Model systems from which reference electronic structure data was determined for parametrization of diagonal and off-diagonal terms.

Diagonal Term	Model	Potential
Pt-Cl	$PtCl_2$	Morse
Pt-N	$[Pt(NH_3)_2]^{2+}$	Morse
Angle (L-M-L)	$[Pt(NH_3)_2Cl_2]$	VALBOND
Non-bonded	Pt/N/Cl/H–He	Morse
Off diagonal Term	$[Pt(NH_3)_2Cl_2]$	Scaled Morse (see equation 5.11)

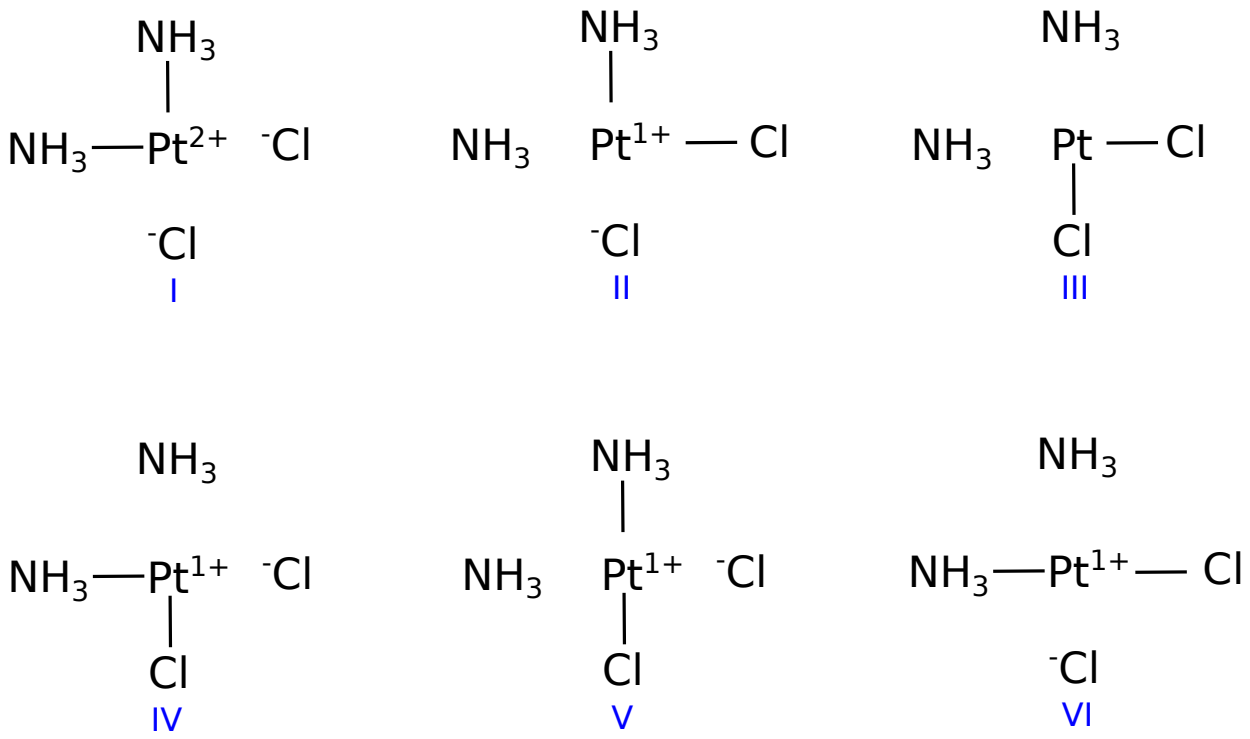

Figure 5.7.: The six resonance structures of cisplatin. Resonance structures II and IV are chemically equivalent as are structures V and VI.

For structural validation, the minimized geometry from MS-VALBOND was compared with the corresponding crystal structure,[227] see Figure 5.8 and Table 5.5. It is found that bond lengths and angles from MS-VALBOND agree to within less than 2 % with the X-ray data. Specifically, MS-VALBOND yields bond distances Pt-N and Pt-Cl in cisplatin of 2.07 Å and 2.36 Å, respectively, compared with 2.05 Å and 2.32 Å from the X-ray crystal structure.[227] Also, the deviation for all three angles (N-Pt-N, Cl-Pt-Cl and Cl-Pt-N) compared to their experimental[227] values are less than 2°.

Table 5.5.: Comparison of selected geometrical parameters with their corresponding crystal data[227]. The bond distances are in Å and angles are in degree.

Geometric parameters	MS-VALBOND	Experiment[227]
Pt-Cl	2.36	2.32
Pt-N	2.07	2.05
Cl-Pt-Cl	90.1	91.6
N-Pt-N	91.7	90.2
Cl-Pt-N	87.6	88.9

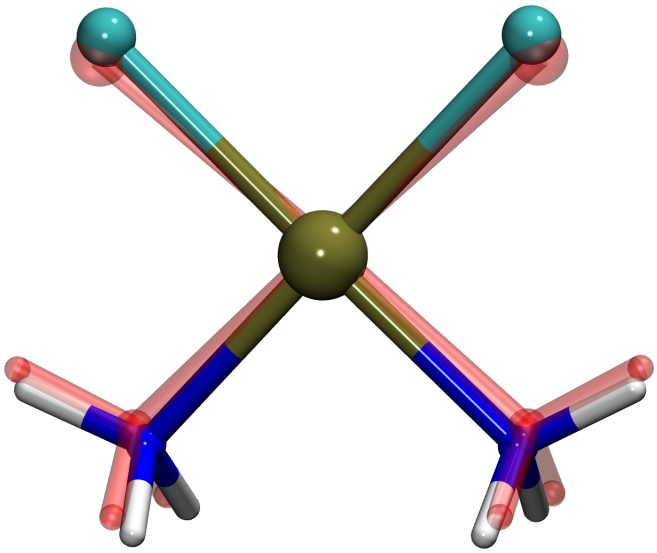

Figure 5.8.: MS-VALBOND optimized structures of cisplatin along with the crystal structure[227] (transparent red). Atom color code used, Pt (ocher), Cl (cyan), N (blue) and H (white).

A further validation of the MS-VALBOND force field for cisplatin was done by computing the infrared spectrum. The spectrum was calculated from the dipole moment auto-correlation function $C(t) =< \mu(0)\mu(t) >$ from a 1 ns MD simulation in gas phase. The total dipole moment $\mu(t)$ was recorded along the trajectory and correlated over 2^{15} time origins separated by 1 fs to yield $C(t)$. Then the spectral signal $C(\omega)$ was computed from the fast Fourier transform (FFT) with a Blackman filter. Finally, the infrared spectrum $A(\omega)$ was determined by Boltzmann weighting $C(\omega)$ according to

$$A(\omega) = \omega \left[1 - \exp\left(-\frac{\omega}{k_B T}\right)\right] C(\omega) \tag{5.16}$$

Here ω, k_B and T are the frequency, Boltzmann constant and temperature, respectively. Figure 5.9 reports the computed IR-spectra (black trace) compared with the experimentally determined[229]

Table 5.6.: Calculated IR spectrum from the dipole moment auto-correlation function form MD simulations of 1 ns and experimental vibrational frequencies of cisplatin. Assignments are based on the power spectra for each bond distances and angles mentioned.

Assignment	Computed Frequency (cm^{-1})	Experimental Frequency[229] (cm^{-1})
ν_{Pt-N}	410	469
ν_{Pt-Cl}	360	323
ν_{N-Pt-N}	258	256
$\nu_{Cl-Pt-Cl}$	159	156
$\nu_{Cl-Pt-N}$	75	92 – 99
δ_{NH_3} (wag)	881	927
δ_{NH_3} (bend)	1510	1545
ν_{N-H}	3415	3500

vibrational frequencies (no intensity information is available from experiments). A direct comparison for the most important modes is provided in Table 5.6 and shows that they compare favourably. This is particularly true for the L-M-L bending frequencies for all three N-Pt-N, Cl-Pt-Cl and N-Pt-Cl angles which match very well with their experimental frequencies[229] (see Table 5.6). On the other hand the Pt-N and Pt-Cl stretch frequency deviate by about 50 cm^{-1} from the experiments.[229] Finally, the peak at $\sim$ 900 cm^{-1} in the computed spectrum corresponds to the NH_3 wagging vibration and also agrees closely with experiment (at 927 cm^{-1}).

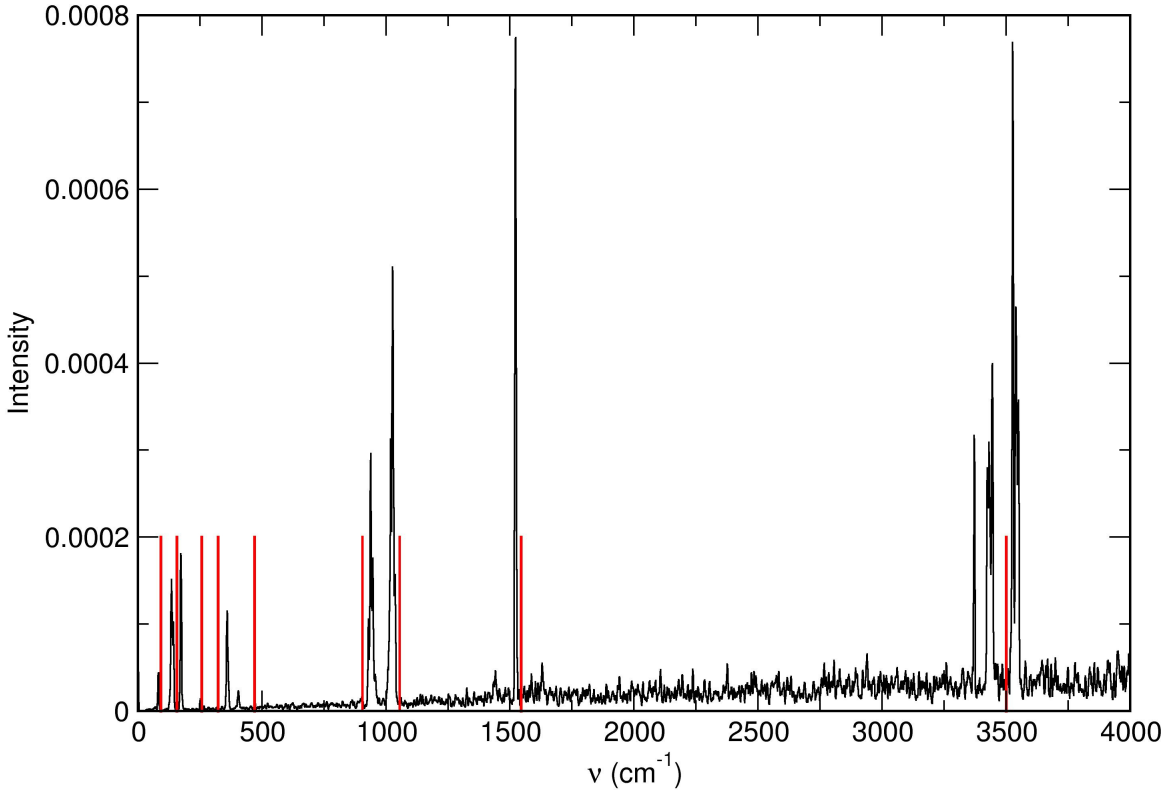

Figure 5.9.: Computed IR-spectra from the dipole moment auto-correlation function from 1 ns MD simulation along with the experimental[227] peak positions assigned by red lines.

Finally, the quality of the MS-VALBOND force field was also established by comparing to electronic structure calculations for thermally populated structures. For this an MD simulations at 50 K was carried out from which 50 structures were randomly selected. Their energies were determined at the B3LYP level of theory with the 6-31G(d,p) basis set for all atoms except Pt for which LANL2DZ basis is used. These energies are then correlated with the MS-VALBOND and shown in Figure 5.10. The root mean square deviation in energy ($RMSD_E$) between DFT and MS-VALBOND is 0.33 kcal/mol which is within chemical accuracy and further demonstrates the quality of the MS-VALBOND parametrization for this TM complex.

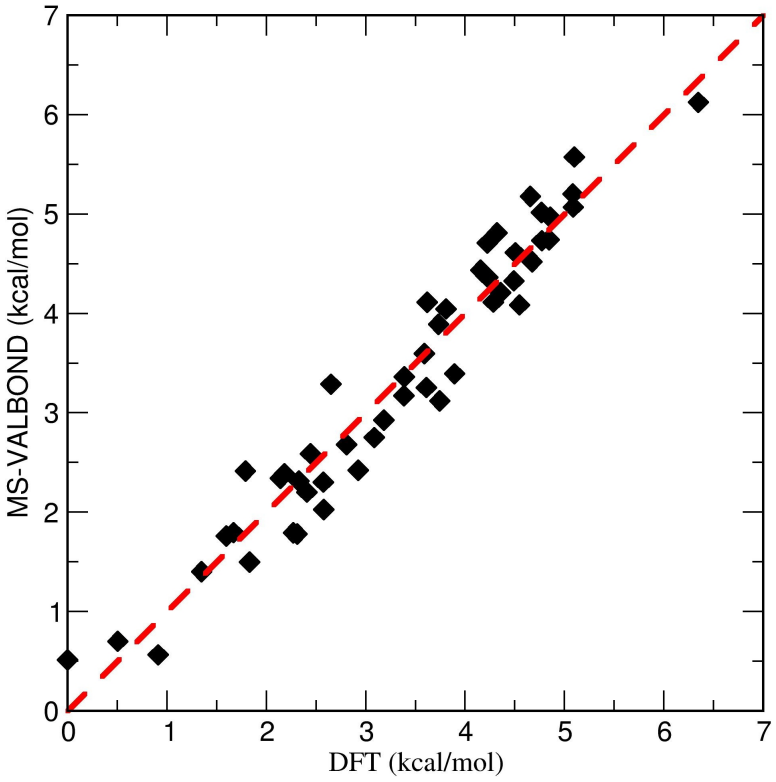

Figure 5.10.: Energy comparison of 50 structure obtained from MD simulations MS-VALBOND and DFT (B3LYP/6-31G(d,p) and LANL2DZ basis on Pt). The $RMSD_E$ between two methods is 0.33 kcal/mol.

Figure 5.11 shows the variation in occupation number of each resonant structure of cisplatin during the MD simulations. From Figure 5.11, it is clear that resonant structure I has the largest occupation number because the two bonded ligands (NH_3) are strong ligands and the angle between them is 90° which is the equilibrium angle for sd^1 hybridization. It is also noticed that because the two Cl^- are weaker ligands, state III has a lower occupation number compared to state I even though the angle between the ligands is 90°. Both resonant structures II and IV are chemically equivalent and have similar occupation number distribution (see top panel Figure 5.11). Since the angle between the bound ligands for resonant structure V and VI is 180° and is far from the sd^1 hybridization angle (90°), they are highest in energy and their occupation is lowest.

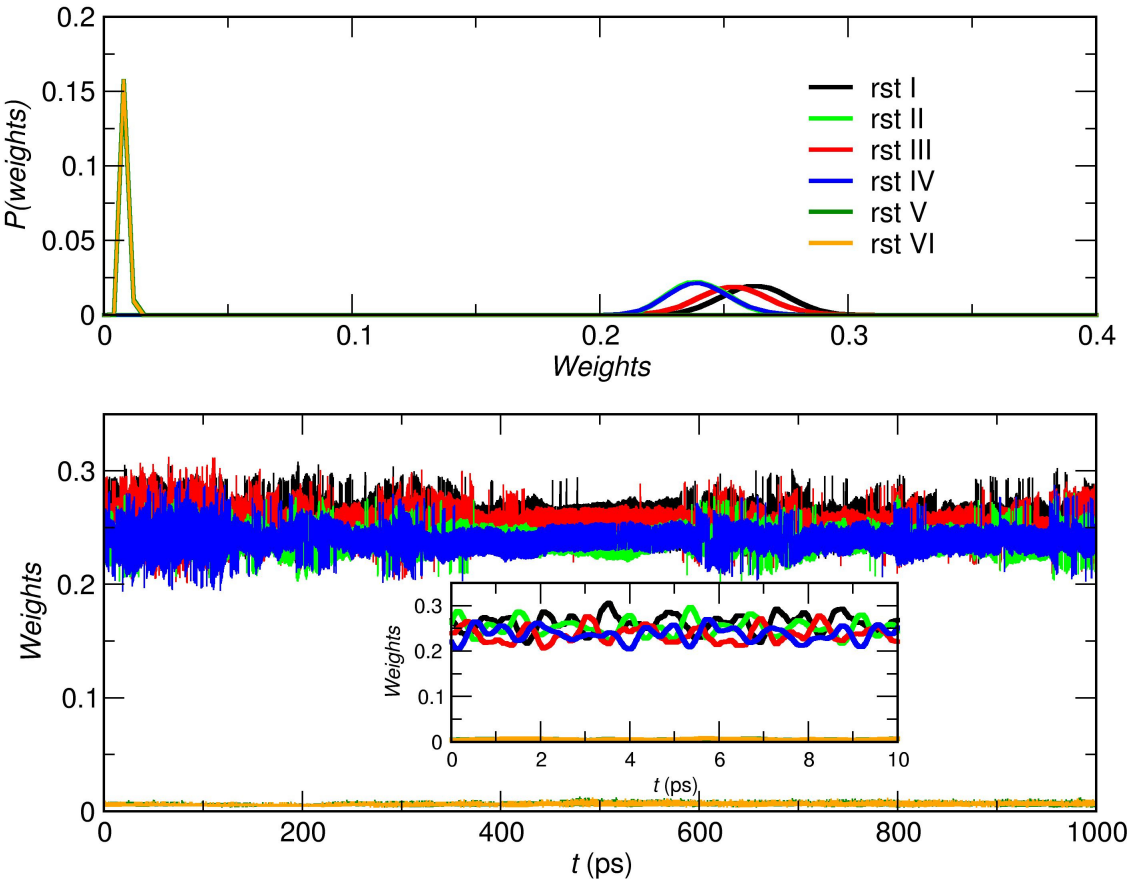

Figure 5.11.: Variation of occupation number (bottom) of each resonance structure of cisplatin during the MD simulations and corresponding probability distribution (top) are shown here.

5.6. The BrMe+Cl⁻ Reaction

As a last example the bimolecular nucleophilic substitution (S_N2) reaction between methylbromide and chloride ion in aqueous solution is studied. Bromomethane (CH_3Br) is used as fumigant for several pests like mites, fungi, spiders etc[230]. Methylbromides are mainly used for soil fumigation. However, their exposure to the environment are very hazardous as they are responsible for the ozone depletion in stratosphere[230,231]. On the other hand chlorine species are found in marine boundary layer where CH_3Br enters into the atmosphere. Thus, they can help in destructing hazardous methylbromides by reacting with them. S_N2 reactions and the solvent effects on the kinetics are very important in organic chemistry[232]. Also, the BrMe + Cl^- → Br^- + MeCl S_N2 reaction has been studied both theoretically[221,232,233] and experimentally[220,234].

At the MP2/6-311++G(d,p) and MP2/aug-cc-pVTZ level of theory the enthalpic barrier for the BrMe + Cl^- → Br^- + MeCl reaction in implicit water (polarizable continuum model (PCM), $\epsilon = 78.5$) is 24.6 and 22.4 kcal/mol[221], respectively. This compares quite well with the experimentally measured free energy of activation (24.7 kcal/mol)[220,234]. Previous calculations for halomethane substitution reactions at the MP2 and CCSD level of theory in implicit water also yielded favourable agreement with experiment whereas DFT underestimated the barrier height.[221,235]. As a comparison, the gas-phase barrier for the BrMe + Cl^- → Br^- + MeCl reaction from CCSD/aug-cc-pVDZ calculations is found to be 11.7 kcal/mol, in close agreement with previously computed 11.2 kcal/mol and experimental values 9.5 kcal/mol[236,237].

For the MS-VALBOND parametrization of the BrMe + Cl^- → Br^- + MeCl S_N2 reaction, the diagonal states were described by two Morse potentials and fitted to reference data from CCSD/aug-cc-pVDZ calculations along the C-Br and C-Cl bonds in BrMe or MeCl, respectively. All the Cl/Br-C-H angles were described by VALBOND with a sp^3 hybridization. For the off-diagonal states, the parametrization was carried out by considering two degrees of freedom C-Br and C-Cl bonds in $[Br\text{-}Me\text{-}Cl]^-$ and fitted to Morse potentials V_{Me-Br} and V_{Me-Cl}.

To study the BrMe + Cl^- → Br^- + MeCl reaction in aqueous solution, two reactants Cl^- and MeBr were solvated in a cubic TIP3P water box of length 30 Å. The system is energy minimized, followed by heating and an equilibration of 1 ns at 300 K. The energy barrier of 24.7 kcal/mol (see above) associated with the substitution reaction BrMe + Cl^- → Br^- + MeCl is too high for directly sampling it in unbiased simulations on time scales accessible to conventional MD simulations. In order to validate the present implementation for following chemical reactions without using a bias the reaction barrier is first artificially reduced to 2.3 kcal/mol by decreasing the dissociation energy of the C-Br bond. With this modification the reaction occurs on the 10 ps time scale (see Figure 5.12) in unbiased MD simulations. The total energy is conserved to within 0.2 kcal/mol (see Figure 5.12) which confirms that the present implementation is also suitable to follow chemical reactions in a meaningful fashion.

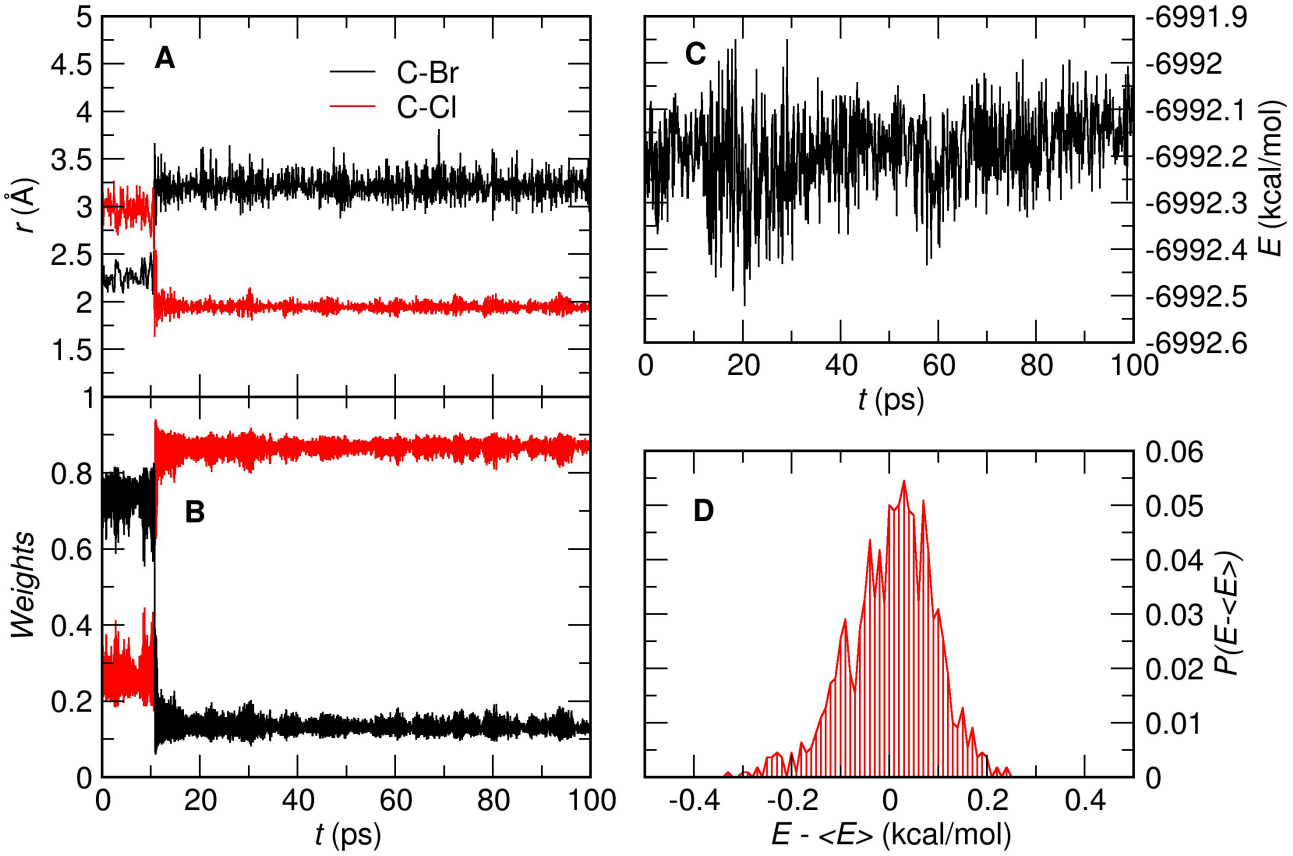

Figure 5.12.: Energy conservation and population of the states for Me-Br + Cl^- reaction in water with reduced barrier height of 2.3 kcal/mol. Panel A shows the two C-Br and C-Cl distance traces. Variation of weights for two states reactant and product during the reaction are shown in panel B. Panel C and D are for the change of total energy during the reaction and the corresponding energy fluctuation distribution respectively.

Next, the S_N2 reaction for BrMe and Cl^- in aqueous solution was investigated using the true potential energy surface with a barrier height of 24.6 kcal/mol. For this, umbrella sampling[238] simulations were performed. The distance difference $\delta = d_{C-Br} - d_{C-Cl}$ was used as the reaction coordinate. The system was prepared as described above, followed by a total of 50 umbrella simulations along the reaction coordinate with $-2.5 \leq \delta \leq 2.5$. For each umbrella window 250 ps of equilibrium simulations (100 ps equilibrium simulation and 150 ps for data accumulation) were carried out. For all umbrella windows a force constant $k = 50$ kcal/mol was used.

The weighted histogram analysis method (WHAM)[239] was used to determine the resultant free energy profile for the BrMe + Cl^- → Br^- + MeCl reaction in water, see Figure 5.13. The computed free energy barrier is 24.6 kcal/mol which agrees well with the experimental[220,234] value of 24.7 kcal/mol. Also, the barrier for the reverse reaction is 26.7 kcal/mol which agrees quite well with experiment that finds 27.8 kcal/mol.[220,221] Finally, the computed free energy difference $\Delta\Delta G = 2.1$ kcal/mol between reactant and product is also consistent with experiment which found 3.1 kcal/mol (see Figure 5.13 red line).[220,221]. Probably, further improvement of the force field would be possible by slightly tuning force field parameters such as the C-H bonds and H-C-H angles.

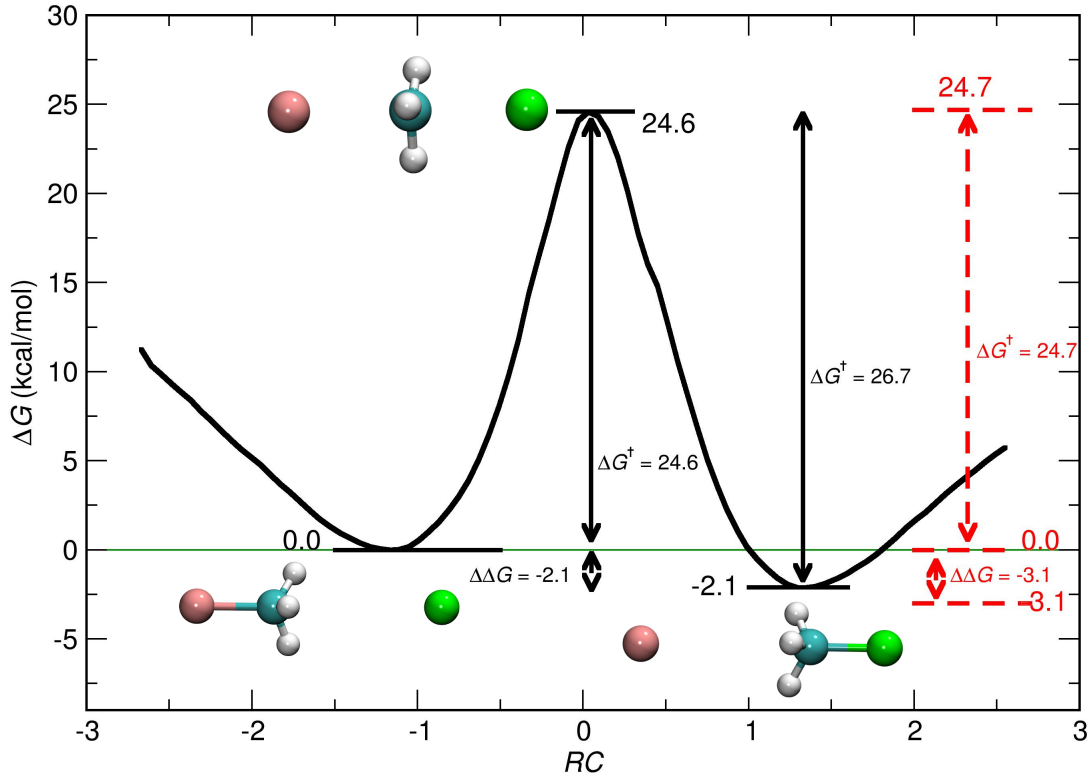

Figure 5.13.: The free energy profile for the BrMe + Cl^- → Br^- + MeCl reaction in water obtained from the umbrella sampling simulations. Experimental values shown in red color[220]. Atom color code used: C (cyan), Br (pink), Cl (green) and H (white).

5.7. Conclusion

The multi-state VALBOND (MS-VALBOND) approach discussed in the present work has been successfully implemented and applied to a range of situations including hypervalent molecules, transition metal complexes and chemical reactions. It is demonstrated that total energy is conserved and, whenever possible, comparison with experiment leads to good agreement for structures, vibrational frequencies or free energy barriers. Hence, quantitative atomistic simulations for hypervalent and metal-containing systems on extended time scales become possible with the present implementation which allows to make contact with experiments and provide additional molecular-level insight from the analysis of the simulations as is possible from MS-ARMD studies.[204,240] This is one of the main differences compared with methods such as ReaxFF which are more suitable for qualitative investigations.

The current implementation is also suitable for applications to larger systems, such as proteins because the reactive subsystem (e.g. a protein active site) can be represented with MS-VALBOND whereas the remainder of the simulation is treated with an empirical force field. Given the flexible implementation it is expected that MS-VALBOND can be applied to a range of challenging problems, including transition metals in biological systems or reactions involving organometallic systems.

6. Kinetic Analysis and Structural Interpretation of Competitive Ligand Binding for NO Dioxygenation in Truncated Hemoglobin N

6.1. Abstract

Conversion of nitric oxide (NO) to nitrate (NO_3^-) by dioxygenation protects cells from lethal NO. Starting from an NO-bound heme, the very first step in converting NO to benign NO_3^- is the ligand exchange reaction $FeNO+O_2 \rightarrow FeO_2+NO$ which is still poorly understood at a molecular level. We present a quantitative account of the reaction in the WT truncated Hemoglobin N (trHbN) and in its Y33A mutant both of which compare very favourably with available experiments for the overall dioxygenation reaction. It is directly confirmed that the ligand exchange reaction is rate limiting in trHbN and that entropic contributions account for 75 % of the difference between WT and the mutant. Residues Tyr33, Phe46, Val80, His81 and Gln82 surrounding the active site sample different ensembles in the ligand-bound and transition state, respectively, and therefore are expected to exercise control over the reaction path. Through comparison with electronic structure calculations the transition state separating the two ligand-bound states is assigned to a ^2A state.

6.2. Introduction

Competitive ligand binding is ubiquitous in biological systems[241]. For inner-shell binding of O_2^- in Cu-Zn superoxide dismutase other ligands including N_3^-, OH^- or F^- have been identified as competitive inhibitors and a typical process is the displacement of water by the substrate.[242–244]. Other such ligand exchange reactions have been observed for antimetastatic Ru(III) complex imidazolium [*trans*-$RuCl_4$(1H-imidazole)(DMSO-*S*)] (NAMI-A), where the DMSO ligand is replaced by water through

the interaction of the complex with human serum albumin[245], or for (NO, H_2O) exchange in the heme-based sensor YddV.[246] Typically, competitive reactions are operative under conditions where ligand 1 (L1) has a weaker affinity towards the protein than ligand 2 (L2) but is available in excess (c[L1] >> c[L2]) due to local physiological conditions. This provides an organism with additional control in regulation.

A biologically relevant competitive process is the conversion of molecular oxygen (O_2) and nitric oxide (NO) to nitrate. Interaction of NO and molecular O_2 is ubiquitous in globins. Both ligands fulfill essential physiological functions: O_2 is responsible for respiration, involved in enzymatic oxidation reaction, and essential for maintaining concentration and strong memory[247] whereas NO regulates smooth muscle relaxation[248] and platelet aggregation in vascular tissues[248–251] and plays important roles in neurotransmission[248,250,252] and influences mitochondrial respiration[253,254].

However, the two ligands also work in concert, specifically in the NO dioxygenation reaction where harmful nitric oxide is converted to benign nitrate to relieve nitrosative stress in bacteria[255] and is relevant for NO-detoxification in blood.[256–259] NO dioxygenation is catalyzed by the oxy-heme groups of flavohemoglobins and truncated hemoglobins in bacteria as well as myoglobin and hemoglobin in mammals.[260] The reaction was first studied for Myoglobin (Mb)[261] followed by studies focusing on nitrate formation in other globins using experimental and computational approaches[262–265]. ^{1}H NMR experiments provide evidence for the conversion of oxygenated Mb (oxyMb) to metmyoglobin (metMb) by reacting with NO[266]. From stopped flow experiments, the second order rate constants for the reaction of NO with oxyHb and oxyMb (process III, see equation 6.1) are 4.36×10^7 and 8.9×10^7 M^{-1} s^{-1}, respectively[262–264].

Because two ligands are involved in competitive ligand binding, the dynamics around the active site involves collisions between and crowding of the ligands. Therefore, both, entropic and enthalpic effects are expected to contribute to the functionally relevant dynamics and the transition state is topologically challenging. If structural information about the TS would be available, the reaction pathway could be manipulated with much more confidence and propensities for different outcomes of the reaction could be rationalized in a considerably more informed fashion. This is of particular importance in enzyme design. However, usually little is known about the transition state which separates the two end points

because it is short lived and hence difficult to directly characterize by experiment.

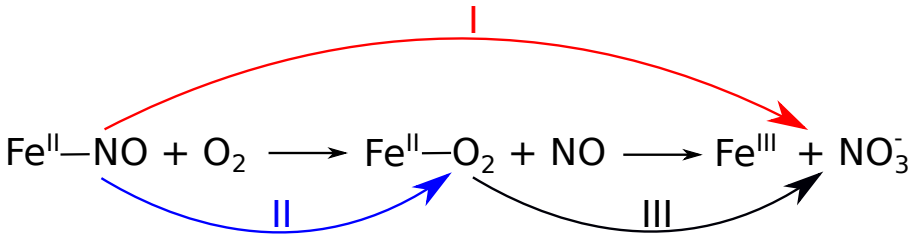

(6.1)

Here we demonstrate that the conformational ensemble and electronic properties of the transition state between NO and O_2-bound truncated Hemoglobin can be characterized using atomistic simulations. Despite various previous kinetic studies[261,263,264,266,267] the mechanistic aspects of NO/O_2 competition in globins at a molecular level are poorly understood. The very first step for dioxygenation is the ligand exchange reaction in which NO is displaced by O_2 (process II, see equation 6.1). The experimental first order rate found for the overall reaction (process I, see equation 6.1) is 1.0×10^{-4} to $4.4\times\ 10^{-3}$ s^{-1} depending on the protein.[268–270] In all these cases the first step - replacement of NO by O_2 - is assumed to be rate limiting. However, such rates are often measured in a rather indirect way. For example, for the Fe^{II}—NO + O_2 reaction the NO-dissociation reaction in trHb(II)-NO + CO was considered[268,269]. From this reaction the dissociation rate ($1.3 \pm 0.3 \times 10^{-4}$ s^{-1}) was measured. Next, the rate for NO_3^- formation (process I see equation 6.1, 1.2×10^{-4} s^{-1}) was obtained from optical measurements on the trHb(II)-NO + O_2 reaction and fitting to a single exponential decay. Such an approach is, however, not sensitive to potentially relevant intermediates and only reports on the overall reaction. To better understand competitive ligand dynamics and reactivity around the heme-iron computational methods are potentially useful provided that they are of sufficiently high quality.

Multi-state adiabatic reactive molecular dynamics (MS-ARMD) are a powerful means to follow ligand-binding and unbinding processes in condensed phase systems[80,271]. This approach combines empirical energy functions to allow bond breaking and bond formation to take place with the sampling efficiency of conventional MD simulations to provide a quantitative understanding of whether and how temporal and structural changes are related.

6.3. Methods

6.3.1. Molecular Dynamics Simulations

The computational system was set up by solvating truncated hemoglobin (trHbN) (protein data bank entry 1IDR)[272] in a TIP3P[114] orthorhombic periodic box of size $78.25 \times 53.10 \times 53.10$ Å^3 (see Figure 6.1). The X-ray structure of trHbN contains an Fe-bound O_2 and a free NO ligand. All MD simulations were carried out with the CHARMM[?] suite of programs and the CHARMM22[101] force field. The equations of motions were propagated using the Velocity-Verlet integrator with a time step $\Delta t = 1$ fs and the non-bonded interactions (electrostatic and Lennard-Jones) were truncated at a distance of 14 Å and switched between 10 and 12 Å. After minimization the solvated system was heated to 300 K and equilibrated for 1 ns. Following this, 10 ns equilibrium MD simulations for both, the bound Fe-NO and bound Fe-O_2 were performed which yielded an RMSD for the protein relative to the X-ray structure of 0.983 Å and 1.100 Å, respectively.

Umbrella Sampling: For the US the system was constrained at different values of the progression coordinate $\rho = \frac{d_{\mathrm{Fe-O_2}}}{d_{\mathrm{Fe-NO}}}$. Here d is the distance between Fe and the geometric center of the O_2 and NO ligands, respectively. The umbrella potential is $U = k(\rho - \rho_0)^2$ and in all simulations the force constant was $k = 100$ kcal/mol[238]. For each umbrella window, 100 ps of equilibrium simulations were carried out and data was accumulated for 2.5 ns. A total of 25 windows between 0.25 and 2.75 along the reaction coordinate for the ligand exchange reaction were performed. The weighted histogram analysis method (WHAM) was used to combine the simulated data and to compute the free energy profile[239]. The error bars were computed from 10 different umbrella sampling results.

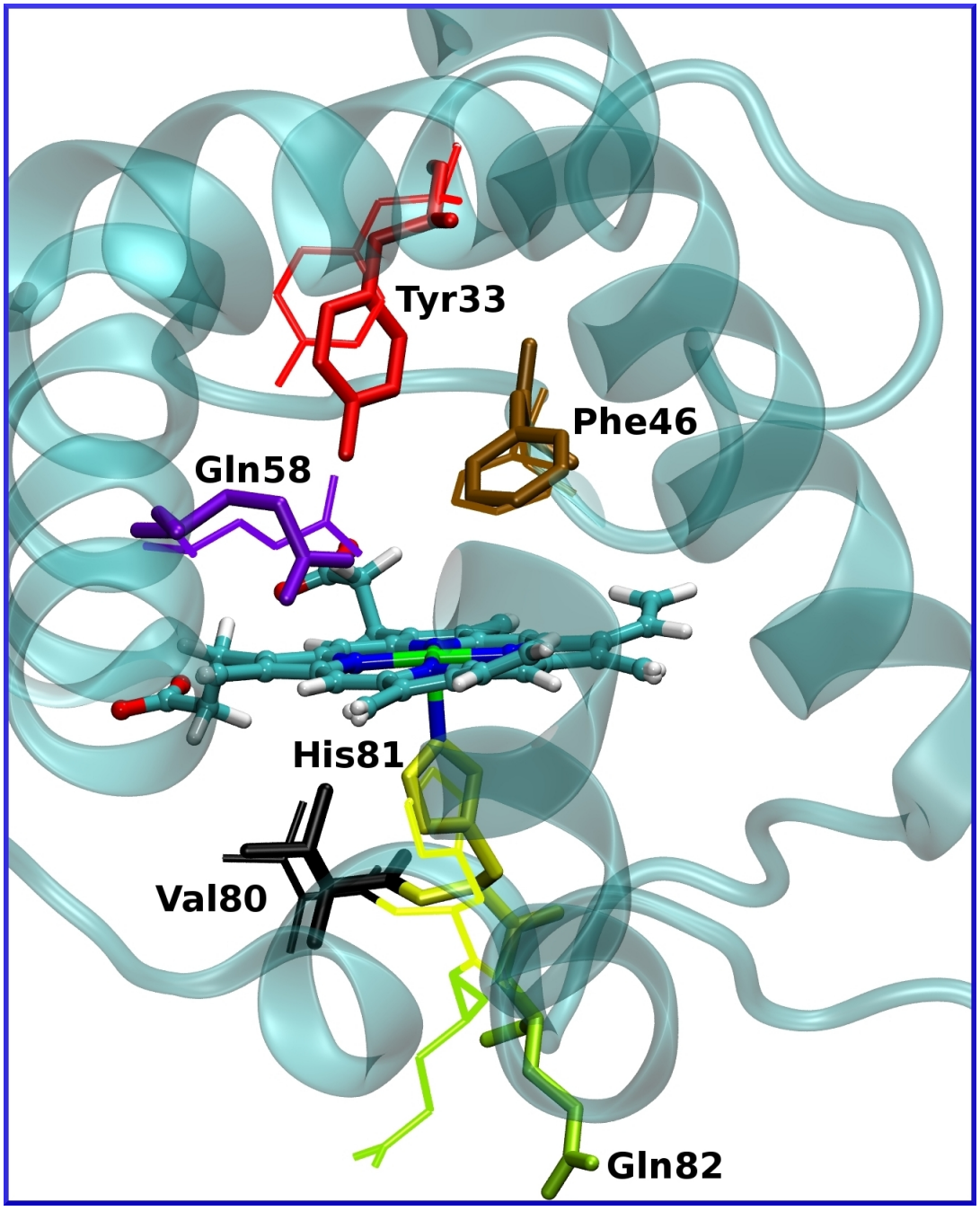

Figure 6.1.: The active site of truncated hemoglobin (ribbon representation) solvated in water. The side chains involved in the ligand exchange reaction are shown in licorice and line representations for bound Fe-NO and the transition state, respectively. The diatomic ligands are not shown. The color code for individual atoms: Fe (green), C (cyan), N (blue), O (red) and H (white).

6.3.2. Force field parametrization for MS-ARMD

MS-ARMD requires force fields for each of the states considered. A "state" is defined by atom connectivities. In practice, the majority of the force field terms in each of the states will be identical except for the bonds that are broken or formed. In the present case, e.g., the equilibrium O_2 bond length differs for the free and Fe–O_2 bound ligand. For the denitrification reaction considered here, four different states were considered: i) Fe-$O_A O_B$ + NO, ii) Fe-$O_B O_A$ + NO, iii) Fe-NO + O_2 and iv) Fe + NO + O_2. Here, O_A and O_B are introduced to label the two ways in which the O_2 molecule can bind to the heme-iron.

6.3.3. Ab initio Calculations for Fe-O_2 complex

Ab initio calculations for heme-bound O_2 (the Fe-O_2 coordination) are complicated due to closely spaced electronic states. A brief summary for the problems encountered are provided here to motivate resorting to experimental data for parametrizing the force fields.

Previous work[273] using the BP86 functional with double-ζ basis set with two p, one d and one f function for iron and 6-31G(d) basis set for all atoms, provides completely different binding curves for triplet (^{3}A) and singlet (^{1}A) states of Fe-O_2 with very low dissociation energy of $\sim$ 5 kcal/mol. Also, earlier calculation[274] for three different geometries considering Fe-oop motion (with the Fe atom, in or out of the porphyrin plane), rigid scans along the Fe-O_2 distance using BLYP and double-ζ plus extra polarization (DNPP) basis set in an implicit solvent results in potential energy curves that neither reflect the results from Refs.[273,275]. On the other hand, a small change of the B3LYP functional (15% exact exchange) together with the cc-pvtz(-f) basis set reproduces the experimental dissociation energy for the Fe-O_2 complex only if dispersion corrections are included[276]. Compared to this, the B3LYP functional with LANL2DZ basis set for iron and the 6-31G(d,p) basis set for all atoms gives a double crossing potential energy surface (^{1}A $\rightarrow$ ^{3}A $\rightarrow$ ^{7}A) with a small dissociation energy of 7 kcal/mol[277]. Finally, recent calculation using the TPSSh-D3/def2-TZVPP/Cosmo ($\epsilon = 10$) method including dispersion corrections gives triplet (^{3}A) and singlet (^{1}A) dissociation curves parallel to each other with a dissociation energy of $\sim$ 15.7 kcal/mol for the singlet state which is 1 kcal/mol larger than the experimental value[275]. Notably, the same method overestimates the ΔH of O_2 binding by 2 kcal/mol. Furthermore, using standard B3LYP-D3/def2-TZVPP/Cosmo calculations ($\epsilon = 10$) without

dispersion correction yields a very low dissociation energy of 5 kcal/mol.[275]. Our own attempts using the B3LYP/6-31G(d,p) method always find the lowest state to be a triplet which does not agree with experiment (singlet state ^{1}A).

Because electronic structure calculations for Fe-O_2 complexes are notoriously difficult, it was decided to base the parametrization of the Fe-NO and Fe-O_2 interactions solely on experimental data. The experimentally determined dissociation energy of NO towards protonated iron tetrapyridylporphyrin is 24.0 ± 0.7 kcal/mol[278] whereas the dissociation energy of O_2 in myoglobin is 14.6 kcal/mol[278]. A similar dissociation energy (24.8 ± 0.7 kcal/mol) for Fe-NO was found for the doubly protonated iron tetrapyridylporphyrin which is an analog of the heme subunit[?] . Hence, $D_e(O_2) = 14.6$ kcal/mol and $D_e(NO) = 24.0$ kcal/mol were used to describe the Morse potentials for Fe-O_2 and Fe-NO, respectively, and the remaining parameters β and r_e for both bonds were those from the literature[279]. The different force field parameters for the five- and six-coordinated states are those from earlier studies[280] except for the Fe-O_2 and Fe-NO bonds. All MS-ARMD force field parameters are provided in Table 6.1

Table 6.1.: MS-ARMD force field parameters used to study the ligand exchange reaction in trHbN. Atom types are reported in the Figure below, where N/O_A and O/O_B label the NO and O_AO_B (i.e O_2) ligands, respectively.

	State I ($Fe-O_AO_B$ + NO)			**State II** ($Fe-O_BO_A$ + NO)			**State III** ($Fe-NO+O_2$)			**State IV** ($Fe+NO+O_2$)		
Bond (Morse)	D_e (kcal/mol)	β ($Å^{-1}$)	r_e (Å)	D_e (kcal/mol)	β ($Å^{-1}$)	r_e (Å)	D_e (kcal/mol)	β ($Å^{-1}$)	r_e (Å)	D_e (kcal/mol)	β ($Å^{-1}$)	r_e (Å)
$Fe-O_AO_B$	14.600	2.215	1.800									
$Fe-O_BO_A$				14.600	2.215	1.800						
$Fe-NO$							24.000	2.776	1.732			
Bond (Harm)		k (kcal/mol/$Å^2$)	r_e (Å)		k (kcal/mol/$Å^2$)	r_e (Å)		k ($Å^{-1}$)	r_e (Å)		k (kcal/mol/$Å^2$)	r_e (Å)
Fe-NPH		270.200	1.980		270.200	1.980		270.200	1.980		272.200	2.100
Fe-NE2		65.000	2.200		65.000	2.200		65.000	2.200		65.000	2.100
Angle		k (kcal/mole/rad^2)	θ_e (°)		k (kcal/mole/rad^2)	θ_e (°)		k (kcal/mole/rad^2)	θ_e (°)		k (kcal/mole/rad^2)	θ_e (°)
$Fe-O_A-O_B$		67.500	122.00									
$Fe-O_B-O_A$					67.500	122.000						
$Fe-N-O$								70.000	134.000			
$O_A-Fe-NE2$		75.000	165.000									
$O_B-Fe-NE2$					75.000	165.000						
$N-Fe-NE2$								50.000	179.000			
$NPH-Fe-NPH$		14.390	90.000		14.390	90.000		14.390	90.000		80.000	90.000
$NPH-Fe-NE2$		50.000	90.000		50.000	90.000		50.000	90.000		50.000	107.0
Charges		(e)			(e)			(e)			(e)	
O_A		-0.131			-0.129			0.021			0.021	
O_B		-0.129			-0.131			-0.021			-0.021	
N		0.021			0.021			0.127			0.021	
O		-0.021			-0.021			-0.227			-0.021	
L-J potential		ϵ (kcal/mol)	$R_{min}/2$ (Å)		ϵ (kcal/mol)	$R_{min}/2$ (Å)		ϵ (kcal/mol)	$R_{min}/2$ (Å)		ϵ (kcal/mol)	$R_{min}/2$ (Å)
O_A		0.159	2.050		0.159	2.050		0.159	2.050		0.159	2.050
O_B		0.159	2.050		0.159	2.050		0.159	2.050		0.159	2.050
N		0.200	2.000		0.200	2.000		0.200	2.000		0.200	2.000
O		0.159	2.050		0.159	2.050		0.159	2.050		0.159	2.050

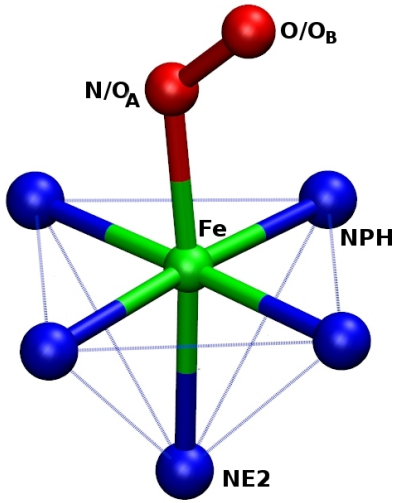

6.4. Results

Based on this parametrization the system (see Figure 6.1) was set up for MS-ARMD[80] and umbrella sampling[238] (US) simulations for determining the free energy for ligand exchange using progression coordinate $\rho = \frac{d_{\mathrm{Fe-O_2}}}{d_{\mathrm{Fe-NO}}}$. The free energy barrier associated with the $\mathrm{Fe^{II}-NO+O_2 \rightarrow Fe^{II}-O_2+NO}$ reaction is 19.7 kcal/mol, see Figure 6.2. Using transition state theory, such a barrier corresponds to a rate of 4.5×10^{-3} $\mathrm{s^{-1}}$ which agrees well with rates from experiments (Process I, see equation 6.1) ranging from 1.0×10^{-4} to 4.4×10^{-3} $\mathrm{s^{-1}}$ depending on the protein considered and confirms that the ligand exchange reaction (process II, see equation 6.1) is the rate limiting step[268,269]. This is also consistent with the fact that process III ($\mathrm{Fe\text{-}O_2 + NO \rightarrow Fe(III) + NO_3^-}$) is fast as it occurs on the 10 to 100 ps time scale[265].

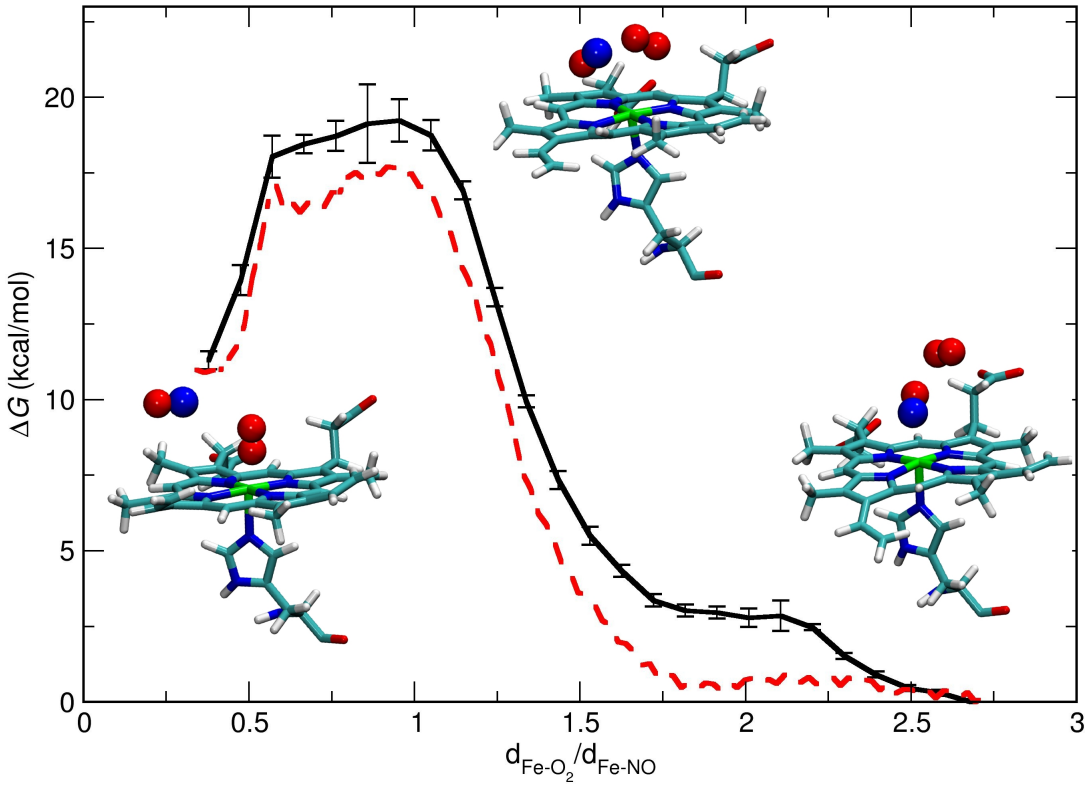

Figure 6.2.: Free energy profile including error bars for the ligand exchange reaction in WT trHbN from umbrella sampling (black trace). The structures of $\mathrm{O_2}$-bound ($\rho = 0.25$), NO-bound ($\rho = 2.5$) and the transition state ($\rho \sim 1.0$) are also shown. The TS region is broad and involves a distributed structural ensemble. The red dashed line shows the free energy profile for the ligand exchange reaction for the Y33A mutant.

For a more complete characterization of the transition state, an additional 1 ns umbrella sampling simulation around the TS was carried out. The transition state ensemble sampled is broad, see Figure 6.2. From these simulations, 100 coordinates and velocities were collected, each separated by 10 ps. Using these initial coordinates and velocities, ligand rebinding simulations were performed for 100 ps, which occurs 86 out of the 100 simulations. 45 trajectories finish in an Fe-NO bound state, whereas 41 trajectories end up with Fe-O_2 and in 14 cases both ligands remain unbound. The rebinding fraction for the NO ligand is 52.3 % compared to 47.7 % for O_2. Hence, the transition state ensemble is representative of a true TS which is characterized by an equal probability for the two processes[281,282].

The electronic properties of the TS can be further characterized from DFT calculations. For an ensemble of 50 structures energies of the (His-heme + O_2 + NO) system were determined in their ^2A, ^4A and ^6A states. The correlation between the ^2A and the MS-ARMD energies is $R^2 = 0.98$, whereas the ^4A and ^6A do not correlate at all (see Figure 6.3). Furthermore, it is found from additional DFT calculations that at infinite separation the ^2A state correlates with either a ^{1}heme $+^2$ (O_2 + NO) or a ^{3}heme $+^2$ (O_2 + NO) whereas other asymptotic states can be excluded (see Figure 6.4).

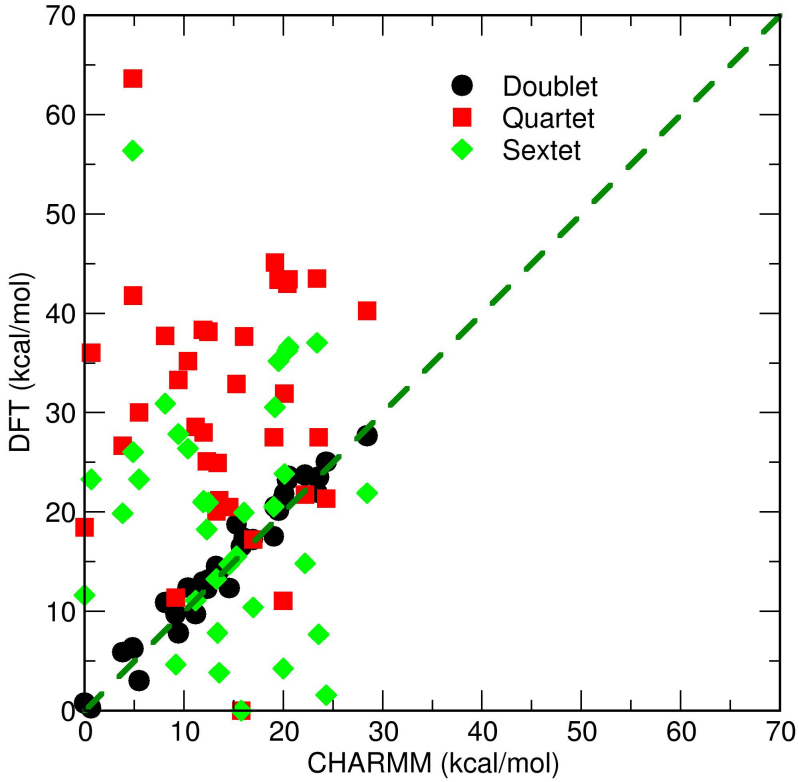

Figure 6.3.: Comparison of energies between DFT (B3LYP/6-31G(d,p)) and MS-ARMD for 50 structures from the TS ensemble. Doublet state DFT energies correlates well ($R^2 = 0.98$) with the MS-ARMD energies which provides an assignment of the TS to a ^2A electronic state.

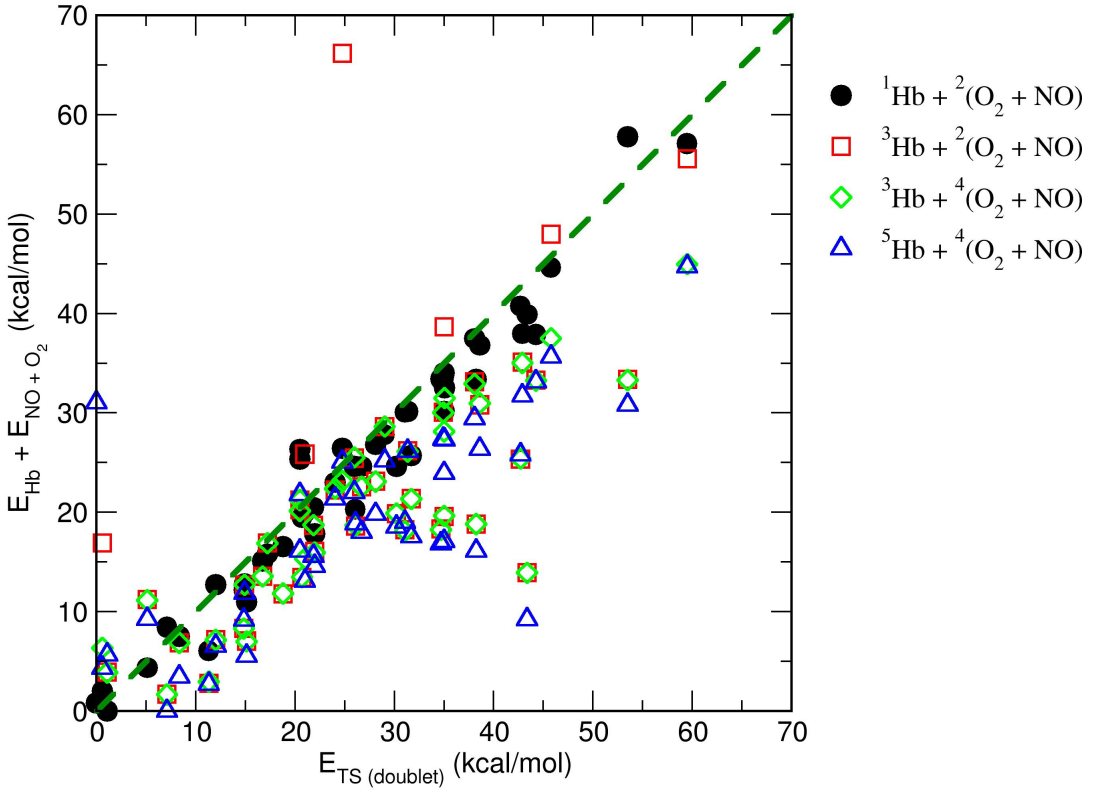

Figure 6.4.: Spin contribution of Hb and ligands towards doublet state of the TS. All calculations carried out at the level of B3LYP/6-31G(d,p). Correlation between total energies of the ^2A (Hb + O_2 + NO) complex with the possible asymptote ^{1}Hb+^{2}(O_2+NO), ^{3}Hb+^{2}(O_2+NO), ^{3}Hb +^{4} (O_2 + NO) and ^{5}Hb +^{4} (O_2 + NO). The good correlation ($R^2 = 0.96$) between the ^2A (Hb + O_2 + NO) and the ^{1}Hb +^{2} (O_2 + NO) fragments suggests that Hb is in a low spin state in the TS.

Experimentally, it is found that the NO dioxygenation rate depends on the particular type of globin, i.e. Ngb[268,283], Hb[268,269,284,285], or Mb[269]. For example, mutation of the Phe62 gate residue (controls the diffusion of ligands to the active site cavity through channel I) in trHbN to Trp, Tyr, Ala and Ile, decreases the overall rate for NO dioxygenation by a factor of two to three[200,286,287]. It has also been observed that the Y33A mutation leads to doubling the rate compared to the WT protein.[284,288] This illustrates the importance of the environment which constitutes the active site for the NO dioxygenation reaction. To quantify the role of the active site residues in the ligand exchange reaction, separate 1 ns equilibrium MD simulations for the reactant and product states were carried out. The average protein structures from the simulations and the umbrella sampling at the TS ($\rho = 1.01$) were computed and compared. The most prominent differences for the WT are found in regions where His81 binds to the

heme and in the active site (see Figure 6.5).

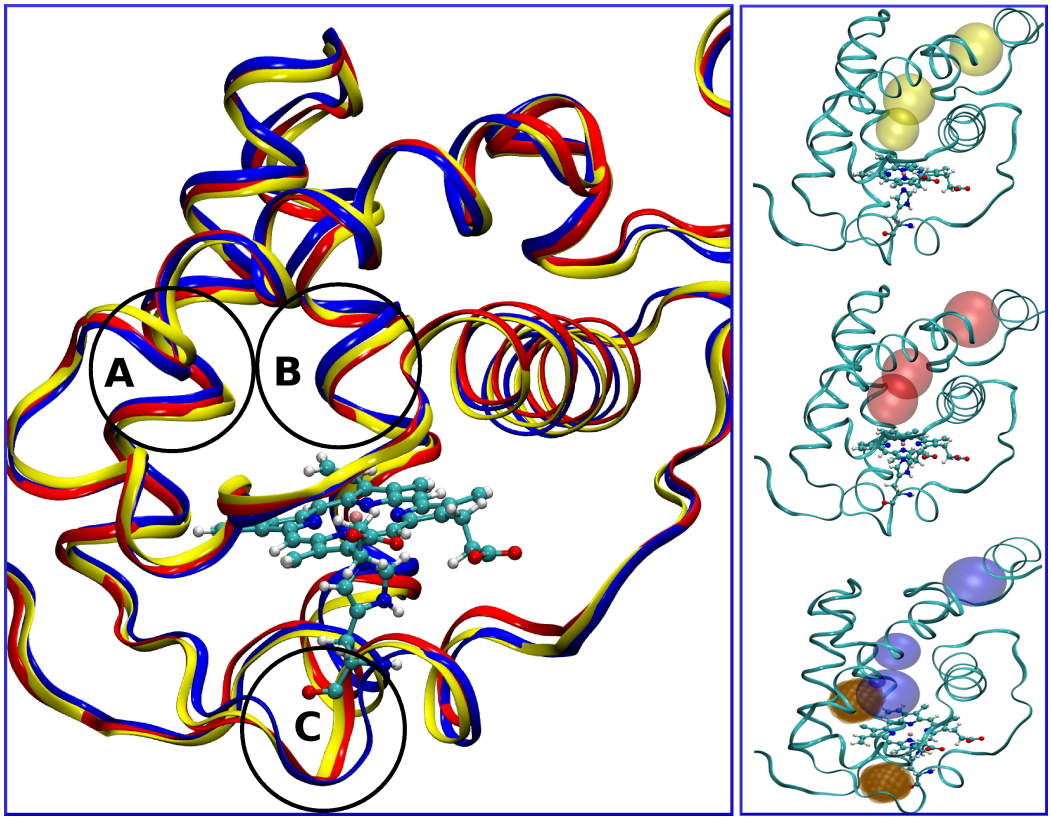

Figure 6.5.: Average protein structure of the three states: Fe-NO (yellow), Fe-O_2 (red) and the transition state (Fe + NO + O_2) (blue) (left panel). The most important differences between the three structures are encircled and labeled by A, B and C (active site and proximal site). Pockets in the reactant (upper right), product (right middle) and transition state (bottom right) are shown in yellow, red and blue spheres respectively. The extra pocket in the proximal side and the expanded pocket in the active site for transition state are shown in dotted ocher spheres (right bottom). The cavity/pocket volumes were computed using the GHECOM program.[289]

The interplay between side chain orientation and ligand exchange was further characterized by comparing Ramachandran (Φ, Ψ) maps for the Fe-NO bound and transition state structures. The average Φ and Ψ values from the simulations for the Fe-NO + O_2 state are in accord with the X-ray structure of trHbN (see Figures 6.6 and 6.7).[272] Both Φ and Ψ angle distributions were computed for three active site residues: Tyr33, Phe46, Gln58. For Tyr33, $P(\Phi)$ in the reactant and TS state are very similar (see

Figures 6.6 and 6.10) whereas the peak position and distribution for $P(\Psi)$ differ. Similar observations were made for Phe46 (see Figure 6.7 and 6.8). However, for Gln58, both distributions, $P(\Phi)$ and $P(\Psi)$ are very similar in the two states (see Figures 6.7 and 6.8). Differences in $P(\Phi)$ and $P(\Psi)$ are also found for Val80, His81 and Gln82 (see Figures 6.6, 6.10 and 6.7) which are at the proximal site of the heme (see Figure 6.1). Most prominently, the $\Psi-$orientation of His81 between the reactant and the transition states changes by $-70°$. This is a consequence of the out-of-plane motion of the iron atom in the transition state compared to the bound state (see Figure 6.10). This rotation and the motion of the Fe-atom toward the proximal site lead to an increased size of the active site in the TS.

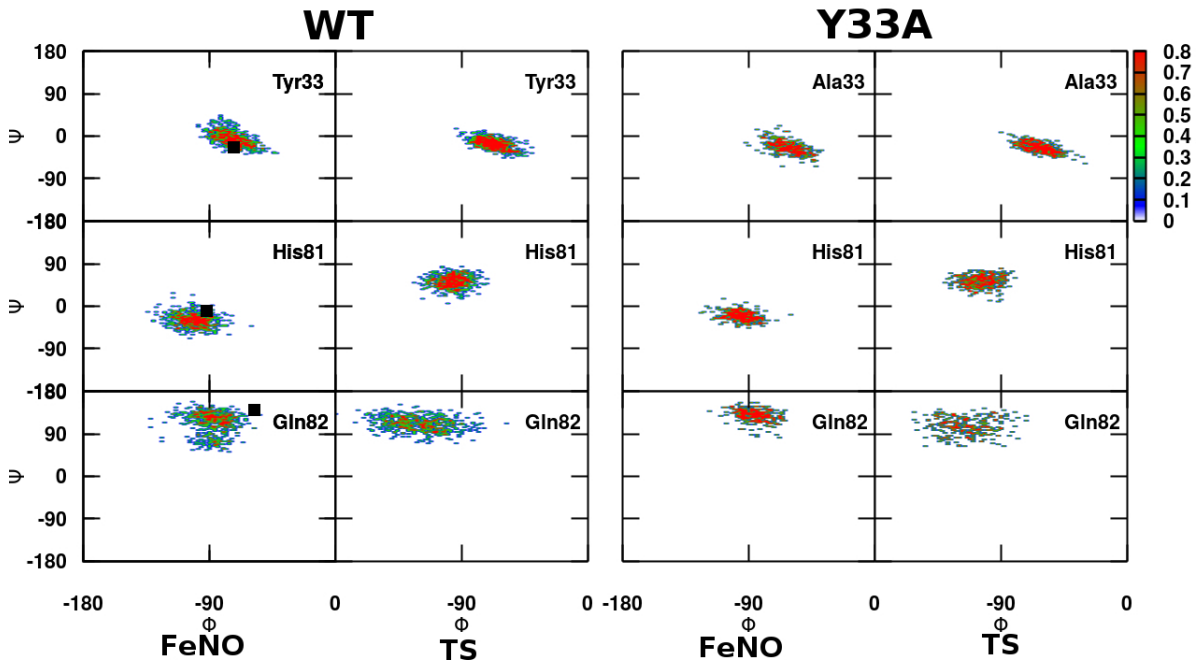

Figure 6.6.: Distribution of Φ and Ψ angles of the side chains in bound Fe-NO and transition state for the wild type (WT) protein (left panel) and for the Y33A mutant (right panel). The black squares in WT indicate results from the X-ray structure[272]. The deviation for Q82 may be due to its solvent exposure, see Figure 6.1. The $(\phi_{\max}, \psi_{\max})$ values of Tyr33 in the Fe-NO and the TS for the WT are $(-70.0°, -15.0°)$ and $(-67.0°, -7.0°)$ respectively. On the other hand, for the Y33A mutant the values for Ala33 are $(-65.3°, -26.6°)$ and $(-63.5°, -23.9°)$ in the Fe-NO and TS respectively.

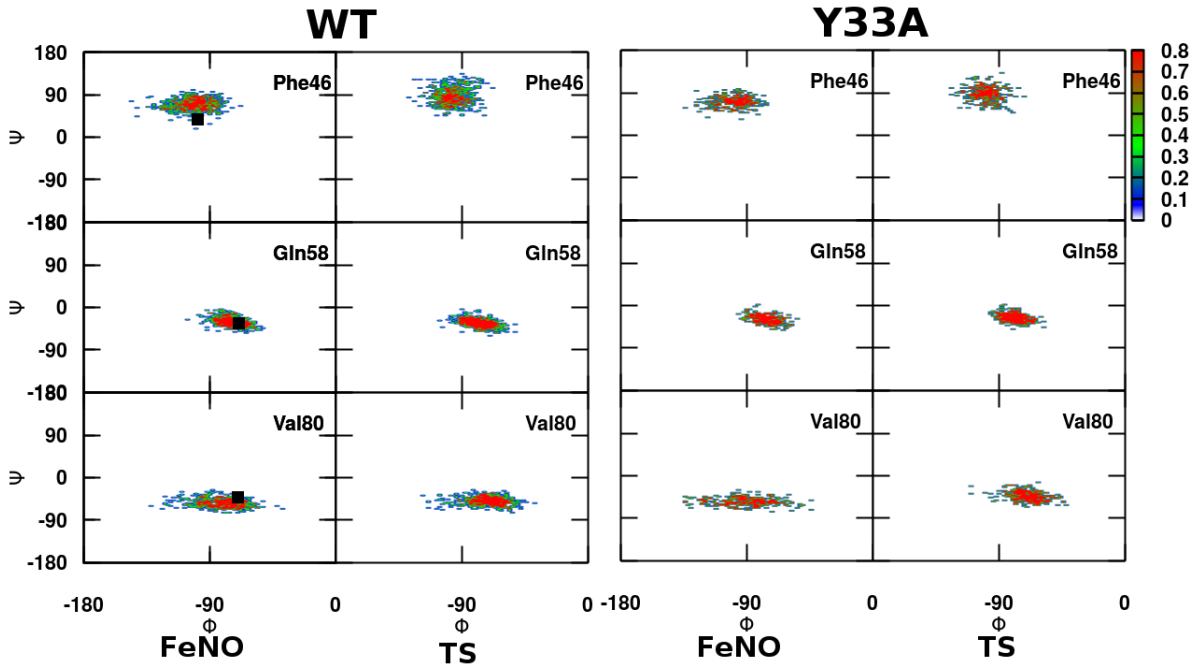

Figure 6.7.: Distribution of Φ and Ψ angles of the side chains in bound Fe-NO and transition state for the wild type (WT) protein (left panel) and for the Y33A mutant (right panel). The black squares in WT represents the X-ray structure data[272]. All angles are in degree.

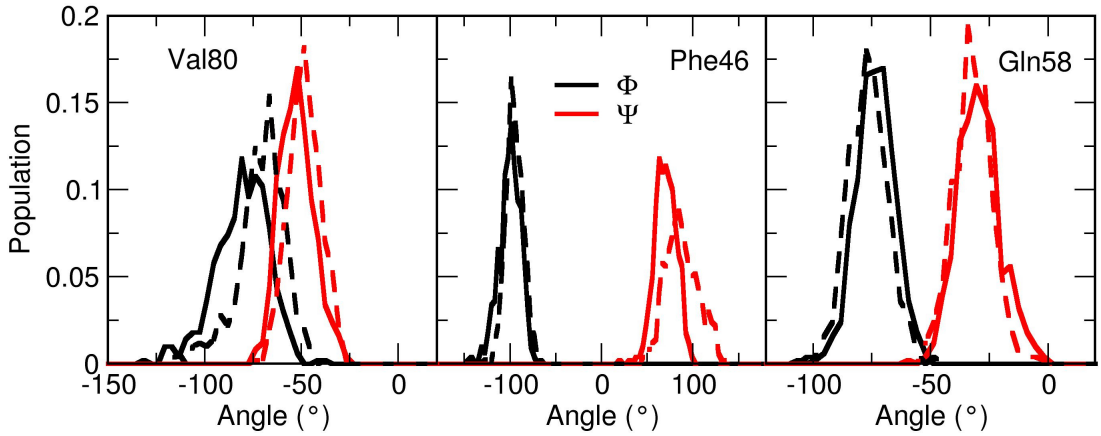

Figure 6.8.: Distributions $P(\Phi)$ (black) and $P(\Psi)$ (red) of the Ramachandran angles for Fe-NO bound (solid line) and the transition state (dashed line) for WT protein. The distributions were built from 1 ns of equilibrium simulation for Fe-NO state and umbrella sampling in the TS ($\rho = 1.01$).

The insignificant changes in the probability distributions for Gln58 between the reactant and the TS (see Figure 6.8) indicate that this residue does not participate appreciably in the reaction and hence

the overall rate should depend little on mutating this residue. This is indeed found in experiments for which a minor increase from $(2.2 \pm 0.3) \times 10^8$ $M^{-1}s^{-1}$ (WT) to $(2.6 \pm 0.4) \times 10^8$ $M^{-1}s^{-1}$ (Q58A) is found for nitrate formation.[284] Conversely, the width and position of the maximum of $P(\Psi)$ for Tyr33 differs appreciably between reactant and TS and for Val80 both, $P(\Phi)$ and $P(\Psi)$, change. Concomitantly, the rate coefficients increase by more than a factor of two (and hence the free energy barrier decreases by ≈ 1.7 kcal/mol based on transition state theory) upon Alanine mutation of these two residues, to $(4.6 \pm 0.9) \times 10^8$ $M^{-1}s^{-1}$ and $(4.7 \pm 0.6) \times 10^8$ $M^{-1}s^{-1}$, for the Y33A and V80A mutants, respectively.[284].

To support these hypotheses, the free energy surface and reaction barrier height for ligand exchange was explicitly determined from umbrella sampling simulations for the Y33A mutant. In agreement with the above argument, the barrier height for the $Fe^{II} - NO + O_2 \rightarrow Fe^{II} - O_2 + NO$ reaction is lowered by $\Delta\Delta G = 1.5$ kcal/mol compared to WT, see Figure 6.2 which is close to the value determined from experiment (~ 1.7 kcal/mol) . The difference between WT and the Y33A mutant can be traced back to the stabilizing interaction between the ligands and the -OH group of the Tyrosine at position 33 in the WT protein which is absent in the Alanine-mutant.

The distributions $P(\Phi, \Psi)$ were also determined for Ala33 in the Y33A mutant, see Figure 6.6 and were found to be almost identical in the reactant and at the TS (see Figure 6.9). Hence, Ala33 participates little in the reaction. This is different from the situation in the WT where $P(\Phi, \Psi)$ for Tyr33 in the reactant and at the TS state differs.

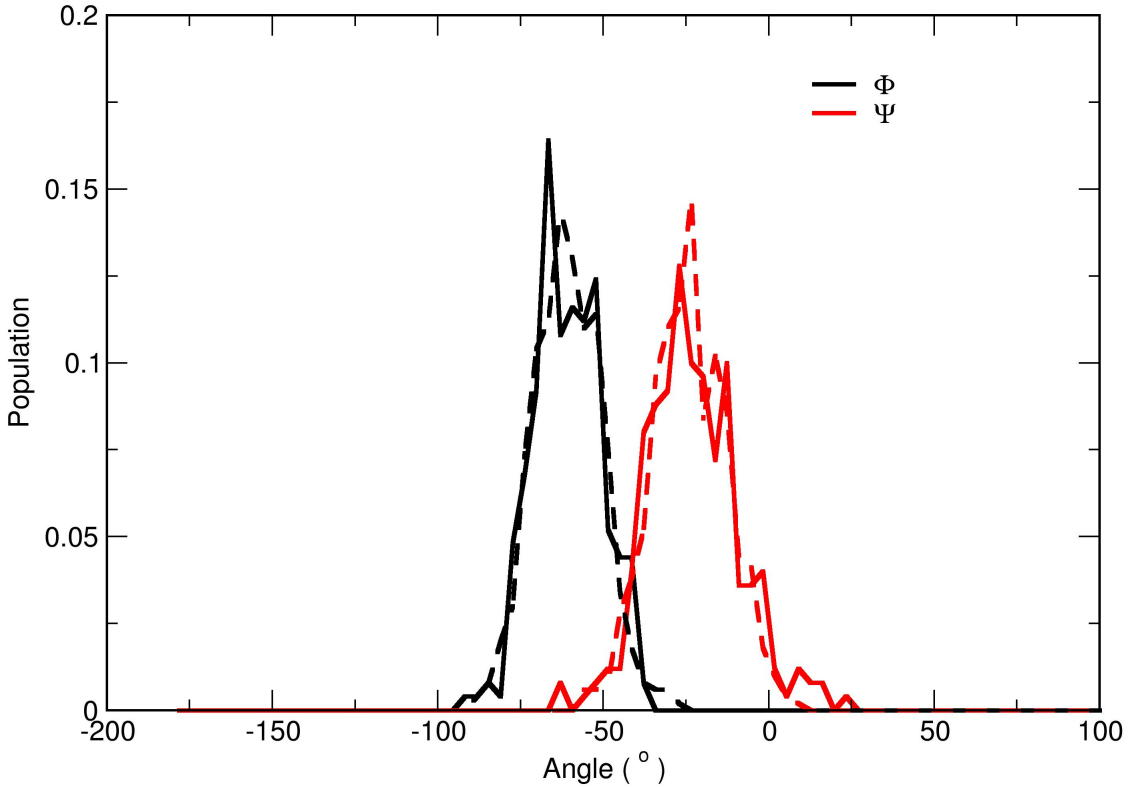

Figure 6.9.: Distributions $P(\Phi)$ (black) and $P(\Psi)$ (red) of the Ramachandran angles for Fe-NO bound (solid line) and the TS (dashed line) for Ala33 residue in the Y33A mutant. The distributions were built from 1 ns of equilibrium simulation for Fe-NO state and umbrella sampling in the TS ($\rho = 1.01$).

Upon ligand dissociation (NO or O_2) from the heme the Fe atom moves below the porphyrin plane towards His81 which leads to further displacements of residues Val80, Gln82 and Gly83. This generates a new pocket on the proximal side in the TS with a volume of $\sim$ 30 Å^3 which corresponds to the volume of one water molecule (see Figure 6.5). Also, the size of the active site (distal site) pocket in the TS (197 Å^3) expands by $\sim$ 40 Å^3 compared to the Fe-NO bound state (157 Å^3) due to the iron atom moving below the heme-plane and the movement of the Phe46 ring (Figure 6.8).

Comparison of the volume of the active site in the TS indicates an increase by more than 10 % in pocket volume between the WT (197 Å^3) and Y33A mutant (234 Å^3). This increase in pocket volume increases entropy and hence decreases the free energy and the barrier for rebinding. This agrees with a decrease in the FeNO+O_2 $\rightarrow$ FeO_2+NO barrier height for the Y33A mutant (red curve in Figure 6.2) compared to WT (black trace in Figure 6.2) by 1.5 kcal/mol. The decreased barrier for Y33A may be

due to favorable entropic contributions. An enthalpic origin of that magnitude is unlikely due to the small dipole moments of both ligands. This was explicitly verified by computing average interaction energies (over 500 structures from 1 ns simulation in the TS) between the ligand and the surrounding protein which are −3.83 kcal/mol for the WT compared with −3.40 kcal/mol for the Y33A mutant i.e only a difference of $\Delta H = 0.4$ kcal/mol compared to $\Delta G = 1.5$ kcal/mol, leaving $-T\Delta S = 1.1$ kcal/mol for the entropic contribution. It is also of interest to note that the interaction energies of the free ligands in the WT reactant (Fe-NO) and product (Fe-O_2) states are –2.7 and –2.8 kcal/mol, respectively, which also suggests that in moving to the transition state a certain amount of entropic penalty is to be paid due to spatial constraint.

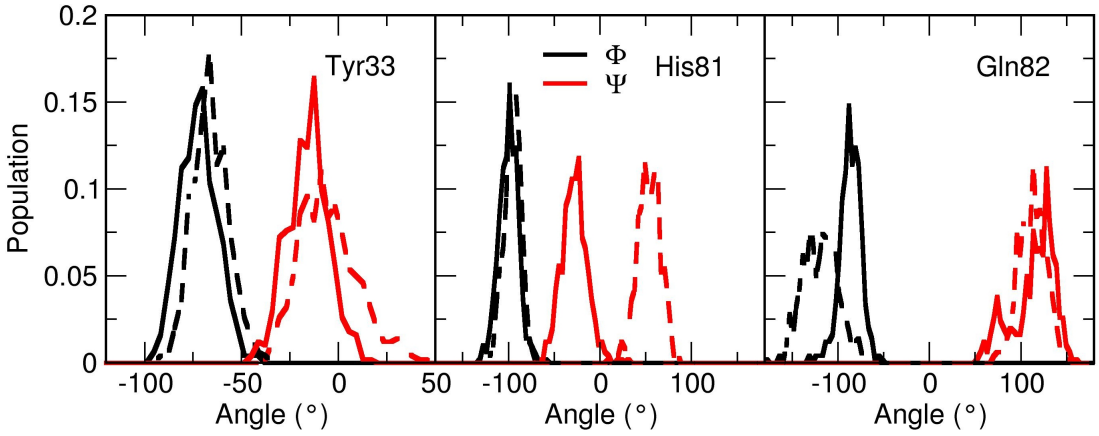

Figure 6.10.: Distributions $P(\Phi)$ (black) and $P(\Psi)$ (red) of the Ramachandran angles for Fe-NO bound (solid line) and the transition state (dashed line) for WT protein. The distributions for the Fe-NO bound state (solid line) and TS state (dashed line) were built from 1 ns equilibrium and umbrella simulations $\rho = 1.01$ respectively.

6.5. Conclusion

Overall, the computed rate for the ligand exchange reaction (process II) of 4.5×10^{-3} s^{-1} compares well with experiments (process I) that range from 1.0×10^{-4} to 4.4×10^{-3} s^{-1} depending on the protein considered[268,269] and is consistent with a 10 to 100 ps time scale ($k \sim 10^{10}$ s^{-1}) for process III (NO_3^- formation).[265] Analysis of the conformational dynamics in the reactant and transition state suggests that Tyr33 and Val80 directly affect the rate of process II whereas Gln58 does not. This also

agrees with experiments which find rate enhancements by more than a factor of two for the Y33A and V80A mutants but insignificant changes for the Q58A variant. Ramachandran maps for the reactant and TS structures suggest that the transition state in the WT is loose (more flexible) which is also found from analysis of the conformational ensemble, see Figure 6.6 and 6.10. On the other hand, the dissociating ligands never leave the active site. Hence, the present simulations provide a quantitative assessment of the ligand exchange reaction (process II) for both the WT and Y33A mutant of trHbN. The analysis of the underlying dynamics provides interpretations for the influence of individual residues on the transition state ensemble and the reaction as a whole. This is the basis for simulation-guided exploration of the molecular basis of reaction mechanisms in enzyme catalysis.

Part IV.

Conclusion

7. Conclusions and Outlook

Considering the high applicability of TM towards catalysis, light-harvesting materials design and enzymatic reactions, it is of utmost importance to understand the physical and chemical properties of the TM complexes at the molecular level. In this thesis, we present the development of force fields and new methods for atomistic simulation of TM complexes to explore the exchange and reorganization of solvent molecules around the metal complexes in response to structural change and electronic excitation of TM complexes. Furthermore, using atomistic simulations, metastable and transition states involved during the photo-dissociation and enzymatic reactions in metalloenzymes are characterized, this not only complemented experimental findings but also has potential to be very helpful for protein engineering. The two chapters in this thesis provides brief introduction about the TM complexes and their application followed by a detailed theoretical description of the different methods employed.

Chapter 3 describes the degree of solvation and solvation dynamics involving several spectroscopically characterized states in aqueous $[Fe(bpy)_3]$ solution using the VALBOND force field. It is observed that during the photo-excitation of $[Fe_{LS}(bpy)_3]$ to $[Fe(III)(bpy)_3]$ state, the degree of solvation decreases. However, relaxation from the non-equilibrium excited state to the $[Fe(II)_{HS}(bpy)_3]$ state occurs in the picosecond time scale and this does not affect the degree of solvation. It is also noted that the change in the degree of solvation during the spin crossover process is largely dependent on the charge delocalization and only a little on structural changes in the metal complexes. One of the main advantages of force field methods is that they allow to sampling of conformational dynamics in a meaningful fashion, from which reliable average properties can be determine and compared with experimental data for atomistic interpretation of dynamics of solutes in solution.

In chapter 4, the control of hydration around the metal center in the bioactive ligand containing $[Cu(Imidazole)_4]$ complex was studied by using both atomistic and hybrid QM/MM simulations. From the simulations, it is found that there are two asymmetrically coordinated axial water molecules around the metal center this is confirmed by computing XANES spectra along the MD trajectories. The

exchange dynamics of solvent water molecules around the metal atom takes place on the picosecond time scale and is coupled to the Cu-Imidazole plane (Cu-N-N-N dihedral angle). Thus, by slightly modifying the ligands in the metal complexes, it is possible to control the hydration structure around the metal center and hence its catalytic properties.

In the next chapter the nitric oxide dioxygenation reaction in trHbN was explored. In particular, starting from a HbNO state, the very first step of the reaction sequence, the ligand exchange reaction was studied. The computed rate constant agrees very well with the experimental rate and also confirms that the ligand exchange reaction is the rate determining step. From detailed analysis of the conformational dynamics of active site in the reactant and transition state, it is observed that both Tyr33 and Val80 directly affect the rate of the ligand exchange reaction. This is specifically confirmed by Y33A mutation, where the barrier associated with the ligand exchange reaction is lowered by ~ 2 kcal/mol compared to WT protein. On the other hand Gln58 has an insignificant effect on the ligand exchange reaction. This kind of simulation-guided exploration of the reaction mechanisms at the molecular level in enzyme catalysis provides a basis for tuning their efficiency.

The final chapter describes the development of the new multi-state VALBOND (MS-VALBOND) and its successful application to a wide range of systems including hypervalent molecules ClF_3, transition metal complexes (cisplatin) and chemical reactions $BrMe + Cl^- \rightarrow Br^- + MeCl$ in aqueous solution. The implementation of MS-VALBOND is based on the original VALBOND force field and allows easy switching between each of the resonance structures characterized by individual force fields. The main advantage of this method is that using a single force field parameter set, highly complicated and unusual shapes of hypervalent molecules and metal complexes can be captured. Furthermore, this method is also very useful to describe pseudoratation in hypervalent molecules and specifically the barrier associated with the pseudoratation in ClF_3 is very well reproduced compared to its experimental value. This method is also capable of simulating chemical reactions both in the gas-phase and condensed phase as it considers charge redistribution on the atoms during the reaction based on the weights to each of the states involved, which is very important for correctly describing the solute-solvent interactions.

In summary, this thesis provides important information about the difficulty in modeling TM complexes and how the metal specialized VALBOND force field overcome those difficulties to describe unusual shapes in metal complexes and hypervalent molecules. On the other hand both MS-ARMD and MS-VALBOND methods are very useful to describe the reaction mechanism and their kinetics both in the gas-phase and condensed phase by using simple empirical force fields which allows one to sample

the conformational space extensively. To enhance the applicability of the newly developed methods and force fields, further works are desirable by applying the force fields to biological systems containing TM ions.

Part V.

Bibliography

References

[1] Greenwood, N.; ; Earnshaw, A. *Chemistry of the Elements (Second Edition)*; Butterworth-Heinemann: Oxford, 1997.

[2] Jain, S.; Reddy, K.; Gupta, C.; Reddy, T. *J. Phys. Chem. Lett.* **1973**, *21*, 150–152.

[3] Smit, T.; Haas, C.; Nieuwpoort, W. *Theor. Chim. Acta.* **1977**, *43*, 277–286.

[4] Dahl, E. W.; Szymczak, N. K. *Ang. Chem. Intern. Ed.* **2016**, *55*, 3101–3105.

[5] Dudev, M.; Wang, J.; Dudev, T.; Lim, C. *J. Phys. Chem. B* **2006**, *110*, 1889–1895.

[6] Richens, D. *Chem. Rev.* **2005**, *105*, 1961–2002.

[7] Noyori, R.; Kitamura, M. In *Modern Synthetic Methods*; Modern Synthetic Methods, Vol. 5; pp 115–198.

[8] Andreini, C.; Bertini, I.; Cavallaro, G.; Holliday, G. L.; Thornton, J. M. *J. Biol. Inorg. Chem.* **2008**, *13*, 1205–1218.

[9] Dennison, C. *Coord. Chem. Rev.* **2005**, *249*, 3025 – 3054.

[10] Zhang, C.; Zhang, F.; Zhou, P.; Zhang, C. *Front. Biol.* **2016**, *11*, 119–131.

[11] Solomon, E. I.; Szilagyi, R. K.; DeBeer George, S.; Basumallick, L. *Chem. Rev.* **2004**, *104*, 419–458.

[12] Pufahl, R. A.; Singer, C. P.; Peariso, K. L.; Lin, S.-J.; Schmidt, P. J.; Fahrni, C. J.; Culotta, V. C.; Penner-Hahn, J. E.; O'Halloran, T. V. *Science* **1997**, *278*, 853–856.

[13] Hazes, B.; Kalk, K. H.; Hol, W. G.; Magnus, K. A.; Bonaventura, C.; Bonaventura, J.; Dauter, Z. *Prot. Sci.* **1993**, *2*, 597–619.

[14] Gross, E. *Photosynth. Res.* **1993**, *37*, 103–116.

[15] Canters, G.; Gilardi, G. *FEBS Lett.* **1993**, *325*, 39–48.

[16] Ratajczak, R.; Mitchell, R.; Haehnel, W. *Biochim. Biophys. Acta.* **1988**, *933*, 306–318.

[17] Giardina, B.; Messana, I.; Scatena, R.; Castagnola, M. *Crit. Rev. Biochem. Mol. Biol.* **1995**, *30*, 165–196.

[18] Jagirdar, B. R. *Resonance* **1999**, *4*, 63–81.

[19] 19.

[20] Rondi, A.; Rodriguez, Y.; Feurer, T.; Cannizzo, A. *Acc. Chem. Res* **2015**, *48*, 1432–1440.

[21] Kalyanasundaram, K.; Gratzel, M. *Coord. Chem. Rev.* **1998**, *177*, 347–414.

[22] Wadman, S. H.; Kroon, J. M.; Bakker, K.; Havenith, R. W. A.; van Klink, G. P. M.; van Koten, G. *Organometallics* **2010**, *29*, 1569–1579.

[23] Hage, K. E.; Brickel, S.; Hermelin, S.; Gaulier, G.; Schmidt, C.; Bonacina, L.; van Keulen, S. C.; Bhattacharyya, S.; Chergui, M.; Hamm, P.; Rothlisberger, U.; Wolf, J.-P.; Meuwly, M. *Struct. Dyn.* **2017**, *4*, 061507.

[24] Kim, T. K.; Lee, J. H.; Wulff, M.; Kong, Q.; Ihee, H. *Chem. Phys. Chem.* **2009**, *10*, 1958–1980.

[25] Ihee, H.; Wulff, M.; Kim, J.; Adachi, S. *Int. Rev. Phys. Chem.* **2010**, *29*, 453–520.

[26] Ki, H.; Oang, K. Y.; Kim, J.; Ihee, H. *Ultrafast X-Ray Crystallography and Liquidography*; Johnson, MA and Martinez, TJ, Ed.; Annual Review of Physical Chemistry, Vol. 68, 2017.

[27] Bressler, C.; Chergui, M. *Chem. Rev.* **2004**, *104*, 1781–1812.

[28] Chen, L. *Ann. Rev. Phys. Chem.* **2005**, *56*, 221–254.

[29] Chergui, M.; Zewail, A. H. *Chem. Phys. Chem.* **2009**, *10*, 28–43.

[30] Rini, M.; Dreyer, J.; Nibbering, E. T. J.; Elsaesser, T. *Chem. Phys. Lett.* **2003**, *374*, 13–19.

[31] Herbst, J.; Heyne, K.; Diller, R. *Science* **2002**, *297*, 822–825.

[32] Popp, A.; Ujj, L.; Atkinson, G. H. *Proc. Natl. Acad. Sci.* **1996**, *93*, 372–376.

[33] Cannizzo, A.; van Mourik, F.; Gawelda, W.; Zgrablic, G.; Chergui, M. *Ang. Chem. Intern. Ed.* **2006**, *45*, 3174–3176.

[34] Moret, M.-E.; Tavernelli, I.; Chergui, M.; Rothlishberger, U. *Chem. Eur. J.* **2010**, *16*, 5889–5894.

[35] Szymczak, J. J.; Hofmann, F. D.; Meuwly, M. *Phys. Chem. Chem. Phys.* **2013**, *15*, 6268–6277.

[36] Moret, M.-E.; Tavernelli, I.; Rothlisberger, U. *J. Phys. Chem. B* **2009**, *113*, 7737–7744.

[37] Daku, L. M. L.; Hauser, A. *J. Phys. Chem. Lett.* **2010**, *1*, 1830–1835.

[38] Jin, H.; Goyal, P.; Das, A. K.; Gaus, M.; Meuwly, M.; Cui, Q. *J. Phys. Chem. B* **2016**, *120*, 1894–1910.

[39] Malavasi, L. *Structural Characterization Techniques: Advances and Applications in Clean Energy*; Pan Stanford, 2016.

[40] Eriksson, L. *Theoretical Biochemistry: Processes and Properties of Biological Systems*; Theoretical and Computational Chemistry; Elsevier Science, 2001.

[41] Thiel, W. *Wiley Interdiscip. Rev. Comput. Mol. Sci.* **2014**, *4*, 145–157.

[42] Stewart, J. *J. Comput. Chem.* **1989**, *10*, 209–220.

[43] Dewar, M.; Zoebisch, E.; Healy, E.; Stewart, J. *J. Am. Chem. Soc.* **1985**, *107*, 3902–3909.

[44] Thiel, W.; Voityuk, A. *J. Chem. Phys.* **1996**, *100*, 616–626.

[45] Dewar, M. J.; Jie, C.; Yu, J. *Tetrahedron* **1993**, *49*, 5003 – 5038.

[46] Savary, F.; Furet, E.; Weber, J. *Comput. Theor. Chem.* **1995**, *330*, 191 – 195.

[47] Ridley, J.; Zerner, M. *Theor. Chim. Acta* **1973**, *32*, 111–134.

[48] McNamara, J. P.; Hillier, I. H. *Phys. Chem. Chem. Phys.* **2007**, *9*, 2362–2370.

[49] Jorgensen, W.; Tiradorives, J. *J. Am. Chem. Soc.* **1988**, *110*, 1657–1666.

[50] MacKerell, A.; et al. *J. Phys. Chem. B* **1998**, *102*, 3586–3616.

[51] Weiner, S.; Kollman, P.; Case, D.; Singh, U.; Ghio, C.; Alagona, G.; Profeta, S.; Weiner, P. *J. Am. Chem. Soc.* **1984**, *106*, 765–784.

[52] Deeth, R. J.; Anastasi, A.; Diedrich, C.; Randell, K. *Coord. Chem. Rev.* **2009**, *253*, 795–816.

[53] Shriver, D. F.; Atkins, P. W. . *Inorganic chemistry*, 3rd ed.; New York W.H. Freeman and Co, 1999.

[54] Deeth, R. *Coord. Chem. Rev.* **2001**, *212*, 11–34.

[55] Root, D. M.; Landis, C. R.; Cleveland, T. *J. Am. Chem. Soc.* **1993**, *115*, 4201–4209.

[56] Cleveland, T.; Landis, C. R. *J. Am. Chem. Soc.* **1996**, *118*, 6020–6030.

[57] Landis, C. R.; Cleveland, T.; Firman, T. K. *J. Am. Chem. Soc.* **1998**, *120*, 2641–2649.

[58] Firman, T. K.; Landis, C. R. *J. Am. Chem. Soc.* **2001**, *123*, 11728–11742.

[59] Tubert-Brohman, I.; Schmid, M.; Meuwly, M. *J. Chem. Theory Comput.* **2009**, *5*, 530–539.

[60] Hohenberg, P.; Kohn, W. *Phys. Rev.* **1964**, *136*, B864–B871.

[61] Ziesche, P.; Kurth, S.; Perdew, J. P. *Comput. Mater. Sci.* **1998**, *11*, 122 – 127.

[62] Becke, A. D. *J. Chem. Phys.* **1993**, *98*, 5648–5652.

[63] Elstner, M. *Theor. Chem. Acc.* **2006**, *116*, 316–325.

[64] Elstner, M.; Seifert, G. *Phil. Trans. R. Soc. A* **2014**, *372*, 20120483.

[65] Larsen, E.; La Mar, G. N. *J. Chem. Educ.* **1974**, *51*, 633.

[66] Gresh, N.; Cisneros, G. A.; Darden, T. A.; Piquemal, J.-P. *J. Chem. Theo. Comp.* **2007**, *3*, 1960–1986.

[67] Piquemal, J.; Gresh, N.; Giessner-Prettre, C. *J. Phys. Chem. A* **2003**, *107*, 10353–10359.

[68] Piquemal, J.-P.; Chevreau, H.; Gresh, N. *J. Chem. Theo. Comp.* **2007**, *3*, 824–837.

[69] Devereux, M.; Gresh, N.; Piquemal, J.-P.; Meuwly, M. *J. Comp. Chem.* **2014**, *35*, 1577–1591.

[70] Pauling, L. *J. Am. Chem. Soc.* **1931**, *53*, 1367–1400.

[71] Pauling, L. *The Nature of the Chemical Bond and the Structure of Molecules and Crystals: An Introduction to Modern Structural Chemistry*; George Fisher Baker Non-Resident Lecture Series; Cornell University Press, 1960.

[72] Pauling, L. *Proc. Natl. Acad. Sci. U. S. A.* **1976**, *73*, 274–275.

[73] Leach, A. *Molecular Modelling: Principles and Applications*; Pearson Education; Prentice Hall, 2001.

[74] Frenkel, D.; Smit, B. *Understanding Molecular Simulation: From Algorithms to Applications*; Academic Press, 2001.

[75] Verlet, L. *Phys. Rev.* **1967**, *159*, 98–103.

[76] Rappé, A.; Pietsch, M.; Wiser, D.; Hart, J.; Bormann-Rochotte, L.; Skiff, W. *Molecular Engineering* **1997**, *7*, 385–400.

[77] van Duin, A.; Dasgupta, S.; Lorant, F.; Goddard, W. *J. Phys. Chem. A* **2001**, *105*, 9396–9409.

[78] Warshel, A.; Weiss, R. M. *J. Am. Chem. Soc.* **1980**, *102*, 6218–6226.

[79] Nutt, D. R.; Meuwly, M. *Biophys. J.* **2006**, *90*, 1191–1201.

[80] Nagy, T.; Yosa Reyes, J.; Meuwly, M. *J. Chem. Theo. Comp.* **2014**, *10*, 1366–1375.

[81] Danielsson, J.; Meuwly, M. *J. Chem. Theo. Comp.* **2008**, *4*, 1083–1093.

[82] Tarnovsky, A. N.; Gawelda, W.; Johnson, M.; Bressler, C.; Chergui, M. *J. Phys. Chem. B* **2006**, *110*, 26497–26505.

[83] Yano, J.; Yachandra, V. K. *Photosynth. Res.* **2009**, *102*, 241–254.

[84] Joly, Y. *Phys. Rev. B* **2001**, *63*, 1251201–12512010.

[85] Stöhr, J. *NEXAFS Spectroscopy*; Springer Series in Surface Sciences; Springer, 1992.

[86] Seah, M. P.; Dench, W. A. *1978 NPL Report Chem 82*, National Physics Laboratory, Div. of Chemical Standards, Teddington, Middlesex.

[87] Bunau, O.; Joly, Y. *J. Phys. Condens. Matter* **2009**, *21*.

[88] Bressler, C.; Milne, C.; Pham, V.-T.; ElNahhas, A.; van der Veen, R. M.; Gawelda, W.; Johnson, S.; Beaud, P.; Grolimund, D.; Kaiser, M.; Borca, C. N.; Ingold, G.; Abela, R.; Chergui, M. *Science* **2009**, *323*, 489–492.

[89] Zhang, W.; et al. *Nature* **2014**, *509*, 345–8.

[90] Haldrup, K.; et al. *J. Phys. Chem. A* **2012**, *116*, 9878–9887.

[91] Harlang, T. C. B.; et al. *Nat. Chem.* **2015**, *7*, 883–889.

[92] Balzani, V.; Juris, A.; Venturi, M.; Campagna, S.; Serroni, S. *Chem. Rev.* **1996**, *96*, 759–833.

[93] Savini, A.; Bellachioma, G.; Ciancaleoni, G.; Zuccaccia, C.; Zuccaccia, D.; Macchioni, A. *Chem. Comm.* **2010**, *46*, 9218–9219.

[94] Gaus, M.; Cui, Q.; Elstner, M. *WIREs: Comput Mol Sci* **2014**, *4*, 49–61.

[95] Piquemal, J.-P.; Williams-Hubbard, B.; Fey, N.; Deeth, R. J.; ohad Gresh, N.; Giessner-Prettre, C. *J. Comp. Chem.* **2003**, *24*, 1963–1970.

[96] Deeth, R. J. *Inorg. Chem.* **2008**, *47*, 6711–6725.

[97] Comba, P.; Hambley, T. W.; Martin, B. *Molecular Modelling of Inorganic Compounds*; VCH, Weinheim, 1995.

[98] Tubert-Brohman, I.; Schmid, M.; Meuwly, M. *J. Chem. Theo. Comp.* **2009**, *5*, 530–539.

[99] Huang, J.; Häussinger, D.; Gellrich, U.; Seiche, W.; Breit, B.; Meuwly, M. *J. Phys. Chem. B* **2012**, *116*, 14406–14415.

[100] Szymczak, J. J.; Hofmann, F. D.; Meuwly, M. *Phys. Chem. Chem. Phys.* **2013**, *15*, 6268–6277.

[101] A. D. MacKerell, J.; et al. *J. Phys. Chem. B* **1998**, *102*, 3586.

[102] Root, D. M.; Landis, C. R.; Cleveland, T. *J. Am. Chem. Soc.* **1993**, *115*, 4201–4209.

[103] Cleveland, T.; Landis, C. R. *J. Am. Chem. Soc.* **1996**, *118*, 6020–6030.

[104] Landis, C. R.; Cleveland, T.; Firman, T. *J. Am. Chem. Soc.* **1998**, *120*, 2641–2649.

[105] Vanommeslaeghe, K.; Hatcher, E.; Achary, S.; Kundu, S.; Zhong, J.; Shim, E.; Darian, O.; Lopes, P.; Vorobyov, I.; MacKerell Jr, A. D. *J. Comp. Chem.* **2010**, *31*, 671–690.

[106] Reed, A. E.; Weinstock, R. B.; Weinhold, F. *J. Chem. Phys.* **1985**, *83*, 735–746.

[107] Frisch, M. J.; et al.; *Gaussian09 Revision D.01*; Gaussian Inc. Wallingford CT 2009.

[108] Hehre, W. J.; Ditchfield, R.; Pople, J. A. *J. Chem. Phys.* **1972**, *56*, 2257–2261.

[109] Meuwly, M.; Becker, O. M.; Stote, R.; Karplus, M. *Biophys. Chem.* **2002**, *98*, 183–207.

[110] Inskeep, R. G. *J. Inorg. Nucl. Chem.* **1962**, *24*, 763 – 776.

[111] Gerasimova, T. P.; Katsyuba, S. A. *Dalton Trans.* **2013**, *42*, 1787–1797.

[112] Batten, S. R.; Murray, K. S.; Sinclair, N. J. *Acta. Cryst. C* **2000**, *56*, 320.

[113] Figgis, B. N.; Skelton, B. W.; White, A. H. *Aust. J. Chem.* **1978**, *31*, 57.

[114] Jorgensen, W. L.; Chandrasekhar, J.; Madura, J. D.; Impey, R. W.; Klein, M. L. *J. Chem. Phys.* **1983**, *79*, 926–935.

[115] Ryckaert, J.-P.; Ciccotti, G.; Berendsen, H. J. C. *J. Comp. Phys.* **1977**, *23*, 327–341.

[116] Impey, R. W.; Madden, P. A.; McDonald, I. R. *J. Phys. Chem.* **1983**, *87*, 5071–5083.

[117] Koneshan, S.; Rasaiah, J. C.; Lynden-Bell, R. M.; Lee, S. H. *J. Phys. Chem. B* **1998**, *102*, 4193–4204.

[118] McQuarrie, D. A. *Statistical Mechanics*; Harper's Chemistry Series: New York, 1976.

[119] Allen, M. P.; Tildesley, D. J. *Computer Simulation of Liquids*; Clarendon Press, Oxford, 1987.

[120] Alexander, B. D.; Dines, T. J.; Longhurst, R. W. *J. Chem. Phys.* **2008**, *352*, 19–27.

[121] Villalba, M. E. C.; Güida, J.; Varetti, E.; Aymonino, P. *Spectrochimica Acta Part A: Molecular and Biomolecular Spectroscopy* **2001**, *57*, 367 – 373.

[122] van der Spoel, D.; van Maaren, P. J.; Berendsen, H. J. C. *J. Chem. Phys.* **1998**, *108*, 10220–10230.

[123] Ludwig, R.

[124] Moret, M.-E.; Tavernelli, I.; Röthlisberger, U. *J. Phys. Chem. B* **2009**, *113*, 7737–7744.

[125] Lee, M. W.; Carr, J. K.; Göllner, M.; Hamm, P.; Meuwly, M. *J. Chem. Phys.* **2013**, *139*, 054506.

[126] Park, J.; Lee, T.; Park, J.; Lim, M. *J. Phys. Chem. B* **2013**, *117*, 2850–2863.

[127] Elber, R. *Recent Developments in Theoretical Studies of Proteins*; World Scientific: Singapore, New Jersey, London, Hongkong, 1996.

[128] Auböck, G.; Chergui, M. *Nat. Chem.* **2015**, *7*, 629–633.

[129] Pham, V.; Penfold, T.; van der Veen, R.; Lima, F.; El Nahhas, A.; Johnson, S.; Beaud, P.; Abela, R.; Bressler, C.; Tavernelli, I.; Milne, C.; Chergui, M. *J. Am. Chem. Soc.* **2011**, *133*, 12740–12748.

[130] Bressler, C.; Chergui, M. *Ann. Rev. Phys. Chem.* **2010**, *61*, 263–82.

[131] Lascombe, J.; Perrot, M. *Farad. Discuss.* **1978**, *66*, 216–230.

[132] Willis, M. S.; Monaghan, S. A.; Miller, M. L.; McKenna, R. W.; Perkins, W. D.; Levinson, B. S.; Bhushan, V.; Kroft, S. H. *Am. J. Clin. Path.* **2005**, *123*, 125–131.

[133] Prashanth, L.; Kattapagari, K.; Chitturi, R.; Baddam, V.; Prasad, L. *J. Dr. NTR Univ. Health Sci.* **2015**, *4*, 75–85.

[134] Josko, O.; Natasa, S. *J. Clinic. Toxicol.* **2011**, *S:3001*, 1–18.

[135] Adman, E. T. In *Metalloproteins: Structural Aspects*; C.B. Anfinsen, F. M. R., John T. Edsall; Eisenberg, D. S., Eds.; Advances in Protein Chemistry, Vol. 42; Academic Press, 1991; pp 145 – 197.

[136] MacPherson, I. S.; Murphy, M. E. P. *Cell. Mol. Life Sci.* **2007**, *64*, 2887–2899.

[137] Culotta, V. C.; Klomp, L. W. J.; Strain, J.; Casareno, R. L. B.; Krems, B.; Gitlin, J. D. *J. Biol. Chem.* **1997**, *272*, 23469–23472.

[138] Carrera, F.; Marcos, E. S.; Merkling, P. J.; Chaboy, J.; Muòoz-Pàez, A. *Inorg. Chem.* **2004**, *43*, 6674–6683.

[139] Lippard, S. J.; Berg, J. *Principles of Bioinorganic Chemistry*; Principles of Bioinorganic Chemistry; University Science Books, 1994.

[140] Blumberger, J. *J. Am. Chem. Soc.* **2008**, *130*, 16065–16068.

[141] Yang, L.; Powell, D. R.; Houser, R. P. *Dalton Trans.* **2007**, 955–964.

[142] Festa, R. A.; Thiele, D. J. *Current Biology* **2011**, *21*, R877 – R883.

[143] Tainer, J.; Getzoff, E.; Richardson, J.; Richardson, D. *Nature* **1983**, *306*, 284–287.

[144] Tian, S.; Liu, J.; Cowley, R. E.; Hosseinzadeh, P.; Marshall, N. M.; Yu, Y.; Robinson, H.; Nilges, M. J.; Blackburn, N. J.; Solomon, E. I.; Lu, Y. **2016**, *8*, 670–677.

[145] Das, A. K.; Solomon, R. V.; Hofmann, F.; Meuwly, M. *J. Phys. Chem. B* **2016**, *120*, 206–216.

[146] Penfold, T. J.; Curchod, B. F. E.; Tavernelli, I.; Abela, R.; Rothlisberger, U.; Chergui, M. *Phys. Chem. Chem. Phys.* **2012**, *14*, 9444–9450.

[147] Persson, I.; Persson, P.; Sandstrom, M.; Ullstrom, A.-S. *J. Chem. Soc. Dalton Trans.* **2002**, 1256–1265.

[148] Chaboy, J.; Munoz-Paez, A.; Merkling, P.; Marcos, E. *J. Chem. Phys.* **2006**, *124*, 0645091–0645099.

[149] Powell, D. H.; Furrer, P.; Pittet, P.-A.; Merbach, A. E. *J. Phys. Chem.* **1995**, *99*, 16622–16629.

[150] Bryantsev, V. S.; Diallo, M. S.; van Duin, A. C. T.; Goddard III, W. A. *J. Phys. Chem. A* **2008**, *112*, 9104–9112.

[151] Pasquarello, A.; Petri, I.; Salmon, P.; Parisel, O.; Car, R.; Toth, E.; Powell, D.; Fischer, H.; Helm, L.; Merbach, A. *Science* **2001**, *291*, 856–859.

[152] Okan, S.; Salmon, P. *Mol. Phys.* **1995**, *85*, 981–998.

[153] Salmon, P. S.; Neilson, G. W.; Enderby, J. E. *J. Phys. C: Solid State Physics* **1988**, *21*, 1335–1349.

[154] Salmon, P.; Neilson, G. *J. Phys. Condens. Matter* **1989**, *1*, 5291–5295.

[155] Neilson, G.; Newsome, J.; Sandstrom, M. *J. Chem. Soc. Faraday Trans. II* **1981**, *77*, 1245–1256.

[156] Benfatto, M.; D'Angelo, P.; Della Longa, S.; Pavel, N. *Phys. Rev. B* **2002**, *65*, 1742051–1742055.

[157] Frank, P.; Benfatto, M.; Qayyam, M.; Hedman, B.; Hodgson, K. O. *J. Chem. Phys.* **2015**, *142*, 0843101–08431014.

[158] Beagley, B.; Eriksson, A.; Lindgren, J.; Persson, I.; Pettersson, L.; Sandstrom, M.; Wahlgren, U.; White, E. *J. Phys.-Condens. Mat.* **1989**, *1*, 2395–2408.

[159] Sham, T.; Hastings, J.; Perlman, M. *Chem. Phys. Lett.* **1981**, *83*, 391–396.

[160] Frank, P.; Benfatto, M.; Hedman, B.; Hodgson, K. O. *Inorg. Chem.* **2012**, *51*, 2086–2096.

[161] Liu, X.; Cheng, J.; Sprik, M. *J. Phys. Chem. B* **2015**, *119*, 1152–1163.

[162] Amira, S.; Spangberg, D.; Hermansson, K. *Phys. Chem. Chem. Phys.* **2005**, *7*, 2874–2880.

[163] Liu, X.; Lu, X.; Meijer, E. J.; Wang, R. *Phys. Chem. Chem. Phys.* **2010**, *12*, 10801–10804.

[164] Blumberger, J.; Bernasconi, L.; Tavernelli, I.; Vuilleumier, R.; Sprik, M. *J. Am. Chem. Soc.* **2004**, *126*, 3928–3938.

[165] de Almeida, K. J.; Murugan, N. A.; Rinkevicius, Z.; Hugosson, H. W.; Vahtras, O.; Agren, H.; Cesar, A. *Phys. Chem. Chem. Phys.* **2009**, *11*, 508–519.

[166] Schwenk, C.; Rode, B. *J. Chem. Phys.* **2003**, *119*, 9523–9531.

[167] Schwenk, C.; Rode, B. *J. Am. Chem. Soc.* **2004**, *126*, 12786–12787.

[168] Marini, G.; Liedl, K.; Rode, B. *J. Phys. Chem. A* **1999**, *103*, 11387–11393.

[169] Xiang, J. Y.; Ponder, J. W. *J. Chem. Theo. Comp.* **2014**, *10*, 298–311.

[170] El-Nahas, A.; Tajima, N.; Hirao, K. *J. Mol. Struc-Theochem.* **1999**, *469*, 201–213.

[171] Burda, J.; Pavelka, M.; Simanek, M. *J. Mol. Struc. Theochem.* **2004**, *683*, 183–193.

[172] Frank, P.; Benfatto, M.; Szilagyi, R.; D'Angelo, P.; Della Longa, S.; Hodgson, K. *Inorg. Chem.* **2005**, *44*, 1922–1933.

[173] Bryantsev, V. S.; Diallo, M. S.; Goddard, W. A., III *J. Phys. Chem. A* **2009**, *113*, 9559–9567.

[174] Rios-Font, R.; Sodupe, M.; Rodriguez-Santiago, L.; Taylor, P. R. *J. Phys. Chem. A* **2010**, *114*, 10857–10863.

[175] Becke, A. D. *J. Chem. Phys.* **1993**, *98*, 5648–52.

[176] Hay, P. J.; Wadt, W. R. *J. Chem. Phys.* **1985**, *82*, 270–283.

[177] Evans, D. J.; Holian, B. L. *J. Chem. Phys.* **1985**, *83*, 4069–4074.

[178] Gaus, M.; Cui, Q.; Elstner, M. *J. Chem. Theo. Comp.* **2011**, *7*, 931–948.

[179] Elstner, M.; Porezag, D.; Jungnickel, G.; Elsner, J.; Haugk, M.; Frauenheim, T.; Suhai, S.; Seifert, G. *Phys. Rev. B* **1998**, *58*, 7260–7268.

[180] Cui, Q.; Elstner, M.; Kaxiras, E.; Frauenheim, T.; Karplus, M. *J. Phys. Chem. B* **2001**, *105*, 569–585.

[181] Gaus, M.; Goez, A.; M. Elstner *J. Chem. Theo. Comp.* **2012**, *9*, 338–354.

[182] Gaus, M.; Jin, H.; Demapan, D.; Christensen, A. S.; Goyal, P.; Elstner, M.; Cui, Q. *J. Chem. Theo. Comp.* **2015**, *11*, 4205–4219.

[183] Rowley, C. N.; Roux, B. *J. Chem. Theo. Comp.* **2012**, *8*, 3526–3535.

[184] Norman, M. R. *Phys. Rev. B* **2015**, *91*, 140505(R).

[185] Hay, P.; Wadt, W. *J. Chem. Phys.* **1985**, *82*, 270–283.

[186] Lomachenko, K. A.; Garino, C.; Gallo, E.; Gianolio, D.; Gobetto, R.; Glatzel, P.; Smolentsev, N.; Smolentsev, G.; Soldatov, A. V.; Lamberti, C.; Salassa, L. *Phys. Chem. Chem. Phys.* **2013**, *15*, 16152–16159.

[187] Gaur, A.; Shrivastava, B. D. In *International Conference on Recent Trends in Physics (ICRTP 2014)*; Univ Grants Commiss; Journal of Physics Conference Series, Vol. 534; International Conference on Recent Trends in Physics (ICRTP), Devi Ahilya Univ, Sch Phys, Indore, India, Feb 22-23, 2014.

[188] Migliorati, V.; Mancini, G.; Chillemi, G.; Zitolo, A.; D'Angelo, P. *J. Phys. Chem. A* **2011**, *115*, 4798–4803.

[189] Chillemi, G.; Pace, E.; D'Abramo, M.; Benfatto, M. *J. Phys. Chem. A* **2016**, *120*, 3958–3965.

[190] Lifson, S.; Warshel, A. *J. Chem. Phys.* **1968**, *49*, 5116–5129.

[191] Levitt, M.; Lifson, S. *J. Mol. Biol.* **1969**, *46*, 269–279.

[192] Hwang, M. J.; Stockfisch, T. P.; Hagler, A. T. *J. Am. Chem. Soc.* **1994**, *116*, 2515–2525.

[193] Maple, J. R.; Hwang, M. J.; Stockfisch, T. P.; Dinur, U.; Waldman, M.; a nd A. T. Hagler, C. S. E. *J. Comp. Chem.* **1994**, *15*, 162–182.

[194] Rick, S.; Stuart, S. *Potentials and Algorithms for Incorporating Polarizability in Computer Simulations*; Reviews in Computational Chemistry, Vol. 18, 2002.

[195] Shi, Y.; Xia, Z.; Zhang, J.; Best, R.; Wu, C.; Ponder, J. W.; Ren, P. *J. Chem. Theo. Comp.* **2013**, *9*, 4046–4063.

[196] Lopes, P. E. M.; Huang, J.; Shim, J.; Luo, Y.; Li, H.; Roux, B.; MacKerell, A. D., Jr. *J. Chem. Theo. Comp.* **2013**, *9*, 5430–5449.

[197] Kramer, C.; Gedeck, P.; Meuwly, M. *J. Chem. Theo. Comp.* **2013**, *9*, 1499–1511.

[198] Lee, M. W.; Carr, J. K.; Goellner, M.; Hamm, P.; Meuwly, M. *J. Chem. Phys.* **2013**, *139*.

[199] Jakobsen, S.; Bereau, T.; Meuwly, M. *J. Phys. Chem. B* **2015**, *119*, 3034–3045.

[200] Cazade, P.-A.; Tran, H.; Bereau, T.; Das, A. K.; Klaesi, F.; Hamm, P.; Meuwly, M. *J. Chem. Phys.* **2015**, *142*.

[201] Warshel, A.; Levitt, M. *J. Mol. Biol.* **1976**, *103*, 227–249.

[202] Alagona, G.; Ghio, C.; Kollman, P. A. *J. Mol. Biol.* **1986**, *191*, 23–27.

[203] Bash, P. A.; Field, M. J.; Karplus, M. *J. Am. Chem. Soc.* **1987**, *109*, 8092–8094.

[204] Das, A. K.; Meuwly, M. *Ang. Chem. Intern. Ed.* **2018**, *in print*.

[205] Eckenhoff, W. T.; Pintauer, T. *Inorg. Chem.* **2010**, *49*, 10617–10626.

[206] Cobeljic, B.; Pevec, A.; Turel, I.; Spasojevic, V.; Milcic, M.; Mitic, D.; Sladic, D.; Andelkovic, K. *Polyhedron* **2014**, *69*, 77–83.

[207] Das, A. K.; Meuwly, M. *J. Phys. Chem. B* **2017**, *121*, 9024–9031.

[208] Weinhold, F.; Landis, C. *Valency and Bonding: A Natural Bond Orbital Donor-Acceptor Perspective*; Cambridge University Press, 2005.

[209] Magnusson, E. *J. Am. Chem. Soc.* **1990**, *112*, 7940–7951.

[210] Pimentel, G. *J. Chem. Phys.* **1951**, *19*, 446–448.

[211] Rundle, R. *J. Am. Chem. Soc.* **1963**, *85*, 112–113.

[212] Coulson, C. **1964**, 1442–&.

[213] Landis, C. R.; Weinhold, F. *Inorg. Chem.* **2013**, *52*, 5154–5166.

[214] Braida, B.; Hiberty, P. C. *J. Phys. Chem. A* **2008**, *112*, 13045–13052.

[215] Glowacki, D. R.; Orr-Ewing, A. J.; Harvey, J. N. *J. Chem. Phys.* **2015**, *143*.

[216] Appleton, T.; Clark, H.; Manzer, L. *Coordination Chemistry Reviews* **1973**, *10*, 335 – 422.

[217] Jahn, H. A.; Teller, E. *Proceedings of the Royal Society of London A: Mathematical, Physical and Engineering Sciences* **1937**, *161*, 220–235.

[218] *The American Society of Health-System Pharmacists.* **2016**.

[219] Kelland, L. *Nat. Rev. Cancer* **2007**, *7*, 573–584.

[220] Bathgate, R.; Moelwynhughes, E. *J. Chem. Soc.* **1959**, 2642–2648.

[221] Pedraza-Gonzalez, L.; Galindo, J. F.; Gonzalez, R.; Reyes, A. *J. Phys. Chem. A* **2016**, *120*, 8360–8368.

[222] Bash, P.; Field, M.; Karplus, M. *J. Am. Chem. Soc.* **1987**, *109*, 8092–8094.

[223] Purvis, G.; Bartlett, R. *J. Chem. Phys.* **1982**, *76*, 1910–1918.

[224] Dunning, T. *J. Chem. Phys.* **1989**, *90*, 1007–1023.

[225] Muetterties, E.; Phillips, W. *J. Am. Chem. Soc.* **1957**, *79*, 322–326.

[226] Hannon, M. J. *Pure Appl. Chem.* **2007**, *79*, 2243–2261.

[227] Ting, V. P.; Schmidtmann, M.; Wilson, C. C.; Weller, M. T. *Ang. Chem. Intern. Ed.* **2010**, *49*, 9408–9411.

[228] Bates, D.; Watts, D. *Nonlinear regression analysis and its applications*; Wiley series in probability and mathematical statistics; Wiley: New York, 1988.

[229] Georgieva, I.; Trendafilova, N.; Dodoff, N.; Kovacheva, D. *Spectrochim. Acta Mol. Biomol. Spectrosc.* **2017**, *176*, 58–66.

[230] Bell, C.; Price, N.; Chakrabarti, B. *The Methyl Bromide Issue*; Wiley Series in Agrochemicals & Plant Protection; Wiley, 1996.

[231] Bulathsinghala, A. T.; Shaw, I. C. *Hum. Exp. Toxicol* **2014**, *33*, 81–91.

[232] Adamovic, I.; Gordon, M. *J. Phys. Chem. A* **2005**, *109*, 1629–1636.

[233] Pagliai, M.; Raugei, S.; Cardini, G.; Schettino, V. *J. Mol. Struct. Theochem.* **2003**, *630*, 141–149.

[234] Bogdanov, B.; McMahon, T. *Int. J. Mass Spectrom.* **2005**, *241*, 205–223.

[235] Liu, P.; Li, C.; Wang, D. *J. Phys. Chem. A* **2017**, *121*, 8012–8016.

[236] Li, C.; Ross, P.; Szulejko, J.; McMahon, T. *J. Am. Chem. Soc.* **1996**, *118*, 9360–9367.

[237] Schmatz, S.; Botschwina, P.; Stoll, H. *Int. J. Mass Spectrom.* **2000**, *201*, 277–282.

[238] Kottalam, J.; Case, D. A. *J. Am. Chem. Soc.* **1988**, *110*, 7690–7697.

[239] Kumar, S.; Rosenberg, J. M.; Bouzida, D.; Swendsen, R. H.; Kollman, P. A. *J. Compt. Chem.* **1992**, *13*, 1011–1021.

[240] Soloviov, M.; Das, A. K.; Meuwly, M. *Ang. Chem. Intern. Ed.* **2016**, *55*, 10126–10130.

[241] Ma, B.; Shatsky, M.; Wolfson, H.; Nussinov, R. *Protein Sci.* **2002**, *11*, 184–197.

[242] Smirnov, V. V.; Roth, J. P. *J. Am. Chem. Soc.* **2006**, *128*, 16424–16425.

[243] Sheng, Y.; Abreu, I. A.; Cabelli, D. E.; Maroney, M. J.; Miller, A.-F.; Teixeira, M.; Valentine, J. S. *Chem. Rev.* **2014**, *114*, 3854–3918.

[244] Lintuluoto, M.; Yamada, C.; Lintuluoto, J. M. *J. Phys. Chem. B* **2017**, *121*, 7235–7246.

[245] Webb, M. I.; Walsby, C. J. *Dalton Trans.* **2011**, *40*, 1322–1331.

[246] Lambry, J.-C.; Stranava, M.; Lobato, L.; Martinkova, M.; Shimizu, T.; Liebl, U.; Vos, M. H. *J. Phys. Chem. Lett.* **2016**, *7*, 69–74.

[247] Winder, R.; Borrill, J. *Psychopharmacology* **1998**, *136*, 349–356.

[248] Chachlaki, K.; Garthwaite, J.; Prevot, V. *Nat. Rev. Endocrinol.* **2017**, *13*, 521–535.

[249] Rees, D. D. *Nitric Oxide and Infection*; Fang, F. C., Ed.; Springer US: Boston, MA, 2002.

[250] Vincent, S. R. *Prog. Neurobiol.* **2010**, *90*, 246–255.

[251] Eberhardt, M.; et al. **2014**, *5*.

[252] Ignarro, L. *Nitric Oxide: Biology and Pathobiology*; Elsevier Science, 2000.

[253] Brown, G. C. *FEBS Letters* **1995**, *369*, 136 – 139.

[254] Brown, G. C.; Borutaite, V. *Cardiovascular Research* **2007**, *75*, 283–290.

[255] Poole, R.; Hughes, M. *Mol. Microbiol.* **2000**, *36*, 775–783.

[256] Bang, I.-S.; Liu, L.; Vazquez-Torres, A.; Crouch, M.-L.; Stamler, J. S.; Fang, F. C. *J. Biol. Chem.* **2006**, *281*, 28039–28047.

[257] Tinajero-Trejo, M.; Denby, K. J.; Sedelnikova, S. E.; Hassoubah, S. A.; Mann, B. E.; Poole, R. K. *J. Biol. Chem.* **2014**, *289*, 29471–29482.

[258] Kollau, A.; Russwurm, M.; Neubauer, A.; Rechberger, G.; Schmidt, K.; Koesling, D.; Fassett, J.; Schrammel, A.; Mayer, B. *Nitric Oxide Biol. Chem.* **2016**, *54*, 8–14.

[259] Carabet, L. A.; Guertin, M.; Lague, P.; Lamoureux, G. *J. Phys. Chem. B* **2017**, *121*, 8706–8718.

[260] Gardner, P. *J. Inorg. Biochem.* **2005**, *99*, 247–266.

[261] Doyle, M. P.; Hoekstra, J. W. *J. Inorg. Biochem.* **1981**, *14*, 351 – 358.

[262] Eich, R. F.; Li, T.; Lemon, D. D.; Doherty, D. H.; Curry, S. R.; Aitken, J. F.; Mathews, A. J.; Johnson, K. A.; Smith, R. D. .; George N. Phillips, J.; ; Olson, J. S. *Biochem.* **1996**, *35*, 6976–6983.

[263] Herold, S.; Exner, M.; ; Nauser, T. *Biochem.* **2001**, *40*, 3385–3395.

[264] Gladwin, M.; Lancaster, J.; Freeman, B.; Schechter, A. *Nature Medicine* **2003**, *9*, 496–500.

[265] Mishra, S.; Meuwly, M. *J. Am. Chem. Soc.* **2010**, *132*, 2968–2982.

[266] Fl ögel, U.; Merx, M. W.; G ödecke, A.; Decking, U. K. M.; Schrader, J. d. *Proc. Natl. Acad. Sci.* **2001**, *98*, 735–740.

[267] Gardner, P. R.; Gardner, A. M.; Brashear, W. T.; Suzuki, T.; Hvitved, A. N.; Setchell, K. D.; Olson, J. S. **2006**, *100*, 542 – 550.

[268] Ascenzi, P.; Bolognesi, M.; Visca, P. *Biochem. Biophys. Res. Commun.* **2007**, *357*, 809 – 814.

[269] Ascenzi, P.; Gullotta, F.; Gioia, M.; Coletta, M.; Fasano, M. *Biochem. Biophys. Res. Commun.* **2011**, *406*, 112 – 116.

[270] Tejero, J.; Santolini, J.; Stuehr, D. J. *FEBS J.* **2009**, *276*, 4505–4514.

[271] Soloviov, M.; Das, A. K.; Meuwly, M. *Angew. Chem. Int. Ed.* **2016**, *55*, 10126 – 10130.

[272] Milani, M.; Pesce, A.; Ouellet, Y.; Ascenzi, P.; Guertin, M.; Bolognesi, M. *EMBO J.* **2001**, *20*, 3902–3909.

[273] Jensen, K. P.; Ryde, U. *J. Biol. Chem.* **2004**, *279*, 14561–14569.

[274] Franzen, S. *Proc. Natl. Acad. Sci.* **2002**, *99*, 16754–16759.

[275] Kepp, K. P. *Chem. Phys. Chem.* **2013**, *14*, 3551–3558.

[276] Siegbahn, P. E. M.; Blomberg, M. R. A.; Chen, S.-L. *J. Chem. Theo. Comp.* **2010**, *6*, 2040–2044.

[277] Ali, M. E.; Sanyal, B.; Oppeneer, P. M. *J. Phys. Chem. B* **2012**, *116*, 5849–5859.

[278] Antonini, E.; Brunori, M. *Hemoglobin and myoglobin in their reactions with ligands*; Frontiers of biology; North-Holland Pub. Co., 1971.

[279] Schaad, O.; Zhou, H.; Szabo, A.; Eaton, W.; Henry, E. *Proc. Natl. Acad. Sci.* **1993**, *90*, 9547–9551.

[280] Meuwly, M.; Becker, O. M.; Stote, R.; Karplus, M. *Biophys. Chem.* **2002**, *98*, 183 – 207.

[281] Bolhuis, P.; Chandler, D.; Dellago, C.; Geissler, P. *Annu. Rev. Phys. Chem.* **2002**, *53*, 291–318.

[282] Dellago, C.; Bolhuis, P. G. In *Atomistic Approaches in Modern Biology: From Quantum Chemistry to Molecular Simulations*; Reiher, M, Ed., 2007; Vol. 268, pp 291–317.

[283] Tejero, J.; Gladwin, M. T. *Biol. Chem.* **2014**, *395*, 631–639.

[284] Koebke, K. J.; Waletzko, M. T.; Pacheco, A. A. *Biochem.* **2016**, *55*, 686–696.

[285] Ascenzi, P.; Bolognesi, M.; Milani, M.; Guertin, M.; Visca, P. *Gene* **2007**, *398*, 42–51.

[286] Oliveira, A.; Singh, S.; Bidon-Chanal, A.; Forti, F.; Marti, M. A.; Boechi, L.; Estrin, D. A.; Dikshit, K. L.; Luque, F. J. *PLoS One* **2012**, *7*.

[287] Cazade, P.-A.; Meuwly, M. *Chem. Phys. Chem.* **2012**, *13*, 4276–4286.

[288] Lama, A.; Pawaria, S.; Bidon-Chanal, A.; Anand, A.; Gelpi, J. L.; Arya, S.; Marti, M.; Estrin, D. A.; Luque, F. J.; Dikshit, K. L. *J. Biol. Chem.* **2009**, *284*, 14457–14468.

[289] Kawabata, T.; Go, N. *Proteins: Struct., Funct., Bioinf.* **2007**, *68*, 516–529.

Part VI.

Appendix

Computational Chemistry

International Edition: DOI: 10.1002/anie.201604552
German Edition: DOI: 10.1002/ange.201604552

Structural Interpretation of Metastable States in Myoglobin–NO

*Maksym Soloviov, Akshaya K. Das, and Markus Meuwly**

Abstract: *Nitric oxide binding and unbinding from myoglobin (Mb) is central to the function of the protein. By using reactive molecular dynamics (MD) simulations, the dynamics following NO dissociation were characterized in both time and space. Ligand rebinding can be described by two processes on the 10 ps and 100 ps timescale, which agrees with recent optical and X-ray absorption experiments. Explicitly including the iron out-of-plane (Fe-oop) coordinate is essential for a meaningful interpretation of the data. The proposed existence of an "Fe-oop/NO-bound" state is confirmed and assigned to NO at a distance of approximately 3 Å away from the iron atom. However, calculated XANES spectra suggest that it is diffcult to distinguish between NO close to the heme-Fe and positions further away in the primary site. Another elusive state, with Fe–ON coordination, was not observed experimentally because it is masked by the energetically more favorable but dissociative ^{4}A state in this region, which makes the Fe–ON local minimum unobservable in wild-type Mb. However, suitable active-site mutations may stabilize this state.*

Characterizing the structure, motions, and functional dynamics of biomolecules is essential for understanding their function. The motions usually involve stable states at their endpoints, which are separated by one or several metastable states (intermediates).[1,2] Experimentally, it is possible to directly and structurally characterize states with sufficiently long lifetimes.[3,4] However, when the lifetime of a state is too short to stabilize only indirect means to infer its existence are available. Optical spectroscopy can reveal the existence of short-lived states through spectral shifts. In Myoglobin (Mb), more direct interrogation of the iron environment is possible with X-ray absorption spectroscopy (XAS)[5] or multidimensional spectroscopy.[6,7] However, associating timescales with particular geometrical arrangements of the involved atoms is usually difficult, except for a few favourable cases.[4] Under such circumstances, computational investigations become a meaningful complement to study the dynamics of the system of interest.

The motion of photodissociated ligands in globular proteins has been studied for a long time. Small molecules that can reversibly bind to the protein active center are ideal, sensitive probes of the interior of such complex systems. Nitric oxide (NO) is a physiologically relevant ligand[8–10] that is involved in modulating blood flow, thrombosis, and neural activity. Experimentally, the binding kinetics of NO to the heme group in myoglobin (Mb) have been studied extensively by time-resolved spectroscopic methods from the UV/Vis to the mid-IR[11–17] region and by resonance Raman[14] techniques. In all cases, the rebinding kinetics are multiexponential, with time constants ranging from the sub-picosecond range to several hundred picoseconds. However, they can be grouped into two general classes: processes on the 10 ps timescale and processes on the 100 ps timescale.[12,14–16,18,19]

Recent experiments have followed the interplay between the Fe out-of-plane (Fe-oop) and the NO ligand motion in a time-resolved fashion.[5,14,16] This work points towards a direct coupling between these two degrees of freedom on the 10 to 100 ps timescale. The structural characterization of these states, however, remained unclear. Furthermore, earlier studies have attempted to characterize the metastable Fe–ON state,[20] and it remains to be determined why this motif that is commonly observed in model compounds[21] is absent in the protein environment despite a stabilization of 5 kcal mol^{-1} or more.[22]

The atomistic dynamics are essential for protein function and provide the basis for the interpretation of the timescales involved at a structural level. Molecular dynamics (MD) simulations are ideal for addressing such questions. In combination with validated energy functions, such simulations can provide the "missing link" between time-resolved experiments and the underlying atomic motions.[4,23,24] For NO interacting with heme in Mb, such potential energy surfaces (PESs) for the bound ^{2}A and ligand-unbound ^{4}A state are available.[25]

Generating a statistically significant number of QM/MM trajectories to analyze and resolve the interplay of the motions involved is beyond current computational methods for systems such as MbNO. For quantitative and meaningful computational investigations, suitable representations that preserve the accuracy of the interpolated PES are used in the simulations. Here, a parameter-free, reproducing kernel Hilbert space (RKHS) based representation, which exactly reproduces the reference data from quantum-chemical calculations, is employed (for details on the PESs, see the Supporting Information).[26,27] RKHS is based on smoothness criteria of the interpolant and has been successfully applied for the study of van der Waals complexes.[28,29]

The present work investigates the reactive dynamics between the ^{4}A and ^{2}A PESs following photodissociation of the NO ligand from the heme iron in Mb. Due to the narrow energy gap between the two states and the existence of two substrates on the ^{2}A PES, interesting dynamics can be expected. By comparison with the experimentally determined rebinding timescales and spectroscopic studies, structural questions related to the molecular dynamics can be addressed.

[*] Dr. M. Soloviov, A. K. Das, Prof. M. Meuwly
Department of Chemistry, University of Basel
Klingelbergstrasse 80, 4056 Basel (Switzerland)
E-mail: m.meuwly@unibas.ch

Supporting information for this article can be found under: http://dx.doi.org/10.1002/anie.201604552.

To follow the reactive dynamics between the ^{2}A and ^{4}A states, 300 independent simulations were run for a maximum time of 200 ps or until the bound Fe–NO state was formed. Photodissociation was induced by instantaneously switching the force field to the ^{4}A state,[30] which introduces around 50 kcal mol^{-1} of energy into the system,[25] which is comparable with the photon energies used in experiments (49–81 kcal mol^{-1}).[31] The rebinding kinetics are given in Figure 1, which shows the fraction of rebound NO as a function of time. The rebinding kinetics on the sub-nanosecond timescale follow a multiexponential decay with two time constants, $\tau_1 \approx 10$ ps and $\tau_2 \approx 150$ ps, which also depend on the asymptotic separation Δ of the two states (see Table S1 in the Supporting Information). The shift Δ relates the asymptotic energies of the ^{2}A and the ^{4}A PESs for NO at an infinite separation from the heme Fe (see the Supporting Information).

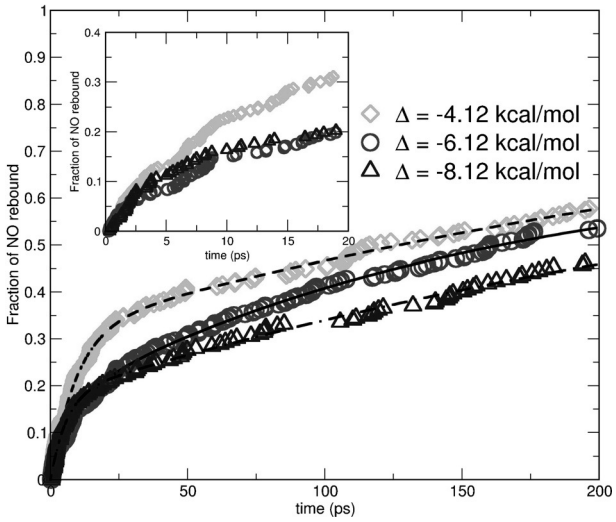

Figure 1. Kinetics and corresponding exponential fits for NO rebinding to the heme Fe after photoexcitation. Simulations were run for three different values of the asymptotic shift Δ.

Typical ligand trajectories are shown in Figure 2. Panel A reports the rebinding on the 1 ps timescale whereas panels B and C represent the rebinding on the timescales τ_1 and τ_2. For τ_1, the ligand only samples the immediate neighborhood of the heme iron center before rebinding. On the 100 ps timescale, rebinding occurs from regions further away. For $\Delta = -6.1$ kcal mol^{-1}, the total numbers of rebinding trajectories are 17 (rebinding within 2 ps), 28 ($2 \le t < 10$), and 115 ($10 \le t < 200$), and 140 rebind on timescales greater than 200 ps, that is, the rebinding efficiency within 200 ps is approximately 55 %. This compares with a rebound fraction of 75 % on the 200 ps timescale as recently determined by XAS measurements.[5]

The simulations described thus far used the PESs fitted to the DFT data and included environmental effects (see the Supporting Information). Corresponding simulations with 200 independent runs on the DFT-only PESs yielded rebinding of 195 trajectories within 200 ps with rebinding times of 2 and 15 ps. This is one order of magnitude faster than for simulations on the refined PESs, which treat the Fe-oop coordinate more accurately and explicitly. This finding is also consistent with previous simulations based on DFT-only PESs.[19,32] Hence explicitly including the Fe-oop motion is essential for quantitative results.

A complementary view of the different rebinding timescales can be gained by analyzing the maximum distance between the Fe center and the ligand during a rebinding simulation. The 300 trajectories were grouped into those that rebind on very short timescales ($\tau < 2$ ps), within 10 ps, and on timescales longer than 10 ps. The individually normalized probability distribution functions (pdfs) are shown in Figure S5. No NO migration to neighboring xenon-binding sites was observed on the 200 ps timescale because escape to the closest Xe site (Xe4), for example, occurs within 1 to 10 ns.[33,34]

Previous experimental and computational investigations[12,19,30,32,35–37] had found that the recombination kinetics of MbNO are non-exponential and involve two to three timescales, depending on the model used. The earliest reports reported timescales of 27.6 ps and 279.3 ps in a double-exponential fit.[12] Later, optical and IR experiments found short timescales ranging from 5 to 30 ps and longer timescales between 100 and 200 ps.[35–37] The experiments all agree on the existence of two sub-nanosecond timescales that differ by about one order of magnitude. Previous computations with reactive force fields typically found somewhat shorter rebinding times, between 5 ps and 20 ps,[19,32] depending on the asymptotic separation Δ.[38] The current simulations found multiple timescales in the 10 to 100 ps range that are in agreement with the optical and IR experiments. A more rapid component on the 1 to 2 ps timescale was also observed. The influence of Fe doming is clearly visible in the rebinding kinetics (see Figure 1). This results confirms that the force fields used here were of reasonable quality and allow to directly address a number of hypotheses.

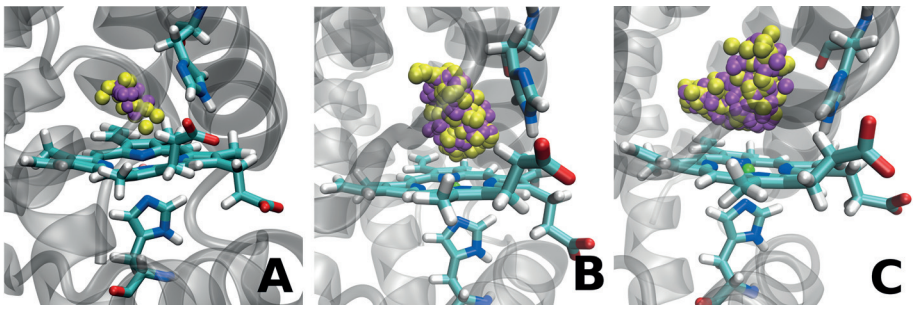

Figure 2. Typical trajectories for different rebinding timescales. NO positions are shown in yellow (N) and magenta (O). A) The picosecond process ($\tau = 1.6$ ps), B) the 10 picosecond process ($\tau = 42.1$ ps), and C) the 100 picosecond process ($\tau = 160.2$ ps).

First, direct connections with a recently proposed transient structure in the ^{2}A state can be made.

Picosecond time-resolved[14] and XAS[5] experiments have suggested that the Fe-oop and the NO ligand motion are closely coupled. Interpretation of the experiments provided evidence for an Fe-oop, ligand-bound structure with a lifetime of 30 ± 10 ps. The present simulations on the ^{2}A PES alone indeed show the transient stabilization of such a state. The maximum lifetime was found to be 27 ps, and 41.7 % of the trajectories showed such a state (see Figure S3). Although they underestimate the experimentally determined lifetime of 30 ± 10 ps, the present simulations support the existence of such a state.

Another structurally elusive state that has been found for heme model compounds is the Fe–ON isomer.[21,39,40] Such a structure is sufficiently stabilized (by several kcal mol^{-1}) in NO-bound Mb, which should make it observable in IR experiments.[22] However, no such state has been found experimentally.[20] Simulations on the ^{2}A state alone show that the ligand is stabilized for tens of picoseconds in the Fe–ON state. However, when the reactive ^{2}A+^{4}A PES with a shift of $\Delta = -6.1$ kcal mol^{-1} (which best reproduces the DFT energies) is used, the Fe–ON configuration cannot be stabilized because in the region of the Fe–ON minimum, the repulsive ^{4}A state is lower in energy than the ^{2}A state. Hence, the ^{2}A minimum of the Fe–ON state is masked by the ^{4}A state and cannot be stabilized in wild-type Mb.

The asymptotic separation Δ depends on the chemical environment of the heme group. Hence, Δ changes when the environment is modified, for example, through amino acid mutation or embedding the heme group into a different protein. The effect of such changes can be quantified by simulations on the reactive ^2A+^4A PES with different Δ values. Reducing the asymptotic separation by 5 kcal mol^{-1} ($\Delta = -11.1$ kcal mol^{-1}) further destabilizes the Fe–ON state (Figure S6 A). For $\Delta = -6.1$ kcal mol^{-1} (Figure S6 B), the Fe–ON state is insignificantly sampled, and the system rebinds efficiently into the Fe–NO state. On the other hand, when the asymptotic separation is reduced to $\Delta = -1.1$ kcal mol^{-1} (Figure S6 C), the Fe–ON state is populated for extended periods of time during which spectroscopic characterization of this state should be possible. For comparison, a recent spectroscopic study found the dynamics of NO rebinding in Mb to be 2.5 times slower than in cytochrome c owing to the different active-site architectures.[41] According to transition-state theory, a factor of 2.5 corresponds to an energy difference of 0.5 kcal mol^{-1}. The thermodynamic stability of Mb upon mutation has been found to vary between -2 and $+6$ kcal mol^{-1},[42] which suggests that modifications in the active site can potentially stabilize the Fe–ON conformation through differential stabilization of the bound state relative to the unbound state.

With the coordinates from the reactive MD simulations, it is possible to provide a structural interpretation of the ca. 10 ps and 100 ps timescales found in the rebinding simulations. It is of particular interest to investigate in what respect the dynamics of these two states differ. Probability distribution functions of the a) NO ligand, b) all active-site residues, and c) all His64 side-chain atoms projected onto the heme plane are shown in Figure 3.

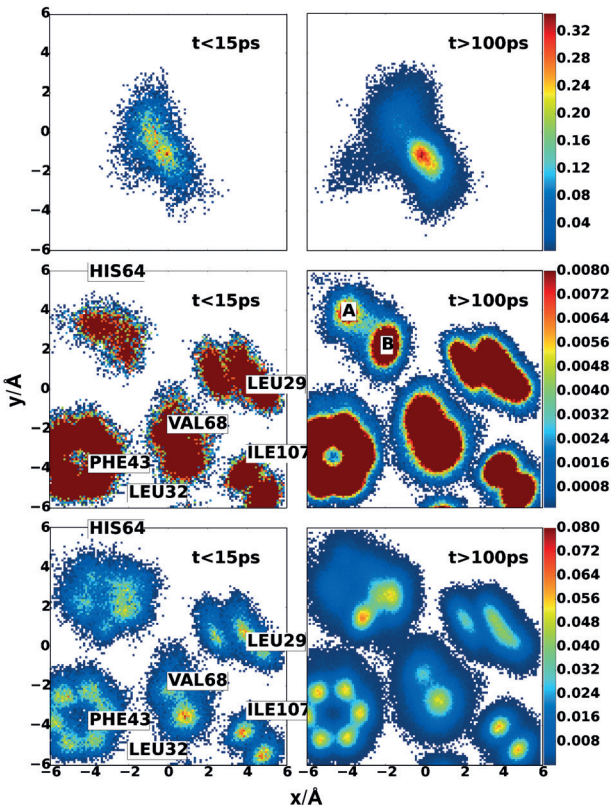

Figure 3. Top: The (*x*,*y*) probability distribution function for the rebinding of the free NO ligand on the $t < 15$ ps (left) and $t > 100$ ps (right) timescales. Middle: The (*x*,*y*) probability distribution functions for the NE2 atom of His64 on the two timescales. The two states for NE2 are labeled (A) and (B) and clearly distinguishable. Also shown are pdfs for all side-chain atoms of Phe43, Val68, Leu29, and Ile107. For Phe43, the phenyl ring is always parallel to the heme plane, and all six carbon atoms are clearly distinguishable. Bottom: As in the middle panel, but for the entire side chain of His64 and with different maximum heights of the pdfs.

The pdfs show that the NO ligand explores a much larger space for long rebinding times than for short rebinding times (Figure 3, top row). Furthermore, the NE2 atom of residue His64 occupies two clearly distinguishable states (A and B) in trajectories with long rebinding times, which are absent for rebinding within $\tau_1 = 10$ ps (Figure 3, middle row). The middle row emphasizes that for timescales τ_1, the His64 NE2 atom occupies space away from the iron center (located at (0,0)) whereas for longer timescales, the atom pushes in towards the heme iron by almost 2 Å, which hinders ligand rebinding. The estimated barriers, $\Delta G^{NE2}\rightarrow = 2.5$ kcal mol^{-1} for the forward and $\Delta G^{NE2}\rightarrow = 4.0$ kcal mol^{-1} for the reverse reaction, suggest that on the 100 ps timescale, state A is destabilized relative to state B. The corresponding barrier heights for the other His64 side-chain atoms range from 0.5 to 1.5 kcal mol^{-1}. Hence, on average, state B is separated from state A by a barrier of about 2 kcal mol^{-1}, with state B being lower in energy than state A.

The two states (A: green; B: red) are shown in Figure 4 together with the X-ray structure 1HJT[43] (gold). State A ("His64 out") is associated with the short rebinding timescale (10 ps) whereas state B ("His64 in") corresponds to the slow

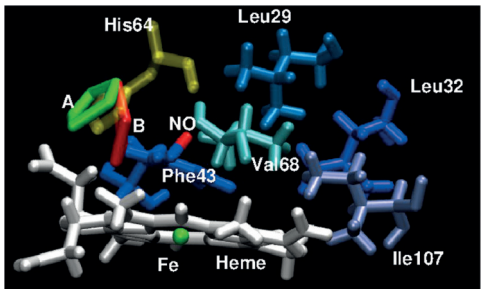

Figure 4. States A (green) and B (red) as found from the per-atom pdfs of the His64 side-chain atoms. The X-ray reference structure is shown in gold.

(100 ps) component. The barrier height corresponds to an interconversion time A⇄B on the sub-nanosecond timescale, which is supported by the explicit simulations and compares well with previous findings for CO-bound Mb with interconversion times of a few hundred picoseconds.[6,44]

For direct comparison with the XAS experiments, XANES spectra were computed (see the Supporting Information) for randomly selected MD-sampled structures with bound NO (40 structures), unbound NO within 3.5 Å of the heme Fe (20 structures), and unbound NO within 5.0 Å (10 structures). For the bound state, the computed spectrum ($I_b(E)$) agrees well with the experimental one up to 7.15 keV. For higher energies, the absorption signal is correctly described, but the computed intensity is too high (see Figure 5, top panel). The unbound structures yield $I_{ub,s}$ and $I_{ub,l}$ for the short and long Fe–NO separations, respectively, and nearly superimpose (Figure 5, inset) despite the different NO separations. Upon ligand photodissociation, the peak at 7.12 keV shifts to lower energy, and the intensity decreases between 7.12 and 7.15 keV and increases between 7.15 and 7.18 keV compared to the spectrum for the bound state. All of these features are consistent with previous experiments on MbNO and deoxy-Mb.[5,14]

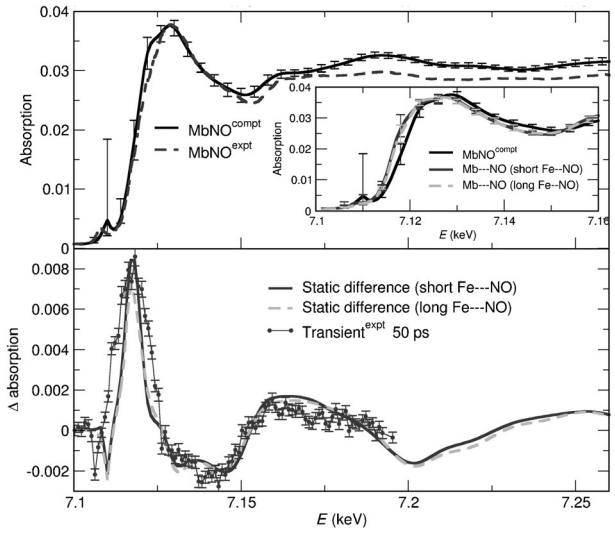

Figure 5. Top: Computed XANES spectrum for MbNO (black) compared to the experimental one (dashed). Vertical bars indicate the minimum and maximum absorption for all snapshots and are caused by conformational sampling. The inset compares computed spectra for MbNO and two sets of photodissociated systems (solid and dashed gray lines, see the main text). Bottom: Static difference spectra (solid and dashed gray lines) compared to the experimental transient at 50 ps (red).

The experimentally observed transient at 50 ps is compared with the averaged absorbance differences $\Delta I_{ub,s} = I_b - I_{ub,s}$ and $\Delta I_{ub,l} = I_b - I_{ub,l}$ in Figure 5. The two computed difference spectra are quite similar, except for slightly reduced amplitudes around 7.13 keV and 7.15 keV and an enhancement around 7.16 keV for $\Delta I_{ub,s}$ compared to $\Delta I_{ub,l}$ despite the two very different ligand positions. In both cases, the Fe-oop position ranges from 0.3 to 0.15 Å below the plane although for $\Delta I_{ub,s}$, positions closer to the in-plane position ($d = 0$) are also occupied. Compared to the experimental transient, $\Delta I_{ub,s}$ and $\Delta I_{ub,l}$ trace the major features but differ from it in the width of the 7.12 keV peak and the behavior between 7.13 and 7.15 keV. Figure S7 suggests that the presence or absence of photodissociated NO affects the XANES spectrum over the entire energy range from 7.10 to 7.15 keV and not just around 7.15 keV as previously assumed[5] because the signal also depends on the motion of the Fe atom relative to the heme plane. Within the signal-to-noise ratio of the experiment, it cannot be determined whether the ligand is close to the heme Fe or further away from it. It should be recalled that experimentally, a mixture of NO-bound and NO-unbound structures is measured because the photolysis yield is not 100 %.

In conclusion, reactive MD simulations have given non-exponential kinetics for ligand rebinding. The determined timescales (10 and 100 ps) confirmed those from optical and IR experiments. The influence of the Fe-oop coordinate on the rebinding reaction has been directly established. The two timescales are associated with two structurally different states of the His64 side chain, "out" (state A) and "in" (state B), which control ligand access and rebinding dynamics. Although energetically accessible, the metastable ^{2}A Fe–ON state is likely to be unobservable in wild-type Mb because in this region of configurational space, the repulsive ^{4}A state is lower in energy, preventing stabilization. The present work supports a recently proposed, transient Fe-oop/NO-bound structure with a lifetime of up to 30 ps. The computed XAS spectra are in line with the experimentally recorded ones but are unable to distinguish between structures with photodissociated NO "close to" or "far away" from the heme Fe in the active site. The present work provides an atomistically refined picture and structural explanations and assignments for a range of experimental observations, which are all sensitive to the Fe-oop dynamics of NO after photodissociation in native Mb.

Acknowledgments

We acknowledge fruitful discussions with Chris Milne and helpful comments from Peter Hamm and Majed Chergui. This work was supported by the Swiss National Science Foundation through grant 200021-117810, and the NCCR MUST.

Keywords: metastable states · myoglobin · nitric oxide · reactive molecular dynamics

How to cite: *Angew. Chem. Int. Ed.* **2016**, *55*, 10126–10130
Angew. Chem. **2016**, *128*, 10280–10285

[1] S. Fischer, K. W. Olsen, K. Nam, M. Karplus, *Proc. Natl. Acad. Sci. USA* **2011**, *108*, 5608–5613.
[2] J. G. Menting et al., *Proc. Natl. Acad. Sci.* **2014**, *111*, E3395–E3404.
[3] I. Schlichting, J. Berendzen, G. Phillips, R. Sweet, *Nature* **1994**, *371*, 808–812.
[4] F. Schotte, M. Lim, T. A. Jackson, A. V. Smirnov, J. Soman, J. S. Olson, G. N. Phillips, M. Wulff, P. A. Anfinrud, *Science* **2003**, *300*, 1944.
[5] M. Silatani, F. A. Lima, T. J. Penfold, J. Rittman, M. Reinhard, H. Rittmann-Frank, C. Borca, D. Grolimund, C. J. Milne, M. Chergui, *Proc. Natl. Acad. Sci. USA* **2015**, *112*, 12922–12927.
[6] K. A. Merchant, W. G. Noid, D. E. Thompson, R. Akiyama, R. F. Loring, M. D. Fayer, *J. Phys. Chem. B* **2003**, *107*, 4–7.
[7] J. Bredenbeck, J. Helbing, K. Nienhaus, G. U. Nienhaus, P. Hamm, *Proc. Natl. Acad. Sci. USA* **2007**, *104*, 14243–14248.
[8] P. Pacher, J. S. Beckman, L. Liaudet, *Physiol. Rev.* **2007**, *87*, 315–424.
[9] J. O. Lundberg et al., *Nat. Chem. Biol.* **2009**, *5*, 865–869.
[10] T. Traylor, V. Sharma, *Biochemistry* **1992**, *31*, 2847–2849.
[11] P. Cornelius, R. Hochstrasser, A. Steele, *J. Mol. Biol.* **1983**, *163*, 119–128.
[12] J. W. Petrich, J. C. Lambry, K. Kuczera, M. Karplus, C. Poyart, J. L. Martin, *Biochemistry* **1991**, *30*, 3975.
[13] D. Ionascu, F. Gruia, X. Ye, A. Yu, F. Rosca, C. B. A. Demidov, J. S. Olson, P. M. Champion, *J. Am. Chem. Soc.* **2005**, *127*, 16921–16934.
[14] S. G. Kruglik, B.-K. Yoo, S. Franzen, M. H. Vos, J.-L. Martin, M. Negrerie, *Proc. Natl. Acad. Sci. USA* **2010**, *107*, 13678.
[15] J. Kim, J. Park, T. Lee, M. Lim, *J. Phys. Chem. B* **2012**, *116*, 13663–13671.
[16] B.-K. Yoo, S. G. Kruglik, I. Lamarre, J.-L. Martin, M. Negrerie, *J. Phys. Chem. B* **2012**, *116*, 4106–4114.
[17] S. Kim, G. Jin, M. Lim, *J. Phys. Chem. B* **2004**, *108*, 20366.
[18] D. R. Nutt, M. Meuwly, *Biophys. J.* **2006**, *90*, 1191.
[19] J. Danielsson, M. Meuwly, *J. Chem. Theory Comput.* **2008**, *4*, 1083.
[20] K. Nienhaus, P. Palladino, G. U. Nienhaus, *Biochemistry* **2008**, *47*, 935.
[21] N. Xu, J. Yi, G. B. Richter-Addo, *Inorg. Chem.* **2010**, *49*, 6253–6266.
[22] D. R. Nutt, M. Karplus, M. Meuwly, *J. Phys. Chem. B* **2005**, *109*, 21118.
[23] D. R. Nutt, M. Meuwly, *Proc. Natl. Acad. Sci. USA* **2004**, *101*, 5998.
[24] M. W. Lee, J. K. Carr, M. Göllner, P. Hamm, M. Meuwly, *J. Chem. Phys.* **2013**, *139*, 054506.
[25] M. Soloviov, M. Meuwly, *J. Chem. Phys.* **2015**, *143*, 105103.
[26] N. Aronszajn, *Trans. Am. Math. Soc.* **1950**, *68*, 337.
[27] T. Hollebeek, T. S. Ho, H. Rabitz, *Annu. Rev. Phys. Chem.* **1999**, *50*, 537.
[28] T. S. Ho, H. Rabitz, *J. Chem. Phys.* **1996**, *104*, 2584.
[29] M. Meuwly, J. M. Hutson, *J. Chem. Phys.* **1999**, *110*, 8338.
[30] M. Meuwly, O. M. Becker, R. Stote, M. Karplus, *Biophys. Chem.* **2002**, *98*, 183–207.
[31] M. Lim, T. A. Jackson, P. A. Anfinrud, *Proc. Natl. Acad. Sci. USA* **1993**, *90*, 5801.
[32] D. R. Nutt, M. Meuwly, *Biophys. J.* **2006**, *90*, 1191–1201.
[33] C. Bossa, M. Anselmi, D. Roccatano, A. Amadei, B. Vallone, M. Brunori, A. Di Nola, *Biophys. J.* **2004**, *86*, 3855.
[34] N. Plattner, M. Meuwly, *Biophys. J.* **2012**, *102*, 333.
[35] Y. Kholodenko, E. Gooding, Y. Dou, M. Ikeda-Saito, R. Hochstrasser, *Biochemistry* **1999**, *38*, 5918–5924.
[36] X. Ye, A. Demidov, P. Champion, *J. Am. Chem. Soc.* **2002**, *124*, 5914–5924.
[37] S. Kim, G. Jin, M. Lim, *J. Phys. Chem. B* **2004**, *108*, 20366–20375.
[38] P. Banushkina, M. Meuwly, *J. Chem. Phys.* **2007**, *127*, 135101.
[39] M. Carducci, M. Pressprich, P. Coppens, *J. Am. Chem. Soc.* **1997**, *119*, 2669–2678.
[40] L. Cheng, I. Novozhilova, C. Kim, A. Kovalevsky, K. A. Bagley, P. Coppens, G. B. Richter-Addo, *J. Am. Chem. Soc.* **2000**, *122*, 7142.
[41] N. T. Hunt, G. M. Greetham, M. Towrie, A. W. Parker, N. P. Tucker, *Biochem. J.* **2011**, *433*, 459–468.
[42] K. P. Kepp, *Biochim. Biophys. Acta Proteins Proteomics* **2015**, *1854*, 1239–1248.
[43] E. A. Brucker, J. S. Olson, M. Ikeda-Saito, G. N. Phillips, *Prot. Struct. Funct. Genet.* **1998**, *30*, 352.
[44] J. Ma, S. Huo, J. Straub, *J. Am. Chem. Soc.* **1997**, *119*, 2541–2551.

Received: May 11, 2016
Published online: July 13, 2016

1 Methods

1.1 Molecular Dynamics Simulations

All molecular dynamics (MD) simulations were carried out using CHARMM[1] with the CHARMM22 force field.[2] The protein was set up as described previously.[3,4] Mb contains 153 amino acid residues, a heme group and a nitrogen oxide molecule. Simulations were carried out for the $\mathrm{His}_{\epsilon}64$ protonation state, which is the more likely state.[5–9] The protein was solvated in a periodic, preequilibrated water box $62.0864 \times 62.0864 \times 62.0864$ Å^3 and the final system contains 23711 atoms. All bonds involving hydrogens were treated using SHAKE[10,11] with a tolerance of 10^{-6}. For the non-bonded interactions a cutoff of 14 Å was used. First, the system was minimized using steepest-descent and adopted basis Newton-Raphson algorithms. Then it was heated from 100 to 300 K during 60 ps and equilibrated for 500 ps. This was followed by production runs, each 200 ps in length, in the NVT ensemble. The time step in all simulations was $\Delta t = 1$ fs.

1.2 Intermolecular interactions

For a given configuration $\vec{X}$ involving N atoms, the total potential energy $V_{\mathrm{tot}}(\vec{X})$ of the system is decomposed as

$$V_{\mathrm{tot}}(\vec{X}) = V_{\mathrm{FF}}(\vec{Q}) + V(R, \theta, \phi). \quad (1)$$

where $V_{\mathrm{FF}}(\vec{Q})$ is the standard CHARMM22 force field[2] and $V(R, \theta, \phi)$ is a purpose-built interaction potential as described below. The coordinates $\vec{Q}$ describe all solvent and most protein degrees of freedom except for (R, θ, ϕ), which are the coordinates for the interactions between the heme-Fe and NO, and the doming coordinate of the heme-Fe. The $R-$coordinate is the distance between Fe and the geometrical center of NO, θ is the angle between R and the NO-molecular axis, and ϕ is the average angle between each of the four heme-nitrogen atoms, the heme-Fe and the N_ϵ of the axial His93. Therefore θ describes the NO-rotation and ϕ corresponds to the heme-doming coordinate, see Figure 1. The doming coordinate describes the transition between an in- and and out-of-plane iron atom upon changing its ligation state from 6- to 5-coordinated (ligand bound to ligand unbound) which were treated with separate parameter sets.[3]

The 3-dimensional PES $V(R, \theta, \phi)$ and its representation as a reproducing kernel Hilbert space (RKHS) has been described previously.[12] Briefly, the PESs for the ^2A and ^4A states are based on more than 1000 electronic structure calculations with the B3LYP[13–16] functional and the 6-31G(d,p) basis set.[17,18]

Gaussian09[19] was used to perform all DFT calculations. The reference points were calculated on a 3-dimensional grid: The $r-$coordinate was scanned between 1.7 and 3.7 Å with step size $\Delta r = 0.1$ Å, the distance d between the heme-Fe and the heme-plane included positions $d = 0.2$, 0.1 Å above the plane, the in-plane position $d = 0.0$ Å, and $d = -0.1$, –0.3 and –0.5 Å below the plane. The $\theta-$grid was an 11-point Gauss-Legendre grid, which improves

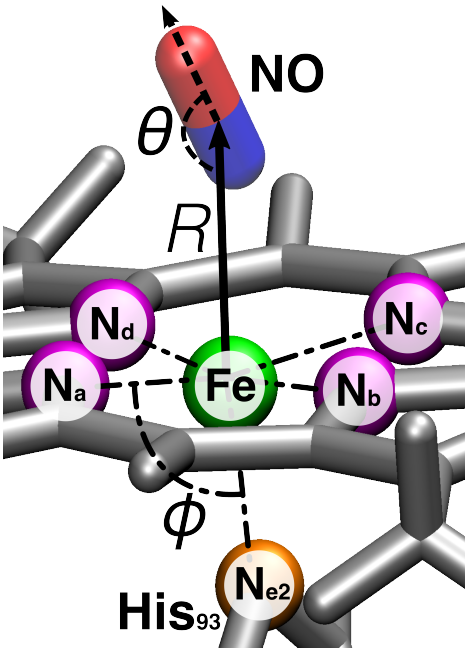

Figure 1: Relevant coordinates for the energetics of bound and unbound NO. Heme-nitrogens N_a to N_d (purple) heme-Fe (green), N_ϵ of His93 (orange), the N and O atoms of NO molecule are blue and red. The distance between the heme Fe and the center of the NO molecule is R, θ is the angle between R and the NO-molecular axis, and ϕ is the average angle between each of the four heme-nitrogen atoms, the heme Fe and the N_ϵ of the axial His93.

the stability of the fitted PES.[4,20,21] The out-of-plane distance used in the DFT grid was translated into an average angle ϕ between the heme-nitrogen, heme-Fe and the N_ϵ of the axial histidine ligand. The DFT system is symmetric and therefore the out-of-plane distance can be related to the ϕ angle via standard trigonometry. The ^{2}A and ^{4}A PESs are represented as

$$V(R,\theta,\phi) = \sum_{\lambda=0}^{10} V_\lambda(R,\phi) P_\lambda(\cos(\theta)) + V_{\rm lr}(\phi) \tag{2}$$

where P_λ are Legendre polynomials, V_λ are radial strength functions, and $V_{\rm lr}$ describes the doming in the asymptotic, long range (lr) region $R \to \infty$ and is represented as a harmonic potential:

$$V_{\rm lr}(\phi) = \frac{1}{2} k(\phi - \phi_e)^2 \tag{3}$$

Here, k is the force constant and ϕ_e is the equilibrium position (for ^2A: $k = 0.16$ kcal/mol/deg^2

and $\phi_e = 95.6°$; for ^4A: $k = 0.11$ kcal/mol/deg^2 and $\phi_e = 93.64°$). Both k and ϕ_e are parametrized during the optimization of the potential $V(R, \theta, \phi)$. The radial strength functions $V_\lambda(R, \phi)$ are represented as a reproducing kernel,[22]

$$V_\lambda(R, \phi) = \sum_{i,j} \alpha_{\lambda,i,j} \cdot \mathcal{K}(R, R_i) \cdot \mathcal{G}(\phi, \phi_j) \tag{4}$$

where $\mathcal{K}(R, R_i)$ is a radial reproducing kernel[23,24] and $\mathcal{G}(\phi, \phi_j)$ is a Gaussian reproducing kernel.[25] The $\alpha_{\lambda,i,j}$ are coefficients which follow from a singular value decomposition.[26–28] In parametrized form, the radial reproducing kernels are

$$\mathcal{K}(R, R_i) = \frac{1}{14} r_>^{-7} \left(1 - \frac{7}{9}\frac{R_<}{R_>}\right) \tag{5}$$

where $R_>$ and $R_<$ are the greater and smaller distance, respectively, for any pair of $R-$values. The Gaussian kernel is defined as

$$\mathcal{G}(\phi, \phi_j) = \exp(-\frac{(\phi - \phi_j)^2}{2\sigma}) \tag{6}$$

where σ is the width of the kernel and its value of 5.0° was optimized so that the kernels efficiently overlap and the optimization result in smallest error on the test set.

All electronic structure calculations were carried out with the electronic configuration corresponding to Fe(II)NO. This follows previous work[4] which showed that isomerization between Fe-NO and Fe-ON involves lower energy pathways for Fe(II)NO compared to Fe(III)NO and is also consistent with a study of nitric oxide sensing by mutant myoglobin.[29] Furthermore, the computed structure for Fe(II)NO is bent which agrees with X-ray crystallography of MbNO whereas Fe(III)NO is linear.[4,30,31]

1.3 Multistate PES

Up to this point the ^{2}A and ^{4}A PESs are independent. However, for reactive MD simulations they need to be related to each other such that asymptotically (for $R \to \infty$) the relative energetics between the two states reflects their true energetic ordering. This is described by a scalar constant Δ which is added to the energy of the ^{4}A state. In situations where dynamics on multiple, potentially crossing PESs can occur, smooth dynamics around the crossing region needs to be ensured. Here, we use multi state-ARMD (MS-ARMD) which is based on mixing PESs depending on their relative energies.[32] The method relies on mixing all PESs for a given configuration $\vec{x}$ according to exponentially distributed and energy-dependent weights w_i whereby PESs with lower total energy have larger weights. The total PES on which the dynamics takes place is thus

$$V_{\text{effective}}(R, \phi, \theta) = \sum_{i=1}^{N} w_i \cdot V_i(R, \theta, \phi) \tag{7}$$

where the $w_i(x)$ are the normalized weights of the i-th PES

$$w_i = \frac{w_{0,i}}{\sum_{i=1}^{N} w_{0,i}}. \tag{8}$$

The $w_{0,i}$ are raw weights, defined as

$$w_{0,i} = \exp\left(-\frac{V_i(R, \phi, \theta) - V_{min}(R, \phi, \theta)}{\sigma}\right) \tag{9}$$

where $V_{min}(R, \phi, \theta)$ is a minimal energy PES, and $\sigma = 5.0$ kcal/mol controls the width over which the PESs are mixed. The advantage of such a procedure is that it allows to combine several PESs exhibiting different bonding patterns as is required in empirical force fields, leads to a smooth overall PES and analytical gradients can be computed. It was shown that the total energy along individual trajectories is conserved which also allows simulations in the NVE ensemble.[32] On the other hand, compared to time-based switching the implemen-

tation and the fitting of the PESs are somewhat more involved.

Because the Fe-oop motion for the ^4A PES (corresponding to the N_{porph}–Fe–$N_{\epsilon_{His93}}$ force field term) is only approximately parametrized in the CHARMM22 force field, it needs to be corrected when the ^{2}A and ^{4}A PESs are mixed in the reactive simulations. For this, a correction potential $V_c(\phi) = A(1 - e^{B(\phi - C)})^2 + D$ was used for $\phi-$values between 90° and 95 ° to best reproduce the reference DFT energies in the crossing region. The parameters for $V_c(\phi)$ are $A = 12.0$ kcal/mol, $B = 0.37$ deg^{-1}, $C = 89.0$ deg, and $D = -19.0$ kcal/mol.

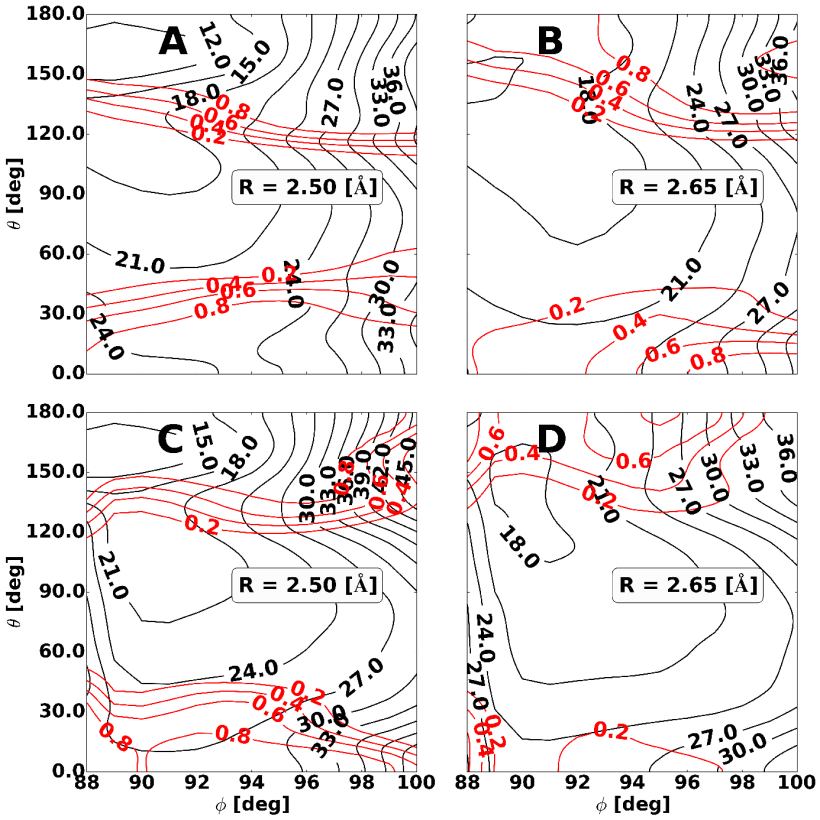

Figure 2: Effective PES for the different R, θ and ϕ. (A,B) DFT only based PES, (C,D) DFT based PES combined with the CHARMM FF. Black contours show the effective PES (in kcal/mol). Red contours show the weight of the ^2A PES in the effective PES (the weight ranges from 0.0 to 1.0, and a weight of 1.0 means that only the ^2A PES is contributes to the effective PES).

The evolution after photodissociation was probed by running 50 independent simulations.

They started from the bound state (^2A) and the Fe-NO bond was broken. The excitation process was induced by instantaneously switching to the ^4A state.[3] The propagation time τ on the excited state ranged from τ = 100 to 750 fs to assess the sensitivity of the final distribution of the ligands on this parameter (see Figure S3). During the excitation the NO molecule moves away from the heme-Fe. When the system is switched to the full reactive ^2A + ^4A PES (see below) the NO molecule can rebind to the heme-Fe. For comparing the effect of different evolution times τ the distribution of Fe-CoM(NO) distances and the rebinding times to form the thermodynamically stable Fe-NO state on the ^2A PES were determined for each value of τ. It is found that for $\tau \geq 250$ fs no major changes in either of the two properties occur and for the subsequent work $\tau_{^4A}$ = 500 fs was used. Such a value is also representative in view of the 300 fs derived from earlier experiments on MbCO.[33,34] The 50 trajectories initially considered all end up in the Fe-NO bound state within 150 ps.

1.4 Ligand Dynamics in the Active Site

The maximal distance between the Fe and the ligand sampled during the rebinding simulation. The probability distribution function for the maximum distance of the ligand to the heme-Fe atom from trajectories rebinding on very short time scales ($\tau < 2$ ps), within 10 ps and longer than 10 ps is shown in Figure 5.

1.5 Rebinding Kinetics

Depending on the asymptotic separation Δ of the two states (see SI) the time scales vary. The rapid component has an amplitude of 15-30 % compared with 50 to 60% for the slow process.

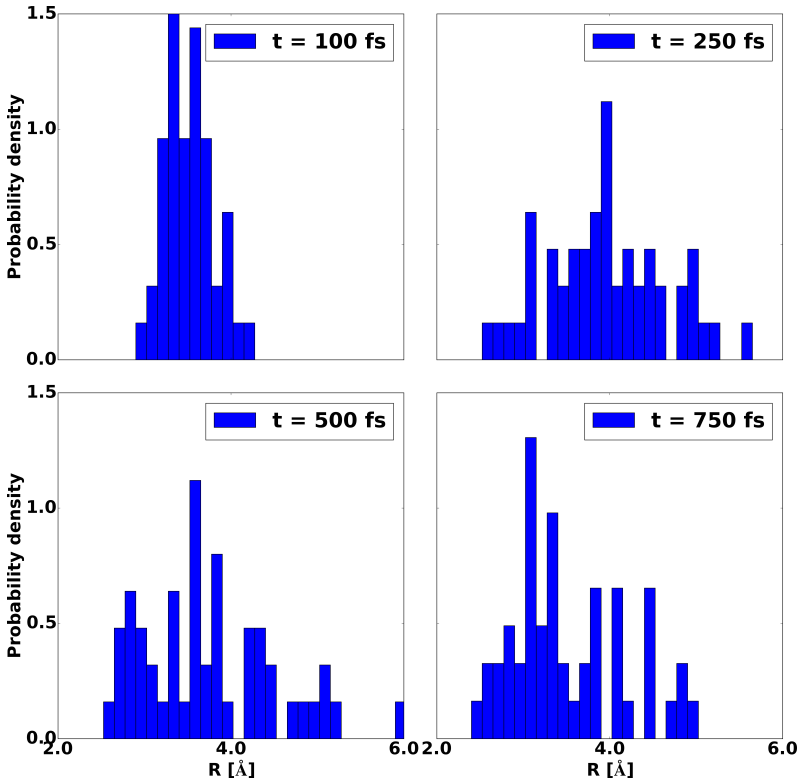

Figure 3: **A-D**) Probability densities of final states after evolving the 50 independent simulations on the excited PES for (**A** - 100 fs, **B** - 250 fs, **C** - 500 fs, **D** - 750 fs).

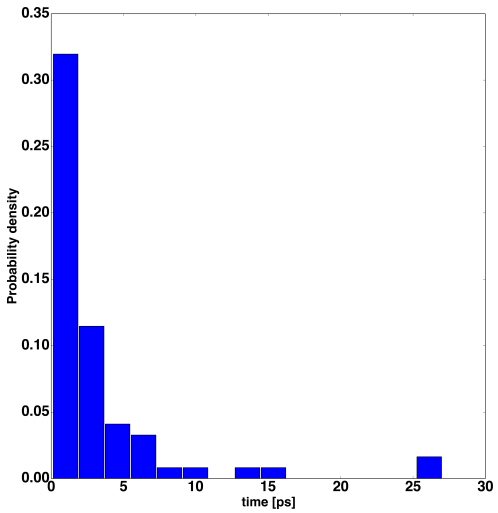

Figure 4: Lifetime of the proposed[35] Fe–oop, ligand-bound structure from simulations on the ^2A PES. The longest lifetime observed was 27.8 ps.

1.6 Computation of the XANES spectra

For each of the 20 structures the transient XAS spectrum was determined using the FDMNES package.[36] In the calculations a self-consistent potential of radius 6 Å around the Fe-atom

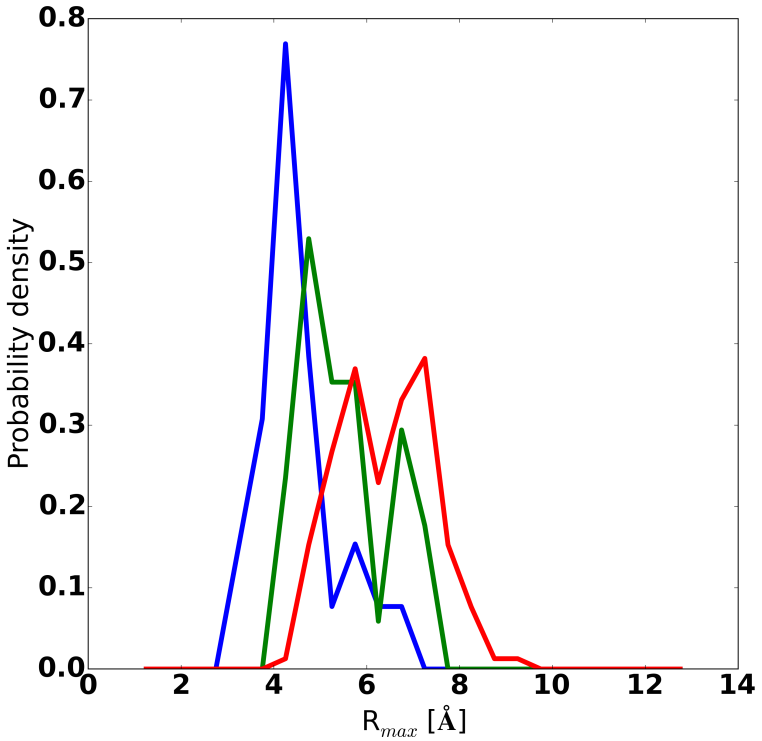

Figure 5: Distribution of the maximum heme Fe–NO distance for the rebinding trajectories with. The blue curve corresponds to trajectories that rebind within $\tau_{\mathrm{reb}} < 2.0$ ps, the green curve to those with $2.0 < \tau_{\mathrm{reb}} < 10.0$ ps and the red curve to $\tau_{\mathrm{reb}} > 10.0$ ps.

was used and the interaction with the X-ray field was described using the electric quadrupole approximation. Many-body effects and the core hole lifetime broadening were included by convoluting the signal according to

$$\Gamma_f(E - E_f) = \Gamma_{\mathrm{hole}} + \Gamma_{\mathrm{max}} \left(\frac{1}{2} + \frac{1}{\pi} \arctan \left[\frac{\pi}{3} \frac{\Gamma_{\mathrm{max}}}{E_l} \left(\epsilon - \frac{1}{\epsilon^2} \right) \right] \right) \tag{10}$$

Table 1: Amplitudes a_i and rebinding times τ_i of the double exponential fits depending on the asymptotic separation Δ.

Δ [kcal/mol]	a_1	τ_1 [ps]	a_2	τ_2 [ps]
-2 kcal/mol	0.17	5.71	0.63	339.6
0 kcal/mol	0.16	8.52	0.52	157.0
$+2$ kcal/mol	0.31	9.49	0.59	350.0

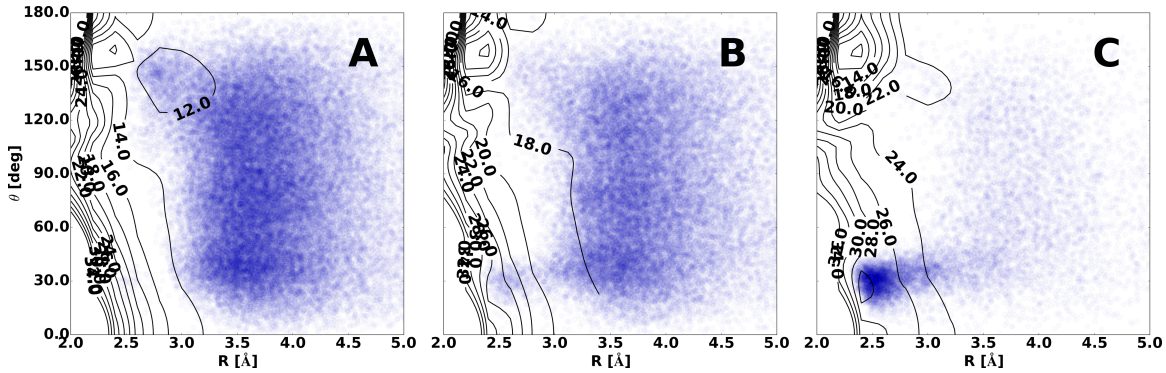

Figure 6: Isomerization trajectories from Fe–ON → Fe–NO process on the effective PES with different shifts Δ between the ^2A and ^4A PESs. (A) $\Delta = -11.1$ kcal/mol, (B) $\Delta = -6.1$ kcal/mol, (C) $\Delta = -1.1$ kcal/mol. Shifting the ^2A and ^4A closer to each other (panel C) leads to exposing the Fe–ON minimum.

with $\epsilon = (E - E_f)/E_{\text{ctr}}$, E_f is the Fermi energy, and the parameters are the total height $\Gamma_{\text{max}} = 15$ eV, the inflection point $E_{\text{ctr}}E_f = 30$ eV, and the inclination $E_l = 25$ eV. $\Gamma_{\text{hole}} = 1.81$ eV is the core hole lifetime. This procedures follows the one used in earlier work.[37]

The influence of the presence and absence of the photodissociated NO ligand for the XANES spectrum is shown in Figure 7. It is found that for NO closer to the heme-Fe the influence is more pronounced but does not vanish for locations 5 Å away from the iron atom. Also, the sensitivity of the difference signal as a function of energy changes. The maximum influence is found around the edge.

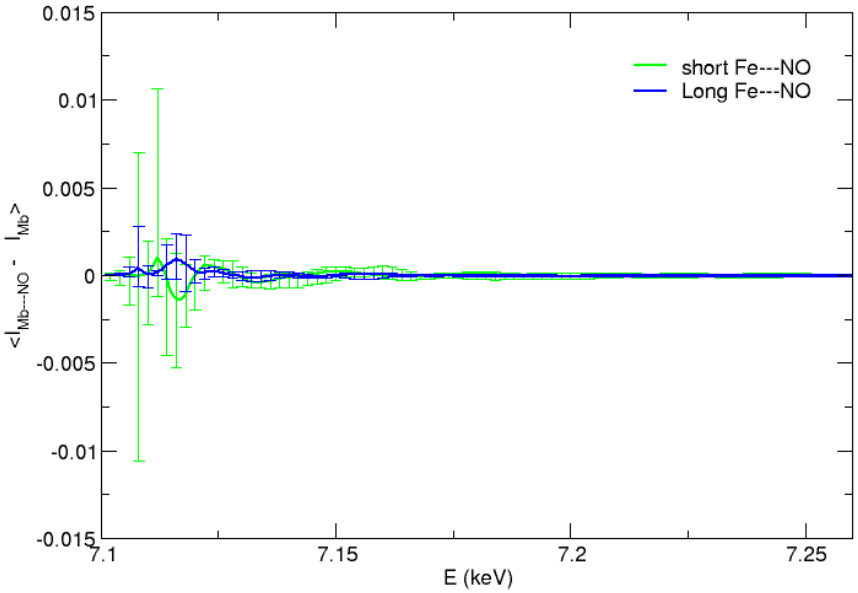

Figure 7: Influence of the presence and absence of the NO-ligand for the two sets of photodissociated snapshots (see main text): NO within 3.5 Å of the heme-Fe (20 structures) and NO-unbound (NO within 5.0 Å (10 structures). For each structure the XANES spectrum was calculated with and without the NO ligand presence and the averaged difference is reported together with the minimum and maximum difference (fluctuation bars).

References

(1) B. R. Brooks, C. L. Brooks III, A. D. J. Mackerell, L. Nilsson, et al, *J. Comp. Chem.*, **2009**, *30*, 1545.

(2) A. D. MacKerell, Jr. et al., *J. Phys. Chem. B*, **1998**, *102*, 3586.

(3) M. Meuwly, O. M. Becker, R. Stote, M. Karplus, *Biophys. Chem.*, **2002**, *98*, 183–207.

(4) D. R. Nutt, M. Karplus, M. Meuwly, *J. Phys. Chem. B*, **2005**, *109*, 21118.

(5) J. Johnson, D. Lamb, H. Frauenfelder, J. Muller, B. McMahon, G. Nienhaus, R. D. Young, *Biophys. J.*, **1996**, *71*, 1563–1573.

(6) C. Rovira, B. Schulze, M. Eichinger, J. D. Evanseck, M. Parrinello, *Biophys. J.*, **2001**, *81*, 435–445.

(7) K. A. Merchant, W. G. Noid, D. E. Thompson, R. Akiyama, R. F. Loring, M. D. Fayer, *J. Phys. Chem. B*, **2003**, *107*, 4–7.

(8) M. Meuwly, *Chem. Phys. Chem.*, **2006**, *7*, 2061–2063.

(9) K. Nienhaus, J. S. Olson, S. Franzen, G. U. Nienhaus, *J. Am. Chem. Soc.*, **2005**, *127*, 40–41.

(10) J. P. Ryckaert, G. Ciccotti, H. J. C. Berendsen, *J. Chem. Phys.*, **1977**, *13*, 327.

(11) M. Yoneya, H. J. C. Berendsen, K. Hirasawa, *Mol. Simulation*, **1994**, *13*, 395.

(12) M. Soloviov, M. Meuwly, *J. Chem. Phys.*, **2015**, *143*, year.

(13) A. D. Becke, *J. Chem. Phys.*, **1993**, *98*, 5648.

(14) C. Lee, W. Yang, R. Parr, *Phys. Rev. B*, **1988**, *37*, 785.

(15) S. Vosko, L. Wilk, M. Nusair, *Can. J. Phys.*, **1980**, *58*, 1200.

(16) P. Stephens, F. Devlin, C. Chabalowski, M. Frisch, *J. Chem. Phys.*, **1994**, *98*, 11623.

(17) G. Petersson, M. A. Al-Laham, *J. Chem. Phys.*, **1991**, *94*, 6081.

(18) G. Petersson, A. Bennett, T. Tensfeldt, M. A. Al-Laham, W. A. Shirley, J. Mantzaris, *J. Chem. Phys.*, **1988**, *89*, 2193.

(19) M. J. Frisch et al. *Gaussian 09 Revision A.1*, Gaussian Inc. Wallingford CT 2009.

(20) M. Meuwly, J. M. Hutson, *J. Chem. Phys.*, **1999**, *110*, 8338.

(21) S. Lammers, S. Lutz, M. Meuwly, *J. Comp. Chem.*, **2007**, *29*, 1048.

(22) N. Aronszajn, *Trans. Amer. Math. Soc.*, **1950**, *68*, 337.

(23) T. S. Ho, H. Rabitz, *J. Chem. Phys.*, **1996**, *104*, 2584.

(24) T. Hollebeek, T. S. Ho, H. Rabitz, *Ann. Rev. Phys. Chem.*, **1999**, *50*, 537.

(25) T. Hangelbroek, A. Ron, *J. Func. Analysis*, **2010**, *259*, 203.

(26) C. Eckart, G. Young, *Psychometrika*, **1936**, *1*, 211.

(27) M. R. Hestenes, *J. Soc. Ind. Appl. Math.*, **1958**, *6*, 52.

(28) G. H. Golub, W. Kahan, *J. Soc. Ind. Appl. Math.: Ser. B, Num. Analysis*, **1965**, *2*, 205.

(29) M. Negrerie, S. Kruglik, J. Lambry, M. Vos, J. Martin, S. Franzen, *J. Biol. Chem.*, **2006**, *281*, 10389–10398.

(30) A. Rich, R. Armstrong, P. Ellis, P. Lay, *J. Am. Chem. Soc.*, **1998**, *120*, 10827–10836.

(31) E. Brucker, J. Olson, M. Ikeda-Saito, G. Phillips, *Prot. Struct. Funct. Genet.*, **1998**, *30*, 352–356.

(32) T. Nagy, J. Y. Reyes, M. Meuwly, *J. Chem. Theo. Comp.*, **2014**, *10*, 1366–1375.

(33) J. Martin, A. Migus, C. Poyart, Y. Lecarpentier, R. Astier, A. Antonetti, *Proc. Natl. Acad. Sci.*, **1983**, *80*, 173.

(34) P. A. Anfinrud, C. Han, R. M. Hochstrasser, *Proc. Natl. Acad. Sci.*, **1989**, *86*, 8387.

(35) S. G. Kruglik, B.-K. Yoo, S. Franzen, M. H. Vos, J.-L. Martin, M. Negrerie, *Proc. Natl. Acad. Sci.*, **2010**, *107*, 13678.

(36) Y. Joly, *Phys. Rev. B*, **2001**, *63*, year.

(37) M. Silatani, F. A. Lima, T. J. Penfold, J. Rittman, M. Reinhard, H. Rittmann-Frank, C. Borca, D. Grolimund, C. J. Milne, M. Chergui, *Proc. Natl. Acad. Sci.*, **2015**, *112*, 12922 – 12927.

CURRICULUM VITAE

Akshaya Kumar Das

University of Basel
Department of Physical Chemistry
Klingelbergstrasse 80
4056 Basel, Switzerland

akdasiitk90@gmail.com
Phone: +41 789679245

Academic Profile

PhD

Institute	: Department of Physical Chemistry, University of Basel, Switzerland
Year	: 2018
Research Supervisor	: Prof. Markus Meuwly
Title of Thesis	: Molecular Interpretation of the Structure, Dynamics and Reactivity of Metal Complexes and Enzymes

M. Sc.

Institute	: Deaprtment of Chemistry, Indian Institute of Technology Kanpur, India
Subject	: Chemistry
Year	: 2012
Research Supervisor	: Prof. Nisanth N. Nair
Thesis Title	: Mechanistic study of "on water" reaction using hybrid QM/MM molecular dynamics

B. Sc.

Institute	: Department of Chemistry, Ravenshaw University, Odisha, India
Subject	: Chemistry with Honors, Physics and Mathematics as ancillary
Year	: 2010

Research Interest

Computational Chemistry/Biophysics

- Study of organic reactions in aqueous environment, enzymatic reactions and heterogeneous catalyst
- Protein conformational change, protein-ligand interaction and protein-lipid(membrane) interaction
- Understanding structure and reactivity of molecules on the surfaces
- Development of methods for molecular spectroscopy

Research Experience

PhD projects (2013-present) in the group of Prof. Markus Meuwly at the University of Basel, Switzerland

- Mechanistic study of denitrification reaction in truncated hemoglobin (trHbN) using Multisurface Adiabatic Reactive Molecular Dynamics (MS-ARMD) implemented in CHARMM. Umbrella sampling method was employed to compute the PMF of the reactions.
- Structural characterization of photo-dissociated NO ligand in myoglobin (Mb) using reactive molecular dynamics and computed XANES spectra
- A new method MS-VALBOND was developed using EVB approach (implemented in CHARMM) allows to model hypervalent molecules, transition metal complexes and simulate chemical reactions both in solution and proteins.
- Development of force fields to model transition metal complexes and enzyme active sites. Particularly, VALBOND-TRANS force field parameters were developed to incorporate trans-influence into the transition metal complexes (For Cu and Fe metals including several ligands with donor atoms N, O, S, P, Cl, Br and H) and helps to model enzyme active sites.
- Structure and dynamics of solvent shell around the transition metal complexes using atomistic simulations. Along with both VALBOND force fields and hybrid QM/MM (using SCC-DFTB) molecular dynamics, XANES spectra were computed (using FDMNES programme) to characterize the solvent structure around the metal complexes.
- Characterization of solvent dynamics around the fluorinated acetonitrile (used as a spectroscopic probe) by computing the 2D-IR spectrum from the frequency fluctuation correlation function (FFCF).

Project Associate (2012-2013) with Prof. Nisanth N. Nair and Prof. Sumit Basu at the Indian Institute of Technology Kanpur, India

- Force field development to study the interaction of PMR-15 with TiO_2 surface by considering adsorption energies obtained from the *ab initio* reference data (using QUANTUMESPRESSO) and to these energies data a Buckingham potential is fitted using GULP a well known molecular dynamics (MD) code for periodic systems.

M. Sc. Project (2012) with Prof. Nisanth N. Nair at the Indian Institute of Technology Kanpur, India

- On the mechanistic study of the Diels-Alder reaction in aqueous medium ("On Water" reactions) using hybrid QM/MM molecular dynamics as implemented in CPMD (Car-Parrinello Molecular Dynamics) along with metadynamics to obtain the free energy profile.

Summer Project (2011) with Prof. Nisanth N. Nair at the Indian Institute of Technology Kanpur, India

- Development of a method for Resonance Raman Spectroscopy to study metalloproteins.

Simulation Packages and Programming Language Experience

- CHARMM
- AMBER
- GULP
- GROMOS
- GAUSSIAN03/09
- CPMD
- QUANTUMESPRESSO
- FDMNES (X-ray absorption spectra calculation)
- FORTRAN 90
- LaTeX
- VMD
- MOLDEN
- Umbrella Sampling, Thermodynamic integration and Metadynamics (For free energy calculations)

Academic Achievements

- University Gold Medal for Academic Excellence in B.Sc (Rank 1^{st}), Ravenshaw University, 2010
- Pravati Mishra Memorial Award (Ravenshaw University).
- Best poster award Swiss Chemical Society Fall Meeting 2015
- Best poster award at Swiss Chemical Society Fall Meeting 2016

Publications

1. Maurus Schmid†, **Akshaya K. Das**†, Clark R. Landis, and Markus Meuwly. Multi-State VALBOND for Atomistic Simulations of Hypervalent Molecules, Metal Complexes and Reactions. *J. Chem. Theo. Comp.*, (In print), 2018. († *equal contribution*)

2. **Akshaya K. Das** and Markus Meuwly. Kinetic Analysis and Structural Interpretation of Competitive Ligand Binding for NO Dioxygenation in Truncated Hemoglobin N. *Angew. Chem. Intern. Ed.*, 57:126, 2018

3. **Akshaya K. Das** and Markus Meuwly. Hydration Control Through Intermolecular Degrees of Freedom: Molecular Dynamics of [Cu(II)(Imidazole)$_4$]. *J. Phys. Chem. B*, 121:9024, 2017

4. Hans Jakob Woerner, Christopher A. Arrell, Natalie Banerji, Andrea Cannizzo, Majed Chergui, **Akshaya K. Das**, Peter Hamm, Ursula Keller, Peter M. Kraus, Elisa Liberatore, Pablo Lopez-Tarifa, Matteo Lucchini, Markus Meuwly, Chris Milne, Jacques-E. Moser, Ursula Rothlisberger, Grigory Smolentsev, Joël Teuscher, Jeroen A. van Bokhoven, and Oliver Wenger. Charge migration and charge transfer in molecular systems. *Structural Dynamics*, 4(6):061508, 2017

5. Maksym Soloviov, **Akshaya K. Das**, and Markus Meuwly. Structural Interpretation of Metastable States in Myoglobin-NO. *Angew. Chem. Intern. Ed.*, 55(34):10126–10130, 2016

6. **Akshaya K. Das**, R. V. Solomon, Franziska Hofmann, and Markus Meuwly. Inner-Shell Water Rearrangement Following Photoexcitation of Tris(2,2'-bipyridine)iron(II). *J. Phys. Chem. B*, 120(1):206–216, 2016

7. Haiyun Jin, Puja Goyal, **Akshaya K. Das**, Michael Gaus, Markus Meuwly, and Qiang Cui. Copper Oxidation/Reduction in Water and Protein: Studies with DFTB3/MM and VALBOND Molecular Dynamics Simulations. *J. Phys. Chem. B*, 120(8):1894–1910, 2016

8. Pierre-Andre Cazade, Halina Tran, Tristan Bereau, **Akshaya K. Das**, Felix Klaesi, Peter Hamm, and Markus Meuwly. Solvation of Fluoro-Acetonitrile in Water by 2D-IR Spectroscopy: A Combined Experimental-Computational Study. *J. Chem. Phys.*, 142(21), 2015

Book Chapter

1. **Akshaya. K. Das** and Markus. Meuwly. Empirical Force Fields for Mechanistic Studies of Chemical Reactions in Proteins. In Voth, GA, editor, *Computational Approaches for Studying Enzyme Mechanism, Pt A*, volume 577 of *Methods in Enzymology*, pages 31–55. 2016

Conference/Posters

- STC-2017 "Big Data in Chemistry - 53rd Symposium on Theoretical Chemistry 2017", Basel, Switzerland (Poster)
- Attained Summer school: "Machine Learning in Atomistic Simulation 2017", Pisa, Italy

- "NCCR Annual Meeting 2017", Grindelwald, Switzerland (poster)
- "Swiss Chemical Society Fall Meeting 2016", University of Zurich, Switzerland (Poster)
- "NCCR Annual Meeting 2016", Angelberg, Switzerland (poster)
- "Swiss Chemical Society Fall Meeting 2015", EPFL Laussane, Switzerland (Poster)
- "Mathematical and Computational Modeling in Life Sciences" 2015, Rigi, Switzerland (Talk and Poster)
- "Swiss Chemical Society Fall Meeting 2014", University of Zurich, Switzerland (Poster)
- "Chemistry Departmental Day 2012", IIT Kanpur, India (Poster)
- "Theoretical Chemistry Symposium 2010 (TCS10)", IIT Kanpur, India

Personal Details

Name	: Akshaya
Surname	: Das
Gender	: Male
Date of birth	: 21st March,1990
Nationality	: Indian
Marital Status	: Single
Permanent Address	: At-Gopalpur, PO-Prathamakhandi, Block-Kuakhia, Dist-Jajpur, PIN-755008, India